

REPORT DOCUMENTATION PAGE				Form Approved OMB No. 0704-0188	
Public reporting burden for this collection of information is estimated to average 1 hour per response, including the time for reviewing instructions, searching existing data sources, gathering and maintaining the data needed, and completing and reviewing the collection of information. Send comments regarding this burden estimate or any other aspect of this collection of information, including suggestions for reducing the burden, to Department of Defense, Washington Headquarters Services, Directorate for Information Operations and Reports (0704-0188), 1215 Jefferson Davis Highway, Suite 1204, Arlington, VA 22202-4302. Respondents should be aware that notwithstanding any other provision of law, no person shall be subject to any penalty for failing to comply with a collection of information if it does not display a currently valid OMB control number. PLEASE DO NOT RETURN YOUR FORM TO THE ABOVE ADDRESS.					
1. REPORT DATE (DD-MM-YYYY) 21-07-2004		2. REPORT TYPE Final Report		3. DATES COVERED (From – To) 25-Apr-01 - 25-Jul-04	
4. TITLE AND SUBTITLE Physics and Chemistry of Microwave Discharge in Gas Flows				5a. CONTRACT NUMBER ISTC Registration No: 2014p	
				5b. GRANT NUMBER	
				5c. PROGRAM ELEMENT NUMBER	
6. AUTHOR(S) Dr. Yuri F. Kolesnichenko				5d. PROJECT NUMBER	
				5d. TASK NUMBER	
				5e. WORK UNIT NUMBER	
7. PERFORMING ORGANIZATION NAME(S) AND ADDRESS(ES) Moscow Technical Club (MTC-IVTAN) Izhorskaya str., 13/19 Mosow 127412 Russia				8. PERFORMING ORGANIZATION REPORT NUMBER N/A	
9. SPONSORING/MONITORING AGENCY NAME(S) AND ADDRESS(ES) EOARD PSC 802 BOX 14 FPO 09499-0014				10. SPONSOR/MONITOR'S ACRONYM(S)	
				11. SPONSOR/MONITOR'S REPORT NUMBER(S) ISTC 00-7027	
12. DISTRIBUTION/AVAILABILITY STATEMENT Approved for public release; distribution is unlimited.					
13. SUPPLEMENTARY NOTES					
14. ABSTRACT There is a growing interest in the general area of Plasma aerodynamics. The purpose of this activity is to create, in a supersonic flow (up to Mach 2) and in the presence of magnetic field by means of MW and RF techniques, the discharges of different structure with full scale of electron concentration. The contractor will investigate the behavior and interaction of these discharges with shock waves under different (up to 1 Tesla) H-field intensity. Comparative analysis of these findings will be of importance for the fundamental plasma technology in a plasma-airflow interaction area, in particular, to change an aerodynamic drag of body by means of RF and MW plasma formation in front of the body and, possibly, for some problems of internal aerodynamics. This work will be vital to the understanding of what the mechanisms are behind drag reduction using plasmas and to the understanding of how to use on-board microwave and radio frequency generation capabilities for supersonic or hypersonic vehicle control.					
15. SUBJECT TERMS EOARD, Physics, Plasma Physics & Magnetohydrodynamics					
16. SECURITY CLASSIFICATION OF:			17. LIMITATION OF ABSTRACT UL	18. NUMBER OF PAGES	19a. NAME OF RESPONSIBLE PERSON WAYNE A. DONALDSON
a. REPORT UNCLAS	b. ABSTRACT UNCLAS	c. THIS PAGE UNCLAS			19b. TELEPHONE NUMBER (Include area code) +44 (0)20 7514 4299

Partner Project 2014p

“Physics and Chemistry of MW Discharge in Gas Flows”

Final Report

**To European Office of Aerospace Research and
Development**

**Period 01.04.2001 – 30.06.2004
(Entire Period of the Project)**

**Project Manager
Dr. Yuri Kolesnichenko**

**Moscow
2004**

Project team

Yu. F. Kolesnichenko	Dr. in Physics and Mathematics, IHT, Project Manager
Yu. I. Anisimov	Dr. in Physics and Mathematics, SPbSU, optic measurements
S. A. Afanas'ev	Engineer, IHT, MW and RF equipment
O. A. Azarova	Dr. in Physics and Mathematics, gas dynamic modeling
V. G. Brovkin	Dr. in Technical Sciences, IHT, MW experiment
A. A. Gorynya	Engineer, ARSRIRE, MW generator
V. I. Ivanov	Engineer, SRIMM, gas dynamic installation
D.V. Khmara	Senior Engineer, kinetic modeling and processing
V. A. Lashkov	Dr. in Technical Sciences, SRIMM, gas dynamic experiment
I.Ch. Mashek	Professor, SPbSU, optic methods
M. I. Rivkin	Dr. in Technical Sciences, ARSRIRE, MW radiation system

Assistance at different stages of investigation by

Dr.'s **V. G. Grudnitsky** and **V. N. Sukhov**,

Eng.'s **E. A. Osetrov** and **A. A. Schmitt**,

technical personnel **A. K. Molodov**, **E. A. Bocharova** and **T. A. Semenova**,

student **K. Semenov**

is greatly acknowledged

CONTENT

Introduction.....	9
1. Experimental facilities and diagnostics.....	14
1.1. Wind tunnel.....	14
1.1.1. Experimental conditions. Nozzle with Mach number 2.1.....	15
1.1.2. Investigation of working flow (nozzle 1.6).....	17
1.1.3. Working flow with nozzle M=1,2.....	17
1.1.4. Microwave unit.....	18
1.2. Diagnostic complex for modified experimental installation.....	20
1.2.1. Microwave parameters measurement.....	20
1.2.2. Probe with pressure transducer.....	20
1.2.3. Digital Schlieren system.....	22
1.2.4. Optical spectral complex. Emission characteristics of MW plasma.....	24
1.2.5. Optical complex for visualization of afterglow areas in airflow and processes of their interaction with AD bodies.....	28
1.2.6. Laser diagnostic complex for investigation of thin spatial structure of MW discharge.....	29
1.2.7. Complex for investigation of MW discharge, ignited by laser spark.....	31
1.3. Flexible scheme for MW and RF energy supply.....	33
2. Experimental research of MW discharges in air and under magnetic field action.....	35
2.1. Free MW discharge in quiescent air and magnetic field.....	35
2.2. Free MW discharge in airflow.....	44
2.3. MW discharge directed by dielectric plate.....	47
2.4. Study of plane MW discharge – gas flow interaction.....	51
2.5. MW and RF ball discharges.....	55
2.6. Separate plasma channel modeling and its study at different conditions.....	59
2.7. Initiation and control of MW discharge by external plasma channel.....	62
3. Kinetic modeling of MW plasmoid in air.....	65
3.1. Kinetic scheme assembling.....	65
3.1.1. Reactions and rate constants.....	65
3.1.2. New method for determination of electron-impact rate constants in vibrationally excited gas discharge plasma.....	66

3.1.3. Kinetic mechanisms of heating in plasma.....	71
3.1.4. Specific features of local field behavior.....	73
3.2. Determination of local parameters of inhomogeneous MW plasmoid.....	73
3.2.1. Halo modeling.....	74
3.2.2. Filament: limit curve of heating and the channels of heating.....	75
3.3. Comparison of calculated results with emission spectrum measurements.....	76
Figures to Section 3.....	77
4. MW discharge diagnostics using the method of emission spectroscopy.....	95
4.1. Emission spectrum in air and carbon dioxide non-uniform discharge plasma.....	95
4.1.1. Emission spectrums.....	96
4.1.2. Emission temporal dependencies.....	97
4.1.3. Summarizing of spectrum processing.....	97
4.1.4. Thermodynamic calculation of medium composition.....	99
4.2. Emission spectrum of MW discharge, propagating along dielectric plate.....	100
4.3. Emission spectrums with presence of atomic lines.....	101
4.3.1. Emission of DC spark.....	101
4.3.2. Observation of iron emission from MW discharge.....	102
Figures to Section 4.....	104
5. Experimental investigations of AD-bodies drag under MW energy deposition in supersonic flow.....	115
5.1. Results of exploration of aerodynamic characteristics of a body in supersonic flow with X-polarized MW discharge.....	115
5.1.1. Interaction of blunt body with central-axis-positioned plasmoid.....	115
5.1.2. Interaction of blunt body with off-axis-positioned plasmoid.....	119
5.1.3. Interaction of sphere with central-axis-positioned plasmoid.....	121
5.2. Results of exploration of aerodynamic characteristics of a body in supersonic flow with Y-polarized MW discharge.....	124
5.2.1. MW discharge in the working flow.....	124
5.2.2. Temporary and spatial evolution of Y-polarized plasmoid near the model.....	125
5.3. Interaction of plasmoid with a spike-tipped body.....	128
5.3.1. Sphere with a spike. Schlieren.....	128
5.3.2. Sphere with a spike. Kulite.....	132
5.4. Interaction of thin bodies with central-axis positioned microwave plasmoid. X polarization.....	133
5.5. Scaling in discharge channel – blunt body interaction.....	134
5.5.1. X polarization.....	134
5.5.2. Drag reduction efficiency.....	135

5.5.3. Y polarization.....	136
6. Modeling of energy deposition effects in supersonic flow.....	137
6.1. Non-linear stage of explosive-type energy deposition in MW discharge.....	137
6.1.1. Scenario of MW discharge breakdown evolution.....	138
6.1.2. Problem formulation and solution for general case.....	139
6.1.3. Comparison with the constant pressure case.....	142
6.2. Non-stationary interaction of deposited energy domain with blunt body.....	143
6.2.1. Energy injection in SS flow for drag reduction.....	144
6.2.2. Numeric procedure.....	145
6.2.3. Description of interaction mechanism.....	146
6.2.4. Principle features of interaction.....	147
6.2.5. Scaling.....	149
6.2.6. Asymmetric disturbance.....	150
6.2.7. Detachment SW velocity and comparison with experiment.....	151
6.2.8. Bifurcation – self-organization – effectiveness.....	152
Figures to Section 6.2.....	153
6.3. Non-stationary interaction of cone-shaped bodies with discontinuity.....	160
6.3.1. Non-stationary streamlining with detached bow shock wave.....	160
6.3.2. Non-stationary streamlining with attached bow shock wave.....	163
6.3.3. Quantitative results.....	164
6.4. Stationary interaction of deposited energy domain with AD body.....	169
6.4.1. Streamlining of a blunt body by SS flow with thin infinite discontinuity.....	169
6.4.2. Streamlining of a wedge by SS flow with thin infinite discontinuity.....	173
6.4.3. Interaction efficiency.....	179
6.5. Shock wave interaction with a wide long hot region (analytic results).....	180
6.5.1. Riemann problem formulation. Straight shock wave.....	180
6.5.2. Shock wave on the nose of wedge.....	183
6.6. Spike-tipped body streamlining with energy addition.....	188
6.6.1. Problem formulation for 2D planar geometry.....	188
6.6.2. Interaction with finite-length density well domain.....	190
7. General view on Beamed Energy Deposition method abilities and efficiency.....	193
7.1. Effect of channel off-axis position variation.....	193
7.2. Discharge structural factor for flow control.....	194
7.3. Scaling in discharge channel – blunt body interaction.....	196
7.4. Physics of interaction.....	200
7.4.1. Universal physical mechanism for AD body drag reduction.....	201
7.4.2. Method application range.....	202
7.4.3. Physical efficiency.....	202

7.5. Structure of discharge and discharge performance requirements for efficient application.....	204
Summary.....	205
Main results and conclusions.....	207
Acknowledgments.....	216
References.....	217
List of main publications over the Project implementation period.....	219
Appendixes.....	220
Appendix A.....	221
Appendix B.....	230
Appendix C.....	231
Appendix D.....	247

List of acronyms

2-D – two dimensional
AD – aerodynamic
BSW – bow shock wave
CCD – charge coupled device
CW – continuous wave
DR – dissociative recombination
EM – electromagnetic
EOA – electron-optical amplifier
HF – high frequency
HV – high voltage
LV – low voltage
LBD – low-threshold ball discharge
LED - light emitted diode
MW – microwave
MWD – microwave discharge
PC – personal computer
RF – radio-frequency
RT – rotational-translational
SMD – stimulated microwave discharge
SS – supersonic
UV – ultra-violet
VDF – vibration distribution function
VT – vibration-translation
VV – vibration-vibration
VV' – non-resonant vibration-vibration

Notations

ρ - gas density

v - velocity

ε - specific energy of gas

p – gas pressure

Q – dissipated power per unit mass

T – gas temperature

γ - specific heats ratio constant

T_e – electron temperature

σ - electron conductivity

E – electric field intensity

H – magnetic field strength

λ - wavelength of EM radiation

k – wave number

ω - angular frequency

ω_H – cyclotron frequency

n_e – electron concentration

ν_i - ionization frequency

ν_m – frequency of elastic collisions of electrons with molecules

N – neutral particles concentration

Δ - SW stand-off

α - angle of the attached oblique shock

β - angle between flow axis and contact line

χ - wedge angle

L – longitudinal length of discontinuity

d – transverse dimension of discontinuity

R, D – radius and diameter of AD model

η - interaction efficiency

μ_0 – magnetic permittivity of vacuum

Introduction

This Report covers more than 3 years of the Project 2014p “Physics and Chemistry of MW Discharge in Gas Flows” implementation. The sense of the Project is obtaining and investigation of MW discharges under different conditions and application the most perspective of them to plasma aerodynamic purposes.

Permanent interest during the last decade in application of gas discharges for aerodynamic purposes has resulted in arising of new discipline – plasma aerodynamics. Fast progress in such directions as flow control by MHD and/or energy deposition, drag reduction, plasma-assisted combustion and others, is a result of significant international efforts in this area [1-3] and some demand from traditional aerodynamics, faced to new challenges in its development.

The idea of focusing of electromagnetic beams for distant energetic coupling with quiescent gas or gas flow has emerged in the 60th of the previous century and was stimulated entirely by fast progress in MW and laser techniques. In spite the initial optimistic hopes for application of such systems were changed soon by much more realistic ones due to recognizing of the actual systems complexity and not so rapid progress in efficiency, the activity in scientific area reserved to itself a deep sign. Just by the end of 70th – beginning of 80th new discipline has appeared, which not so long ago was named as plasma aerodynamics. Looking at its path, one can note, that plasma aerodynamics proved to be that catalyst, which has led both to re-comprehension of well-known phenomena and to discovering new ones in several basic disciplines, such as gas discharge, gas dynamics and kinetic processes. Their non-linear interaction has exactly formed this new discipline. Its brief description can be given by using prefix non-: non-stationary, non-uniform, non-equilibrium.

Application of MW technique is not the easiest way for obtaining of discharge in airflow. This technique is sufficiently more complicated than, say DC or RF. But such options of microwave technique as distant action and speed of light energy delivery at defined point, electronic control of microwave beam focus shape and position, high efficiency of generation and suitable properties of microwave discharge makes it attractive for application. Probably the main advantage of microwaves is ability to create discharge distantly from aerodynamic body, without any connection with it, without use of electrodes and so on. Moreover, on the contrary of DC and RF one can dispose in front of a body MW discharge domains of defined shape and orientation and control their position in dependence of mission requirements. First experiments with free-

localized MW discharge in supersonic aerodynamics were carried out in 1997 by our team [4,5]. The basic idea is to modify flow parameters in front of a supersonic body by creation of discharge and, as a result, get the desired modification in aerodynamic coefficients. This trend can be specified as Beamed Energy Deposition for Plasma-Aerodynamic Application.

Plasma objects action on a flow in the vicinity of a body, as well as shock waves propagation in low-temperature plasma were investigating especially intently. Already the first experiments in this area revealed a kind of specific plasma action on the shock wave. While entering the discharge domain, shock wave decayed in two or more ones, its intensity diminished dramatically up to becoming invisible. The velocity of the leading wave – precursor - sufficiently increased. Sometimes a precursor origination led to electromagnetic effects appearing.

Two main reasons for effect explanation were proposed – gas heating (thermal mechanism) and/or plasma action (non-thermal mechanism). The last mechanism, if it would actually exist, might be extremely efficient, as power level for creation in gas medium electrons (and positive ions) of 10^{-5} content is very low.

For a long time the activity of investigation teams was aimed at finding out the conditions for non-thermal mechanism realization and sometimes the results were encouraging, i.e. gas heating seemed to be not enough for the observed effect explanation. But since first pioneer experiments, no direct proof of such mechanism existence was obtained. Meanwhile, thermal component is present in any type of energy deposition system, being useful or parasite in dependence of its intend.

Nevertheless, up to now the physical basis of the effect of SW interaction with discharge plasma is far from consensus among investigators. The variety of plasma creation methods and discharge modes lead to such a complication of situation that sometimes it seems as troubled. The idea of key experiments in this area, the conditions of which are to be purified to the extent of undoubted treatment, has led to the first experiments on drag reduction by means of MW discharge action. MW method of plasma generation in front of a body in supersonic flow being rather flexible is simpler for analysis, as free from the influence of boundaries.

Already the first experiments showed significant peculiarities in gas dynamic characteristics. Streamlining of the AD body while the discharge region was passing through the shock demonstrated its unstable behavior - fast jumps of the bow shock wave were revealed. The instant drag reduction recalculated from the measured mean one turned out to be about 50%.

Meanwhile, processing of MW discharge emission spectra indicated gas temperature rise in plasma region as not exceeding 50K. Thus, preliminary results gave some reasons to expect realization of non-thermal mechanism.

But soon it became evident that the obtained experimental data are not sufficient for a valid determination of the sequence of processes that underlie the observed phenomenon and therefore for identification of the background of the effect. Careful investigation of this phenomenon became far-going challenge for background of plasma aerodynamics. New stage of exploration became real since 2000 due to the support of the US Air Forces - EOARD. The objective of this stage was formulated as clarification of the process of MW plasma interaction with gas-dynamic structure of a flow near the AD bodies including quantifying of the main physical and chemical parameters.

The key scientific problems that are to be investigated in more or less details on this way can be formulated as follows:

- ◆ Investigation of the nature of airflow influence on MW discharge parameters.
- ◆ Control of non-equilibrium plasma objects in airflow, their structure and local parameters, including magnetic field application.
- ◆ Airflow heating by means of external energy supply.
- ◆ Shock wave modification characteristics under interaction with plasma objects in the presence of electric and magnetic fields.
- ◆ Spatial-temporal measurements of local plasma parameters in Plasma-Aerodynamic experiments
- ◆ Kinetic processes in flows study – rates, instabilities, and mutual influence plasma and gas dynamic structures.

The investigation paradigm includes 4 steps. The first step is working out such diagnostic tools that allow spatial-temporal monitoring of the phenomenon under investigation and creation of the preliminary physical model. The next includes enhancement of supersonic flow quality, as well as MW facility abilities to enlarge the area of investigation. The third stage provides full-scale model formulation. The fourth one is aimed at application of the knowledge obtained to new areas of interest. Material presented here reflects the results of activity of the first three steps.

Thus, the motivation for our persistent efforts, which are supported by the EOARD since 2000 through ISTC Projects #1779p and #2014p, is determination of the limitations for efficient

drag/flow control by means of MW discharge domains interaction with supersonic aerodynamic bodies of different shape and creation of physical basis for these phenomena.

The structure of the Report.

The first Section is devoted to description of the modernized wind tunnel, parameters of the working flow and microwave facility, including generator, radiating and focusing systems. The decisive role of diagnostics for solving the problem itself and for providing modern experiment in such a complicated area as plasma aerodynamics is evident. Most of experiments in this area can not be analyzed properly for the lack of essential information about the main discharge-flow parameters. For this reason the diagnostic abilities were sufficiently enhanced that allowed to obtain new important and valid information about the object under investigation. The part of activity connected with diagnostics is also presented in Section 1.

Finding out of conditions for efficient influence on AD characteristics can be divided in two general trends. The first is aimed at specifying of desirable parameters of disturbance in airflow, which effects in a defined manner on AD-body characteristic. The second one defines how to create this disturbance in a flow by means of electric discharge. The first trend is mostly gas dynamic one, the second – electrodynamic and kinetic.

In accordance with such approach, the results of our investigation are presented in two groups of Sections. In Sections 2-4 MW discharge structure evolution issue including electrodynamic and kinetic modeling and experiment is considered. Synchronized information about the main electrodynamic and gas dynamic parameters in plasma aerodynamic investigation is presented, as well as the results of efforts in optic information processing for determination of the main local parameters of MW discharge in quiescent gas and supersonic flow.

In Sections 5-6 experimental data and modeling of energy deposition in supersonic flow for drag reduction of a blunt body is given. In experiment attention is focused on eliminating of the spatial-temporal gas dynamic details of MW discharge region interaction with SS flow. Time-resolved Schlieren and chemiluminescent imaging along with stagnation pressure evolution registering are applied for this purpose. Single-shoot method is worked out and realized. It should be noticed that time-resolved imaging of discharge regions spatial evolution, including interaction with the shock layer is fulfilled for the first time (Section 6).

Modeling is aimed at getting answer at the following questions: what are the optimal geometry (shape) of disturbance and parameters inside it; what type of energy deposition rate -

quasi-static or explosive – is more efficient; what are scaling laws for the incoming parameters. Both modeling and experiment deals with non-stationary interaction of gas dynamic discontinuity with AD body in supersonic flow.

In Section 7 the obtained results are summarized. The problems are outlined. The efficiency of EM energy concentration, it's coupling with gas and plasma and air heating is also analyzed.

Section “Main results” is a summary of the activity implemented and the most important results obtained

We hope that the results of these investigations will contribute not only in plasma aerodynamics in its classic area, but also in the adjacent areas, such as internal aerodynamics and plasma-assisted combustion, MHD flow-control and plasma cloaking.

Investigation is implemented by the unified team from Institute of High Temperatures Russian Academy of Sciences (Moscow), Scientific-Research Institute of Mechanics and Mathematics of St.-Petersburg State University and All-Russian Scientific-Research Institute of Radio Equipment (St.-Petersburg).

1. Experimental facilities and diagnostics

The set of measures was undertaken for raising of precision and reliability of the results to be obtained: modernization of the wind tunnel, improvement of existing and application of new diagnostic equipment.

To investigate such delicate effects as formation and evolution of a vortex in a shock layer on a body it was necessary to create high-quality conditions of experiment performance, as well as possess of diagnostic equipment with high spatial and temporal resolution. For this reason the deep modernization of the wind tunnel was accomplished. The new wind tunnel allows creation uniform supersonic working flows with Mach numbers 1.3-2.1 and static pressure 25-50Torr. The working flow diameter is enlarged from 20mm to 60mm, this gave us opportunity to test a more wide range of aerodynamic models and to obtain some scaling relations. New digital Schlieren system is constructed, which allows obtaining single-shot images of bodies streamlining with time exposure about $0.5\mu\text{s}$ and relatively high spatial resolution. Imaging is synchronized with a certain phase of a process under investigation. The measuring channel, which registers the weak discharge afterglow, let us observe evolution of an excited gas region under its interaction with investigated body. Measurements of pressure on the body surface while interaction of microwave plasmoid with bow shock wave are also performed. Such complex approach let us raise validity and reliability of measurements. Blunt cylinder, hemisphere and cone are tested as experimental bodies.

Thus, the main aim of this activity is to fulfill comprehensive investigation of plasma – shock interaction in a sufficiently enhanced-quality supersonic flow and to verify the physical model proposed.

1.1. Wind tunnel

Experiments were conducted on aerodynamic wind tunnel which provided 60 mm diameter working supersonic flow [3,4]. The wind tunnel has changeable profile nozzle for Mach number from 1,3 to 3.

The general scheme of the wind tunnel is presented in Fig.1.1.

The main feature of the wind tunnel is that a special air ejector is placed after the test section. It has high pumping efficiency. The setup consists of fore-chamber (1), feeding tube for

different working gases (2), control valve of fore-chamber, supersonic nozzle (3), test section (4), AD model (5), diffuser (6), feeding air ejector tube (7), air ejector (8), and output diffuser (12). Air ejector contains fore-chamber (9), supersonic nozzle (10), and mixing section (11). Working regimes of the wind tunnel are tuned by means of the control valves V_e and V_f .

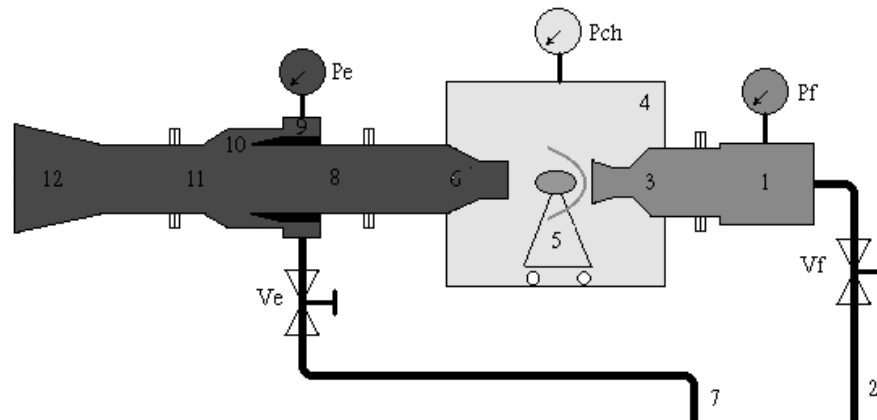


Fig.1.1. The scheme of wind tunnel.

Designations: P_{ch} – pressure in test section, P_e – pressure in ejector fore-chamber, P_f - pressure in fore-chamber, V_f – control valve of fore-chamber, V_e – control valve of ejector.

This setup can create flows of different gases and mixtures.

Distributions of gas dynamic parameters (static and stagnation pressure) have been measured on this working regime of wind tunnel. Measurement was carried out by means of pneumatic probes.

1.1.1. Experimental conditions

Nozzle with Mach number 2.1

The wind tunnel allows to create working flows with sufficiently uniform distribution of gas dynamic parameters (velocity, temperature, pressure) and perform investigations of aerodynamic models with diameter up to 20-25 mm. Under the specified conditions the stable flow-collinear microwave discharge was obtained. All experiments were provided in supersonic flow with Mach number 2.1. The flow core radius is about 25 mm. Reynolds number, based on

model diameter 20 mm is about 4×10^4 . The models were placed at distance 100-130 mm from the exit section of the working nozzle. Non-uniformity of the Mach number in this area is not worse than 5%. Static pressure of the flow could be varied in the range 25-50 Torr.

Static pressure of 25 Torr in test section has been achieved when working nozzle with Mach number 2,1 and output section diameter 60mm is used for creating of supersonic gas flow. Stagnation temperature in the flow was 300K^0 .

Mach number distribution in the working flow was calculated using results of static and stagnation pressure measurements. It can be seen on Fig.1.2. Radius of the flow core is about 25 mm. Reynolds number based on the model diameter 20 mm is 4×10^4 . Models were placed at the distance 100 – 130 mm from the working nozzle. Inhomogeneity of Mach number in this place of the flow is not worse then 5%.

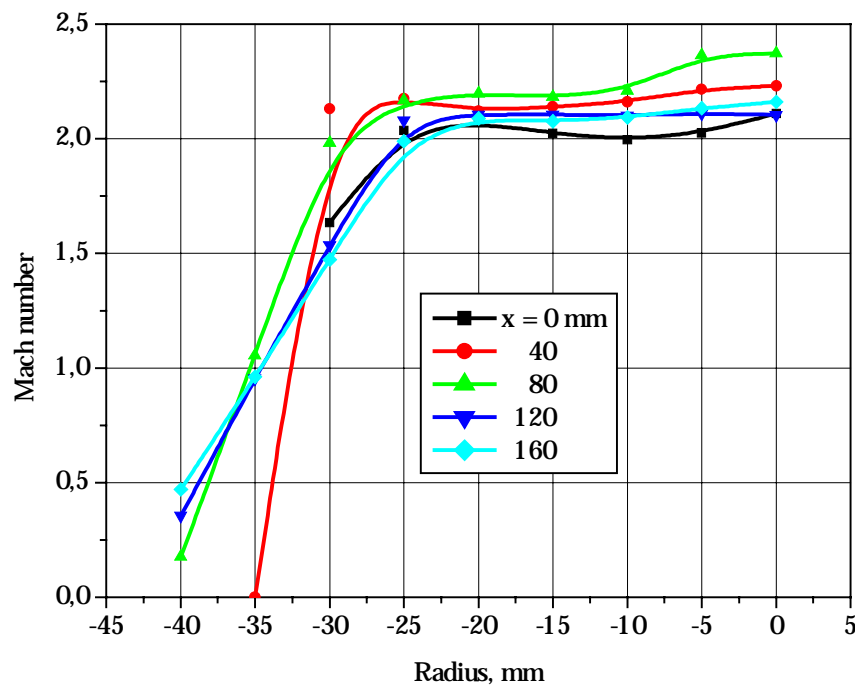


Fig.1.2. Mach-number distribution in the working flow.

The wind tunnel gives opportunity to obtain working flow with good enough homogeneous gas-dynamic parameters (velocity, temperature, pressure) and to investigate model with diameter up to 20 – 25 mm. Microwave discharge is obtained in the working flow under the mentioned conditions.

1.1.2. Investigation of working flow (nozzle 1.6)

Measurements were made in the area of the working flow where models would be placed. Pressure in test section was 46 Torr.

On Fig.1.3 distribution of Mach number in three sections of the flow can be seen (r – distance from the axis of the flow). Homogeneity of the working flow is good enough. Mach number of the flow is 1,52. Deviation of Mach number from its middle value is not more than 2%. The core diameter of the flow is about 40 mm.

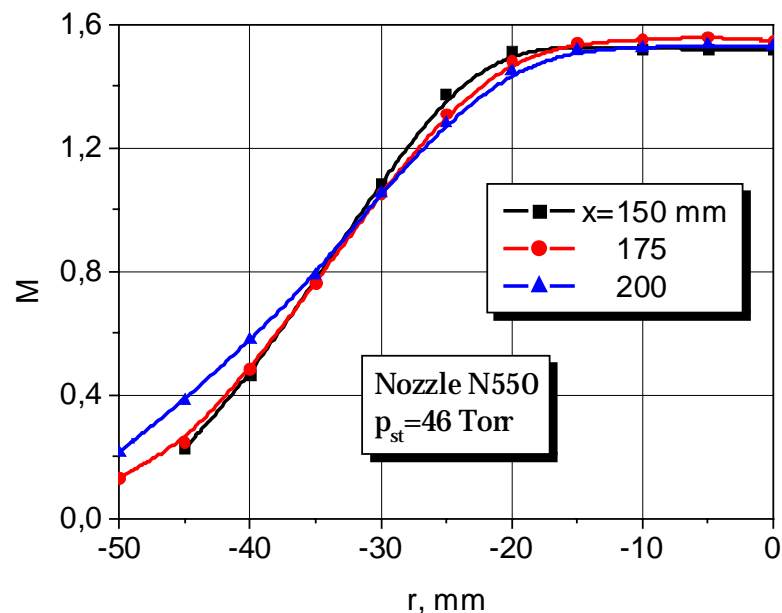


Fig.1.3. Distribution of Mach number in the three cross-sections of the flow.

1.1.3. Working flow with nozzle M=1.2

Result of measurements of Mach number distribution in the working flow is presented on Fig.1.4. Pressure in the test section in these experiments was about 65 Torr. Good enough homogeneity of gas dynamic parameters in the working flow can be seen (not worse than 5%). The core of the working flow is decreasing via enlarging distance from the output section of the nozzle because of boundary layer growth. It can be remarked on the Figure.

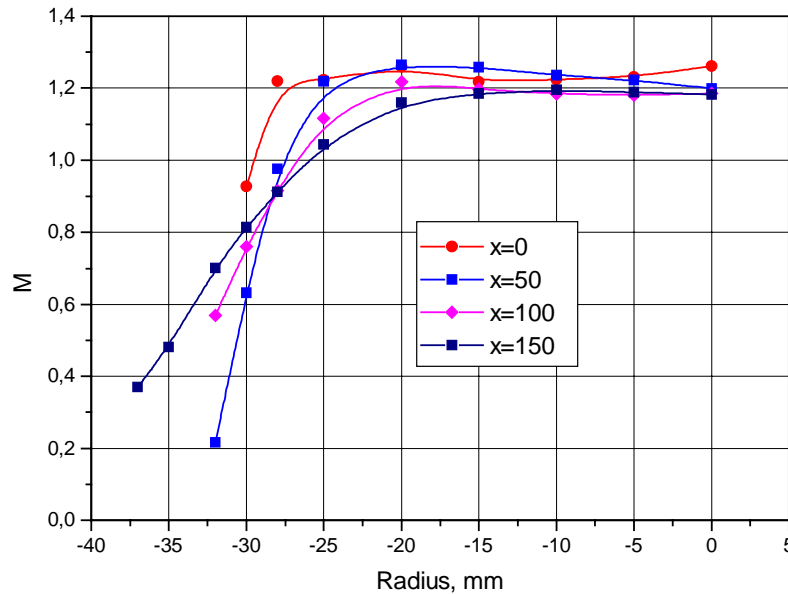


Fig.1.4. Mach number distribution for nozzle M 1,2.

Experimental models. The bodies of classic shape – blunt cylinder, hemisphere, cone and wedge - were used as models in experiment. The models were manufactured out of Teflon in order to minimally disturb the electric field distribution and the size and position of microwave plasmoids. The model size 20 mm was taken as basic one from the flow core dimension, therefore the main portion of experiments was carried out with the models having 20 mm diameter basis.

For scaling factor investigation the models (blunt cylinder and hemisphere) of 8, 12, 16, 20 and 24 mm were manufactured.

The investigated cones had apex angle 40, 80 and 120 degrees.

The pressure sensor was installed in the blunt cylinder on the axis at stagnation point, and on the radius 3 mm and 6mm from it. For the hemisphere these positions were 0 mm (stagnation point) and 4 mm correspondingly.

1.1.4. Microwave unit

The microwave unit is the klystron type generator of high power pulses with the X-range carrying frequency. The microwave pulses come through the wave-guide to the radiator of

parabolic mirror mounted in the working chamber. The wave-guide is hermetically sealed, the radiator is closed up by the radio-transparent unit, the air pressure in the wave-guide is maintained at the level 1.8 atm. The radiator is fixed just under the working flow of the wind tunnel. The mirror is maintained on the ceiling of the test section and focuses the microwave radiation on the flow axis, in the region remote 70-90 mm from the nozzle exit. The ultimate pulse power value attained is 210 kW. The pulse duration range is in between 1.2-2.2 microseconds. The pulse frequency can be as high as 500 Hz. The maximum mean power of the microwave facility is about 400W. The facility can operate with both linear and circular polarization. Electric vector of linearly polarized MW radiation can be X, Y and Z directed (X – along flow direction). Distribution of electric field for X-geometry is presented at Fig.1.5.

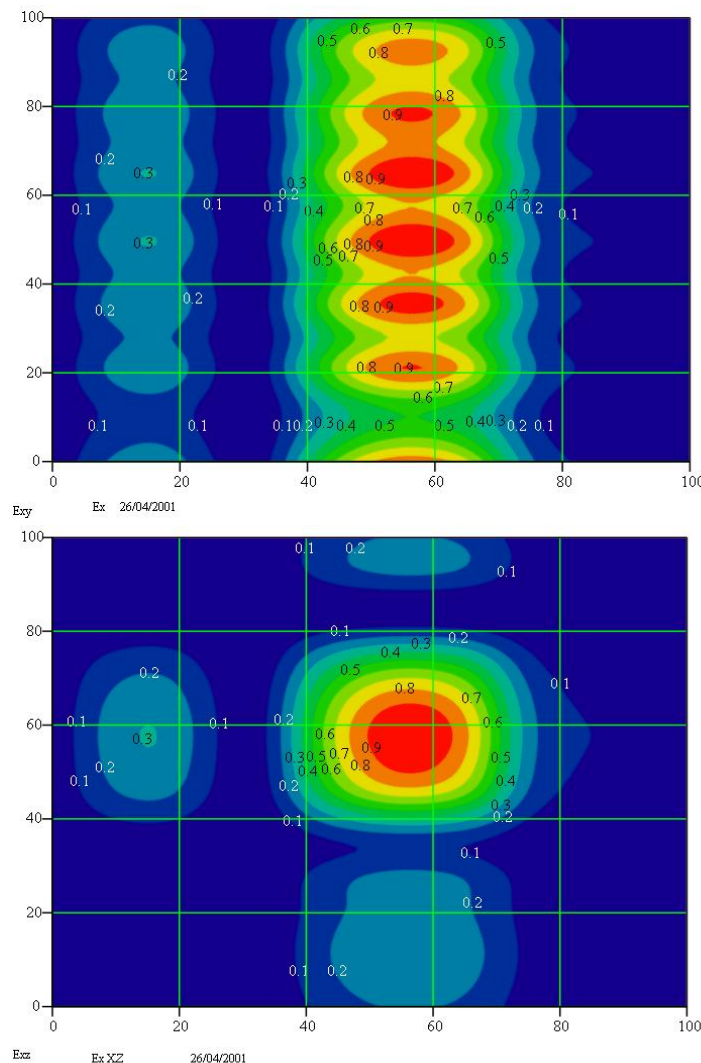


Fig.1.5. Electric field distribution in x-geometry

1.2. DIAGNOSTIC COMPLEX FOR MODIFIED EXPERIMENTAL INSTALLATION

The new gas-dynamic scheme of experimental setup (ejector pumping outside of gas-dynamic chamber) opens the possibility to investigate the plasma-body interaction for a single realization of MW discharge. In our previous experimental activity the MW generator was used with impulse repetition frequency 450 - 500Hz. The output signals (Schlieren, Kulite) were integrated over a number of realizations. Unfortunately, MW energy deposition in supersonic flows is comparatively unstable, breakdown probability in supersonic gas flow significantly varies for each realization of MW impulse. In this situation, some fine space details of Bow-Shocks - MW plasma interaction processes may be lost in the averaged picture. For this reason a single-mode operation is of importance. This operation mode of diagnostic complex demands the essential changing in each of its parts.

1.2.1. MICROWAVE PARAMETERS MEASUREMENT

The spatial distributions of electric fields, created by focusing systems in the working zone in X and Y-geometry is investigated at rather small levels of MW power with the aid of the mobile probe (Fig.1.5). The probe is moving inside of the research area by the coordinate gear.

Comparison of these distributions with calculated ones shows their satisfactory agreement.

The instant values of the input MW power and the instant values of the power having passed through plasmoids in a flow are registered by standard MW - detectors with a bandpass 50 MHz. Their output signals after amplification are analyzed in CAMAC system. The fast Flash ADC F4226 is used for work, its conversion time being about 50 ns.

1.2.2. PROBE WITH PRESSURE TRANSDUCER

For measurements of instantaneous values of stagnation pressure in plasma – AD body interactions, the band-pass of using pressure probe was essentially increased. Practically – for modified probe the resolution time approaches to the theoretical limit for the used type of pressure transducer.

Probe with transducer Kulite was applied both for investigation of plasma-body interaction and for measurement of the working flow parameters. The pressure sensor has been created on base of low-impedance wide band tenzo-resistive differential pressure transducer Kulite, XCS-093, 5 PSI. Its natural frequency is 160 kHz, static sensitivity – about 0.3 mV/Torr. Scheme of the probe, based on the Kulite transducer is shown on Fig.1.6. Transducer is placed in external steel cylindrical case and isolated from it by the Teflon ring. At the same time, this ring separates the measuring pressure and the basic pressure (static pressure in the working chamber). The measuring part of the pressure sensor is connected with the flow area under investigation by the orifice in steel case. The orifice diameter is 2 mm. A differential amplifier with bandpass 0.01-800kHz, and gain level +30dB analyzes an output transducer signal. This signal is recording by the fast flash ADC F4227 in CAMAC system. Flash ADC begins to work simultaneously with synchro-impulse from MW - generator. This permits to measure both the single realizations of pressure signals with comparatively low-level S/N and the averaged signals with excellent S/N level.

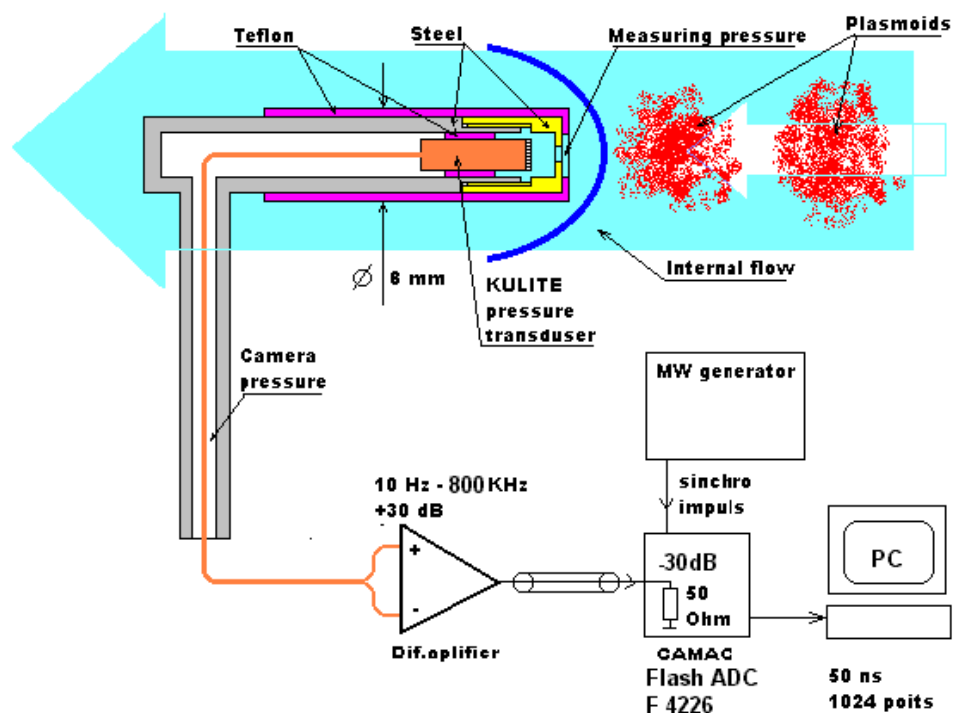


Fig.1.6. Scheme of Kulite probe connection

Transition characteristics of the pressure sensor were investigated on the specially constructed low-pressure shock tube. Calibration was made at the pressures, which are close to that in the working flow of the wind tunnel (of the order 50-80 Torr). The method of probe calibration was also worked out.

The results of calibration show that the constructed pressure probe has resolution time of order 2 μ s and sensitivity 0,209 mV/Torr.

1.2.3. DIGITAL SCHLIEREN SYSTEM

For measurements of instantaneous Schlieren pictures of plasma – AD body interactions, recording of instantaneous plasmoids placing, investigations of spatial distribution of light emitted in active phase of MW discharge, the light source in Schlieren system and CCD camera was essentially modified. In result, we have the resolution time of Schlieren system about 0,5 msec, with high suppression of parasite signal from discharge light. The photometrical regime of CCD camera (with a high linearity for light intensity) and its comparatively short open gate state (12 msec) permits to determinate the plasmoids position and spatial discharge light distribution for a single realization of MW discharge.

In our previous experimental activity the MW generator was used with impulse repetition frequency 450 - 500Hz. Ordinary CCD - TV camera with frame duration 20msec was used for digital analyzing of Schlieren picture. In this case CCD averages about 10 Schlieren images in each frame. This operation mode of Schlieren system has good sensitivity for weak space disturbances in investigation area of Bow-Shock - MW -plasma interactions.

Unfortunately, MW energy deposition in supersonic flows is comparatively unstable (breakdown probability in supersonic gas flow significantly varies for each realization of MW impulse). In this situation, some fine space details of Bow-Shocks - MW plasma interaction processes may be lost in the averaged picture.

Several problems are arising when we begin to construct optical Schlieren system without time-averaging for gas-dynamic objects with maximum velocity volume about (500-1000 m/s):

1. The duration of impulse light source has to be less than (0,3-0,5)msec (space shift of thin details in Schlieren pictures 0,2-0,5 mm), but the energy in light impulse has to be in 10 times more for getting the same Signal/Noise ratio in a single picture.

2. The CCD camera in use has to have open gate time less than duration of MW discharge active phase (2-3mcsec). It is necessary for suppressing of parasite discharge light.
3. For getting the Schlieren pictures at the different time-shift between MW and light impulses one needs to create the precision scheme of synchronization.

The scheme of the developed diagnostics system is presented on the Fig.1.7.

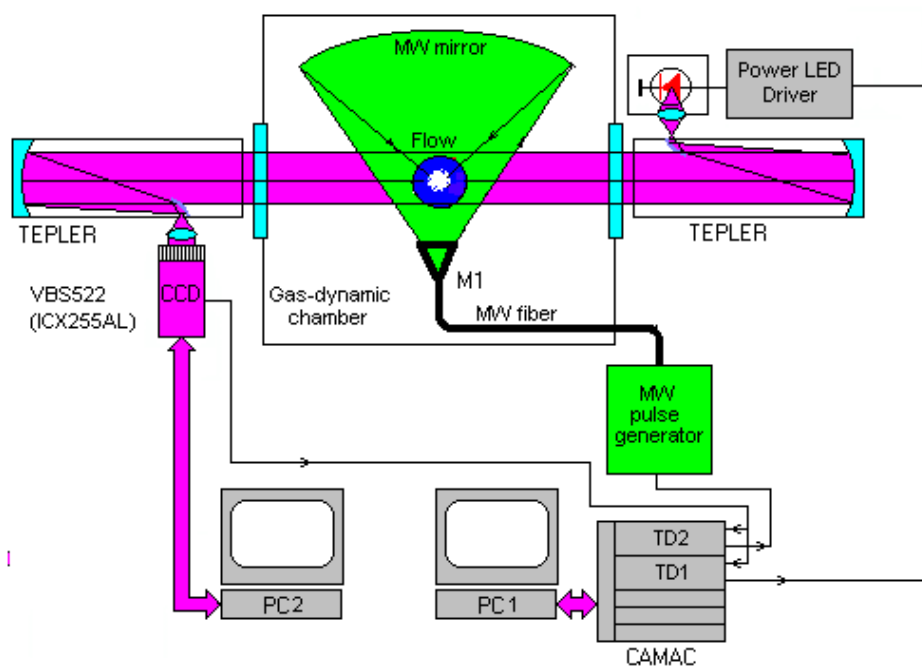


Fig.1.7. Scheme of Single-Shoot operation mode of Digital Schlieren system and Pulse MW generator

Two PC are used in this system. The PC1 checks the two-channel driver of time-delay in CAMAC system. The output signal of driver 1 launches the impulse driver of High-Brightness Light Emitted Diode (LED). Type of this LED is LUXEON STAR/O, amplitude of current pulse-16 A, duration - 0,3mcsec. At these pumping parameters LED generates light impulse with duration 0,5 mcsec, spectral range (400-700) nm and output energy about 3-5 mJ. The duration of this delay is fixed and is equal to 19988 mcsec. For this delay light impulse of LED is positioned inside of minimal interval of the open-gate state CCD (12mcsec). Output signal of

driver 2 launches the MW generator, operating in “external launch” regime. The delays between MW pulse and light pulse are managing by PC1 and can be changed from 0 to 1000 mcsec.

The new Single-Shoot optical diagnostic Schlieren system uses the completely computer-managed digital CCD VBS522 (EVS-company, Russia). It is based on ICX255AL (Sony) chip, has internal synchronous AD converter and uses the LPT -computer port for transfer of images in PC 2. For eliminating of plasma emission light on high-sensitive CCD detector the last operates with minimal open electronic gate time (12mcsec). This time interval is placed at the end of CCD frame, which has standard duration – 20000 mcsec.

Both computers, PC1 and PC2 operate in asynchronous regime. PC1 continuously manages time intervals with accuracy about 1 mcsec. Computer PC2 is used for images recording and camera parameter managing.

1.2.4. EMISSION CHARACTERISTICS OF MW PLASMA. OPTICAL SPECTRAL COMPLEX

The most essential regimes, which have to be realized in spectral complex for analysis of light emitted in active phase of MW discharge are:

- The measurements of temporal dynamic and spatial distribution in behavior of most interesting spectral lines (or integral intensity of discharge light). This channel based on fast photo multiplier with frequency band passes more than 20 MHz. It can be used either with spectrometer (regime of registration of separated spectral line), or without it (regime of registration of integral emitted in discharge light).
- Spectral measurements of some electron spectrums for N₂ with time resolution about 100 nsec. This stroboscopic method permits to investigate comparatively short parts of N₂ spectrums with middle spectral and high temporal resolution. It based on PC – managing scanning diffraction spectrometer with high light gathering power, high sensitivity photo multiplier, operating in stroboscopic regime and Sample – Hold CAMAC system.
- Measurements of time – integrated spectrums of discharge light with high spectral resolution. This method based on high – resolution diffraction spectrometer and PC managed high – sensitive line CCD detector. This channel permits to investigate comparatively wide spectral branches (12 nm) with high spectral resolution (0,1 nm).

General scheme of optic measurements is shown at Fig.1.8. Three measuring channels support investigation of spatial-temporal and spectral characteristics of light emission of MW discharge in supersonic flow. For eliminating of an influence of parasite scattered MW field on the sensitive optical sensors – photo-multipliers (PM) and CCD device - the fiber optics is used. We use quartz - polymer fibers (spectral range from 300 nm to 1100 nm) with numerical aperture 0.4 and core diameters 125 and 400 μm . Two identical optical systems are placed on the coordinate device in the vicinity of the working flow inside of the test section. Their optical scheme for radiation collection and transportation consist of quartz lens and high-aperture optical fiber. The distance between discharge region and the input lens of each optical system is chosen as small, as possible - 230 mm. The relative orifice of the optical systems is about 1/2, in correspondence with high numerical aperture of the fiber in use. Both channels collect the

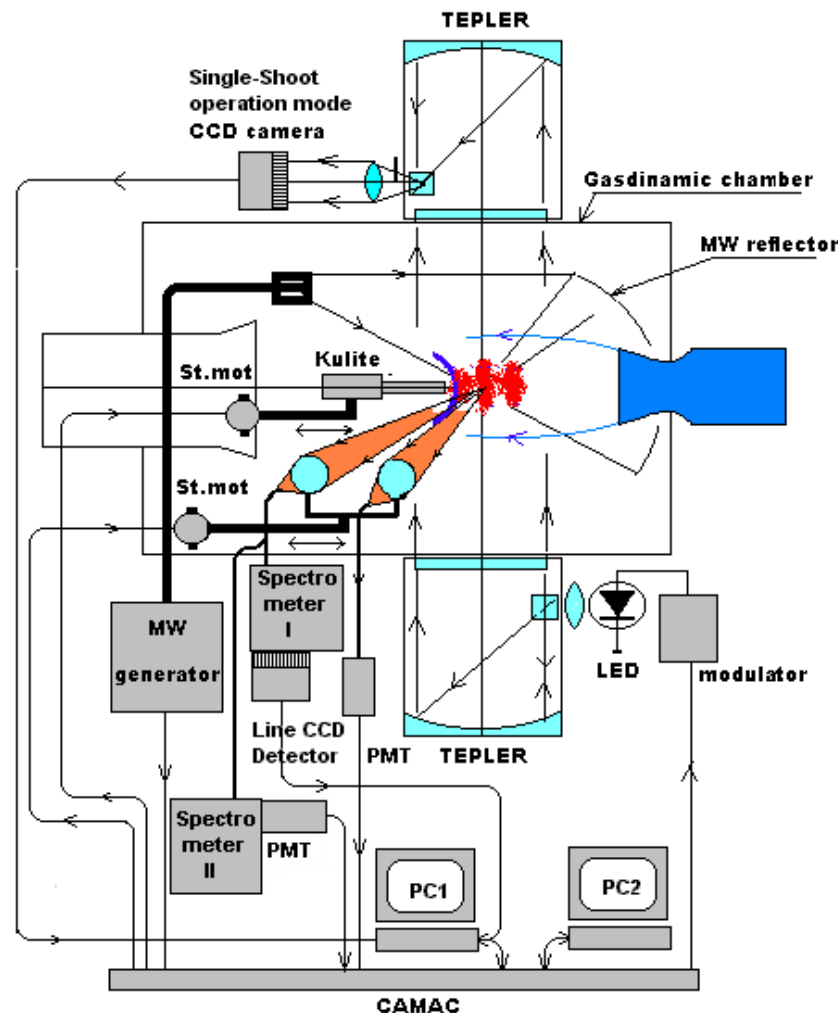


Fig.1.8. General scheme of measuring complex for spectral unvestigations.

emitting light from the same area of discharge. The position of the area to be observed (investigation point, X-coordinate, or Y - coordinate) can be changed by the coordinate device displacement from 0 to 190 mm with 0.3 mm step and 60 mm/s velocity. Dimensions of investigation area, corresponding to core fiber diameter 125 μ m are 1 mm in diameter and 15 mm in length. For core diameter 400 μ m these dimensions are 3 mm and 45 mm correspondingly.

The *first* optical channel is used for temporal and spatial measurements of the emitted light. Its short wave spectral limit is determined by the fiber (300 nm), the long wave limit - by sensitivity of PM (750 nm). The output signal from PM passes through the fast amplifier (equivalent load resistor is 10 kOhm, band-pass about 20 MHz). Signal from the amplifier goes either to the flash-ADC F4226 (temporal measurements in discharge light emitted), or to Sample - Hold (S-H) device (spatial distribution of light emitted by plasmoids). The sample-time of S-H is 100 ns, and the delay time for sampling moment - 1.0-1.5 μ s after beginning of impulse MW power. The last correspond to the maximum level in emitting light for the typical part of discharge realizations. Instantaneous level of light intensity is converted in ADC FK-72 (12 bit, 70 μ s) and is stored in PC memory, where the necessary number of realizations is summing for a defined level of S/N attaining. High sensitivity of this optical channel permits to use it both for investigations of integral luminescence processes in supersonic flow and for measurements in comparatively narrow spectral range, for example 5 - 10 nm. In this case, the light being collected by the optical system then passes through the spectrometer. This operation mode makes it possible to investigate the temporal and spatial behavior of the most essential vibration - rotational spectral bands of discharge radiation.

The *second* optical system is used for spectral measurements. It operates with high-light gathering power spectrometer MDR-2 which has relative orifice 1/2, grids with 1200 1/mm, dispersion 2 nm/mm and spectral width of instrumental profile 0,2 nm for slit 100 μ m. Spectrometer is controlled by the CAMAC system. Optical axis for this spectral channel is perpendicular to the flow axis.

The scanning over the wavelength of the monochromator is made by means of the step-by-step drive. The minimum spectral step is 0.029nm/step. Spectral device has been gauged in the range of wavelengths 300-600nm with Hg-He spectral lamp of type of DRGS-12, worked in standard operation mode. Spectral sensitivity of the device has been gauged in the working wave

length range by means of light-measuring lamp SIRSH 8.5-200-1 with the color temperature about 3000K.

The output radiation of the spectrometer is transformed to an electrical signal by the photoelectric multiplier of the type of the FEU-79. The output signal of the preamplifier is analyzed by the sample-storage circuit. Time of sample is 0.1 μ s, sample delay time is 1-3 μ s. The signal of the sample-storage circuit is recorded by the computer and the spectrometer is tuned in step on the wavelength.

One of the serious problems in spectral measurements in supersonic flows is comparatively short run-time of the working gas-dynamic regime. Usually, this time is limited to about 50 - 70 s and it do not allow getting the spectra with high resolution in wide spectral range - the spectral velocity of tuning turns out be rather fast (0,03 nm/step with step frequency 250 Hz). The output light of spectrometer is detected by photo-multiplier (PM FEU79). It provides two operation modes. The first is the analogue regime, the second – the digital regime (photo-counter). In the analogue regime the output signal of FM passes through trans-impedance transducer (equivalent transducer resistor is 4.7 MOhm, band-pass frequency 1 MHz) and goes to S-H CAMAC device, mentioned above. Time - delay for this channel corresponds to the maximum of signal on transducer output. The digital regime is used comparatively rear, only for registration with maximal spectral resolution.

The *third* spectral channel based on CCD line detector TCD1304AP (TOSHIBA) with special micro-controller and diffraction spectrometer MCD. The light of discharge is collected by a quartz lens, placed inside of experimental chamber and is transmitted in spectrometer through a comparatively short (length about 2 m) quartz-polymer optical fiber with numerical aperture 0.4. CCD detector has pixel size 8 μ m*200 μ m and thin glass window (about 0.5 mm). In front of it the quartz cylindrical lens (F=30 mm) is placed. The line dispersion of spectrometer is 12 A/mm, relative orifice - 1/10, observing area - about 120 A. Spectral coefficient for this CCD is about 0,096 A/pix. Slit width is taken as 100 μ m for all experiments. The middle inclination of spectral sensitivity curve for couple CCD-fiber is 0.5%/A for range 390 nm, and 1.3%/A for 350 nm. The total time of single measurement is to be comparatively long - 20-25 s.

1.2.5. OPTICAL COMPLEX FOR VISUALIZATION OF AFTERGLOW AREAS IN SS FLOWS AND PROCESSES OF THEIR INTERACTION WITH AD BODIES

Investigation of temporal and spatial behavior of afterglow areas, arising in SS flow on the places, when the MW discharge was ignited, is a very important part of diagnostically complex. The data, obtained from these measurements, may be very useful for interpretation of Schlieren picture of Plasma-AD body interactions. Optical complex for observing of weak luminescence in SS flow based on strongly intensified and gating CCD camera. The sensitivity of this camera approaches to sensitivity of photo multiplier, operating in photo counter regime, its minimal open gate state is about 1 mcsec.

High repetition rate of MW impulses (500 Hz) makes it possible to create comparatively simple system for visualization of spatial - temporal behavior of excited gas volume in flow after the end of active phase of MW discharge. In these areas, moving together with flow down the stream, one can observe afterglow, identified with chemiluminescent process in air. This system also can be used for investigation of discharge spatial structure evolution in active phase with microsecond-scale temporal resolution.

For visualization of the moving domains, ordinary CCD TV camera and three-stage Electron-Optical Amplifier (EOA) with electrostatic gate are used (Fig.1.9).

Spectral range of EOA photo-cathode is 360 - 800 nm, amplification factor for brightness - more than 60 000. Each stage has a high-voltage power supply (10 kV), the first stage has electrostatic gate with managing voltage 1 kV. The time of open-gate state can be done as short as 1 -10 μ s, repetition frequency corresponds to frequency of MW discharge and is about 500 Hz. The moments of open - gate state has a time delay relatively MW impulses. This delay is controlled by CAMAC system and changes from 2-3 μ s to 600 μ s. Time-averaged pictures in CCD sensor are recorded in PC. Natural spatial resolution of this EOA is 30 lines/mm for the central part of luminescent anode, but for strobe - regime, in which this EOA is used, this parameter is dramatically lower - about 5-7 lines/mm. In addition, in this operation mode, EOA has an essential distortion. Spatial resolution and distortion of this EOA strongly depends on its open state time.

Spectral range for pictures of active and passive discharge phase is different. Active phase due to high intensity of light emission is monitored either through neutral high-density

optical filter, or different narrow bandpass interference filters - 393 nm (corresponds to 1-4 transition in Nitrogen), 534 nm, and 734 nm. Weak luminescence areas in passive phase of discharge are to be investigated without any filters and in maximal amplification EOA operational mode.

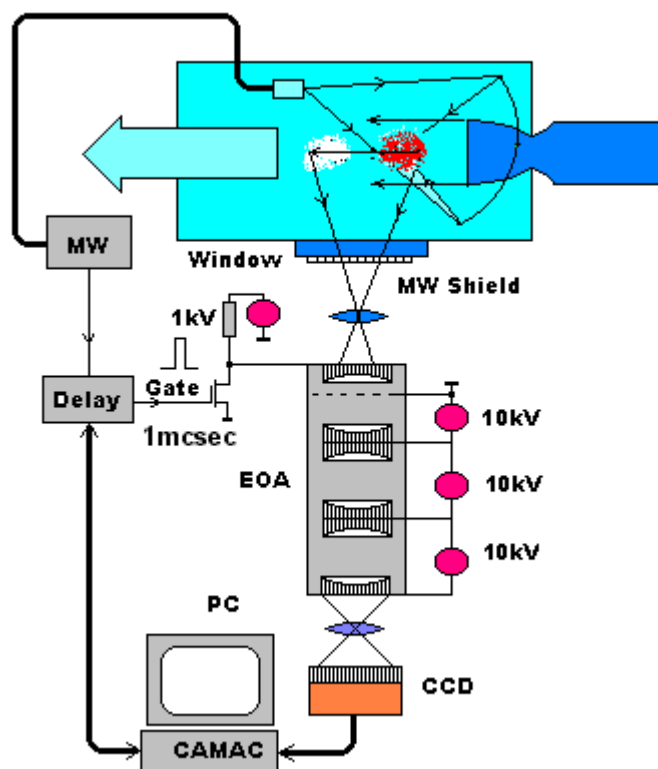


Fig.1.9. Diagnostics system for investigating of exiting gas areas.

1.2.6. LASER DIAGNOSTICAL COMPLEX FOR INVESTIGATION OF THIN SPATIAL STRUCTURE OF MW DISCHARGE

MW discharge at the pressure diapason 20-100 Torr has a very inhomogeneous structure. Preliminary investigations of discharge pictures shows, that in this kind of discharge very thin and brightness filaments are arising inside of main discharge area body (Hallo). One of the possible ways for measuring of electron temperature and concentration in these very thin and spatially unstable objects may be Laser Thomson Scattering Technique. Created laser Thomson

scattering diagnostic complex is based on Q-switched Ruby laser, diffraction spectrometer and intensified CCD camera, mentioned above.

Figure 1.10 describes the experimental scheme for investigation of Thomson scattering in MW discharge in SS flow with static pressure 20 - 50 Torr and Mach number 1.5 - 2.

Impulse Ruby laser of 0.2 J pulse energy and 20 ns pulse duration is used. Output diameter of laser beam is 8 mm. The laser beam is introduced into test gas-dynamic chamber through the converging lens L1 (F=0.5 m), Brewster window (direction of laser beam polarisation is horizontal) and 0.5 m Copper tube with diameter less than wavelength of MW generator. This construction allows to suppress the parasite emission of MW radiation outside test chamber with high efficiency (- (35 – 40) dB). The beam, passed through the plasma, is collected in to the Wood's horn and is absorbed there.

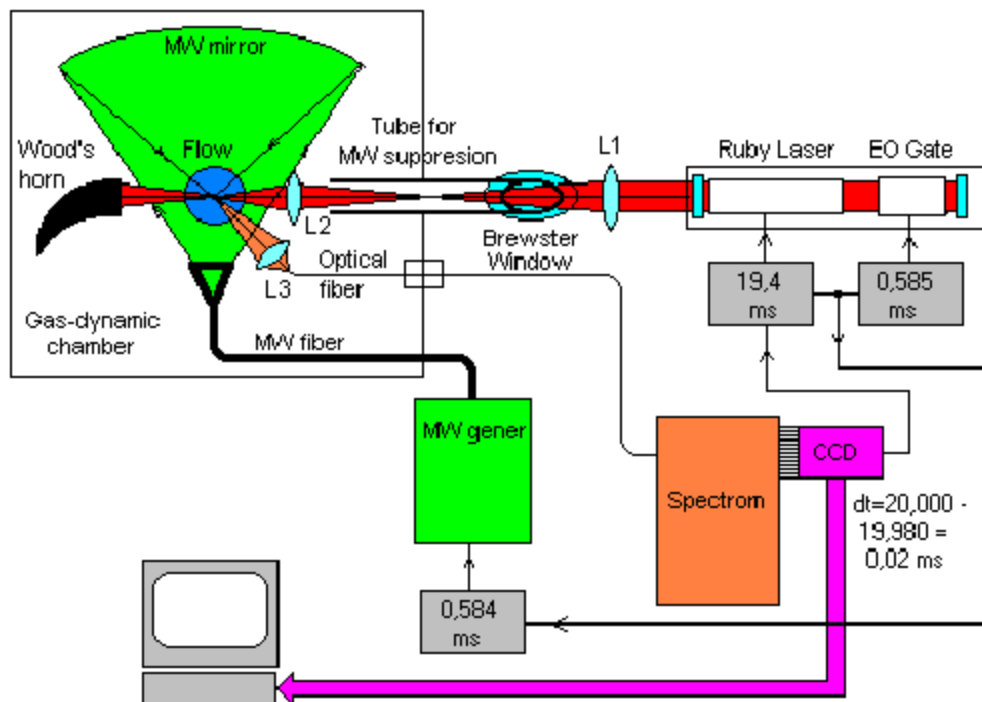


Fig.1.10. Scheme of laser Thomson scattering technique

Laser beam is focusing on to the point of measurement by lens L2. For laser beam divergence $3 \cdot 10^{-3}$ rad and focusing lens with focal length 100 mm, the beam spot diameter is

only 0.6 mm.. Scattering laser light is collected at angle 135^0 by high light gathering power objective L3 (F=50 mm, relative orifice 1/1.16) and is directed in quarts – polymer optical fiber with numerical aperture 0.4 (core diameter 0,4 mm, length 2 m).

From fiber output the collected light is analysing by diffraction spectrometer. Spectrometer has line dispersion 24 A/mm, entrance slit 0.1 mm, relative orifice 1/10 and straight light suppression level 10^{-5} . The output spectrum is monitored by intensified CCD camera. It has stage of Electro - Optical Amplifier (EOA) with gain for brightness of about $3 \cdot 10^4$. Photo-cathode of this EOA has a spectral sensitivity diapason 550-700 nm. Fully PC - monitored CCD camera based on high sensitive chip ICX255AL (SONY).

Laser impulse is synchronised with MW generator pulse and has the varying time-delay relatively MW pulse beginning.

For eliminating of plasma emission light on high sensitive CCD detector the last operates with minimal open electronic gate time (1 μ s). This time interval is placed at the end of frame, which has standard duration – 20000 μ s. Synchronising impulse from CCD (arising in the beginning frame) launches the pumping lamp of Ruby laser with time–delay 19400 μ s. MW generator starts its operation 584 μ s later, and has pulse duration 1.5 μ s. Electro – Optical Laser Gate opens (0.5-3) μ s later than MW impulse begins.

Time resolution of the developing method is about 100 ns. It includes the laser impulse duration and apparatus errors in time-delay generators. Investigated area in a flow is about $0.5 \times 0.5 \times 0.5 \text{ mm}^3$.

1.2.7. COMPLEX FOR INVESTIGATION OF MW DISCHARGE, IGNITED BY LASER SPARK

Several problems are arising in practical applications of MW discharge in plasma-dynamic investigations, especially in pressure range 100-760 Torr. Most important of these - the difficulty of focusing MW radiation for getting the breakdown level of electric field in investigation flow. The next problem is connected with great difficulties in managing of spatial character of MW plasmoids shape. One of the possible ways to solve these problems is using of laser initiator.

The scheme of experimental facility presented on the Fig.1.11. Gas-dynamic chamber ($1 \times 1 \times 1 \text{ m}^3$) may operate as at atmospheric pressure, as in vacuum regime (minimal pressure less than 25 Torr). It contains the MW radiating and focusing system and impulse Q-switched Ruby laser with optical system for laser beam focusing.

X-range impulse MW generator with output power 180 kW and pulse duration $1.2 \mu\text{s}$, via radiating system illuminate the parabolic mirror M1. It has the diameter 0.8 m and focal length about 0.3 m. In focal area of this mirror the complex periodic structure of MW field is arising (see Fig.1.5). This distribution has several maximums, one of these (with a greatest value of

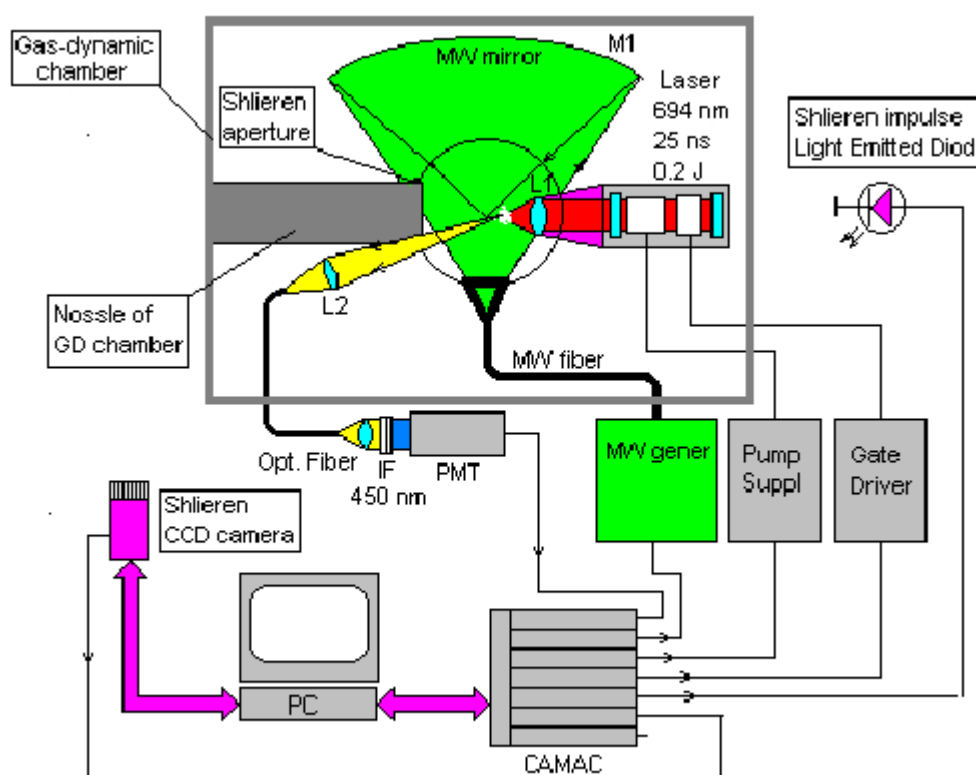


Fig.1.11. Scheme of laser – ignited MW discharge investigation.

electric field) is used as working (main maximum). On this area, placed in the vicinity of main MW maximum, the Ruby laser beam is focused. For eliminating the influence of laser body to MW field distribution, laser beam introduce into this area through the comparatively long tube (lens holder). The focusing quartz lens has a focal length 12 mm.

Ruby laser operates in Q-switched regime and generates the light impulse with 25 ns duration and output energy about 0.22 J.

Digital synchronous Schlieren system mentioned above is used for visualization of shock wave structures arising in working area and recording spatial distribution of emitted discharge light.

Time behaviour of discharges luminosity in working area is measured by fast PMT. Time resolution of this channel better than 30 ns. Spectral range of this channel is definite by interference filter (IF) with wavelength for transmission maximum 450 nm and bandpass 10 nm. Output signal of this channel is recorded in the Flash-ADC in CAMAC system.

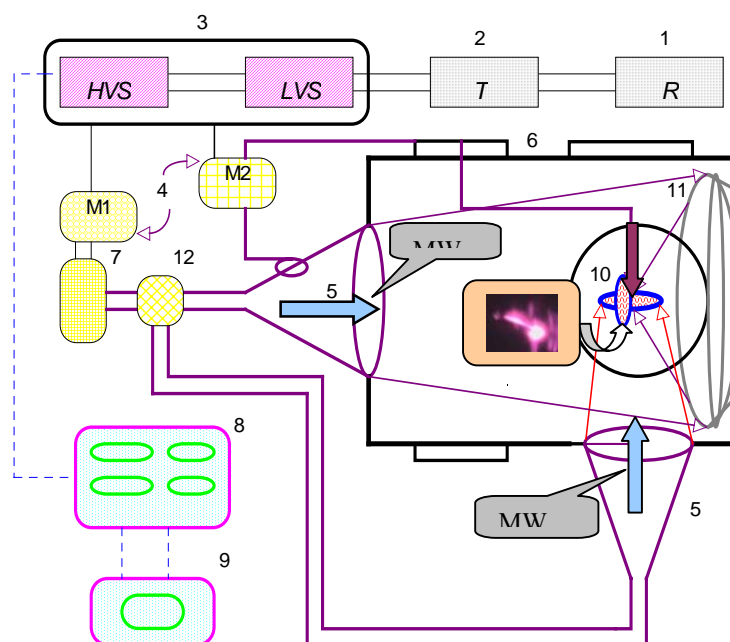
1.3. Flexible scheme for MW and RF energy supply

For the solution of scientific and practical tasks in plasma-aerodynamic experiment the complex set up was created in IHT RAS. It includes two MW and one RF units. Both MW power sources - pulse regime magnetron ($F=13\text{GHz}$, $P\sim 750\text{kW}$, $\tau \sim 5\text{-}50\mu\text{s}$, the pulse leading edge duration is not more than $\sim 0.2\mu\text{sec}$ and the trailing edge duration - not more than $\sim 2\mu\text{sec}$) and CW regime magnetron ($F=2.45\text{GHz}$, $P\sim 600\text{W}$) - can be used separately or in ensemble for carrying out an experimental investigations. Two different schemes of MW energy supply have been realized. The MW beam is focusing inside of vacuum chamber either by lens or by reflector. The special radiating horn was worked out, the great advantage of which is the ability of two-range (13.2 and 2.45 GHz) wave emission at the same time. This two-wavelength-radiating conic horn or the low scattering lens is mounted on the end of vacuum chamber along its longitudinal axis. In the first case the focusing reflector is placed in the opposite end inside of the chamber. So the MW wave travels through the special radiator and reflector and its focusing area is disposed along the chamber axis across the quartz windows. The discharge chamber of 70cm external diameter and 100cm length can be pumped out from 760Torr to 1Torr. Continuous leak of the chamber allows to test different gases. Relatively large volume of the vacuum chamber also allows obtain both subsonic and supersonic flow. All this permitted us to carry out experiments in arbitrary geometry of MW beams and airflow interaction with an extended discharge area (Fig.1.12).

RF unit was also put into operation, which can work either as independent one or as a part of MW installation. This unit has the following parameters: high frequency (RF) value – 40 MHz, the output power level – 30-350 Watts, the working regime – continuous.

So the experimental possibilities increased significantly because we may use of wide range radiation converging at different angle and to work in two experimental planes – at focal area of lens or mirror. We recorded the MW discharge both along and across of the electrical field vector E of propagating MW wave.

At focal areas we may place the pulse extended spark and the electrodes for feed HF energy and for creating of HF discharge. All of that permit us to research the discharges at wide frequency range. Moreover, the combining discharges at different geometry of MW beams and spark interaction were studied in our experiments. The additional facilities – such as nozzle (for airflow creating) or magnets – are easy placed at the working area.



- 1 - regulator, 2 - transformer, 3 - HV - LV sources, modulator,
 4 - magnetron, 5 - wave-guide with lens, 6 - chamber,
 7 - reflectometer, 8 - controller, 9 - registration system,
 10 - discharge region, 11 - MW reflector, 12 - divider.

Fig.1.12. Scheme of the MW setup

2. The main experimental research results of free MW discharge in air

2.1. Free MW discharge in quiescent air and magnetic field

The experimental investigations of stimulated microwave discharges (SMD) are realized in air of relatively high pressure (10-760 Torr) on IHT MW units, described in Section 1.3. In this pressure region MWD has different structures - one of the most significant discharge features - and its formation demonstrates the dynamics of microwave - plasma interaction. It is well seen from photo that the discharge structure consists of bright plasma channels and surrounding plasma areas. Their lighting level and consequently supplied MW energy value, the plasma temperature and concentration depend not only from MW parameters but from external conditions - gas pressure, gas sort, presence or absence of magnetic field, airflow, etc. Discharge size (and volume) and plasma parameters may be adjusted by changing MW power level or pulse duration, but as one of the aims was also to find some plasma control regimes by changing external conditions.

General features. Under atmospheric pressure the visible discharge structure at different projection – cross (Fig.2.1a) and along (Fig.2.1b) vector E – consists of fine channels.

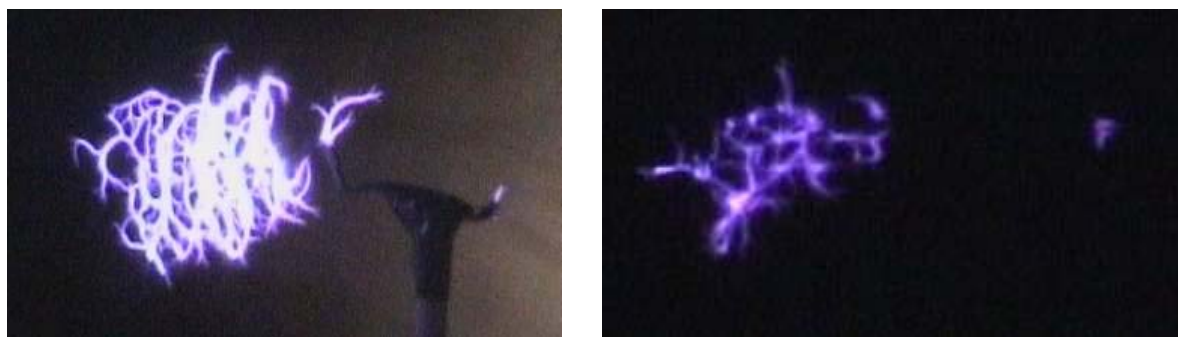


Fig.2.1 (a, b). The discharge structure on EZ and HZ plane ($P \sim 40 \text{ kW/cm}^2$, $\tau = 20 \mu\text{sec}$)

■

The general trends of such discharges evolution are the following:

◆ with increasing of pulse duration and MW power intensity the discharge volume and channel numbers are also increasing;

■

◆ the channels have sinusoidal form at pressure about atmospheric value, diameter of channels changes from 0.1mm (in front channels) up to 2-3mm – their growth velocity reaches up to $\sim 8 \cdot 10^5 \text{ cm/s}$, discharge front velocity $\sim 8 \cdot 10^4 \text{ cm/s}$ (at $P \sim 40 \text{ kW/cm}^2$, $\tau = 20 \mu\text{s}$);

♦ with decreasing of air pressure ($P < 300\text{-}200$ Torr) the diffusion lighting is forming around the channels, the discharge velocity reaches up to $(1\text{-}3)10^5\text{cm/s}$ at pressure about 200-70 Torr and increases up to $\sim 8 \cdot 10^5\text{cm/s}$ at pressure about 30 Torr.

Channel characterization. For plasma channels parameters study the experiments with using of the copper wire electrodes ($\varnothing=0.5\text{mm}$), which were placed in EH plane at 12mm from the initiator, were performed. They were oriented in parallel one to another and in parallel to vector H of propagating MW wave. The distance between the electrodes was 3mm. The electrodes had the floating potential and were connected through the load resistance. The signal at once from resistance took out to oscilloscope. The presence of electrodes in discharge area exerted no influence at discharge structure. The signal was observed when running discharge channel crossed the both electrodes and at load resistance the voltage step arized. The voltage pulse duration was not more than $1\mu\text{sec}$. By changing resistance value one could register the voltage step level changing under different air pressure.

The power developed across the load resistor reaches its largest value when the resistance of external circuit is equal to discharge channel internal resistance. So the characteristic curves of power dependence from the load resistor have same maximum and one can define the demanding value of such resistance and calculate the channel plasma conduction from the expression $\sigma \approx l / R S$. Here S is the square of channel's cross section. According with our estimation for $l = 0.3\text{cm}$, $R \approx 100\Omega$ and channel $\varnothing \sim 0.05\text{cm}$ (at atmospheric pressure) the conduction value is $\sim 1.5 \Omega^{-1} \text{cm}^{-1}$. Then from the expression $N \approx \sigma v_{\text{co}l} / 2.8 \cdot 10^{-4}$ ($v_{\text{co}l} \approx 5.3 \cdot 10^9 \text{p}$, where p is air pressure in Torr) the electron density in channel corresponds to the value $N \sim 10^{16} \text{cm}^{-3}$. We assume the probe method to give correct results at high electron – molecular collisions frequency at air pressure about atmospheric one.

MWD features at magnetic field. At the last year we started the more detailed experimental investigations of microwave discharge structure formation under the magnetic field of different configuration. Study of MWD control possibilities by external and internal means is the main aim of this research. Let us define the discharge control by changing pulse duration and MW power level as an internal means and by adding of special facilities – as an external means. In both cases the MWD structure changing is the main matter of our study. As a rule we fixed the discharge by digital camera with and without magnetic field and determined the visible structure

changing. We also measured the magnetic field level, the discharge thresholds and plasma channel resistance for these cases.

The Hall converter with $\sim 150 \mu\text{V/mT}$ sensitivity was applied to perform the magnetic field intensity measurement at different experimental variants. As a rule MWD propagated at not more than 2cm from the magnet edges. In this area the magnetic field intensity was about 10-30mT. The maximal intensity reached about 140mT (area near the magnet edges) at ring magnet and about 800mT at the plate magnets. The intensity around the electromagnet was not more than 10mT. Nevertheless the action of magnetic field on MWD was rather noticeable.

Magnetic field direction was oriented either parallel or transverse to electric vector E of incident microwaves. Magnetic field intensity changed approximately from 40mT up to 400mT. We tried to record the form of separated channels changing for understanding of discharge visible structure modification as a whole. The discharge observation and registration was carried out at two planes: (EZ) and (HZ). In the measurements of plasma channel parameters the additional electrodes placed at the discharge region were used again.

The discharge channel propagation was studied in stationary magnetic fields with using of electromagnets or permanent magnets of different configuration. They were placed along the caustic (at $\sim 1.5\text{-}2\text{cm}$ from it axis) in such a way that inserted practically no disturbance in the MW field distribution in the focal area. The discharge photos in (EZ) and (HZ) planes are presented below (Fig.2.2) - they demonstrate the channel interaction with transverse magnetic field.

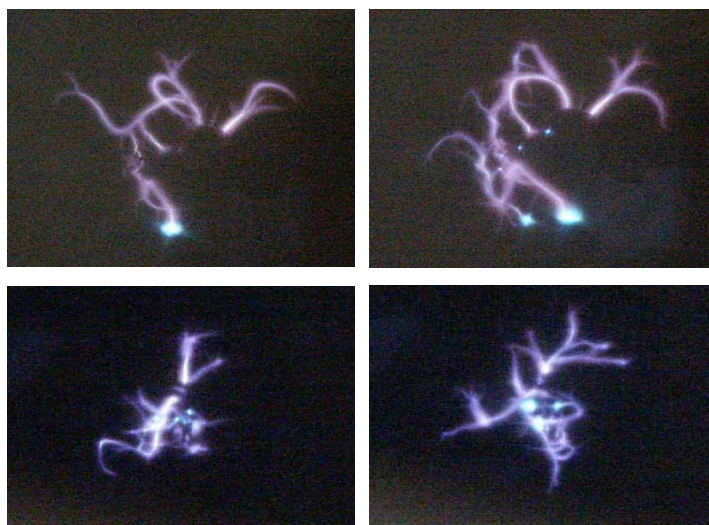


Fig.2.2. MWD structures: (EZ) plane – top photos, (HZ) plane – lower photos; left photos – no magnet, right – with H. $P=745\text{Torr}$, $\tau=10\mu\text{s}$, $W\sim 20\text{kW/cm}^2$.

In this case relatively weak transverse magnetic field ($\sim 40\text{mT}$) was applied. MWD was created at $P=750\text{Torr}$ by MW beam ($\tau=10\mu\text{s}$, $W\cong 20\text{kW}/\text{cm}^2$) focused by the mirror. The main tendencies of a separate discharge channel evolution in applied magnet field are well seen from presented photos. The thin ($\varnothing\sim 0,2\text{mm}$) bright filaments are displayed more clearly in magnet field area. The channels number is increasing and the structure branching is also growing up. The channels volume density increases and thus, the MW radiation absorption also grows. The discharge channels as a rule are oriented along magnetic field lines (see HZ plane photo).

Lower (Fig.2.3) one can see the different discharge structure also at $P=750\text{Torr}$, but at larger MW power ($W\cong 40\text{kW}/\text{cm}^2$, $\tau=10\mu\text{s}$). Here are presented the experimental schema (a) and discharge picture without magnetic field (b). In the next photos (c, d) one can see the obvious and visible structure changing at magnetic field. Practically in all cases the structure becomes more complex with formation circular plasma meshes and vortexes. Plasma swirls are observing along the magnetic force lines. It is very noticeable effect of the discharge structure modifying between the magnets.

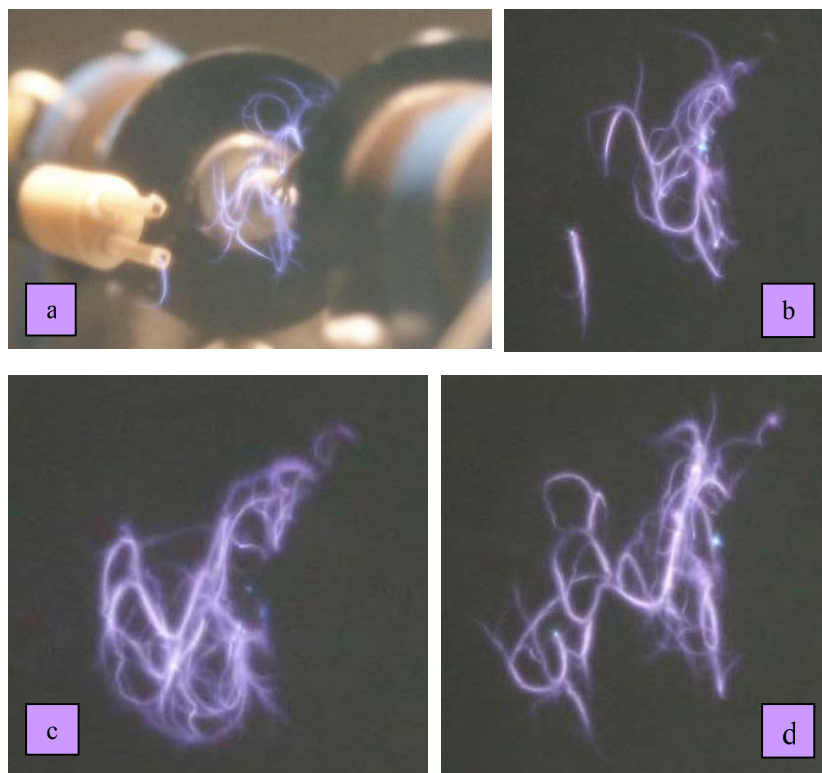


Fig.2.3. Discharge structures photos (c, d) in magnetic field. $H\sim 20\text{mT}$, $P=745\text{Torr}$, $\tau=10\mu\text{s}$, $W\sim 40\text{kW}/\text{cm}^2$.

Measurements of some discharge and plasma channel parameters were made in these experiments by means of electrodes placed at discharge path area. At first we measured the channel resistance without magnetic field (but the electromagnets with core standing near the focal area), then magnetic field was switch on and measurements were repeated. The channel resistance's value turned out very small, of order $\sim 5 - 20\Omega$ and accordingly the channel deposit power level reached up to $\sim 100-150\text{W}$. The channel resistance's at magnetic field is less than without it. So, recalculation on channel's electron concentration gives the value of order $\sim 10^{18}\text{ cm}^{-3}$ (at $P=750\text{Torr}$).

Thus, the tendency of electron concentration increasing at magnetic field was observed. The channel brightness also is increased at magnetic field that is well seen in discharge photo. Note that the discharge velocity decreased of about $\sim 15-20\%$ in magnetic field.

The measurements of SMD breakdown thresholds (Fig.2.4) with and without magnetic field were also performed. The experimental results demonstrated the stable SMD thresholds decreasing in weak magnetic field. Moreover, we tested the threshold regimes and ignited MWD by means of magnetic field switching on.

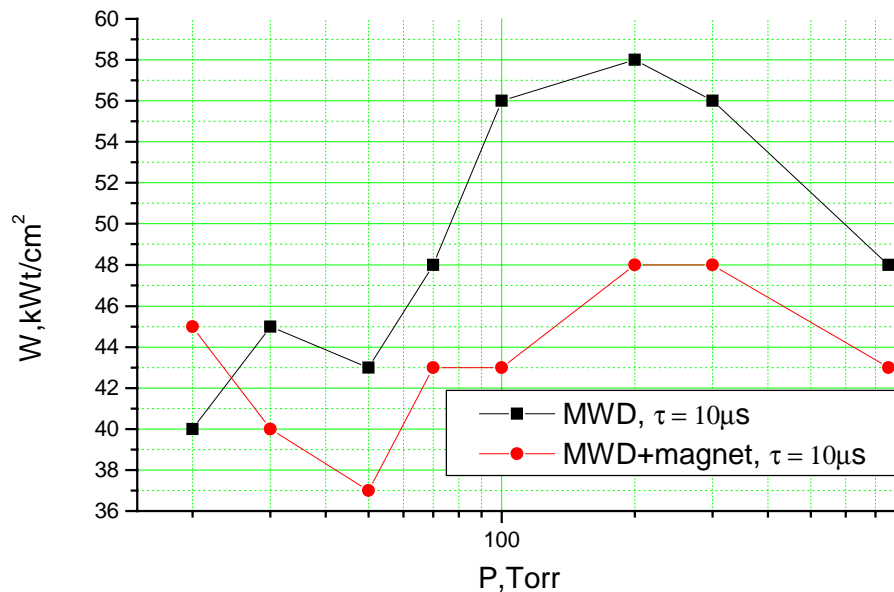


Fig.2.4. The SMD threshold dependence from air pressure ($H \sim 10\text{mT}$)

As experiments show, with magnetic field increasing the discharge structure at first becomes more complex (the channel numbers grows, the turn of channel evolution plane is

observing, the ring and spiral plasma channel are forming) and with its further increasing – more simple (the noted processes are decreasing). It is very important to find the optimal magnet intensity and position relatively to MW beam. The different variants of magnets – discharge relative position were evaluated with using magnets of different configuration. The magnets of ring (Fig.2.5a), cylinder (Fig.2.5d) and plane (Fig.2.5b, c) shape were placed along and across discharge path at the area nearest to the initiation point ($\sim 0.5\text{-}3\text{cm}$ from discharge axis). Practically in all cases the structure becomes more complex with formation circular plasma meshes and vortexes. The discharge as a rule has not passed through the ring magnet - channels are elongating along the ring plane. The channel's color rather often noticeably changed. Plasma swirls are observing along the magnetic force lines.

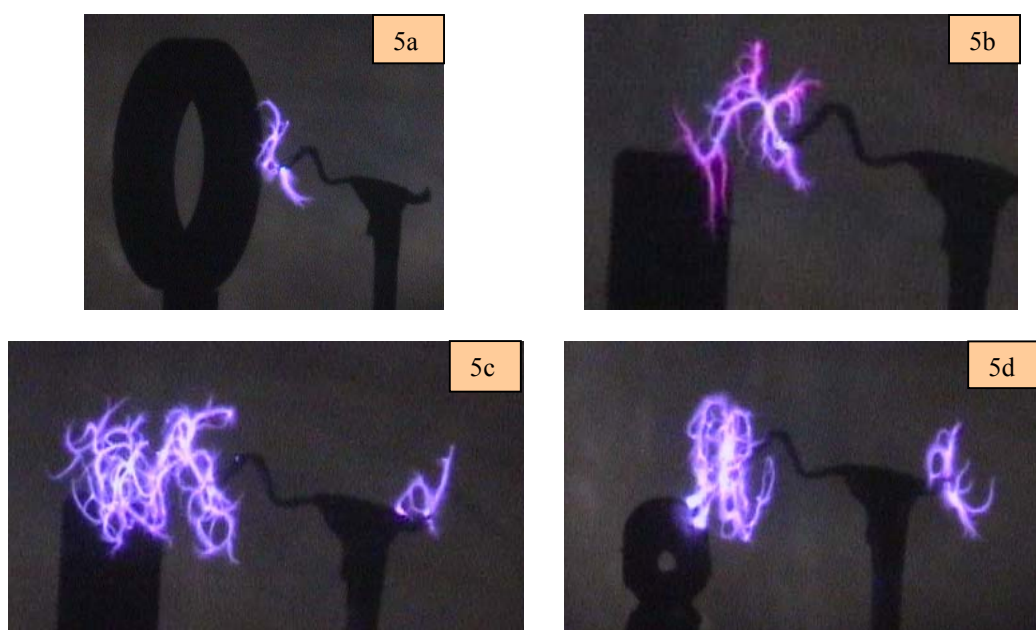


Fig.2.5. The discharges in magnetic field ($P \sim 40 \text{ kW/cm}^2$, $\tau = 30\mu\text{sec}$)

Discharge structure in air between plane magnets is presented at Fig.2.6a, b, c. The initiator is marked by figured pointer and the magnet edges by direct pointers. The magnetic field force lines are oriented along vector E of MW wave. At Fig.2.6b the discharge developed at magnetic attraction field, at Fig.2.6c - at magnetic repulsion field.

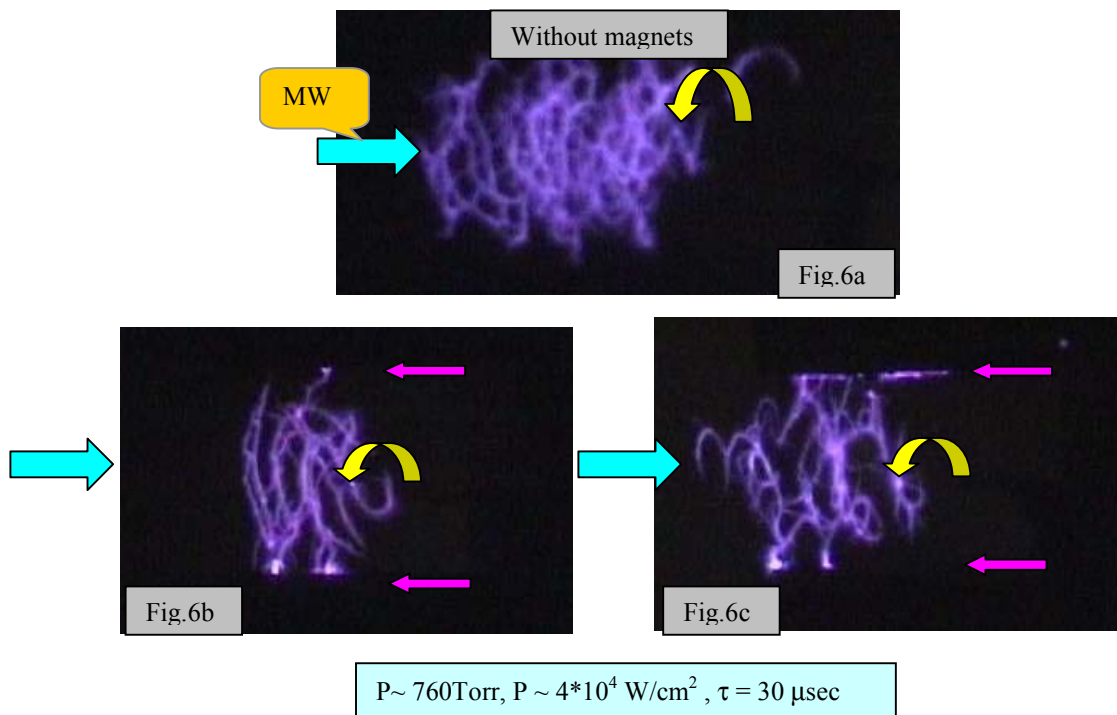


Fig.2.6. Discharge structure in air between plane magnets

The distance between magnets was 22mm, length of magnets - 40mm, the initiator tip was placed in the center. Magnetic intensity is equal to $\leq 200\text{mT}$. It is very noticeable effect of the discharge structure modifying between magnets seen at the discharge pictures. In magnetic attraction field the discharge has tendency to extend along the magnetic field force lines. In magnetic repulsion field the discharge structure also changes with appearance of additional short plasma channels. There are many cases when the discharge stops and extends along vector E (or along external magnetic field) at magnets boundary (Fig.2.5b, 2.6b).

Such effects were revealed as the MWD plasma channels broadening, the increasing of thin plasma channels number, the increasing of channels turn radius near the magnet edges and changing of structure scale in magnetic field are very sensitive to the early plasma channels phase formation because of the important role of moving channel angle to magnetic field direction and propagating direction. Let us consider some examples of discharge stages when it propagates along or cross of the different magnets. We could stop the discharge and increase energy deposition in separate plasma channel by magnet placement. It is necessary to choose the

magnetic field intensity for this aim. The other way of discharge stopping or changing is the placing of magnets at cross variant.



Fig.2.7

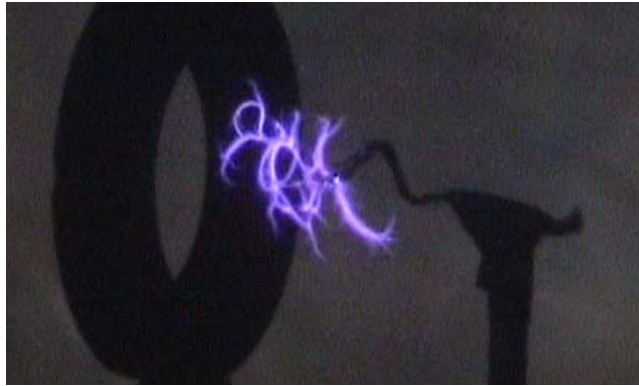


Fig.2.8

On photos Fig.2.7-2.8 the well visible effect of discharge propagation either in side at higher magnetic field intensity (near the ring edge - Fig.2.7) or along ring axis where the field intensity is five times less than at ring edge is presented. The angles of plasma channel inclination to ring plate on initial formation stage are slightly varying but the final picture is strongly different on this photo. Also the visual effect of more thin channels is in propagating discharge (Fig.2.8). So the MW energy is expending either to the structure formation or to the deposition in separated channels (extending up to $\geq \lambda$ and broader).

The structure changing is especially well seen at magnets edge section when discharge propagates between the magnets away from magnetic field. Plasma channels are developing along magnetic force lines when discharge is forming in internal area of magnets (Fig.2.9). After going out from magnets area the discharge takes its usual sinusoidal form (Fig.2.10). It is well seen from the next photos.

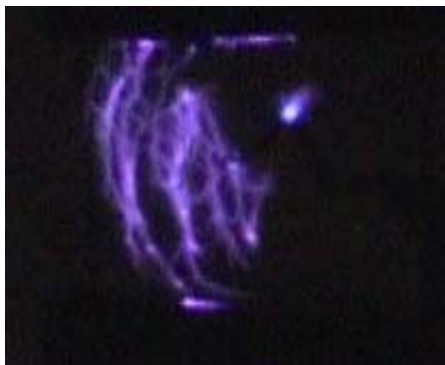


Fig.2.9

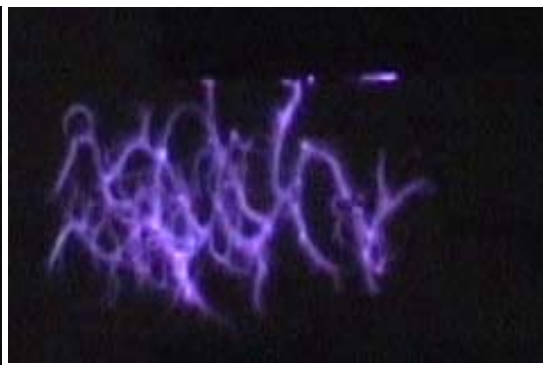


Fig.2.10

Below are presented three photo where we can see the discharge without magnet Fig.2.11(a), then discharge propagated along magnet plate – (b) – initiator tip placed at 15mm from narrow (10mm) horizontal plate and at photo (c) initiator tip placed at 10mm. The closer is the plate the easier the discharge connects with the plate. In case (b) the number of connection points is less but the channel diameter is increasing (or the surrounding lighting is increasing). The number of closed ring channels is also increased.

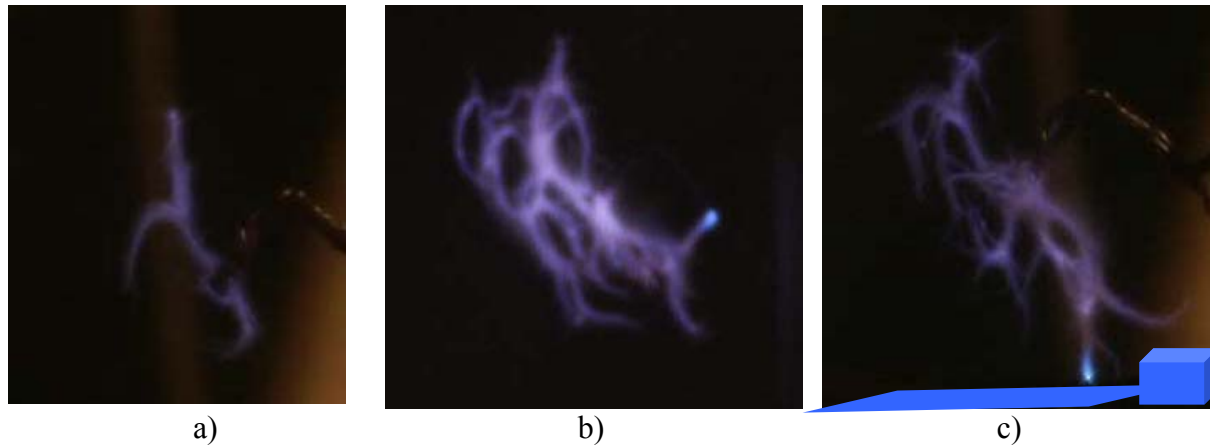


Fig.2.11 MWD near initiator tip, a – no magnet, b, c – magnet plate installed

Very interesting picture is observed when the initiator is placed in the center of ring magnet (Fig.2.12). First of all the discharge threshold level is decreased and the discharge branching is increased. Well seen is the changing of discharge structure, which is transformed to ring channels. Discharge may propagate along ring magnet axis as well as transversely to magnet axis. The discharge volume substantially increases.

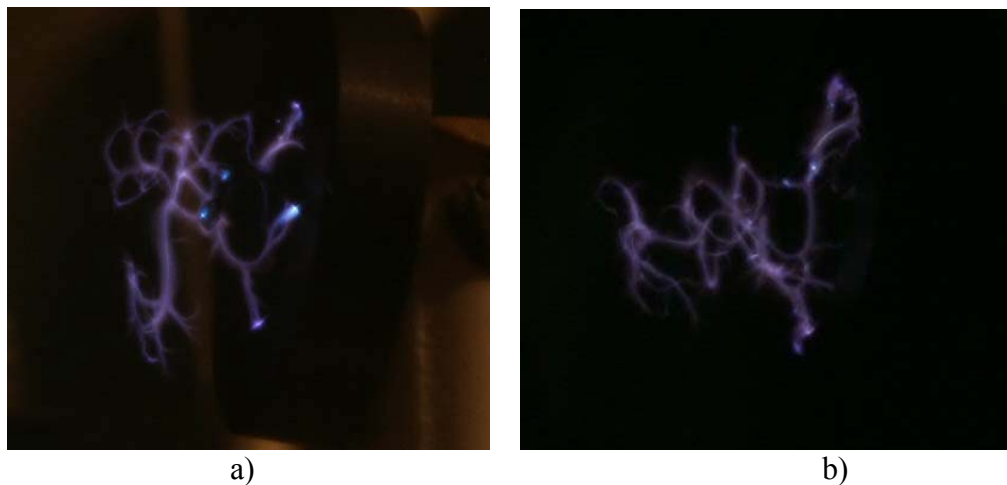


Fig.2.12 MWD near the ring magnet

The main trends of discharge evolution in magnetic field are the following:

- ◆ the obvious changing of separated discharge channels (dimension, geometry, color, resistance etc.) are observing;
- ◆ the discharge channels elongation along magnet forth lines takes place;
- ◆ the discharge structure changing is observing; fine circle meshes ($\varnothing \sim 1\text{mm}$) appear in regular structure;
- ◆ the discharge color changing takes place;
- ◆ the discharge may stops near the magnets boundary.

All the mentioned results are observing more frequently in inhomogeneous area near the magnets edges and along the magnets. It is possible that due to working circular MW frequency ($\omega_F = 8.3 \cdot 10^{10} \text{ s}^{-1}$) and cyclotron frequency [$\omega_B \sim (1.7-3.4) \cdot 10^{10} \text{ s}^{-1}$] closeness the electron gradential drift occurs in such areas. Therefore, here the swirl and circle plasma paths are formed.

The discharge lighting intensity decreases in magnetic field – this fact is also positive from viewpoint of cyclotron resonance availability. The electron temperature may increase in inhomogeneous (in amplified magnetic field) areas by an order of magnitude. Then the discharge lighting spectrum will change with displacement in UV region. So, the visible discharge lighting may decrease. Finally, it can be stated that application of magnetic field makes wider the possibilities of MW plasma parameters control.

2.2. Free MWD in airflow

The interaction of MWD with airflow was studied in cross variant of their location. Free MWD was created in focal area of the mirror along the chamber axis. The airflow was dispensed at angle about $\sim 30-45^\circ$ to MW beam axis. The action effect is well seen in photos (Fig.2.13). Here are presented two discharge projections: (EZ) - the upper photos, (HZ) – the lower photos. The flow presence obviously favors in MW beam interaction with discharge plasma. The channel number is increased at once and they are oriented along air direction movement. So the cross discharge size is increased and the interaction effectiveness of MW beam with plasma rises.

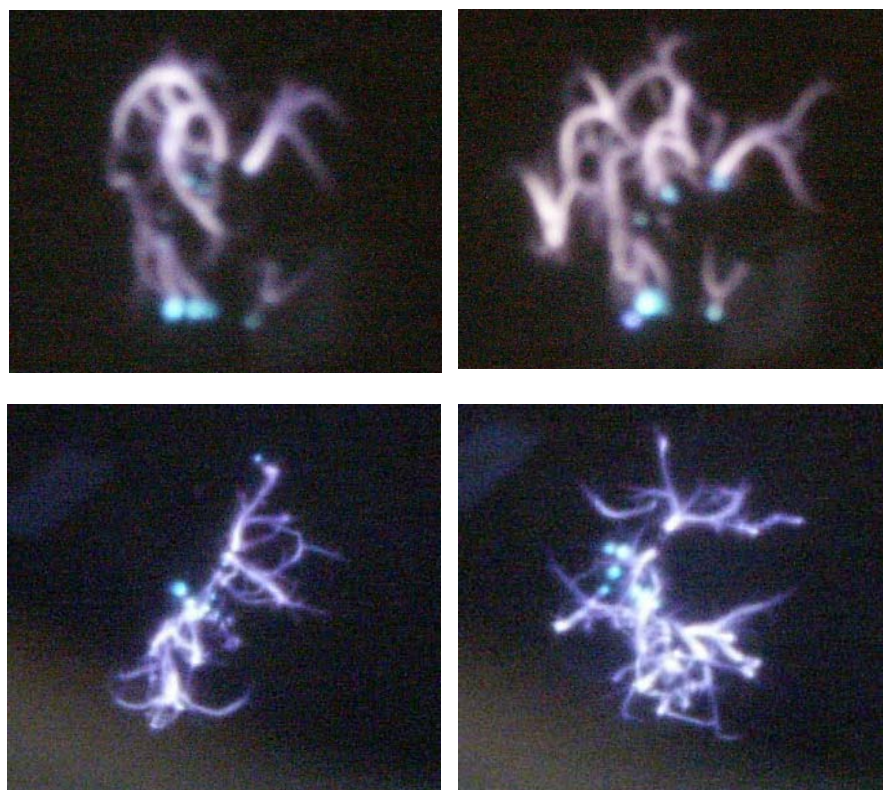


Fig.2.13. The SMD structures in airflow: (EZ) plane – top photos, (HZ) plane – lower photos; left photos – no flow, right – with flow, $P=745\text{Torr}$, $\tau=10\mu\text{s}$, $W\sim 20\text{kW/cm}^2$.

In the case of airflow dispensing along E (Fig.2.13a, b – left photo without airflow) the discharge structure also changed. The additional plasma channels are formed in the flow and oriented along its movement direction. The discharge brightness practically not changed, but the level of transmitted MW energy through the plasma decreased up to $\sim 40\%$ ($\sim 30\%$ without airflow). So the MW beam - plasma interaction processes occur more actively in the flow.

The study of microwave discharge (MWD) interaction with air and argon flows ($V \sim 0.5\text{-}1\text{M}$) was also executed. MWD was created in the focal area of the lens along the chamber axis. The airflow was realized cross to MW beam axis or along it - from lens side or along discharge propagation.

The main features of such interaction are the following:

- modification of MW discharge structure,
- both MW discharge propagation and its drift along gas flow,
- discharge size and color changing,

- increasing of plasma channels number,
- rather strong influence on reflected and transmitted MW signals.

Let us consider some of these effects in more details. Note that the flow velocity was increased practically up to speed of sound and more in our experiments by using gas cylinders charged to a pressure of ~ 150 atm. The redundant gas pressure level was about 2-3atm in gas channel. The non-profiled nozzle was used, which created the gas flow of $\varnothing \sim 1-2$ cm in MW focal area. The nozzle was placed either behind the initiator along MW beam propagation, or ahead of the initiator or at cross-position to MW beam axis. The mean distance between nozzle end and the initiator tip was about 2-3 cm.

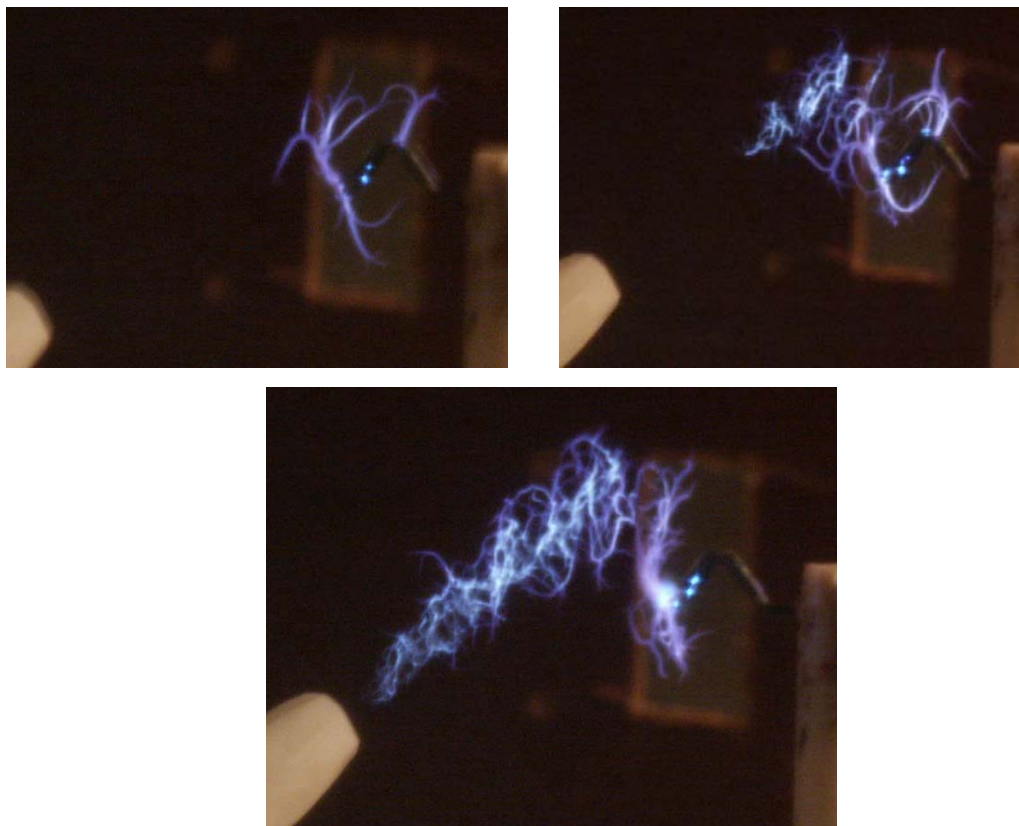


Fig.2.14. MW discharge at contrary argon flow (the top left photo without flow).
The nozzle is placed ahead the initiator.

Very interesting variant of discharge formation is presented in photo (Fig.2.14). In this case the nozzle is placed ahead of the initiator under a small angle to the beam axis (~ 30 degrees). It well seen that the additional plasma channels are also forming in the focal area, but

MW discharge prefers to propagate at cross path in gas with reduced threshold characteristics. The cross discharge does not go all over the flow boundaries and we observe the flow visually. In this case the MW discharge propagates along the gas flow and also changes its size and color. So the direction of MWD propagation may be changed by external action or by using special means - dielectric plate.

2.3. Directed MWD by the dielectric plate

The control over plasma parameters successfully achieved by changing of MW power level, pulse duration and by means of addition magnetic field. But the main features of discharges -as its velocity and size, the temperature and concentration of channels plasma may be also changed by placing of directional systems at EM beam focal area. In this case both MW beam and discharge propagates along such system and the noted above parameters can be dramatically changed. It is possible to create the different discharge form by directed systems (such as the metal or dielectric rod, the dielectric plate, wire and special systems).

The main results were received with directing dielectric plates. The initiator was placed near the plate ($\sim 1\text{-}5\text{mm}$) and ignited the MWD. MW energy is concentrated in the space nearest to the plate and the radiant MW emittance is obviously increased. The threshold discharge level decreased on 2-3 times but the velocity increased up to $\sim 2 \cdot 10^5 \text{cm/s}$. Structure scale changed in such discharges and they become spatially flat along the dielectric plate. The size of such discharges goes over a MW “caustic” limit even at atmospheric pressure and occupy the area about $4 \times 4 \text{cm}$ (Fig.2.15a) - it is twice as larger than the discharge in air without any plate.

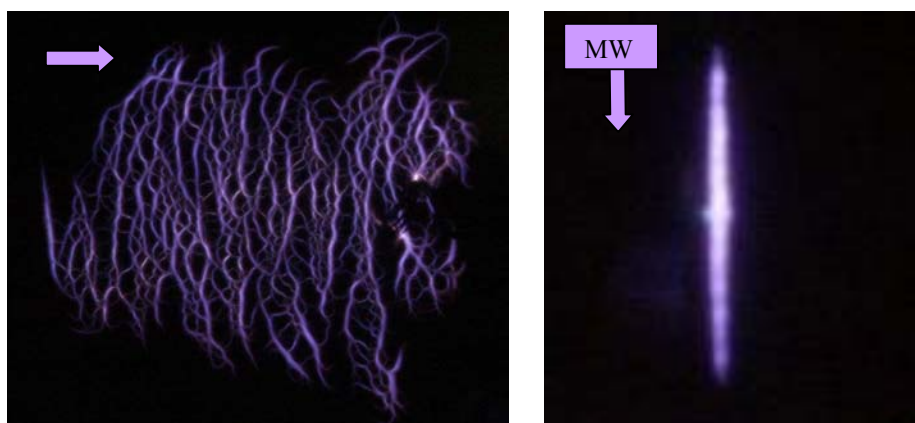


Fig.2.15. MW directed plane discharges: $P \sim 50 \text{kW}$, $\tau = 20 \mu\text{s}$, left - EZ, right – HZ plane

The discharge structure has the view of plasma grating consisting of quarter-wavelength dipoles oriented along electric field vector E . Distances between the dipoles lines are also about quarter-wavelength (of the wave, propagating along the given dielectric plate).

The dynamics of such discharges is also very interesting. The longitudinal and cross discharge velocities are rather high and reach up the value $\sim 2 \cdot 10^5$ cm/sec. The ahead-formed thin channels ($\varnothing \leq 0,1$ mm) have the white color and the later (during the MW pulse) become thicker ($\varnothing \leq 0,3-0,5$ mm) and acquires a bluish-rose color. The separate channel is formed at less than $\sim 0.5 \mu\text{s}$ (the channel length is about $\lambda/4$) and along it one can see the series bright points placed at $\sim 0,3$ mm one from another. Moreover, the reflected plasma layer from such channels is also formed during $\sim 2-3 \mu\text{s}$. Taking into account the discharge velocity, the plasma layer width also reaches the value up to $\sim \lambda/4$. With increasing of MW power level such process becomes periodical with time period about $\sim 3-6 \mu\text{s}$. This process is demonstrated by Fig.2.16 (CH2 – photoelectric multiplier signal, CH3 – MW reflected signal, CH4 – MW probe signal).

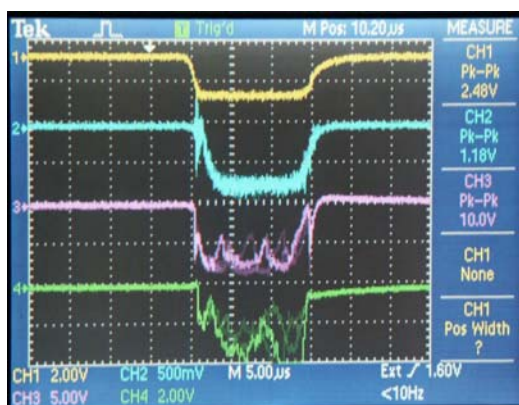


Fig.2.16. Oscillogramm of photoelectric multiplier (CH2) and MW signals (CH3,4)

The additional possibilities of control of the mentioned MW plasma features appeared with external magnetic field applying and by action the airflow on directed MWD. The different variants of magnets – discharge relative position were evaluated with using of magnets being placed along and across discharge path. The magnetic field application at interaction area leads to discharge stop or structure conversion. So we have the possibility to change the sizes and discharge forms by “external” means.

The structure changing is well seen with increasing of pulse duration up to $20\mu\text{s}$ at magnet position placed by its largest plate part along the initiator (Fig.2.17d). The discharge velocity along the dielectric plate is rather high both without and with magnetic field, and reaches the value $\sim 10^5\text{cm/sec}$ at MW energy level not more than 10kW/cm^2 .

Some decrease of velocity values in magnetic field is observing. But the channel parameters are obviously changed in magnetic field. At Fig.2.17a – discharge without magnetic field, b - discharge with magnet placed by its short narrow part, c - with magnet placed by its long narrow part along discharge, at d – magnet placed by its largest plate part along initiator. The research results demonstrate the real possibility of different discharge parameters control. The plasma plate discharge type has more wide control region because of its low threshold and high sensitivity to changing of the external acting.

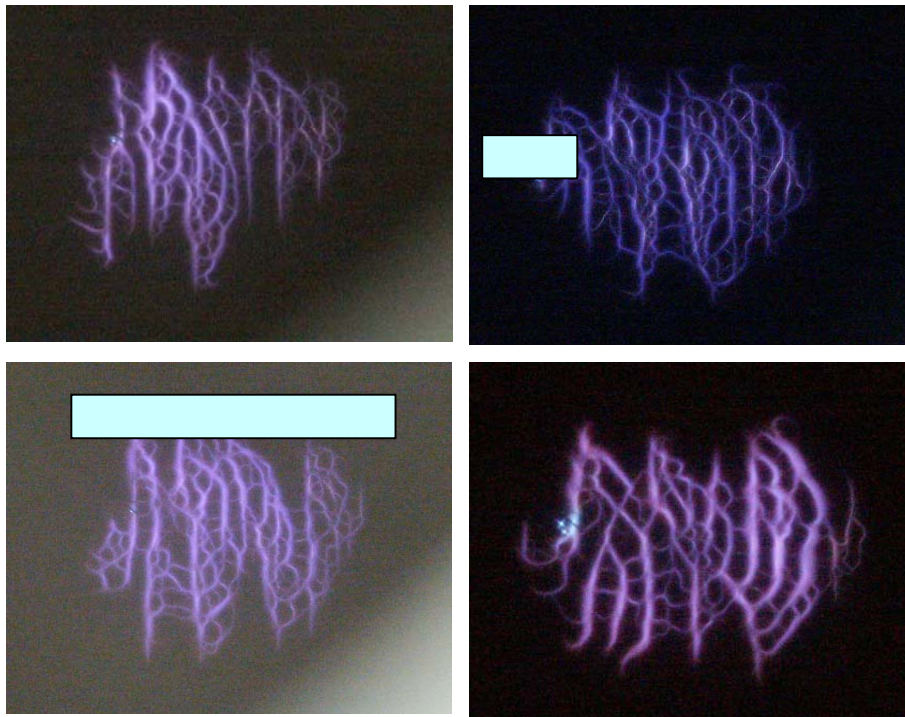


Fig.2.17. SMD structures in magnetic field of different orientation,
 $P=745\text{Torr}$, $\tau=20\mu\text{s}$, $W\sim 20\text{kW/cm}^2$.

Magnetic field levels necessary for visible action at plasma channels parameters may be estimated by comparison of magnetic pressure value ($P_m = B^2 / 2\mu_0$) and gas dynamic electron pressure ($P_e = N_e k T_e$) in plasma channels. For our MW discharge with electron temperatures about $T \sim 1\text{-}10\text{ eV}$ and electron concentrations $N \sim 10^{16}\text{-}10^{18}\text{ cm}^{-3}$ the magnetic field intensity B

of order $\sim 0.2\text{-}2\text{T}$ may act intensively at the MW channels. We used non-symmetric magnetic field configuration with strong field gradients and in such fields bending of channel's trajectories may arise – what we did observe at the channel tips in experiments. In more degree this effect is observed in the case of near-plate MW discharge where electrons move in crossed electric and magnetic fields.

At present experiments we applied the rotating magnets placed at $\sim 2\text{-}4\text{cm}$ from the focal area. For this aim we uncoil the magnetic beam ($\sim 5\text{-}10$ rev. per sec) without synchronization with MW pulse repetition near plasma area and fixed the discharge behavior in the driver mode of digital camera control. The magnetic field direction was oriented transverse to electric vector E and direction of propagated plasma channels and its level changed about several times (\sim from 40mT up to 400mT) at discharge area during rotation.

The different stages of such interaction are presented in photo series (Fig.2.18). At first photo we see the customary structure (the magnet placed at 4cm distances) and the action of magnetic field is rather small. But with the approaching of magnetic field to the discharge the structure changes and all effects becomes more visible. With distances increasing discharge take its own form. The discharge also changed when the different poles of magnet act on it.

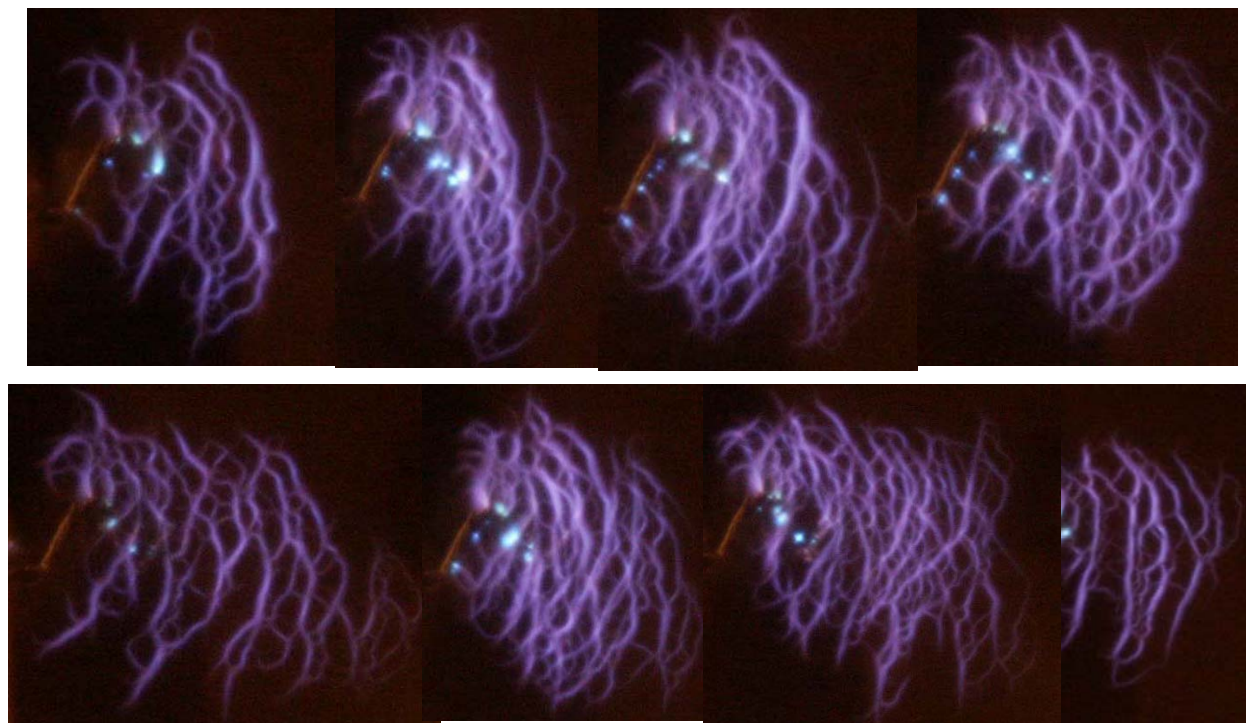


Fig.2.18. MWD at the field of rotating magnets

As this experiment shows, we have more possibilities for discharge parameters control by using pulse magnetic field.

The main results of the present experimental research are the following:

1. The SMD structures are very sensitive even to not large levels of magnetic field. Let us note some discharge structure changing in magnetic field:
 - the increasing of plasma channels in discharge area and at the channels tip ,
 - the spiral and curling plasma channels formation,
 - the channels color changing.
2. The SMD may be ignited or stopped by external magnetic field.
3. The use of directed systems favors to SMD control range widening. Rather large near-plate MW discharge can be created along dielectric plate.

2.4. Study of plane MWD – gas flow interaction

The directed discharges on the dielectric plates are rather well controlling by changing pulse duration and MW power level jointly with gas flow velocity and the direction changing. The study of microwave discharge interaction with air and argon flows was fulfilled. MWD was created in focal area of the lens or of the mirror along the chamber axis with dielectric plate. The flow velocity also was increased practically up to speed of sound $\sim 1\text{M}$. The nozzle was placed either behind the initiator along MW beam propagation, or ahead of the initiator or at cross-position to MW beam axis. The mean distance between nozzle end and the initiator tip was not more than 2-3 cm.

Without flow plasma channels present the converging wave phase front (Fig.2.19). But when compressed gas is injected to the focal area the channel development is significantly changed and the discharge size is increasing in two times. Moreover, plasma channels are setting upright (along vector E). In argon flow injected inside ambient air MW discharge formed the discharge “tube” of $\varnothing \sim 1$ cm. It has white color and the modified structure.

It well seen that the additional plasma channels are also forming in the focal area, but MW discharge prefers to propagate in gas with reduced threshold characteristics. The discharge does not move over the flow boundaries and we observe the flow visually. In this case the MW discharge propagates along the gas flow and also changes its size and color. It well seen that the

additional plasma channels are also forming in the focal area, but MW discharge prefers to propagate in gas with reduced threshold characteristics.

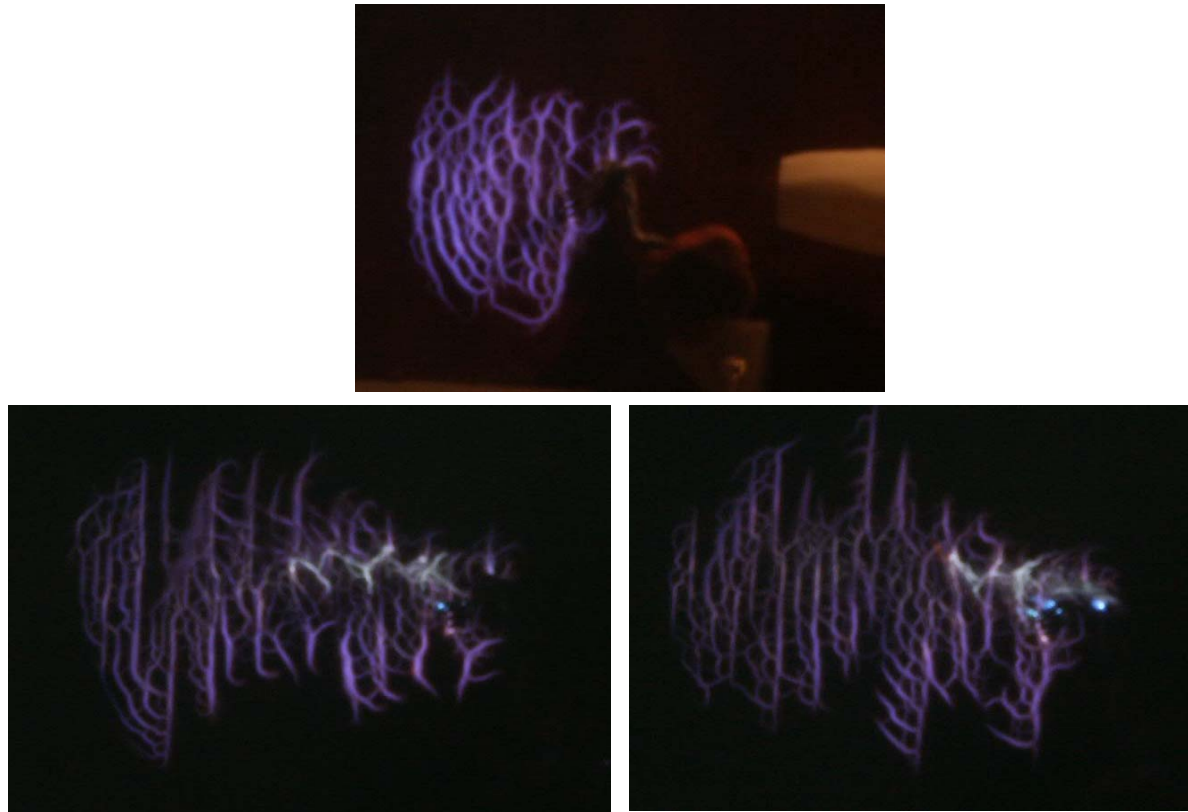


Fig.2.19. MW discharge at tail argon flow (the top photo without flow).
The nozzle is placed behind the initiator.

The part of experiments was performed with rather weak airflow directed cross to the MW beam axis. The MW discharge was created on the polymethylmethacrylate plate. It was found out that the increasing of plasma channels number and some structure modification are also observed in a weak (subsonic) airflow, but the discharge propagates rather stable contrary to the MW beam. In the sonic flow we fixed well seen MW discharge drift and deceleration (Fig.2.20).

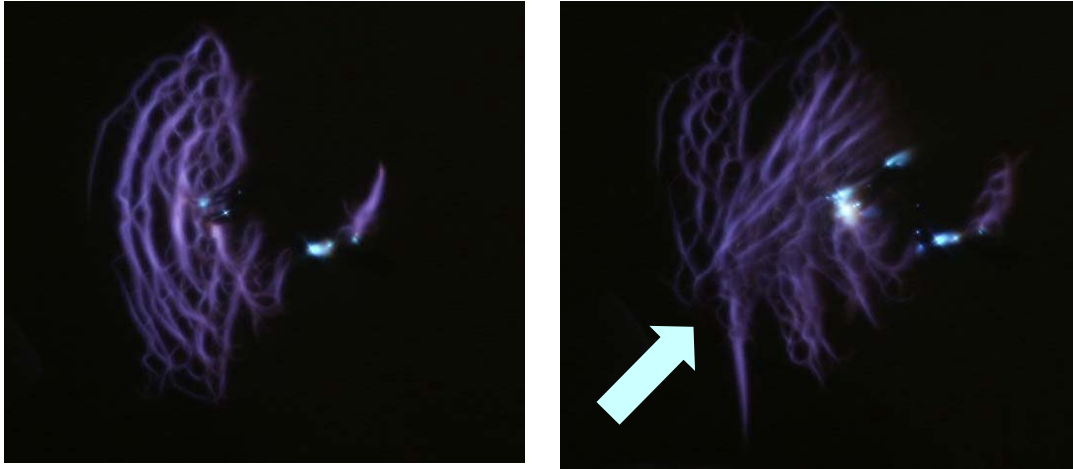


Fig.2.20. MWD at contrary airflow (the left photo without flow). The nozzle is placed ahead the initiator.

Channels come straight and are oriented along the flow. So if the flow velocity is very close (or more) to the discharge velocity the control over propagating plasma processes may be achieved. By changing flow direction we may direct the discharge at demanding side and try to change the interaction conditions. The reflection and transmission increased in this case. The fluctuations of plasma processes are observed on the both signals in the flow.

Below presented is the photo of the discharge in argon flow (Fig.2.21). Here the discharge structure is dramatically changed. May be this occurs due to the large discharge velocity in argon along the plate. So the longitudinal velocity is higher than transverse one and the cross channels have no time for structure forming.



Fig.2.21. Microwave discharge in tail argon flow.

Thus, the main features of such interaction are the following: modification of MW discharge structure, both MW discharge propagation and its drift along gas flow, discharge size and color changing, increasing of plasma channels number, rather strong influence on reflected and transmitted MW signals.

The main results of MWD investigation

Let us summarize the main results of the present experimental research. The stimulated MW discharge structures are very sensitive to rather small levels of magnetic field. This fact is in visible contradiction with the results of paper [1], where modifications in structure of impulse surface dielectric discharge were registered under the magnetic fields of order several Tesla. MW discharge structure modifications in weak magnetic field are as follows: the increasing of plasma channels branching, the spiral and curling plasma channels formation, the channel color changing. The SMD can be ignited or stopped by external magnetic field. Experiments with dynamic magnetic field of rather low level demonstrate the possibility of the discharge parameters and size controlling.

The use of directed systems favors to SMD control range widening. Rather large near-plate MW discharge can be created along dielectric plate; by changing MW power parameters or by using the gas flow and magnetic field the control over such discharges was realized. The MW discharge study under relatively high gas flow velocity ($V \sim 0.7-1M$) demonstrates the possibility of its structure significant modification. MW discharge propagates along the gas flow or drifts down by the gas flow. For the first time low threshold RF ball discharge was ignited. The similarity of ball RF and MW discharges is shown, the fact, which puts aside plasma resonance phenomena in ball discharge formation.

The results of experimental study of MWD interaction with magnetic field and directed systems demonstrate the possibility of MW energy expenditure optimization on creating of the demanding plasma structure, size and volume.

2.5. MW and RF ball discharges

For the solution of different practical and scientific tasks in plasma-aerodynamic complex experiment a new high frequency (RF) unit was set up. It can operate both as independent unit and as a part of MW installation. In the first case the ring electrodes are placing in the vacuum chamber ($\varnothing \sim 7\text{cm}$, $L \sim 20\text{cm}$), where the RF discharge is igniting between electrodes. In the second case the electrodes of different configuration are disposed inside of the large chamber in any section of it, where combined RF-MW discharge is burned. So, in dependence of the task we can study either the RF discharge itself or its interaction with MW discharges.

In our experiments we used the small vacuum tube, which was pumped out to pressure up to 1-100 Torr. The RF discharge was ignited at power level about 30W practically in all mentioned pressure range. The RF discharge was burned between ring electrodes (at very low electric field – the estimation gives the value $\sim 1\text{V/cm}$) in the form of plasma “cable” with $\varnothing \sim 2\text{-}3\text{cm}$ and length $\sim 8\text{-}10\text{cm}$. The discharge has red color shell about 5mm thickness and inner “rod” of white color (Fig.2.22).

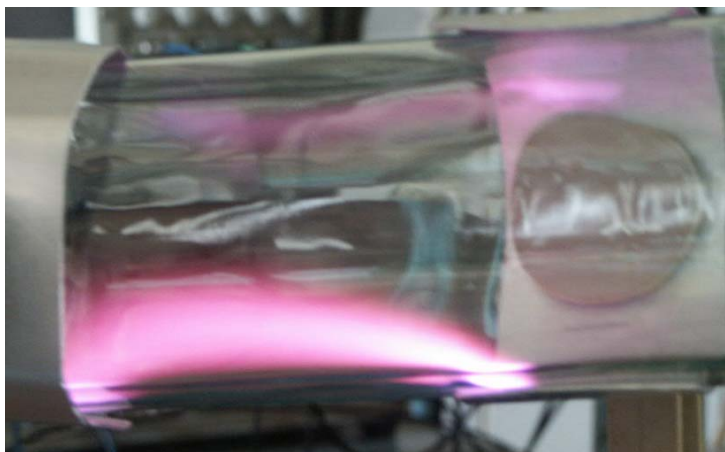


Fig.2.22. RF capacitive discharge in air

Then the initiator was placed in a chamber and for the first time the RF ball discharge was ignited (Fig.2.23). The blue color plasma shell (about 2-3mm thickness) is also formed along the initiator. The red plasma ball ($\varnothing \sim 3\text{-}7\text{cm}$) is igniting on the initiator tip. The thickness of the blue and red color plasma shells decreases with air pressure increasing. It may be proposed

that the temperature is growing in such case and so we performed its measuring by thermocouple.

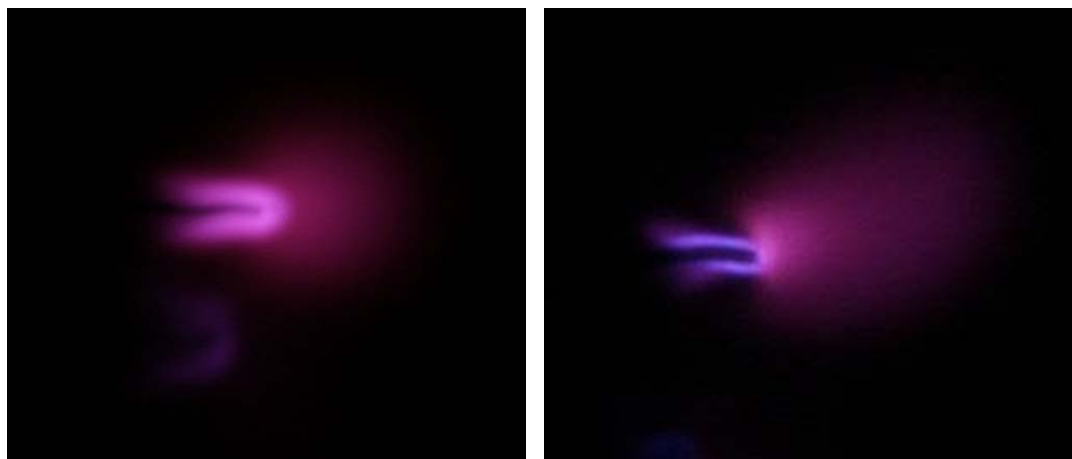


Fig.2.23. RF ball discharge in air (left - $p = 10\text{Torr}$, right – $p = 50\text{Torr}$)

The results of RF discharge temperature measurements are presented in Table1.

Table 1

Air pressure, Torr	4	30	50
Temperature, K	650	900	950

Also investigated was the low-threshold ball discharge (LBD) excited by microwaves ($F=2.45\text{GHz}$) and realized in air of middle pressure (1-50Torr). In this pressure region LBD as the whole has ball lighting structure with bright plasma layers along initiators (Fig.2.24).

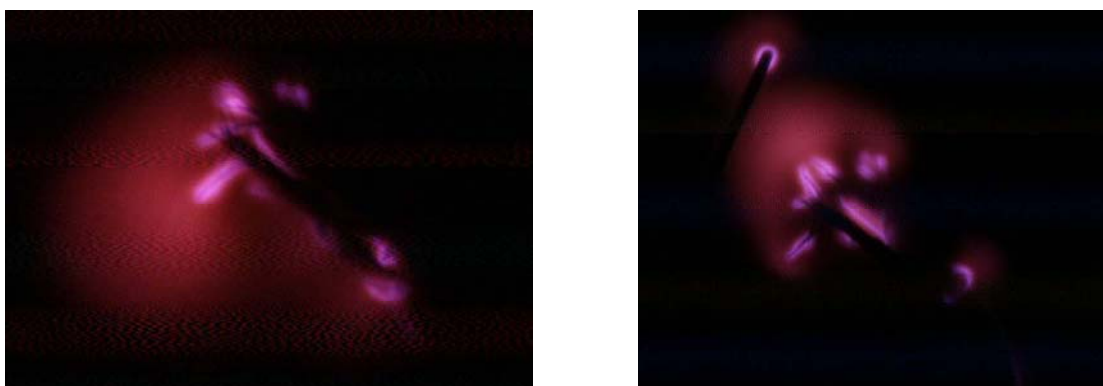


Fig.2.24 (a, b). Ball MW discharges in air ($P \sim 2\text{ Torr}$) without (a) and with (b) magnetic field ($E_{\text{MW}} \sim 10\text{ V/cm}$)

Configuration and sizes of the both plasma regions depends upon microwave - plasma interaction conditions – MW power level, gas pressure and initiator type. It is well seen that the discharge consists of pink - blue plasma channels and red surrounding plasma areas.

Their lighting levels represent the plasma temperature and concentration. In case of LBD it is also the opportunity to adjust discharge size (and volume) and plasma parameters by changing MW power level, magnets placing near discharge area or by airflow acting at LBD. The discharge was stably ignited in air pressure region $\sim 1 - 20$ Torr, non-stable lighting was observed up to 50Torr. Red lighting size decreased from $\varnothing \sim 3-5\text{cm}$ to $\sim 1\text{cm}$ with pressure increasing. Bright plasma layers along initiators changed their size from 3-5mm up to $\sim 1\text{mm}$ also with pressure increasing. LBD plasma current and potential were measured by probes (at $E \sim 10-20\text{V/cm}$) in our experiments. The final values of potential and current reached up $\sim 16\text{V}$ and $\sim 5\text{mA}$ at pressure region 10-30 Torr. Based on these results the input MW power to the discharge is about 30-50% of the mean incident power ($\sim 300-500\text{Watt}$).

Plasma resistance value reaches up to $\sim 5-10\text{KOhm}$. Analysis of MW probe and resistance signals gives the similar results. It is necessary to note that LBD plasma has very good rectifying properties.

The results of MW LBD discharge temperature measurements by means of thermocouple are presented in Table 2.

Table 2

Air pressure, Torr	4	30	50
Temperature, K	800	1000	1400

Comparison of Tables 1 and 2 gives the tendency of temperature growth with increasing of carrying frequency, the fact that looks quite natural.

We also imposed the magnetic field by means of electromagnet or flat magnet placed near the discharge region. At different cases we either put out or ignited the discharge lighting by magnetic field. The discharge lighting level decreases in magnetic field. When we placed the flat magnet the gas temperature decreased as a rule about two times and reached up $\sim 500-700\text{K}$ in pressure interval 2-7 Torr. The plasma potential and current values decreased also up to $\sim 0.8\text{V}$ and $\sim 0.5\text{mA}$ accordingly.

The discharge in airflow has the structure as presented in Fig.2.25. If the flow is directed across the MW beam the LBD emission intensity and the ball size decreased.

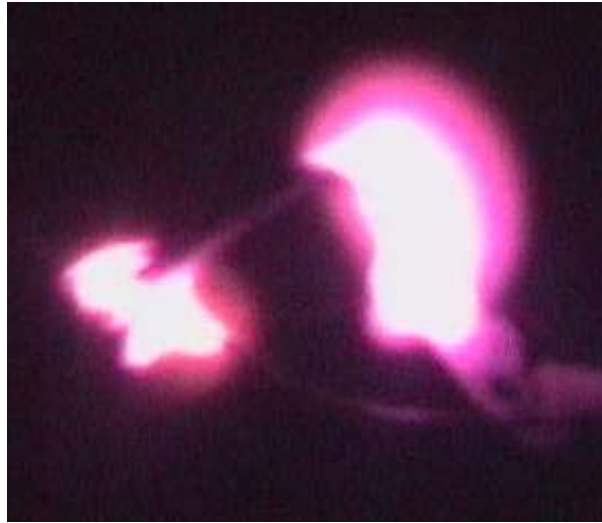


Fig.2.25. The ball discharge in airflow

The MW LBD and RF discharge structures are also looking very likely. This fact excludes any local plasma resonance phenomena for explanation of such low levels of ball discharge maintaining.

2.6. The separate plasma channel modeling and its study at different conditions

The second step of our study was the creating ways search of the separate plasma channel practically similar with MW channel. On our opinion we found the demanding physical object – pulse spark.

Such plasma channel as a pulse spark turned out very flexible experimental object. By special methods one may change its length, current, the breakdown field level and its spatial orientation. Moreover, it may be used for the MWD initiation.

We always observed the complex discharge pictures consisted of simple elements – the separate MW plasma channels. For their detailed study we looked for different types of discharges, which might be used as a model of the separate MW plasma channel. On our opinion the similar plasma channel is the air spark. From one side this complex object presents independent scientific interest, but from other side it may be used as plasma initiator for different wave range discharges. So we decided to check experimentally both these aims, using pulse spark.

We took the pulse magnet energy accumulator (field coil) and created the spark. Its working frequency changed from 3Hz up to 10Hz. Field rising time until the air breakdown level of the spark gap was about 40-80 μ s. The field level depends upon the distance between the electrodes and was not more than ~15-30kV. The time of spark existence was not more than several microseconds. Energy deposition of this object turned out to be very close to the pulse MW energy and was not more than ~ 5J. At first we studied spark under the atmospheric pressure at different experimental conditions – only spark, then spark in the airflow and under the magnetic field. Let us view spark photos and then discuss some of its features.

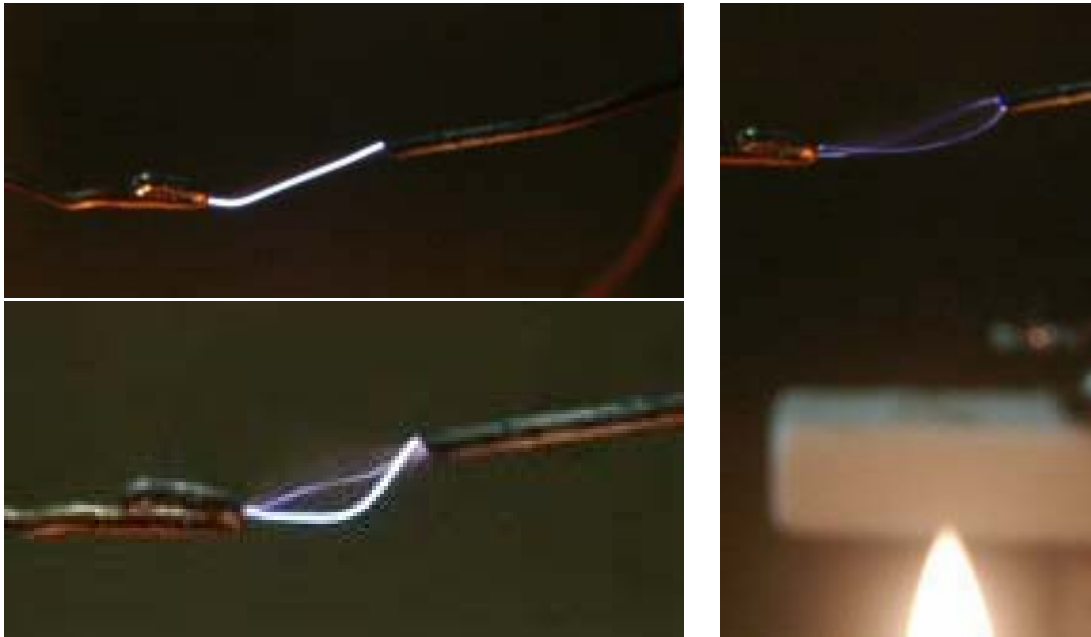


Fig.2.26. Spark under different conditions

As a rule, without external action the discharge channel propagates in straight line. If we have the heating area (Fig.2.26), the discharge channel divided on two weak lighting bending channels. The similar picture is observed when the channel locates at magnetic field. Moreover, it also becomes thinner and more bright. The channel bend radius is changing with magnetic field increasing. We try to measure such change, but the obtained results are very previous and demand future test. At magnetic field well seen is the channel twisting (Fig.2.27b). At presented below photos the magnet consistently was placed closer and closer to the channel – 15mm (Fig.2.27b), 7mm (Fig.2.27c), 4mm (Fig.2.27d). The results of measured channel radius are presented in Table 1.

Note that with magnetic field increasing at the electrodes tips the red color appears. Also the red color layer appears along the channel on magnet side. It is possible that the electron drift in magnet side takes place and so the electron temperature is decreasing in surrounding channel air. May be this effect will be fixed by spectroscopic method in the nearest future.

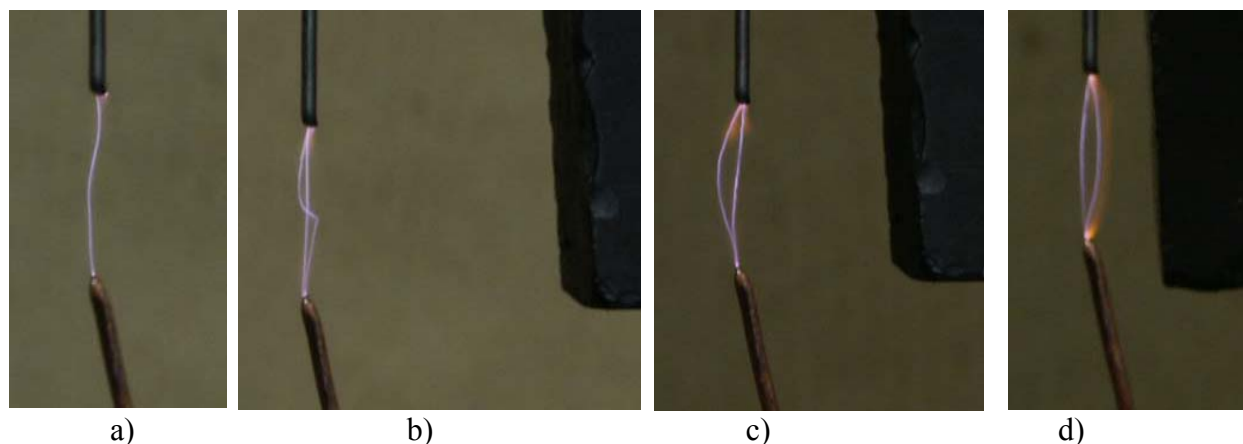


Fig.2.27. Spark without magnet (a) and in magnetic field

Table 1

R, mm	60	30	7
H, mT	12	22	30

Let us shortly observe the spark dynamics. The threshold has two-time stage at rising voltage period on the oil. At first we fix the weak “forerunner”- channel ($\tau \sim 0.2-0.4 \mu\text{s}$), which grows from lower zero electrode (earth) on high voltage electrode with velocity about $\sim (2-4) 10^6 \text{cm/s}$. At the second stage the channel propagates from anode to the earth ($\tau \sim 0.4-0.8 \mu\text{s}$) electrode with velocity of order smaller - 10^5cm/s . The channel lighting level at the second stage is greater on $\sim 30\%$ and its existing time increases at two times. When we placed the magnet near the channel, the existing time of “forerunner” increases up to $2-5 \mu\text{s}$ and the lighting time of the main channel – up to $10-15 \mu\text{s}$. So the magnet permits to increase the plasma existing time and probably the energy deposition level.

Moreover, we performed some experiments with surface discharges. For these aims we have made the ground electrode in form of metal disc and covered it by thin polyethylene film. The upper electrode practically touched the film at the central point (Fig.2.28a). We wanted to check the possibility of creating and control the surface discharges. First of all we carried out the flow-plasma channel interaction. The flow velocity was about $\sim 1.2 \text{M}$ and at atmospheric pressure the picture of several channel formation (Fig.2.28b) during $\sim 100-150 \mu\text{s}$ is well seen.

Practically every following channel replicates the previous one. The dynamic of such process is very interesting but its study demands high-speed camera. At last we fixed the branched surface discharge (Fig.2.28c). So, the processes at MWD and spark discharges are very similar and some discharge properties we may study with using our high voltage spark.

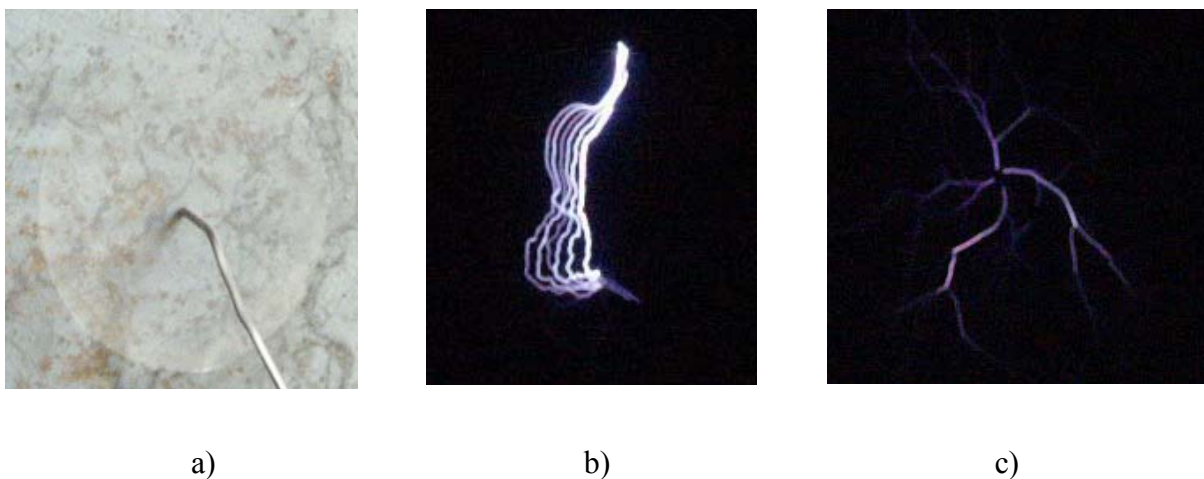


Fig.2.28. Types of surface spark

2.7. The initiation and control of MWD by external plasma channel

One of the most important problems of our study is the MWD initiation possibility by external plasma source. This problem always takes place in crossing beams of different wave range. Not only the initiation question, but also the propagating direction of plasma at combined waves is to be investigated. For this aim the spark is very flexible object. We may easily control the direction of the spark channel with respect to wave polarization and so to achieve demanding discharge size or energy deposition at plasma area. We try experimentally to define the approach to this problem. Some new results are presented below.

Already the first experiments have demonstrated very interesting results (Fig.2.29). We placed horizontal electrodes into the vacuum chamber along its axis at 20mm distances one from another. The nozzle was placed at several cm.

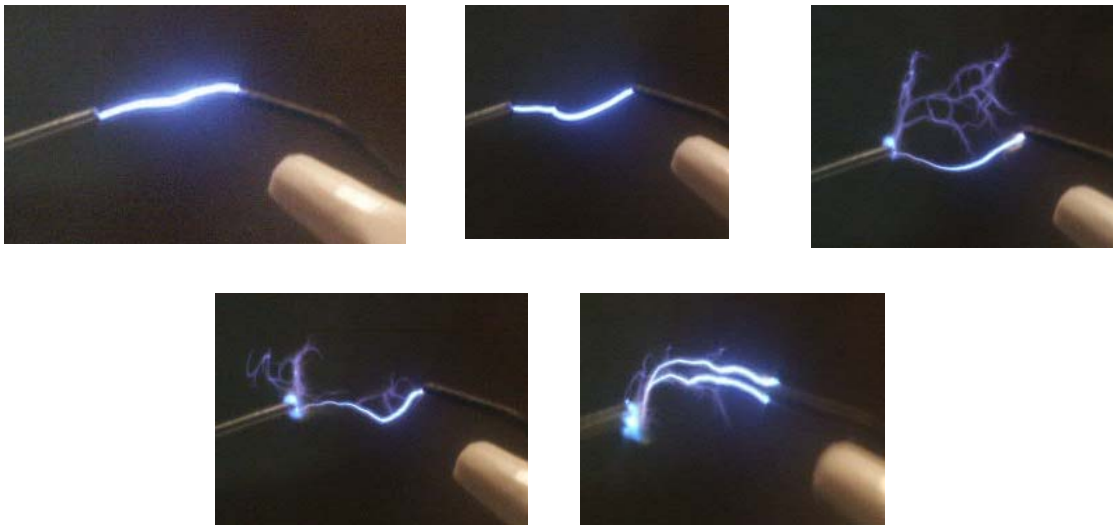


Fig.2.29. Spark-guided MW discharge

The interaction processes are presented here. At the first photo the spark is only shown. The distance between electrodes is 20mm. In the right corner at all photos one can see the nozzle. In the next photo the channel is bending in the supersonic flow. The third and fourth photos demonstrate the MWD – spark interaction. Well seen are the MWD structure changing and the channel deflection from its straight propagating line. The channel brightness is decreased. MWD propagates along and across of the channel. At the latter photo two channels are strongly bending in the supersonic flow and obviously are interacting with microwave. The mutual effect during interaction process is well seen at the photos. Such processes in more degree were fixed when we extended the channel length up to 50mm (Fig.2.30).

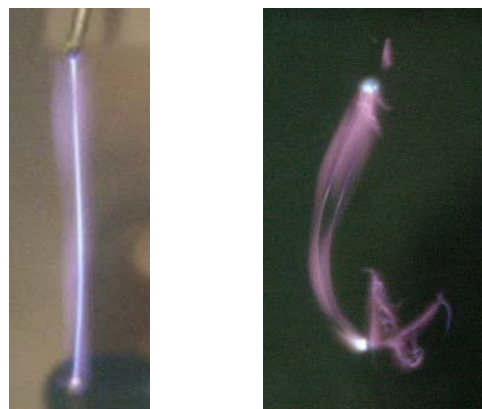


Fig.2.30. Mutual action of spark and MW

On Fig.2.31 the channel was created along polarization direction of microwave and we performed the experiment at lower air pressure $\sim 0.5\text{atm}$. The left picture is the spark only. In the middle only MWD is presented. The last photo demonstrates the interaction MW with spark. Here the MWD initiation is realized by spark plasma. As a rule the MWD vertical size is not more than $\sim 1.5\lambda$ but here discharge develops along spark, not propagates along radiation axes and changes the channel color. So, such interaction process has many features for future study. Let us observe for example some additional photo where the MW interacts with spark at different synchronization periods (time). These results were received for the first time.

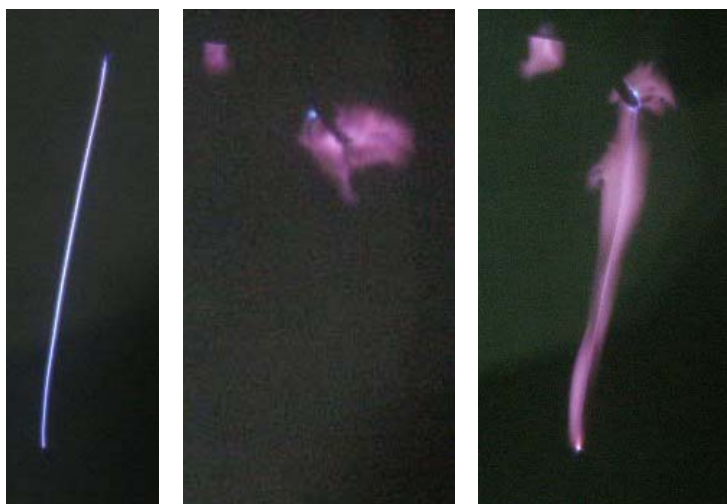


Fig.2.31. Spark (left), MWD (middle) and spark + MWD (right)

At the left photo MW pulse interacts with channel at the late phase of its evolution. As a result only additional blue lighting appears around the channel. But the picture dramatically changes when interaction takes place at the early evolution phase. The channel trajectory most likely presents the force electric line of convergent wave. This effect demands more of our experimental attention because it has a large potential of application.

On our opinion we've selected the flexible model object - the pulse air spark, which is very similar to the separate MW plasma channel and may be used for its study in some cases.

Moreover, for the first time we revealed the effect of very strong interaction of free microwaves with an external plasma channel. At the early evolution phase the channel practically develops along the force electric line of convergent wave. This effect demands more experimental attention and may be of importance both for practical use and/or as a fundamental trend for further research.

3. Kinetic modeling of MW plasmoid in air

Analysis of kinetic and chemical processes in MW discharge active phase and in afterglow is aimed at quantifying of principal MW discharge parameters. Determination of actual discharge parameters during its active phase demands taking into account electrodynamic interaction of the discharge structure with an external electric field. For this purpose calculations of the local parameters of discharge in this phase in air were made at the base of simplified electrodynamics of discharge channel and complete kinetics in it. Plasma parameters and gas composition in zone of discharge region - BSW interaction – afterglow phase – is also of interest.

For active phase of discharge two types of optic signal are available – time-dependent curves of emission and spectra. Processing of these data provides valuable information about local discharge parameters. An adequate kinetic scheme forms the basis for processing.

3.1. Kinetic scheme assembling

3.1.1. Reactions and rate constants

Kinetic scheme for the dry air (78% N_2 и 22% O_2) includes 106 charged and neutral components and about 20000 reactions. Among 106 components 38 are: N , $N_2[X^1\Sigma_g^+]$, O , $O_2[X^3\Sigma_g^-]$, O_3 , NO , NO_2 , NO_3 , N_2O , N_2O_4 , N_2O_5 , $N[{}^2D]$, $N[{}^2P]$, $O[{}^1D]$, $O[{}^1S]$, $N_2[A^3\Sigma_u^+]$, $N_2[B^3\Pi_g]$, $N_2[a^1\Sigma_u^-]$, $N_2[C^3\Pi_u]$, $O_2[a^1\Delta_g]$, $O_2[b^1\Sigma_g^+]$, N_2^+ , N_4^+ , O_2^+ , O^+ , O_3^+ , O_4^+ , NO^+ , NO_2^+ , NO_3^+ , $N_2O_2^+$, O_2^- , O^- , O_3^- , O_4^- , NO^- , NO_2^- , e. The rest are nitrogen and oxygen molecules which can be excited in all vibrational levels – 48 for nitrogen and 33 for oxygen. The kinetic scheme takes into account electron-neutral collisions (vibrational excitation of $N_2[X^1\Sigma_g^+]$, $v=1..8$], excitation of electronic states of N_2 and O_2 , ionization of N_2 , O_2 , NO and O , dissociation of N_2 and O_2 , as well as electron attachment), chemical, energy-exchange, radiative reactions, charge exchange for ions, ion-ion and electron-ion recombination, electron detachment.

Vibrational kinetics, including VV, VV' (vibrational quantum exchange between nitrogen and oxygen molecules) and VT processes are under special consideration. For the ground state of $N_2[X^1\Sigma_g^+]$ the detailed vibrational kinetics (VV and VT-processes) of levels with

$v=0..48$ is introduced. The processes of direct electron level-to-level excitation from the ground state to the excited $N_2[C^3\Pi_u]$ state in the matrix of electron-vibration transitions $e + N_2[X^1\Sigma_g^+, v=0..8] \rightarrow e + N_2[C^3\Pi_u, v=0..4]$ are considered, as well as its radiative quenching in the frame of the second positive nitrogen system $N_2[C^3\Pi_u, v] \rightarrow N_2[B^3\Pi_g, v'] + h\nu$. For this case 35 transitions $v \rightarrow v'$ are taken into consideration: 0-0, 0-1, 0-2, 0-3, 0-4; 1-0, 1-1, 1-2, 1-3, 1-4, 1-5, 1-6; 2-0, 2-1, 2-2, 2-3, 2-4, 2-5, 2-6, 2-7; 3-0, 3-1, 3-2, 3-3, 3-5, 3-6, 3-7, 3-8; 4-2, 4-3, 4-4, 4-6, 4-7, 4-8, 4-9.

The detailed (state-to-state) kinetics of population and emission of $N_2[B^2\Sigma_u^+, v]$ ion was inserted too. Population of $N_2[B^2\Sigma_u^+, v]$ ion state takes place by processes of two types: direct population $e + N_2[X^1\Sigma_g^+, v=0..4] \rightarrow e + N_2[B^2\Sigma_u^+, v'=0..1]$, stepwise population $e + N_2[X^1\Sigma_g^+, v=0..4] \rightarrow e + N_2[X^2\Sigma_u^+, v'=0..2]$ and then $e + N_2[X^2\Sigma_u^+, v'=0..2] \rightarrow e + N_2[B^2\Sigma_u^+, v''=0..1]$. Emission of $N_2[B^2\Sigma_u^+, v]$ can be both spontaneous $N_2[B^2\Sigma_u^+, v''=0..1] \rightarrow N_2[X^2\Sigma_g^+, v'=0..2] + h\nu_{v'',v'}$ and induced by electron impact $e + N_2[B^2\Sigma_u^+, v''=0..1] \rightarrow e + N_2[X^2\Sigma_g^+, v'=0..1] + h\nu_{v'',v}$.

Rate constants for chemical and energy-exchange reactions were taken mainly from reviews [1-3], for electron-ion recombination - from [4], for ion-ion recombination and charge exchange - from [5], for radiative quenching – from [6, 7]. Each rate constant and its temperature dependence were compared with another literature recommendations so, only realistic values were included in kinetic scheme.

Rate constants for vibrational and electron states excitation, ionization, dissociation and attachment in electron-neutral collisions were determined by solving the Boltzmann equation for electron energy distribution function (EEDF) in air under the applied external electric field. We developed and applied a new method for determination of electron-impact rate constants in vibrationally excited gas discharge plasma.

3.1.2. New method for determination of electron-impact rate constants in vibrationally excited gas discharge plasma

The key problem during kinetic modeling of gas discharge plasma is proper determination of swarm data and rate constants of electron-heavy particle interactions, taking into account substantially non-Maxwellian character of electrons energy distribution

function EEDF. For molecular gases at most usual reduced fields E/N (near breakdown threshold) inelastic collisions of electrons significantly influences on electrons energy spectrum. In energy saturated plasma super-elastic collisions play important role too. For gases having sufficiently great cross sections of vibrational excitation such as N_2 , CO_2 , CO and their mixtures, electrons collisions with just vibrationally excited molecules gives main contribution among the others super-elastic collisions.

So EEDF in molecular gases can be described by two parameters E/N and energy deposition in plasma ε . The last parameter corresponds the case of nonzero vibrational population in plasma. Traditionally [8], the problem of the influence of vibrational population on EEDF and related characteristics of electrons was solved in approach of Boltzmann form of vibrational distribution function VDF or of Treanor distribution at high gas temperatures. In both cases vibrational distribution functions characterized by so-called vibrational (Boltzmann) temperature

$$T_v = \frac{E_{10}}{\ln \frac{N_{v=0}}{N_{v=1}}}, \quad (1)$$

E_{10} – the difference of energy between first and zero vibrational levels [K], $N_{v=0}$, $N_{v=1}$ – their populations. At that, specific character of VDF, which is formed during discharge stage under domination of electron-neutral collisions wasn't taken into account. If for pulse duration τ the condition

$$p \cdot \tau < \frac{3.8 \cdot 10^{-20}}{K_{vv}} \quad (2)$$

applies (p – pressure [bar], K_{vv} – rate constant of VV-exchange [cm^3/s]), non-elastic and super-elastic electron-neutral collisions are a single kinetic channel of VDF formation.

CARS-experiments [9, 10] and calculations show that VDF during the pulse of energy pumping of discharge plasma is neither Boltzmann nor Treanor and can't be described by single vibrational temperature. Roughly here allowed “two-temperature approach” (Fig.3.1). Main vibration temperature T_{v1} is a “Boltzmann” one. Second vibrational temperature T_{v2} is determined as average one by population of the levels, which are excited by electron impact (levels 1-10 for N_2 , and 1-4 for O_2). At the same time, own calculations show that for gas mixtures to determinate VDFs of components correctly uses “temperature” approach

unacceptable in general, because of “vibrational temperatures” of each component must be agreed reciprocally and uniquely, but no one knows how beforehand.

We made an attempt to calculate EEDFs and related parameters of electrons in single gases and mixtures based on naturally forming of VDFs during discharge pulse when vibrational excitation by electron impact dominates (limitation (2)), using two parameters for EEDF description: E/N and ε . For rate constants of individual processes it is convenient expression like:

$$K(E/N, \varepsilon) = K_0(E/N, \varepsilon = 0) \times \eta(E/N, \varepsilon) \quad (3)$$

where

$$K_0 = A \times E/N^q \times \exp \left[\frac{E/N_0}{E/N} \right] \quad (4)$$

is traditional (Arrhenius) form for rate constant at zero energy deposition at “zero” VDFs, when relative vibrational populations are

$$\tilde{N}_{v=0}=1, \tilde{N}_{v>0}=0 \quad (5)$$

and η - correction item for vibrationally excited mediums.

Electron energy distribution function was calculated in commonly used “two-term” approach as a result of numerical solving of equation for electron energy spectra $f(u)$:

$$\begin{aligned} & \frac{E^2}{3} \times \frac{u}{\sum_k N_k \times \sigma_{tr,k}(u)} \times \frac{df(u)}{du} + \sum_k \frac{2m}{M_k} \times N_k \times u^2 \times \sigma_{tr,k}(u) \times \left[f(u) + \frac{kT_g}{e} \times \frac{df(u)}{du} \right] + \\ & \sum_k N_k \times B_k \times \varepsilon \times \sigma_{rot,k}(u) \times \left[f(u) + \frac{kT_g}{e} \times \frac{df(u)}{du} \right] = \\ & - \sum_k N_k \times \sum_{ij} \int_u^{u+\varepsilon_{ij}} \sigma_{kij}(u') \times u' \times f(u') \times du' + \sum_k N_k \times \sum_{ji} \int_{u-\varepsilon_{ij}}^u \sigma_{kji}(u') \times u' \times f(u') \times du' \end{aligned}$$

Here index k means the particle (molecule or atom) of the sort k ; e , m , M - charge, mass of electron and heavy particle correspondingly; T_g , E , N and B - gas temperature, electric field, concentration of particles and rotational constants of molecular particles; σ_{tr} and σ_{rot} - are transport cross sections of electron scattering and cross section of molecules rotational excitation; σ_{ij} - cross sections of inelastic electron-neutral collisions (vibrational and electron states excitation, ionization, dissociation) with threshold ε_{ij} of transition between initial i and result j states. Cross sections of reverse process σ_{ji} determinates, based on principle of detailed

balance $\sigma_{ji}(u - \varepsilon_{ij}) = \frac{g_i}{g_j} \times \frac{u}{u - \varepsilon_{ij}} \times \sigma_{ij}(u)$, g_i and g_j are statistical weights of corresponding electron states.

First item of left part of equation describes the increasing of electrons energy in electric field E , second and third items - energy losses at elastic collisions and at molecules rotational excitation in approach of electron “diffusion” along energy axis.

Right side items describe inelastic and super-elastic electron-particle collisions. In first case electron loses energy ε_{ij} transferred heavy particle in excited state, in second - receives the same energy during collisional deactivation of excited state.

The equation for electrons energy was transformed to expression:

$$\ln f(u) = - \int_0^u \frac{T_g}{e} + \frac{\sum_k N_k \times \sum_{i,j} \int_{u'}^{u'+\varepsilon_{ij}} \frac{z \times f(z) \times \sigma_{ij}(z)}{u' \times f(u')} \times dz}{u' \times \sum_k N_k \times \left[\frac{2m}{M_k} \times \sigma_{tr,k}(u') + B_k \times \sigma_{rot,k}(u') \right]} \times \frac{E^2}{3 \sum_k N_k \times \sigma_{tr,k}(u') \times u' \sum_k N_k \times \left[\frac{2m}{M_k} \times u' \times \sigma_{tr,k}(u') + B_k \times \sigma_{rot,k}(u') \right]} \times du'$$

and was calculated using iteration method until relative change of EEDF became less then taken

error. Then normalization of EEDF was obtained carried out as: $\int_0^\infty f(u) \times \sqrt{u} \times du = 1$.

Based on EEDF calculated, the needed characteristics of electrons were determined, including rate constants of individual processes:

$$K_{ij} = \sqrt{\frac{2}{m}} \times \int_0^\infty \sigma_{ij}(u) \times f(u) \times u \times du \quad (6)$$

and drift velocity of electrons:

$$V_{dr} = \frac{1}{3} \times \sqrt{\frac{2e}{m}} \times \frac{E}{N} \times \int_0^\infty \frac{u}{\sigma_m(u)} \times \left(\frac{df(u)}{du} \right) \times du. \quad (7)$$

Usually, in literature sources cross sections for vibronic transitions between two electron states are given as a sum one for all vibrational-vibrational transitions. As a rule, these cross sections data are given for faintly-excited mediums, when condition (2) is realize. In this case, energy

dependence of sum cross section $\sigma_{ij}(u) = \sum_v \sum_{v'} \sigma_{ij,v \rightarrow v'}(u)$ turned out “depended” on vibrational population of initial electron state:

$$\sigma_{ij,v \rightarrow v'}(u) = \tilde{N}_{i,v} \times q_{ij,vv'} \times \sigma_{ij} \left(\frac{E_{j,0}}{E_{j,v'} - E_{i,v}} \times u \right), \quad \text{where} \quad \tilde{N}_{i,v} = \frac{N_{i,v}}{N_{i,0}} \quad \text{is relative}$$

population of vibrational level with quantum number v of initial electron state i , $q_{ij,vv'}$ - Franck-Condon factors for vibronic transitions $i,v \rightarrow j,v'$; $E_{i,v} = E_i + \omega_0 v - \omega_0 x_0 v^2$ is total energy of vibronic state i, v ; E_i - energy of zero vibrational level of electron term i , counted out relative zero level of the ground electron state, ω_0 and $\omega_0 x_0$ are vibrational quantum and anharmonicity value of the term i , correspondingly.

Calculation was carried out in two stages. First stage – calculation of EEDF with zero VDF when fit coefficients A , q and E/N_0 were determined. Fit coefficients in expression (4) for N_2 and air are shown in the tables 1 and 2 in Appendix A.

During the second stage the calculation of EEDF with VDFs of ground electron states are adapted for each pair of E/N and ε was carried out. In the beginning VDFs of all mixture components were taken as “zero” one (5). After calculation of EEDF in zero approach, rate constants (6) and drift velocity (7) were determined.

Then, using these data, calculation of VDFs was carried out. Vibrational distribution functions were calculated in approach of momentary balance between excitation/deactivation of

each vibrational level by electron impact at given E/N and ε as $\frac{\tilde{N}_{k,v'}}{\tilde{N}_{k,v}} = \frac{K_{k,vv'} \times \langle n_e \tau \rangle}{1 + K_{k,v'v} \times \langle n_e \tau \rangle}$,

$K_{k,vv'}$, $K_{k,v'v}$ - are rate constants of vibrational level v' from level v excitation and level v' to level v deactivation for k – component of mixture. Normalization of VDFs are $\sum_v \tilde{N}_{k,v} = 1$.

The value of energy deposition into discharge $\varepsilon = j \times E \times \tau$ (j is current density)

determinates multiplier $\langle n_e \tau \rangle = \frac{\varepsilon}{e \times E \times V_{dr}}$ (n_e – is electron concentration, τ – pulse duration).

The brackets mean that for fixed ε and under limitation for pulse duration (2) neither absolute value n_e , nor dynamics n_e during τ aren't significant.

At obtained VDFs, cross sections of electron states excitation were recalculated according (8). The named procedure was repeated cyclically until change of VDF of all components became less than accepted error (0.01%).

Calculations were carried out in the energy range 0-40 eV for N₂ and 0-50 eV for air with the step of integration 0.02-0.04 eV for $E/N = 80-160$ Td and $\varepsilon = 0-2$ J/cm³·bar.

As a result the dependences $\eta(E/N, \varepsilon)$ were obtained in the form with four fit coefficients $\varepsilon_0, E/N_I, a, b$.

$$\eta = E / N^{b \cdot \gamma} \times \exp \left[\frac{E / N_I - a \cdot E / N}{E / N} \times \gamma \right] \quad \gamma = \tanh \left[\frac{\varepsilon}{\varepsilon_0} \right] \quad (9)$$

The dependences of fit coefficients as a function of individual process threshold shown in Fig.3.2, 3.3. Bottom picture in Fig.3.2 shows dependence of sum non-elastic cross section in nitrogen and air. As it visible, below the first vibrational resonant maximum there is rather strong dependence of fit coefficients as a function of energy deposition, but when threshold of process became greater resonant maximum all dependences turns out weakly depended on threshold. In these pictures envelope solid curves reflects the influence of vibrational population on EEDF as a whole, while scattering – the influence of probability of individual vibronic transitions. For rough evaluation one may take envelope curves, for more precise (less than 5%) evaluation - values from tables 3, 4 of Appendix A.

The influence of energy deposition into discharge on rate constants of electron states excitations and ionization of nitrogen are shown in Fig.3.4. As it visible, natural approach gives about 30-50% excess over Boltzmann approach.

3.1.3. Kinetic mechanisms of heating in plasma

One more problem for formation of adequate kinetic model is the proper selection of mechanism of gas heating in discharge. In addition to heating during vibrational and rotational relaxation (which is taken into account automatically) there are two reliable kinetic channels of short pulse discharge heating: collisional quenching of excited particles and electron-ion recombination. The relation between these channels depended on energy deposition (electron concentration) mainly.

During collisional quenching of electron-excited atoms and molecules energy defect of reaction is distributed between internal and kinetic energies of reaction products. In the most cases the parts of such distribution keep unknown with the exception of the family of reactions as



where $M^* = N_2[A^3\Sigma_u^+]$, $N_2[B^3\Pi_g]$, $N_2[a'^1\Sigma_u^-]$, $N_2[C^3\Pi_u]$. In these cases energy permission/prohibition of reaction realization and permission/prohibition of $M^* \rightarrow M$ vibronic transitions allow to determinate heat effect of reactions.

The relative population of v' vibrational levels of M^* state at the colliding moment is $\tilde{N}_{v'} = \sum_v q_{vv'} \times \tilde{N}_v$, \tilde{N}_v - relative population of v vibrational levels of the ground electronic state, $q_{vv'}$ - Franck-Condon factor for $v \rightarrow v'$ transition. This expression corresponds to the case when M^* state is populated by electron impact from the ground state. As a result of collision, M^* state transits to v'' levels of M state with the possibilities are proportional to $q_{v'v''}$ - Franck-Condon factors of $v' \rightarrow v''$ transitions. At this energy change $E_{v'v''}$ equals the difference between M^*, v' and M, v'' energies. The transitions with $E_{v'v''} < E_{diss}$ turn a forbidden one (E_{diss} - dissociation energy of second colliding particle). The expression $q_{v'v''}(E_{v'v''} - E_{diss})$ determinates heat effect of allowed $M^*, v' \rightarrow M, v''$ transition. Total heat effect E_r of reaction is a sum over heat effects of individual vibronic transitions. Our calculations show that E_r depends on vibrational temperature of ground electronic state weakly. Accepted heat effects of reactions (1a,b) are collected in Table 1 of Appendix B. Reactions, similar (1b), but with participation of oxygen atoms weren't taken into account as a heating channel, because of these reactions lead to N_2 oxidation mainly ($NO+N$) with unknown heat effect.

Another family of energy transfer heating reactions is



where $M = N_2, O_2$, $M^* = N_2, O_2, O_2[a^1\Delta_g], O_2[b^1\Sigma_g^+]$. According [11] *brutto* heat effect of $O[{}^1D]$ collisional quenching is 70% of excitation energy, i.e. 1.38 eV. This value was accepted in the model.

Dissociative recombination of electron with diatomic ions (N_2^+ , O_2^+ , NO^+) is one more class of plasma heating reactions. There are direct measurements of kinetic and internal energy

of reaction products [12-15]. Accepted in the model heat effects of these reactions are shown in Table 2 of Appendix B.

3.1.4. Specific features of local field behavior

During the pulse the magnitude of local field changes under the influence of several factors (correspondingly rate constants of electron-impact reactions change too).

1) Polarization reduction for considered type of MW discharge is
$$\mu_1 = \left[1 + \left(q \times \frac{n_e}{n_e^{crit}} \right)^2 \right]^{-1/2},$$

(q - polarization factor, $n_e^{crit} = 7 \cdot 10^{13} \text{ cm}^{-3}$ critical electron concentration for polarization at atmospheric pressure).

2) During MW pulse as energy spectra (distribution function) of electrons changes owing to polarization reduction and/or the change of pulse profile, the relation ω/v_e changes too (ω - MW angular frequency, $v_e(E/N)$ – effective frequency of electrons collisions), so “ ω/v_e ” - reduction is

$$\mu_2 = \frac{v_e}{[v_e^2 + \omega^2]^{1/2}}.$$

3) Gas particles concentration N is not constant value not only under isobaric conditions, but under isochoric one too (molecular dissociation, chemical transforms etc.). In other words, at each time τ , $N(\tau) = \sum_i N_i(\tau)$, N_i – components of medium and the value E/N turns out the function of time.

Thus, the actual local reduced field is $E/N(\tau) = E_0 \times \mu_1 \times \mu_2 / N(\tau)$. The value $E_0 = 19.5 \times \sqrt{s} \text{ [V/cm]}$ (s – MW power density [W/cm^2]) is the electric field under the condition $n_e = 0$ and in “high pressure limit”, when $\omega/v_e \rightarrow 0$.

3.2. Determination of local parameters of inhomogeneous MW plasmoid

The kinetic model described was applied for modeling of halo and filament with the aim to determinate the local parameters of these plasma objects. In the both cases the initial gas temperature was 200 K and the initial electron concentration was $3 \cdot 10^4 \text{ cm}^{-3}$. Pulse duration was 1.7 mcs with the shape, which was taken from experimental measurements.

3.2.1. Halo modeling

While the halo modeling the medium conditions were taken in isochoric approach (taking into account rather large dimension of halo and short MW pulse). At this, polarization factor was $q = 0.1$ and $n_e^{\text{crit}} = 7 \times 10^{12} \text{ cm}^{-3}$. In Fig.3.5 the dependencies of MW reduced field during the pulse are shown: the measured profile and an actual local field inside the halo. Here rather pronounced fall down of a local field during the second half of MW pulse takes place when the electron concentration is growing up to the values sufficient for “switching on” the polarization reduction.

Fig.3.6 illustrates the influence of energy deposition into discharge ($N_2[X^1\Sigma_g]$ vibrational levels population) on the excitation processes in an example of $N_2[C^3\Pi_u]$ excitation: $e + N_2[X^1\Sigma_g, v=0..8] \rightarrow e + N_2[C^3\Pi_u, v'=0..4]$. The change of process sum rate constant during the pulse is shown for two cases: $K = K(E/N)$ and $K = K(E/N, \epsilon)$. As it is visible, in spite of field amplitude reduction at the end of pulse owing to both the pulse profile and polarization reduction, reaction rate in the second case decreases weakly because of increasing of $N_2[X^1\Sigma_g]$ vibrational population. The same situation is observed for other high threshold processes, including ionization. Enumerated features lead to visible in experiments continuation of N_2 second positive system emission at the end of MW pulse. This can be seen in Fig.3.7, where profiles of 2PG emission are shown in comparison with experiment.

Fig.3.8-3.11 demonstrate dynamics of concentration of charged, excited and neutral particles. The first, what attracts attention – the increasing of electron concentration until the end of pulse, despite continuous field reduction. It is conditioned by increasing of energy deposition: from one side the processes of direct ionization at weak fields are intensified (as it was mentioned above), from another side – associative ionization switches on progressively.

Fig.3.12 demonstrates the fractional curves for heating channels and temperature dynamics for halo. Here the main heating channel during the pulse is collisional quenching of metastables, RT-relaxation is significant only at the fore and back fronts of pulse, i.e. at low E/N . Recombination heating is insignificant: maximal contribution of this branch does not exceed 1%. Gas temperature at the end of pulse is 280 K. Thus, the rate of gas heating in halo is about 50K/mcs, the value typical for E/N range near breakdown threshold.

3.2.2. Filament: limit curve of heating and the channels of heating

Medium conditions for filament modeling were assumed as isobaric ones. For determination of the *limit* curve of filament heating we took depolarization factor equal to zero, i.e. kept only “ ω/v_e ” - reduction as actual one.

Calculations show that filamentation takes place at 0.9mcs. Fig.3.13-3.16 show dynamics of various kinds of particles concentration (analogous to Fig.3.8-3.11 for halo). Electron concentration increases up to $5 \cdot 10^{16} \text{ cm}^{-3}$ at the filamentation completion (Fig.3.13).

The comparative significance of the heating channels and the maximal possible value of gas temperature, which is reached during the filamentation stage, are shown in Fig.3.17. At the beginning of MW pulse (near fore front of pulse) the dominant channel of plasma heating is RT-relaxation, but the value of temperature increasing at that is insignificant because of low electron concentration. During electrons production the channel, which is connected with the collisional quenching of metastables, is a dominant one. One may say that this kind of heating starts up the filamentation process. At the final stage of filamentation, ionization processes are accelerated thus much that recombination heating becomes the single heating channel. Gas temperature increases up to 3500 K.

One of the basic parameters, which define evolution of MW discharge, is the radial dimension of filament. Closeness of the calculated (ultimate 3500K for zero polarization factor) and experimentally obtained (about 3000K) gas temperatures in filament leads to conclusion that its radius should be less than 100 microns. This is very important indication on high efficiency of filament – electromagnetic wave interaction in its evolution.

If take a look at Fig.3.14, where positive ions partial content is shown, one more fact can be noticed. At the ultimate twinkling of filamentation the fast redistribution of ion composition takes place – the atomic ions became dominant ones. This means that at final stage filament plasma becomes heatless one (our calculations show that the contribution of VV, VT relaxation at high degree of dissociation is insignificant). Apparently, the main channel of deposited energy shedding in such situation is an atomic light emission. In this case at the last moment filament must blaze up by atomic emission lines.

3.3. Comparison of calculated results with emission spectrum measurements

Emission spectrums of MW breakdown measured are shown in Fig.3.18 and 19. There are spectrums of second positive (2PG) and first negative (1NG) systems of N_2 .

N_2 [2PG] spectrum. Rotational (gas) temperature defined over rotational bands 0-3, 1-4, 0-4, 3-7 turned out 270 ± 10 K. Vibrational temperature of the $C^3\Pi_u$ -state has been determined separately for each sequence. For the $\Delta v = -3$ sequence only emission in the bands 1-4 and 0-3 is taken into account, whereas for $\Delta v = -4$ averaging is fulfilled over the entire sequence bands. In the first case the temperature is 3150 K, in the second – 3120 K. At the small window of Fig.3.18 and 19 the VDF of the radiating state is shown, which is reconstructed over intensities of the bands of the appropriate sequence. It is readily seen that for $\Delta v = -4$ (Fig.3.19) the vibration distribution function is close to Boltzmann with good precision for almost all bound vibrational levels of $C^3\Pi_u$ -state. For $\Delta v = -3$ the “under-population” of levels with $v > 1$ can be explained by the errors in monochromator transmission function determination near the edge of its operating range.

N_2^+ [1NG] spectrum. Weak emission intensity of this system of bands in comparison with N_2 [2PG] emission provides not so many abilities to carry out exact analysis of discharge plasma characteristics. Nevertheless, one can notice the important fact that rotational spectrum of 1-2 band, which is seen most distinctly, turns out to be flat. This is indicative of high temperature in the $B^2\Sigma_u^+$ system (about 3200 K).

In Fig.3.18 and 3.19 the synthesized spectrums are also shown. The spectrum of N_2 [2PG] was synthesized according calculation results for halo, the spectrum of N_2^+ [1NG] – according results for filament. Comparison of experimental and calculated time dependence of N_2 [2PG] emission was demonstrated in Fig.3.7. The comparison of measured and synthesized spectrums shows rather good agreement, what testify to adequacy of the kinetic model.

Thus, the method for decoding of optic spectra from strongly non-homogeneous object and extraction of optical information from highly non-homogeneous objects can be proposed. Use of species with higher energy level excitation and non-linear dependence of guiding parameter seems to be the single way to distinguish the higher gas temperature. Unification of optic information processing with discharge kinetic modeling sufficiently rises the validity of obtained results.

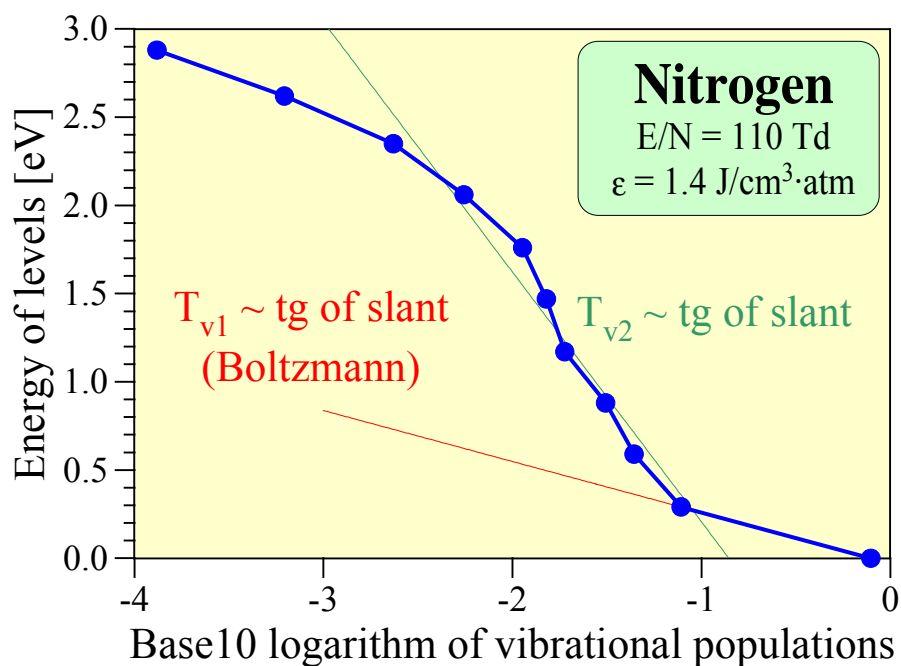


Fig.3.1. Vibrational distribution in nitrogen under domination of vibrational excitation by electron impact

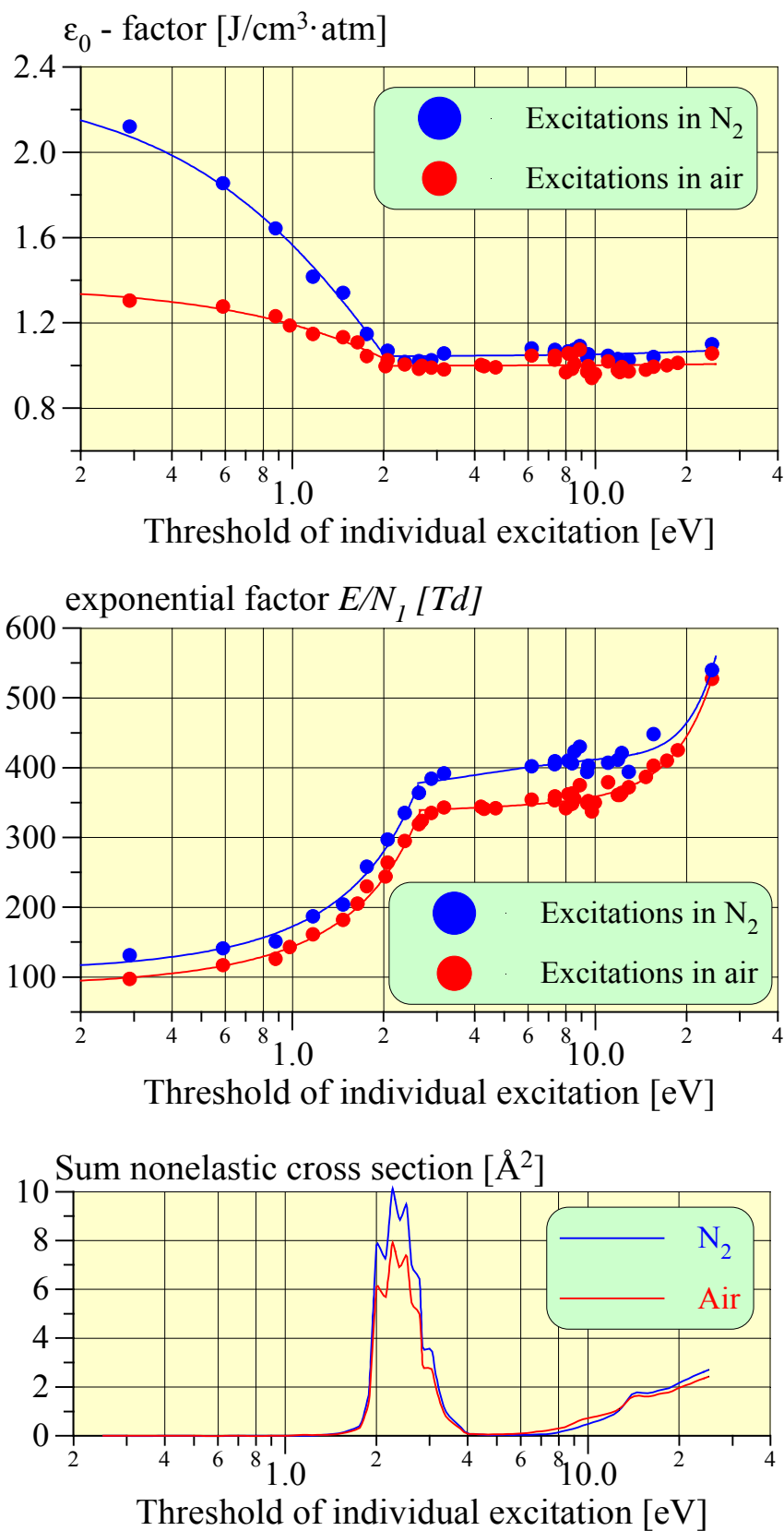


Fig.3.2. Dependencies of ϵ_0 and E/N_1 -factors as a function of process threshold (vibrational and electron states excitations, dissociations, attachments, ionizations)

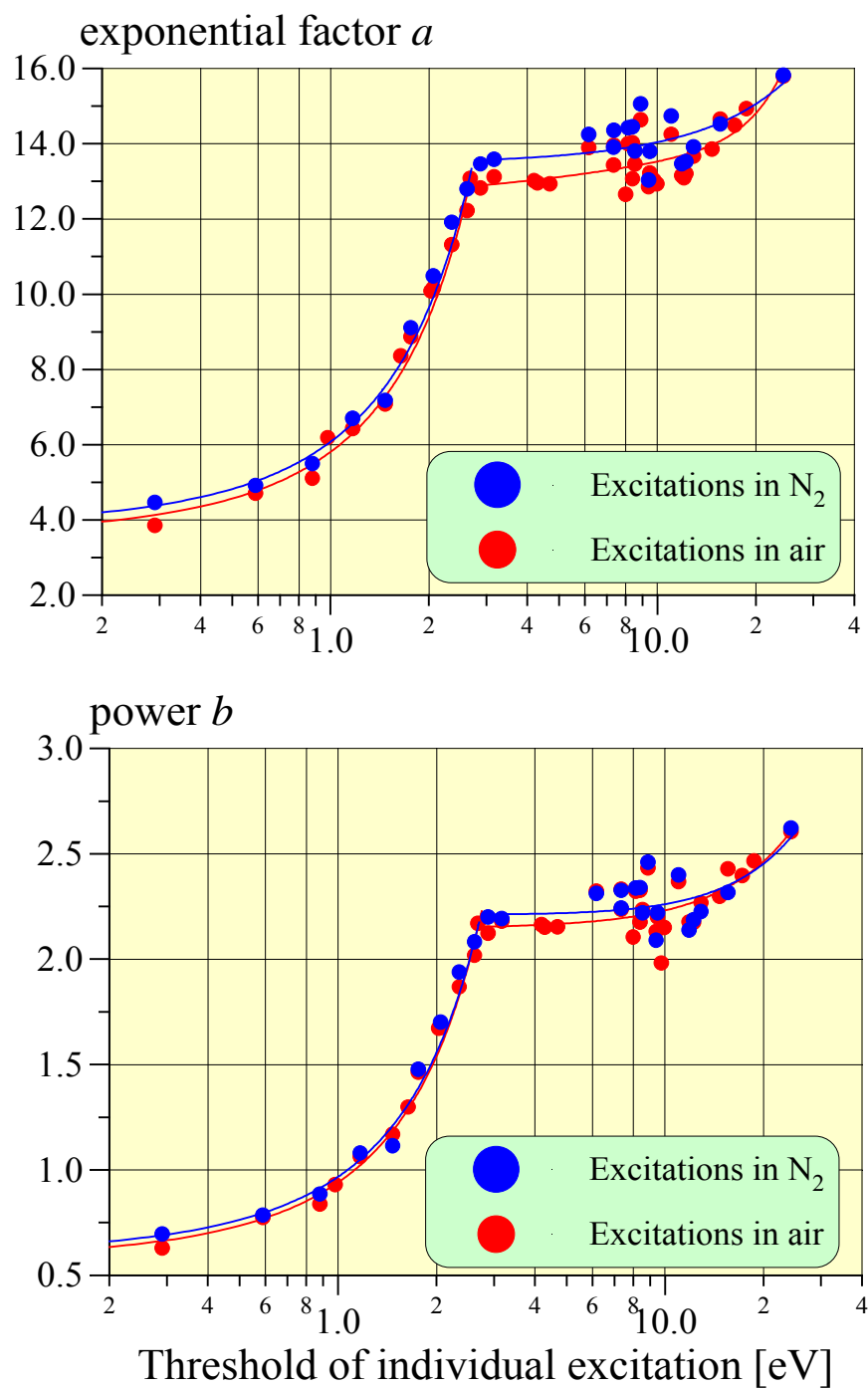


Fig.3.3. Dependencies of a and b -factors as a function of process threshold (vibrational and electron states excitations, dissociations, attachments, ionizations)

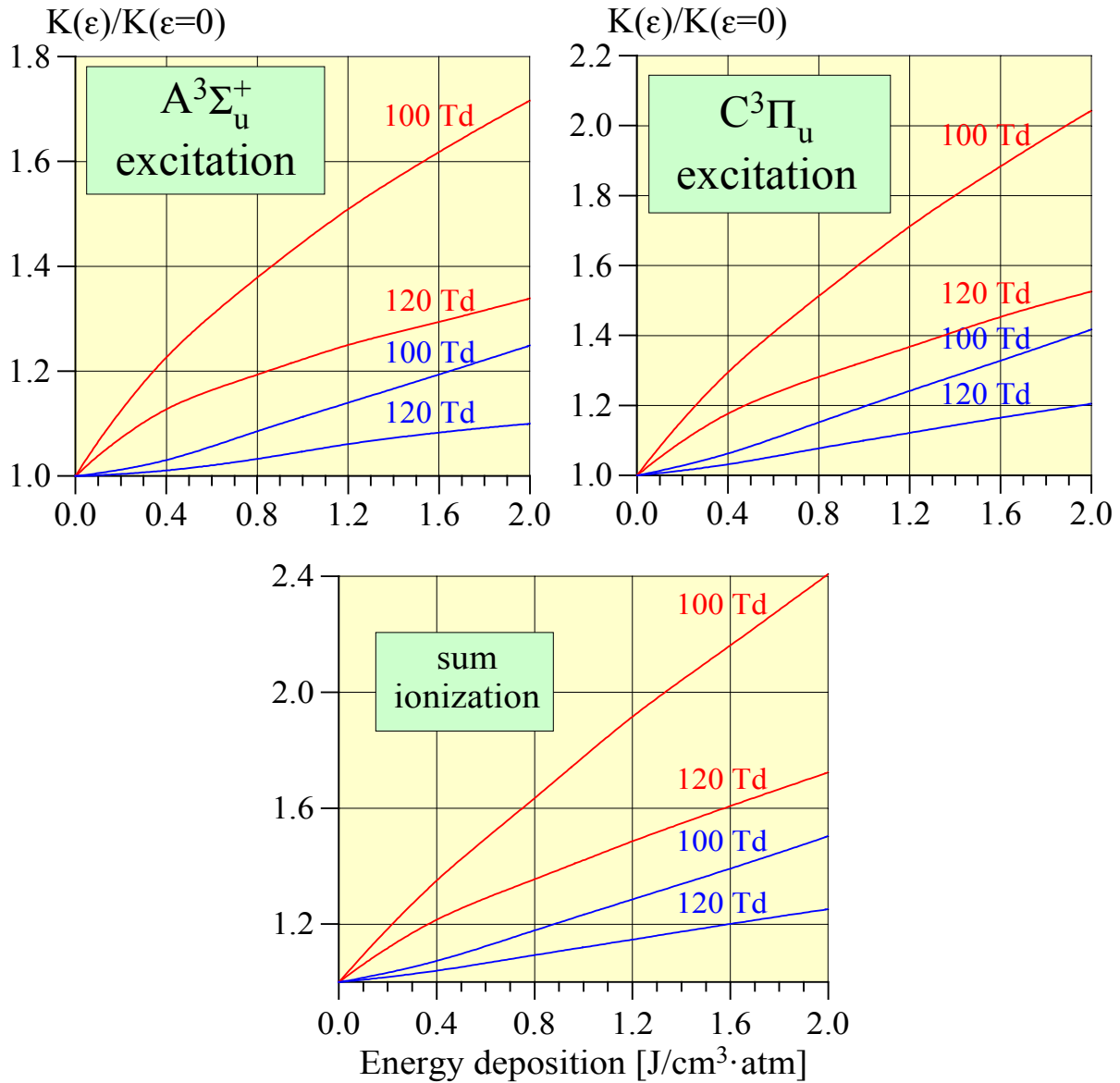


Fig.3.4. Reduced dependencies of excitation and ionization rate constants as a function of energy deposition into discharge in nitrogen at E/N near threshold. Red curves - natural formed VDF, blue curves – calculation in Boltzmann approach of VDF with the temperature corresponds to vibrational population of zero and first levels at e from abscissa axis (see top picture)

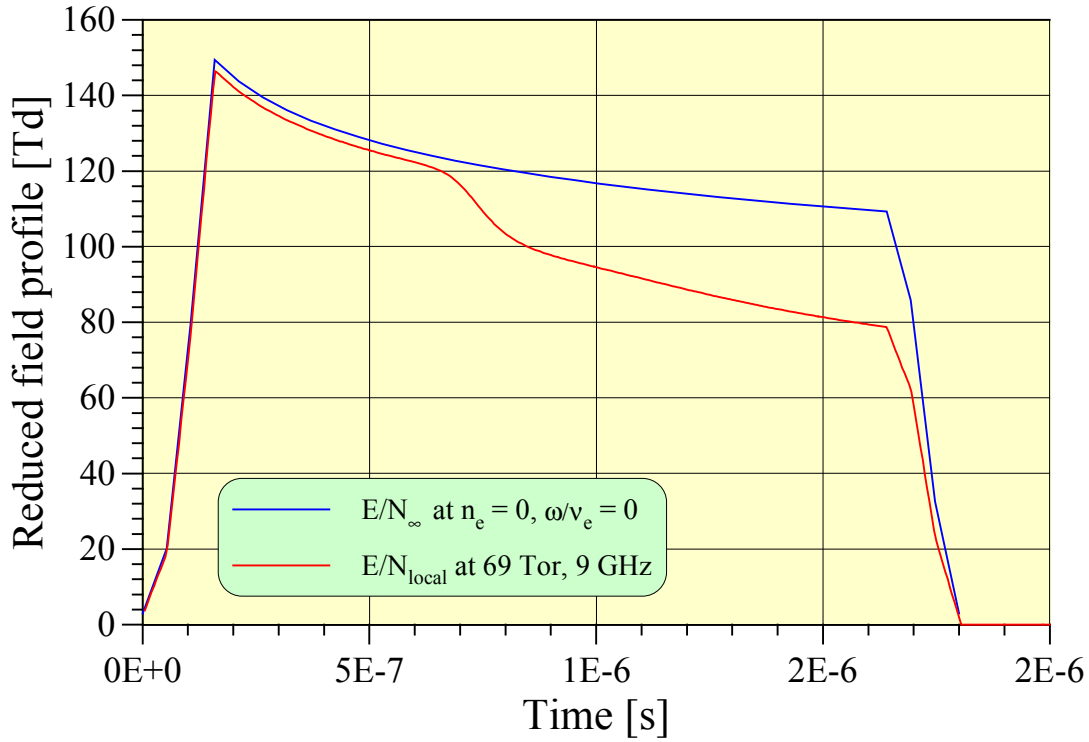


Fig.3.5. MW pulse reduced field profiles: falling and local actual fields

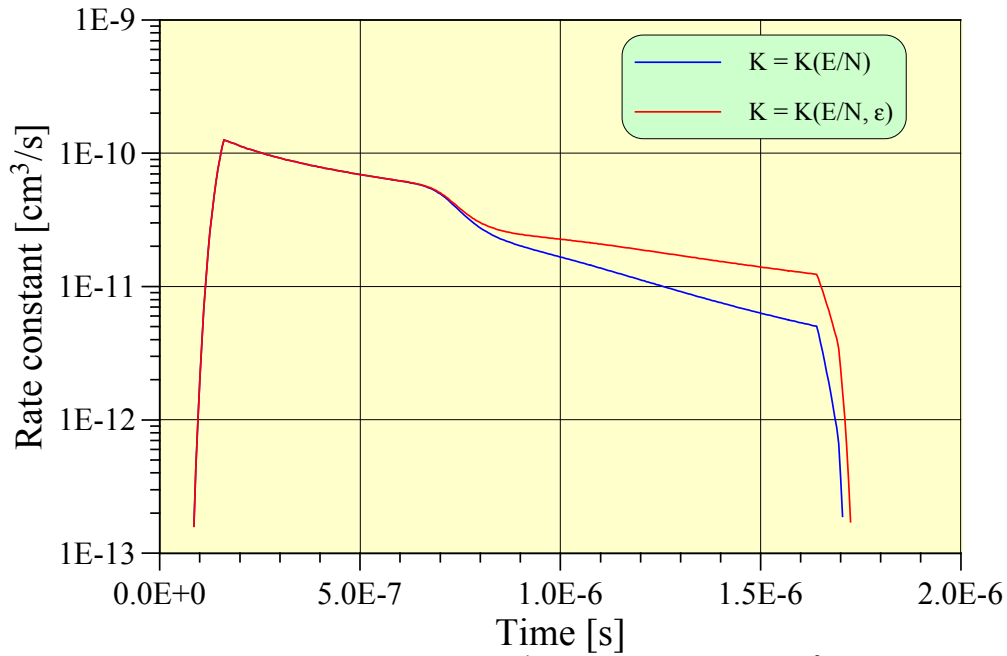


Fig.3.6. Sum rate constant of excitation $e + N_2[X^1\Sigma_g, v=0..8] = e + N_2[C^3\Pi_u, v'=0..4]$ during the MW pulse. — rate constant independent on vibrational distribution of ground state $N_2[X^1\Sigma_g]$ (energy deposition into discharge), — rate constant depended on energy deposition

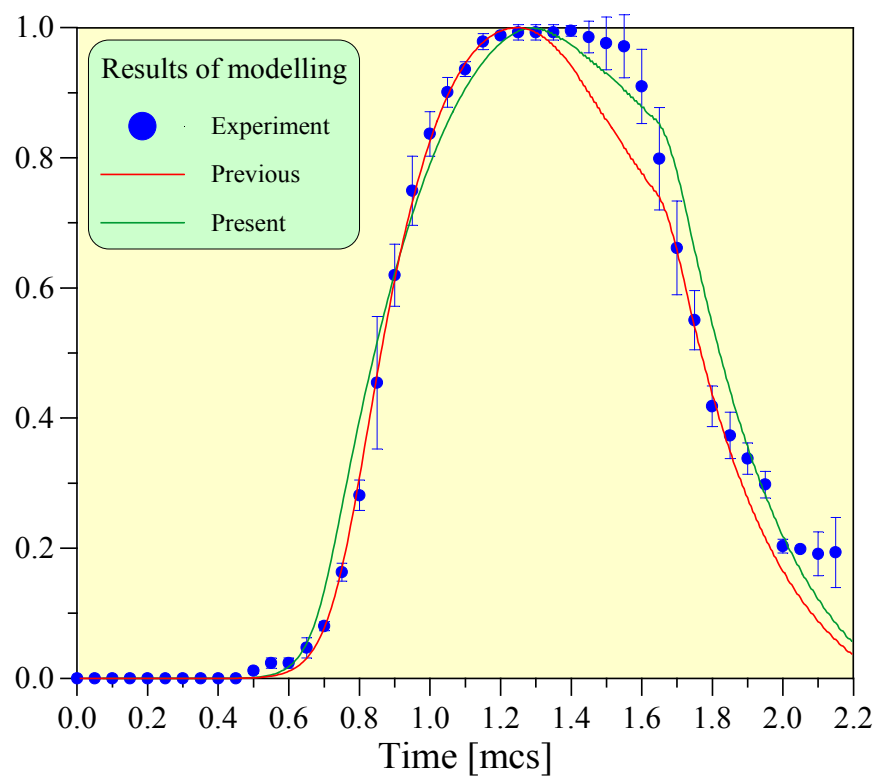


Fig.3.7. $N_2[C^3\Pi_u]$ emission during the pulse. Symbols – experiment. Solid lines - results of modeling: — rate constant of $N_2[C^3\Pi_u]$ excitation by electron impact independent on energy deposition, — rate constant depended on energy deposition

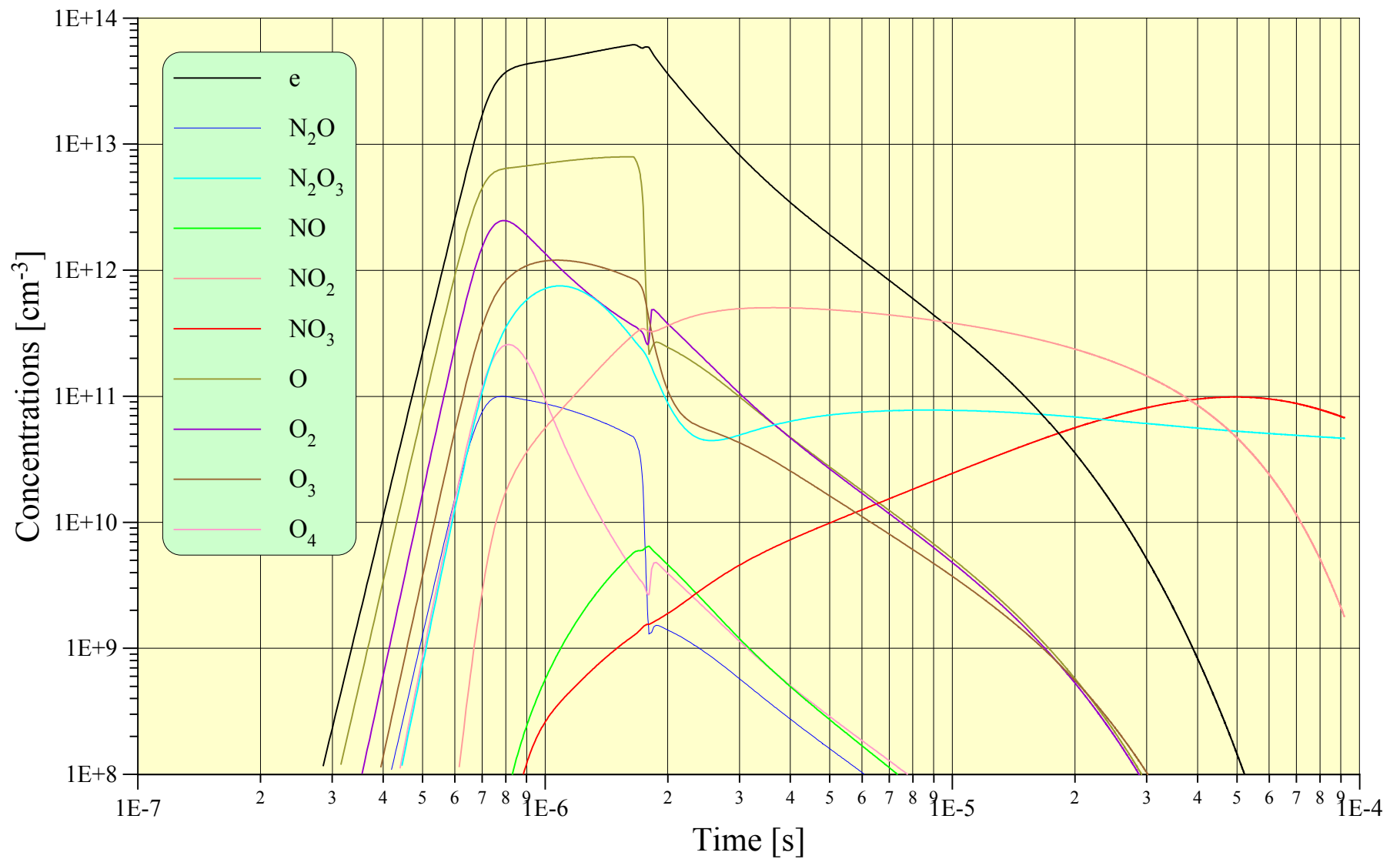


Fig.3.8. Dynamics of halo negative charged particles.

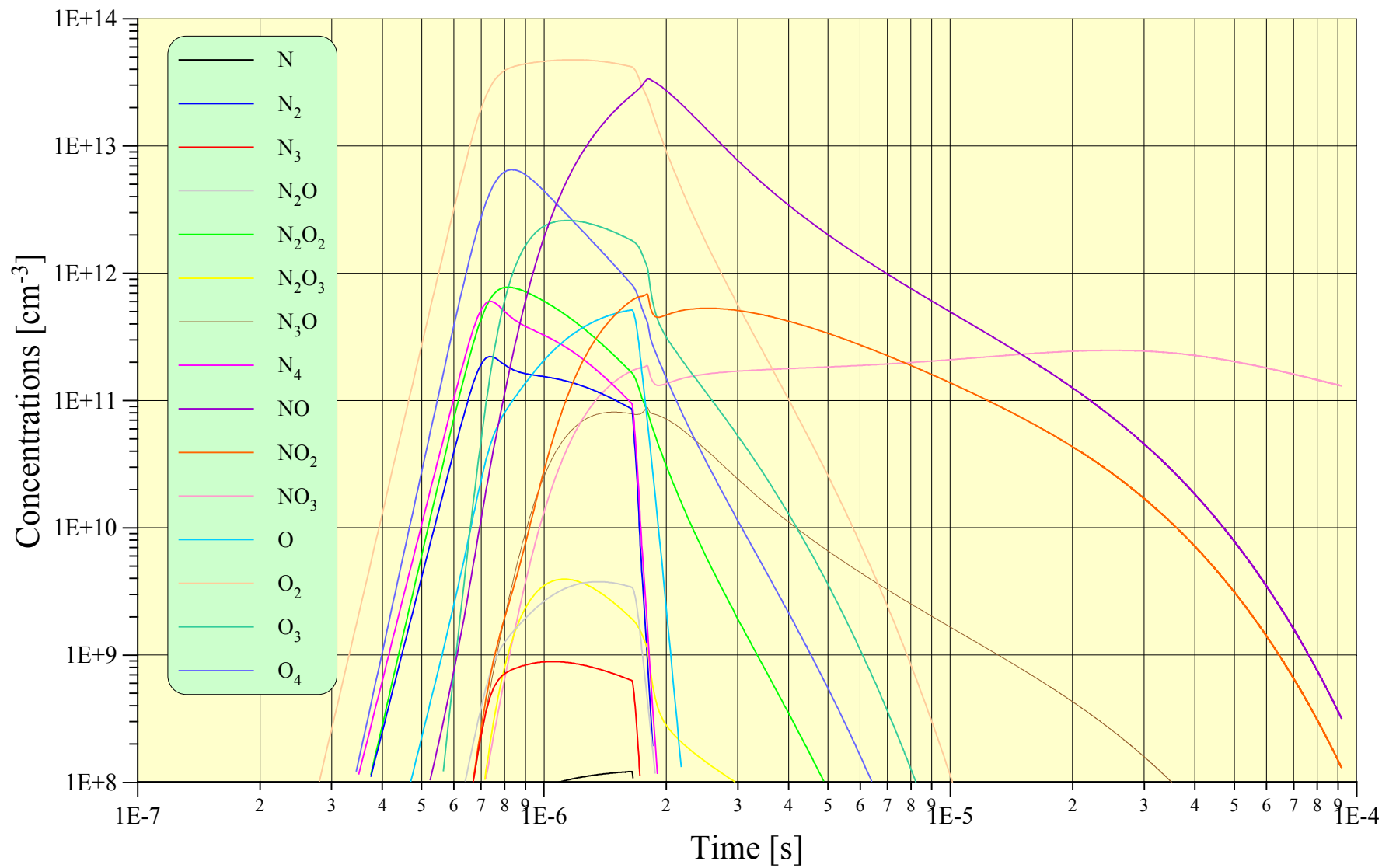


Fig.3.9. Dynamics of halo positive charged particles.

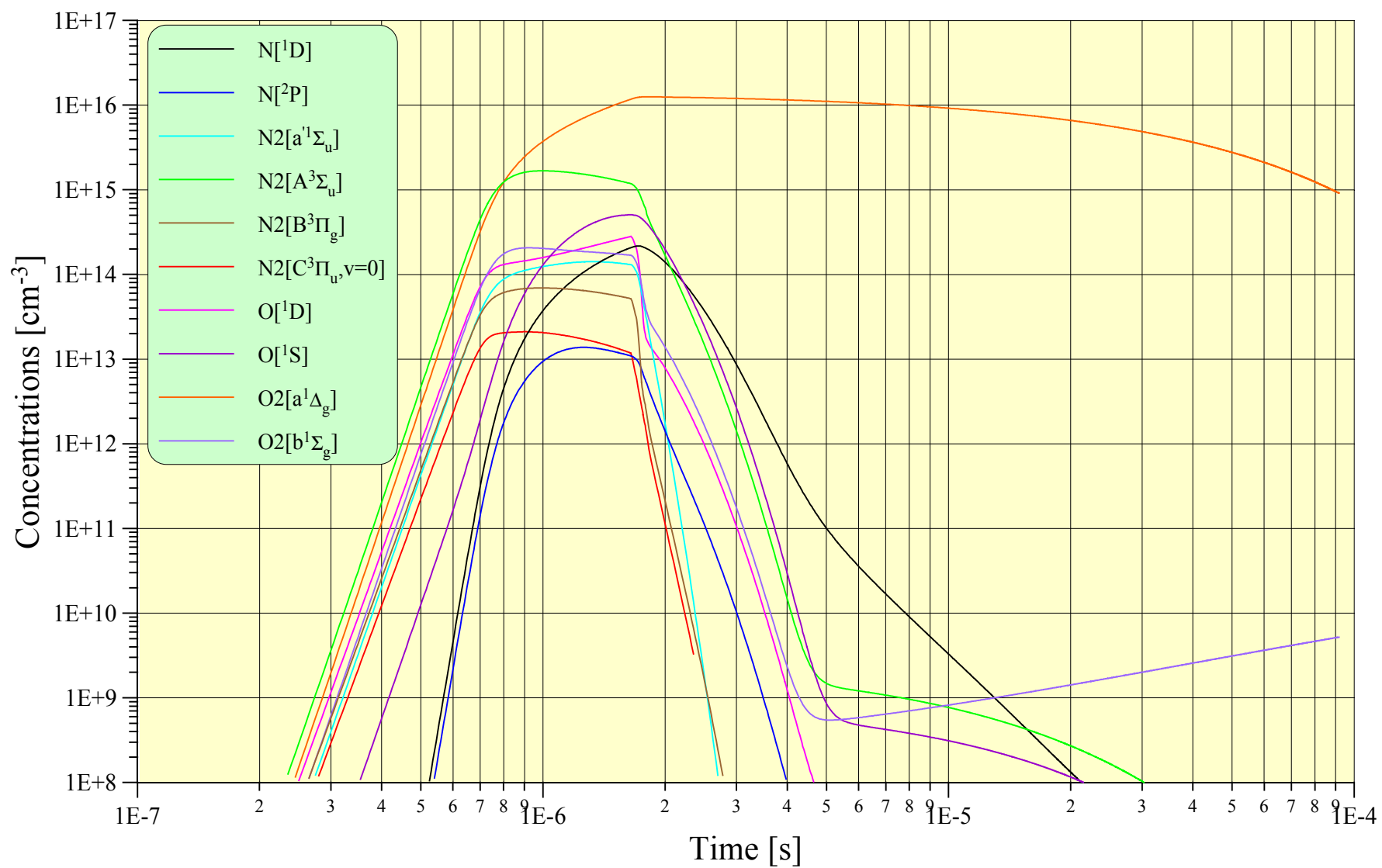


Fig.3.10. Dynamics of halo electron states excited particles.

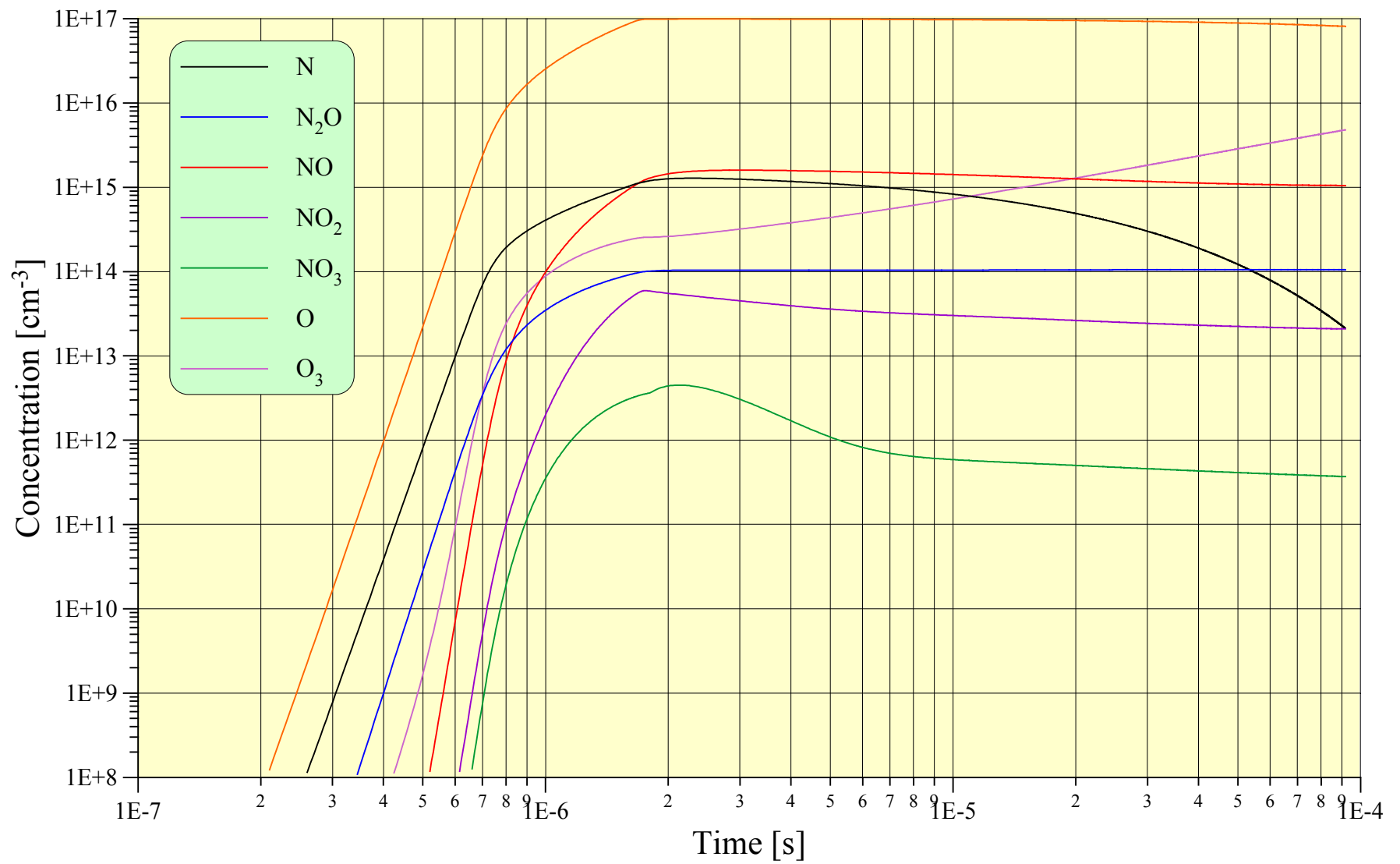


Fig.3.11. Dynamics of halo neutral particles

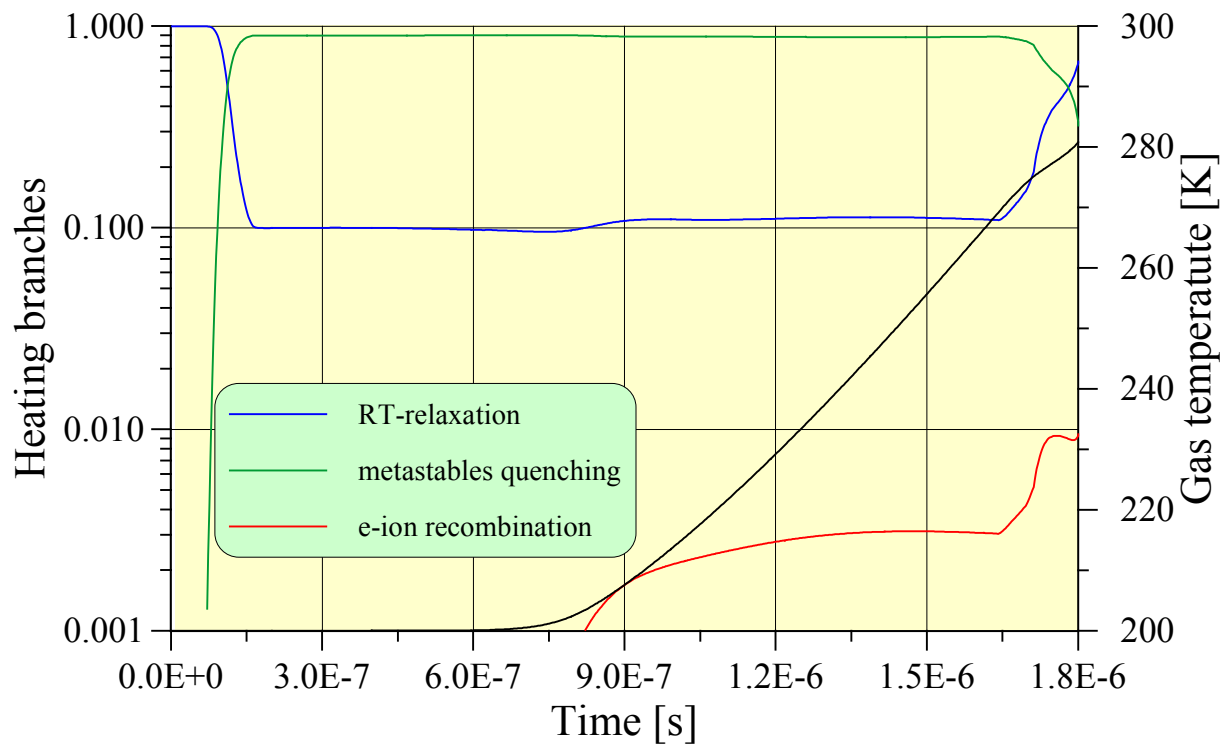


Fig.3.12. Dependence of heating branches fractions in halo and temperature curve

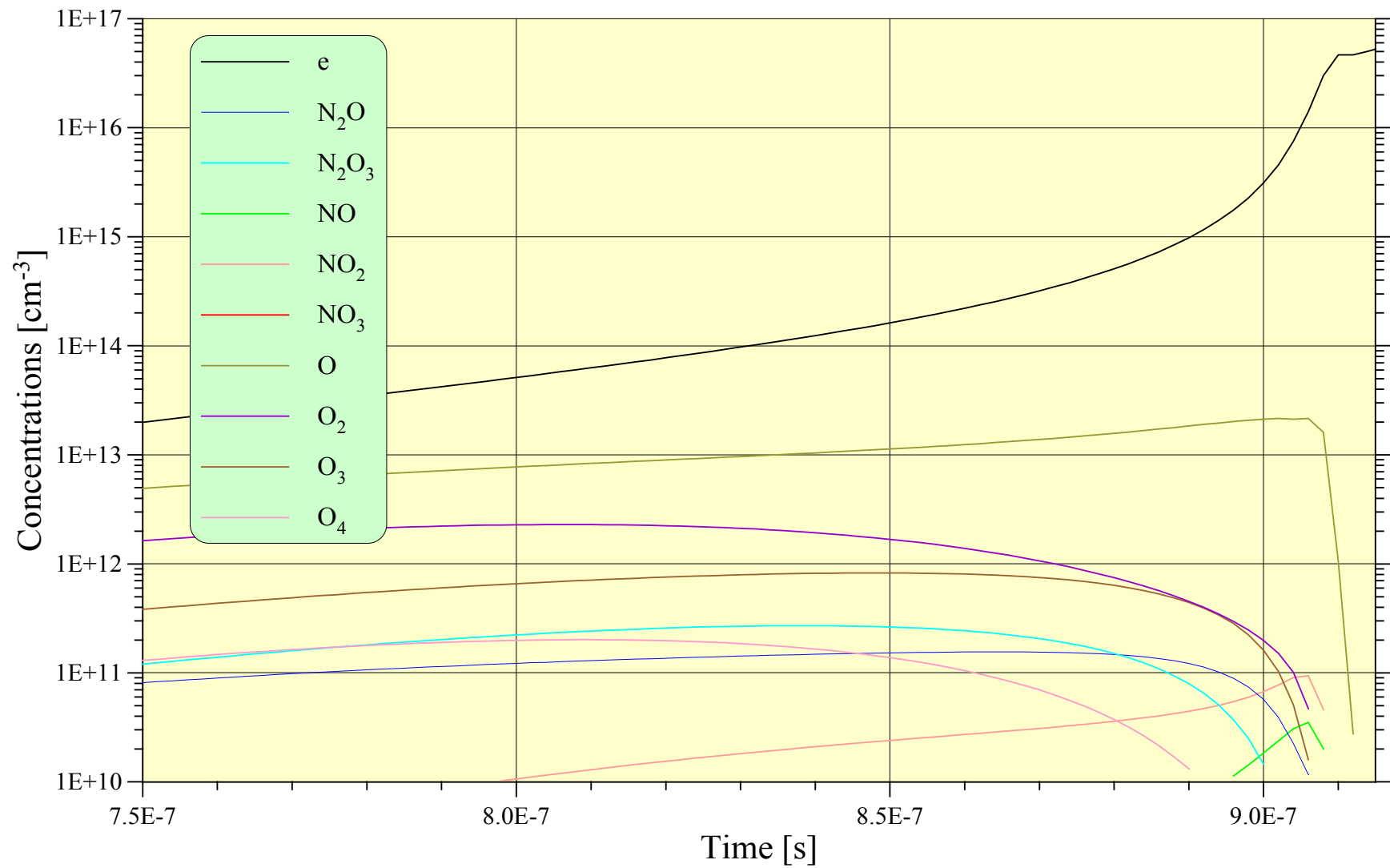


Fig.3.13. Dynamics of filament negative charged particles

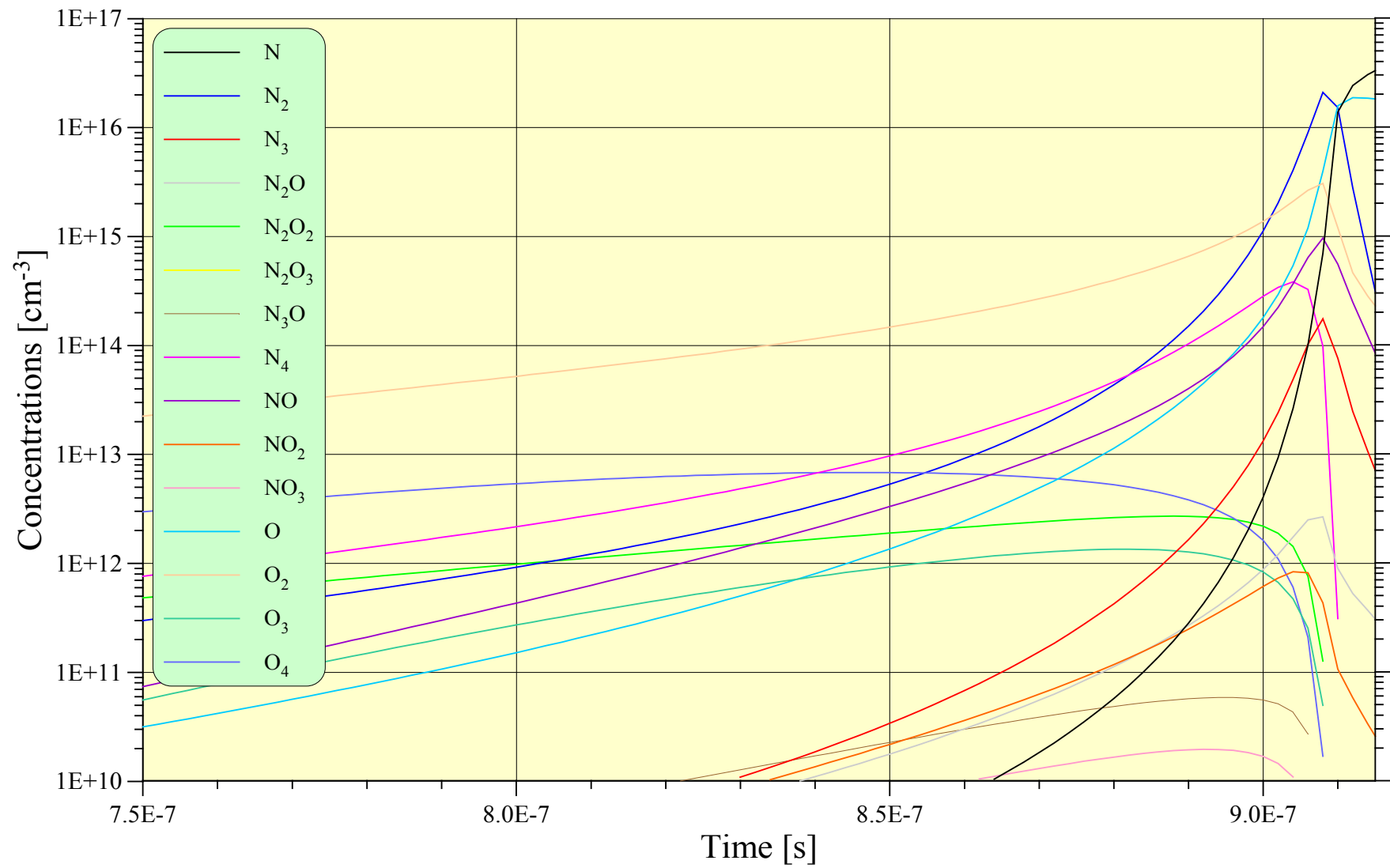
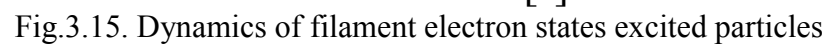


Fig.3.14. Dynamics of filament positive charged particles



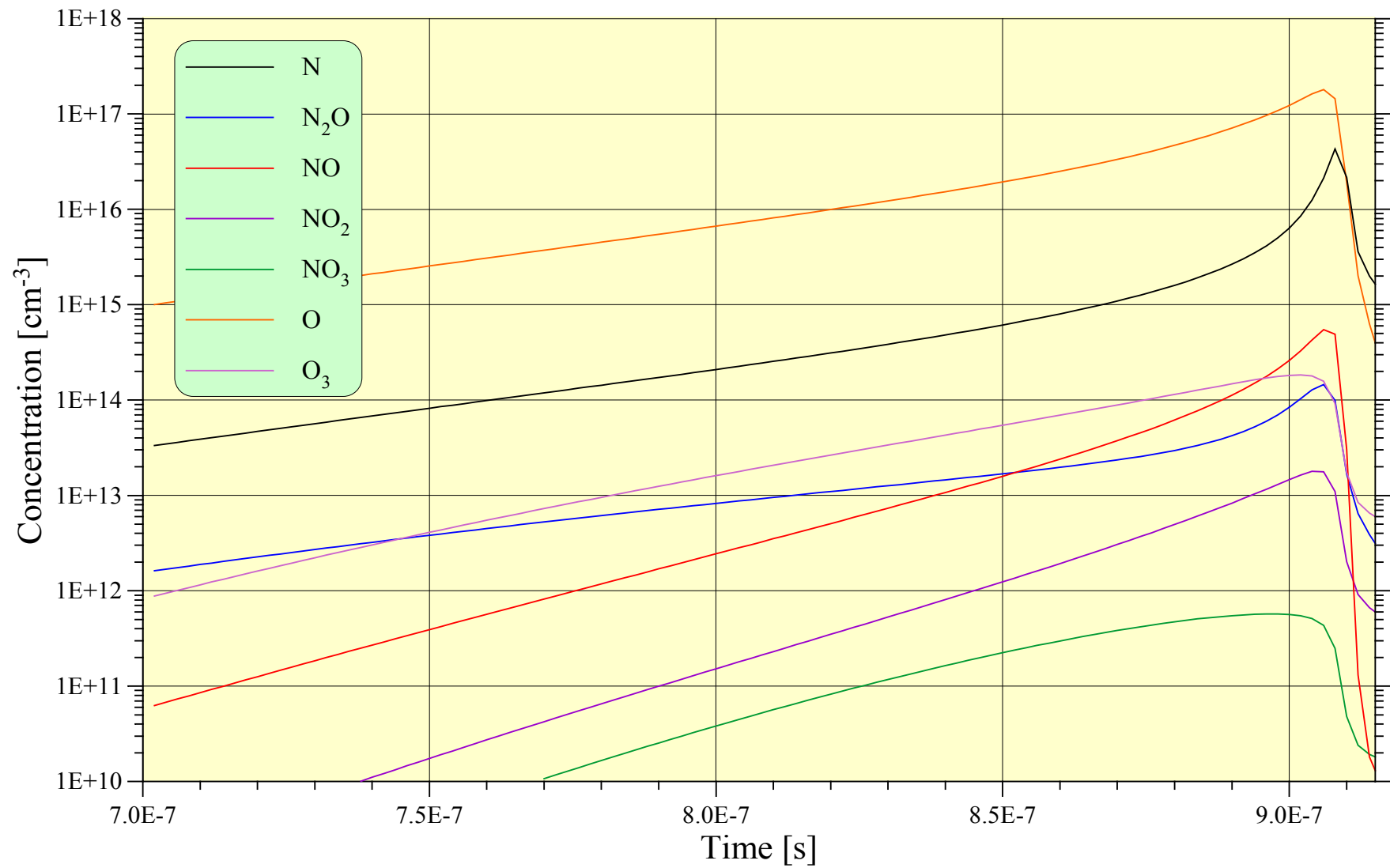


Fig.3.16. Dynamics of filament neutral particles

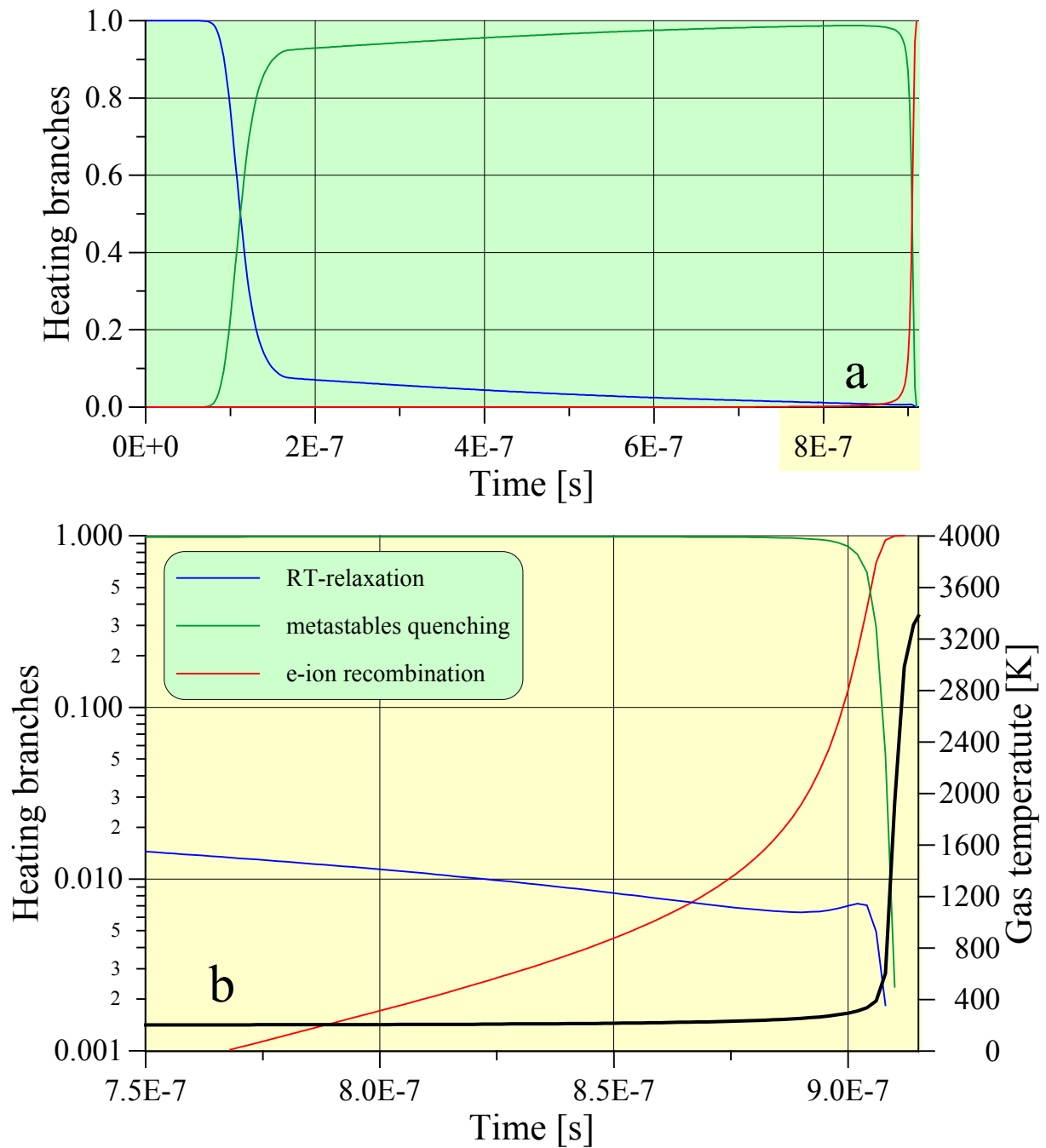


Fig.3.17. Dependence of heating branches fractions during filamentation stage and limit temperature curve.

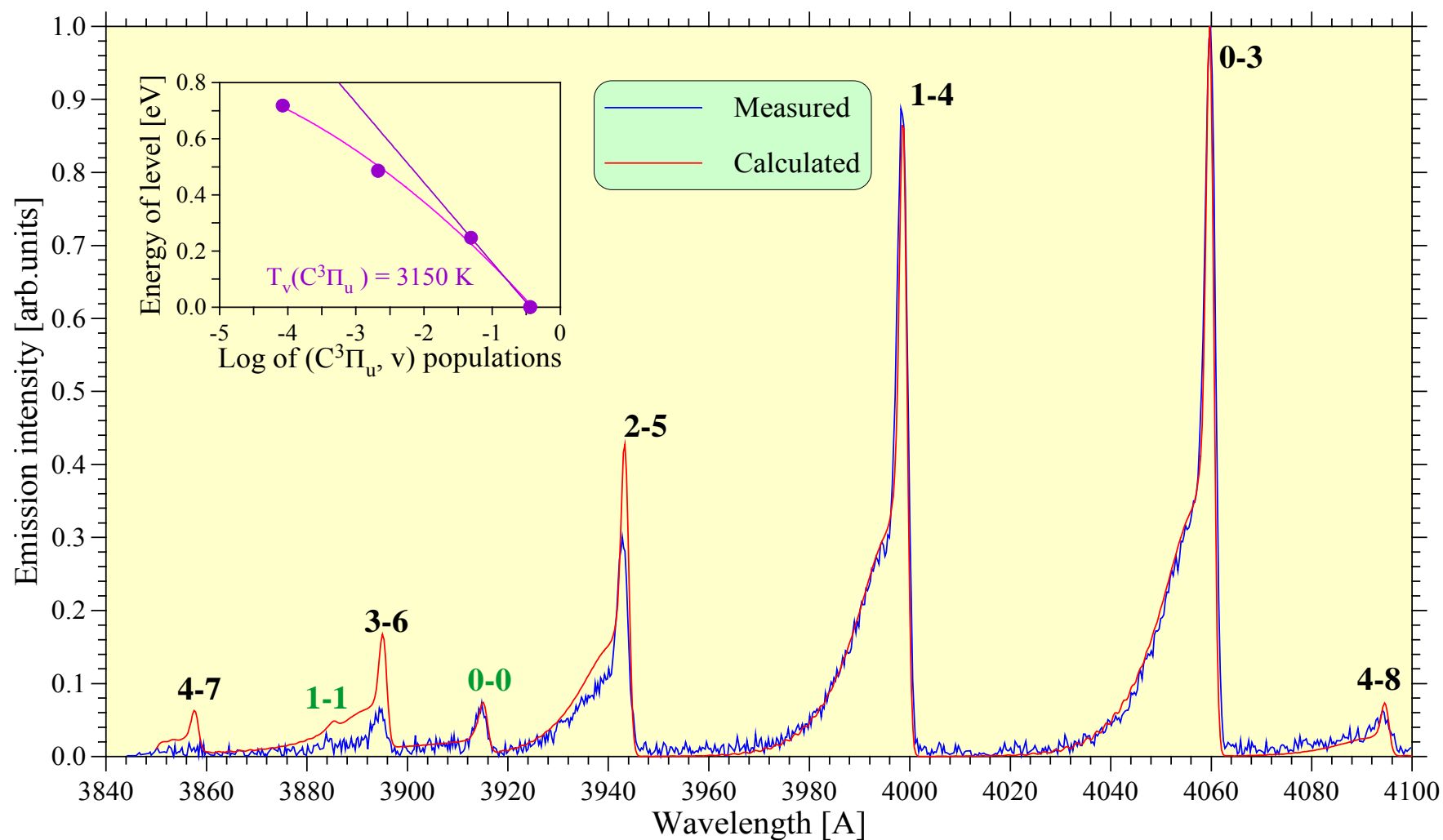


Fig.3.18. Overlapping of $N_2[2PG]$ -3 sequence (black labels) and $N_2[1NG]$ 0 sequence (green labels) bands in N_2 emission spectra. Gas temperatures of medium are: 280 K for $N_2[2PG]$ and 2800 K for $N_2[1NG]$. Vibrational temperature electron states are: 3150 K for $C^3\Pi_u$ and about 5000 K (rough estimation for $B^2\Sigma_u^+$).

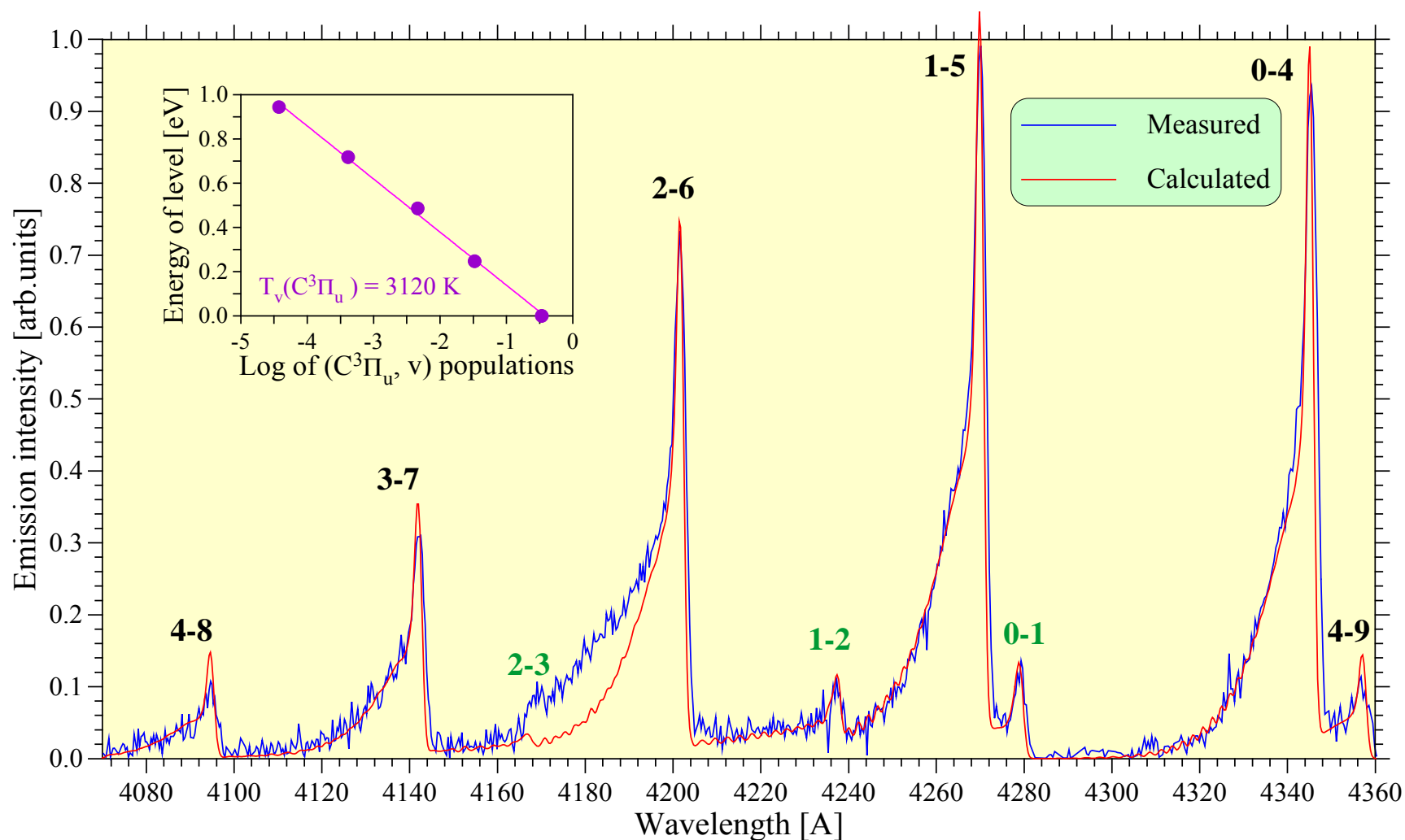


Fig.3.19. Overlapping of N₂[2PG] -4 sequence (black labels) and N₂[1NG] -1 sequence (green labels) bands in N₂ emission spectra. Gas temperatures of medium are: 280 K for N₂[2PG] and 2800 K for N₂[1NG]. Vibrational temperature electron states are: 3120 K for C³Π_u and about 5000 K (rough estimation for B²Σ_u⁺).

4. MW discharge diagnostics using the method of emission spectroscopy

The method of emission spectroscopy is the powerful method for diagnostics of nonequilibrium plasmas. As was noted in 3.3 where the comparison of the measured and synthesized spectrums in air was discussed, the rotational (gas) temperatures of the second positive system and the ionic first negative system of N₂ have difference in order of value - 280K and about 3200 K, correspondingly. Taking into account the strongly non-uniform structure of MW discharge plasma, the most reasonable is to assume that emission of each system takes place from different areas of plasmoid: “low temperature” emission of N₂[2PG] is radiated from cold halo and “high temperature” emission of N₂[1NG] - from thin, but hot filament, mainly. Thus, the analysis of emission spectra allows obtaining information about the local properties of MW discharge. At the same time, if the bands of N₂[2PG] turned out well visible and gas temperature was determined from rotational structure rather fine, the bands of N₂[1NG] were seen much more weakly and filament gas temperature was better an estimation.

4.1. Emission spectrum in air and carbon dioxide non-uniform discharge plasma

Such medium, as commercial carbon dioxide - CO₂ - affords an opportunity for more precise analysis of local parameters of MW plasmoid. Commercial CO₂ has the traces of N₂, O₂ and H₂O. This sort of “mixture” has rich spectrum composition of various molecules and radicals. Experiment was performed at the pressure range of 50 - 100 Torr and microwave power density $\approx 16, 8$ and 4 kW/cm^2 . Microwave pulse duration was of order 50-100mcs. Three types of discharge structures were tested – filamentary, streamer and bulk. Most of the results refer to the filamentary structure, which looks like a collection of dipoles oriented along E-vector of the wave. During experiments along with emission spectrums, the temporal dependences of emission at the most typical wavelengths were carried out. In experiments discharge emission was captured in direction of vector \vec{E} , from MW focal volume of $\approx 15\text{cm}$ length along vector \vec{k} , i.e. from the volume, exceeding the discharge length.

4.1.1. Emission spectrums

The typical panoramic emission spectrum is shown in Fig.4.1. As it is visible, the numerous spectrums of radicals are produced in discharge plasma appears. There are 0-0 band of $\text{OH}(A^2\Sigma^+ - X^2\Pi_i)$, 0-0 band of $\text{N}_2(C^3\Pi_u - B^3\Pi_g)$, -1, 0 and +1 sequences of CN violet system ($B^2\Sigma - X^2\Sigma$) and Swan bands of $\text{C}_2(d^3\Pi_g - a^3\Pi_u)$.

The mostly bright is emission of CN violet system bands in 0 sequence. There is a possibility to determine medium characteristics by cyanogen emission. The fit of synthesized spectrum (sum of branches P_1 , P_2 , R_1 , R_2 , P_{12} , R_{21}) to experimental one is shown in Fig.4.2. For calculations of this and other spectrums the lifetimes of individual vibration levels were taken based on survey of literature sources (see Appendix C). Transition probabilities were taken from [1,2] mainly. Reconstructed gas temperature is about 7500 K and “vibration temperature” 10000 K. Approximately the same result was obtained for -1 and +1 sequences of CN (Fig.4.3, 4.4). So, high gas temperature denotes that filament is the “reactor” of cyanogens production. It is necessary to note that energy cost of CN production in initial $\text{CO}_2\text{-N}_2$ mixture looks rather great: the extraction of C-nucleus from CO_2 molecule is a power consuming process owing to high energy C-O bond mainly. This indirectly confirms aforesaid hypothesis. In principle, so high vibration temperature of $\text{CN}(B^2\Sigma)$ state may indicate that the inverse population of high ($v \geq 6$) vibrational levels isn't excepted.

The emission of $\text{OH}(A^2\Sigma^+ - X^2\Pi_i)$ 0-0 band is shown in Fig.4.5. In this plot synthesized spectrum is also shown. Synthesized spectrum is a sum of P_1 , P_2 , Q_1 , Q_2 , R_1 , R_2 , O_{12} , Q_{12} , P_{12} , R_{21} , Q_{21} , S_{21} branches. Reconstructed over rotation structure gas temperature is about 3000 K. The same value gives the method based on comparison of P and R-branches magnitudes [3].

Like a violet CN bands, C_2 Swan bands are strongly overlapped inside the same sequence. At the same time, the fast bands heads convergence to a single wave limit with increasing of vibrational quantum number ($\approx 4670 \text{ \AA}$ for $\Delta v = +1$) makes blue shadowed sum rotational structure of the sequence clear visible from one hand, and weak depended on vibrational population of emission state - from other one. The spectrums synthesized are the sum of P_1 , P_2 , P_3 , R_1 , R_2 , R_3 , Q_1 and Q_2 rotational branches for each rovibronic transition. The best fit of synthesized spectrum to measured one is shown in Fig.4.6. Despite on not high quality of measured spectrum, the general features of rotational structure are visible quite not bad. This allows to determinate rotational (gas) temperature, which turns out $9500 \pm 500 \text{ K}$.

The emission of the most bright 0-0 band of $N_2(C^3\Pi_u-B^3\Pi_g)$ turns out a weak one. Nevertheless this band allows estimate gas temperature (Fig.4.7), which isn't high: ≈ 1600 K and relates to halo most probably.

4.1.2. Emission temporal dependencies

Because of various emission spectrums have various localization inside discharge, there is important to consider emission temporal development. In Fig.4.8 the curves of spectral emission during MW pulse is shown as a symbols. Each curve is a result of 8-12 oscillograms averaging. The averaging procedure was needed because there was some instability of discharge structure formation at reduced power density (for example Fig.4.9 demonstrates scattering for CN violet emission). As it is seen from Figures, there is about 20 mcs delay of breakdown beginning.

The solid curves in Fig.4.9 are time dependences fits. For OH(A-X) and $N_2(C-B)$ there are linear dependencies during the pulse. This can be possible if emission of these states is uniformed (on average) over the plasma volume behind ionization front during the entire pulse. In other words, linear dependence of emission is conditioned by discharge propagation towards vector \vec{k} . In principle, such situation reasonably corresponds to halo. At this the emission of $N_2(C-B)$ has a delay in comparison with OH(A-X).

The emission of CN(B-X) has a quadratic dependence and hasn't visible delay. It is quite strange: if for emitting states OH($A^2\Sigma^+$) and $N_2(C^3\Pi_u)$ one can reasonable assume one-step excitation (by electron impact) with energy thresholds 9.5 and 11 eV, when the excitation of CN($B^2\Sigma$) is an evidently multi-stage process where during any stage the firm bond C-O must be destroyed. The careful experimental analysis of CN emission could answer these questions.

Relaxation time of light emission after MW pulse termination is about 20mcs. Three plasma channels are active at the same time. Timing jitter in oscillograms is much less in the cases of N_2 and OH than in the case of CN.

4.1.3. Summarizing of spectrum processing

The results of emission spectrums processing in commercial CO_2 are collected in Table 1. In the third column of the Table the conjectural number of reaction steps of emission state formation is given.

Table 1. Summary of observed spectrums processing

Observed spectrums	Emission state (term energy, eV)	Steps of emission state formation	Energy of state formation, eV/particle	Measured temperature, K
N ₂ (2PG)	C ³ Π _u (11.03)	Single	11.03	1600
OH violet	A ² Σ ⁺ (4.05)	Single or Multi	≈ 9	2950±200
CN violet	B ² Σ ⁺ (3.20)	Multi	≈ 20 / 5.4*	7650
C ₂ Swan	d ³ Π _g (2.48)	Multi	≈ 30 / 14.2*	9500±500

* low bound: calculated as a difference of reagents formation enthalpies $\Delta H_f(T=0)$ in gross reactions $2 \text{CO}_2 + \text{N}_2 \rightarrow 2 \text{CN}(\text{B}^2\Sigma^+) + 2 \text{O}_2$ and $2 \text{CO}_2 \rightarrow \text{C}_2(\text{d}^3\Pi_g) + 2 \text{O}_2$

It is clear that formation of N₂(C³Π_u) is a result of direct excitation by electron impact mainly, i.e. production of N₂(C³Π_u) is determined by electron temperature first of all. In other words, efficiency of this state production under nonequilibrium conditions ($T_e \gg T_g$) is weakly coupled with gas temperature of the medium. Earlier we cited experimental data for airflow, where bright spectrum of N₂(2PG) gave gas temperature of 280 K.

Formation of OH(A²Σ⁺) most probably is a complex process, when together with direct excitation - for example, through dissociative excitation of water molecule by electron impact - the step-wise formation of emission state takes place too: $\text{H}_2\text{O} \rightarrow \text{OH} \rightarrow \text{OH}(\text{A}^2\Sigma^+)$. In the last case the efficiency of emission state production can keep the “impress” of medium temperature. It is also clear that CN(B²Σ⁺) and C₂(d³Π_g) formation is obviously multistage process, which must, at least, include the complete decomposition of very firm molecule - CO₂ ($\text{CO}_2 + 16.6 \text{ eV} \rightarrow \text{C} + \text{O} + \text{O}$).

In the fourth column of the Table the energies of emission states formation are shown. First values for OH, CN and C₂ are the energies, one must spend (somehow or other) for the start of fast substances formation. “Fast formation” means the formation process without tempering of intermediate reactions products: the conditions are typical during discharge stage. Second values for CN and C₂ give minimal possible energies, which can be achieved under thermodynamic conditions (total tempering with heat recuperation).

The comparison of energy formation and measured gas temperature by emission of substances, which are formed during multi-step processes, shows the existence of correlation between these data.

The strong difference of gas temperatures measured by emission of various substances is a result of discharge non-uniformity. The experiments with commercial CO₂ quite keep within this hypothesis, but at the same time show that the scheme of MW plasmoid “filament-halo” has more complicated internal intermediate construction - layers like a years rings of the tree.

4.1.4. Thermodynamic calculation of medium composition

For verification of this hypothesis thermodynamic calculation of equilibrium medium composition as a function of the temperature was carried out. Initially (at the room temperature T_0) medium is a “commercial CO₂” - 99% of CO₂ and 1% of humid air under the pressure 100 Torr ($N = 3.5 \times 10^{18} \text{ cm}^{-3}$). It was assumed that medium is under isobaric conditions, i.e. equilibrium concentration of substances at the temperature T is decreased in T_0/T times in comparison with the case of isochoric conditions.

During the calculation 197 equilibrium reaction stages among 40 substances were taken into account. These are: CO₂, N₂, O₂, H₂O, HO₂, NO₂, N₂O, O₃, C₂O, HNO, CO, NO, OH, CN, CH, NH, C₂, H₂, C, O, N, H, O₂⁺, N₂⁺, CO₂⁺, CO⁺, NO⁺, OH⁺, CN⁺, C₂⁺, C⁺, O⁺, N⁺, H⁺, O₂⁻, C₂⁻, O⁻, C⁻, H⁻, e. Because of high temperature range ($T > 2000 \text{ K}$) considered, weak bounded polyatomic substances (molecules and ions) were ignored during the calculations. Equilibrium constants for the stages, necessary for calculations, were determined on the base of data for enthalpies of formation $H(T=0)$ and interpolations for Gibbs energies of substances $\Phi(T)$ from [4]:

$$R \ln K_{eq}(T) = \Delta_r \Phi(T) - \Delta_r H(T=0) / T, \Delta_r - \text{means the difference for stage.}$$

The results of calculation are shown in Fig.4.10. There is notable and at the same time quite predictable result - emission states, formed during multi step processes (CN, C₂) or during partially multi step one (OH), give gas temperatures, which are in a good agreement with the temperatures of maximal concentrations of these substances under equilibrium conditions. In other words, emission of each substance brings information from the plasmoid layer with the temperature not less and not much higher than certain one. So, the most power-consuming substances observation allows to “penetrate” inside the most power-saturated layers of MW plasmoid.

So, emission of species with high-energy production threshold can deliver information about temperature distribution in strongly non-homogeneous discharge structures. Among such species radicals CN, OH, C₂, CH and others play an important role, being also an indicative intermittent products in various combustion processes. Therefore, these species observation in discharge (even in non-flammable gases) is of sufficient interest.

The results obtained in commercial CO₂ allow to look farther:

- a) For investigations of the mediums, which are interesting, one can admix specially some impurities for spectral “enrichment” of discharge. For example, the comparatively poor emission picture in air one can enrich by a small impurities of substances of need;
- b) It seems that combination of emission spectroscopy and emission “tomography” of discharge has a good prospective for discharge diagnostics. Presumably the oblique of such “tomography” is a CCD video camera equipped with the set of narrow-band filters tuned in a standard emission bands or atomic lines.

4.2. Emission spectrum of MW discharge, propagating along dielectric plate

In the spectrum of this kind of discharge CN violet emission dominates (Fig.4.11). Perhaps the source of carbon is the products of dielectric plate decomposition under discharge effect. The sequences -1 , 0 , $+1$ are present. The processing of experimental spectrums rotational structure gave the gas temperature about 8000 K. At that the same temperature is reproduced in different discharge realizations. The comparison of experimental and synthesized spectrums is in Fig.4.11 and Fig.4.12 (for 0-sequence). In addition to bright CN spectrum the following spectrums are observable: R-branch of OH($A^2\Sigma^+ - X^2\Pi_i$), 0 and $+1$ sequences of N₂(2PG) and 0-0 band of NH($A^3\Pi_i - X^3\Sigma$). Fig.4.13 demonstrates short-wave part of emission spectrum. For comparison spectrum of N₂(2PG) was marked ($T_g = T_v = 1500$ K). As it is visible, the peak in the range 3300-3400 Å turns out splitted one, when the smaller peak corresponds to N₂(2PG) 0-0 transition, and bigger one corresponds to NH($A^3\Pi_i - X^3\Sigma$) 0-0 transition (such relation was observed in all realization). Moreover, the superposition of $+1$ sequence of N₂(2PG) and OH($A^2\Sigma^+ - X^2\Pi_i$) takes place, so only R-branch of OH emission is visible distinctly.

4.3. Emission spectrums with presence of atomic lines

The observation of atomic emission from discharge gives a good possibility to determinate such parameters of plasma as electron concentration (owing to Stark broadening effect) and temperature. If to say about “temperature”, which can be measured over relative intensities of atomic lines, we incline to thesis that this one is electron temperature.

4.3.1. Emission of DC spark

Emission of atomic lines was observed during experiments with streamer-like DC spark. There were “calibrating” experiments because of properties of DC spark quite similar to MW streamer. Emission of DC spark shows the presence of atomic lines N II, O II and the most bright 0-0 band of nitrogen second positive system N₂[2PG] (Fig.4.14). Rough estimation of gas temperature over rotational structure of 0-0 band given the value about 1500 K.

The procedure of atomic emission spectrum synthesis is in follow.

The intensity of emission during atomic lines $m \rightarrow n$ transition is determined as

$$I_{mn} = \frac{g_m \times A_{mn} \times N_m}{\lambda_{mn}}, \quad (1)$$

where g_m – stat weight of emission state m , N_m – population of emission state, A_{mn} and λ_{mn} – Einstein coefficient and wavelength of $m \rightarrow n$ transition.

If assume Boltzmann principle for populations of emission states, the expression for relative population is:

$$N_m \propto \exp\left(\frac{E_m}{kT}\right), \quad (2)$$

E_m – energy of state; T – the temperature, which describes excited (emission) states population.

The values of g_m , A_{mn} , λ_{mn} and E_m were taken from [5].

In the medium with free electrons Stark broadening of spectral lines takes place. The relationship between the half width at half maximum of the Stark profile and the electron concentration is expressed as:

$$w[A] = 2.5 \times 10^{-9} \times \alpha_{mn} \times n_e^{2/3},$$

where electron concentration is in cm^{-3} and the parameter α_{mn} weakly depends on n_e and electron temperature T_e and hereinafter is assumed as a constant. The value w is tabulated in [5].

At last, the additional spectral lines broadening is occurred because of the presence of spectrometer hardware broadening, which was 4 Å in our experiments.

Evaluation of electron concentration and temperature was carried out for the wavelength range 4900-5800 Å. The reason of this range choice is in the absence of any bright emission sources except N II. The fit in this wavelength range is in execution of the above-mentioned procedure for each of 80 lines with variation of T , n_e and continuum intensity. As a result the sum spectrum was synthesized. The criterion function of fit was the value of root-mean-square deviation of the calculated spectrum from the measured one. The result of the fit is shown in Fig.4.15. Stark broadening and comparative intensities of peaks give the temperature of 32000 K (2.8 eV) and $n_e = 1.5 \times 10^{16} \text{ cm}^{-3}$. If to compare the measured electron characteristics with the results of kinetic modeling of MW filament (Section 3), there is quite good agreement of the measured characteristics to the case of MW filament scenario with polarization factor $q \approx 0.0005$ (3.5 eV and $1.2 \times 10^{16} \text{ cm}^{-3}$ correspondingly).

4.3.2. The observation of iron emission from MW discharge

The usage of steel initiators for discharge creation gives rise to appearance of Fe I emission spectrums from the volume around the initiator tip. Fig.4.16 demonstrates the overview of Fe I spectrum. The sample of synthesized spectrum is shown in the Fig.4.16, which is a result of early described procedure at $T = 15000 \text{ K}$ and $n_e = 5 \times 10^{15} \text{ cm}^{-3}$. Calculations show that no one value of temperature T in expression (2) does not give agreement for comparative magnitudes of different peaks. This points to the absence of equilibrium of emission states populations. The plot $E_m - \ln(N_m)$ in Fig.4.17 illustrates this thesis. The values N_m were determined from (1) over the measured intensities. As one can see, even taking into account scattering of data, interpolation curve in accepted coordinates is not a linear one. For each group of emission states (≈ 3.5 , ≈ 4.5 , $\approx 6.5 \text{ eV}$) the temperature T_m corresponds their average population (marked in the plot). It is visible that “temperatures” T_m grow with increasing of state energy. The matter is in duality of T_m , which keeps a “seal” of both gas and electron temperature at the same time. At that the processes of ionization and recombination as well as excitation of atoms from ground electron state are the more slow processes in comparison with the processes of electron detachment/capture from the upper excited states. In much cases, the concentrations of electrons and high-excited atoms have

not time to come into equilibrium with total concentration of atoms, but the equilibrium among free electrons and bounded electrons at high-excited states occurs already established. At that the temperature in (2) in a greater extent has sense of electron temperature one.

This result confirms our thesis about the nature of temperature, which is measured over atomic lines intensities.

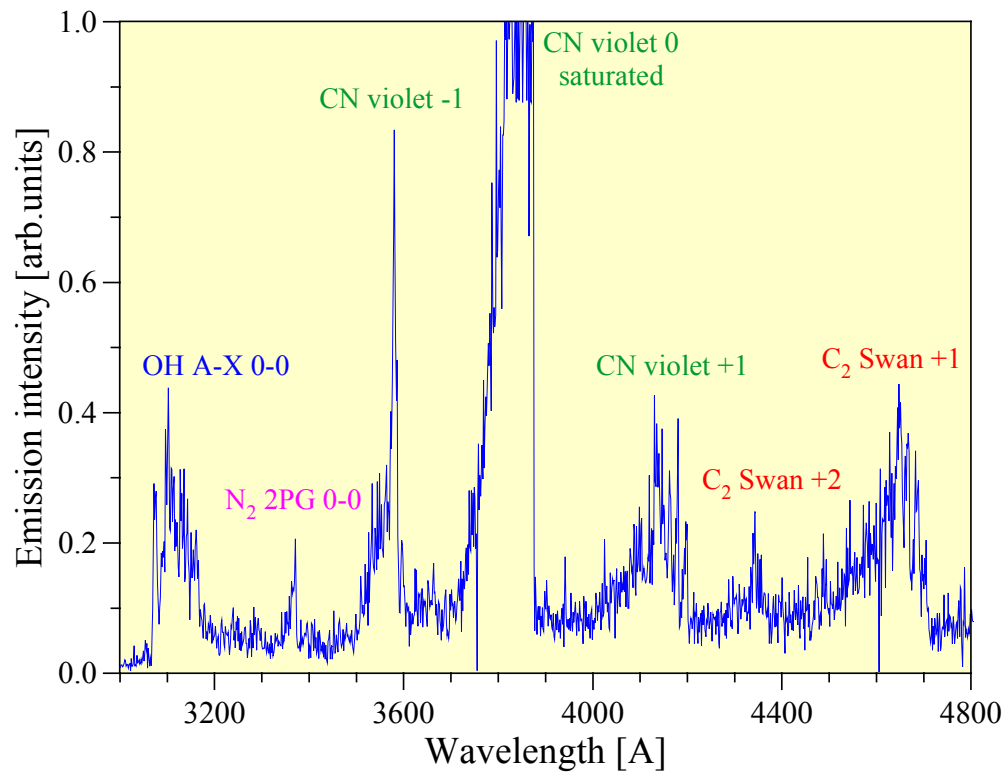


Fig.4.1. Panoramic emission spectrum in commercial CO₂,
P = 100 Tor, s ≈ 16 kW/cm², t = 50 mcs

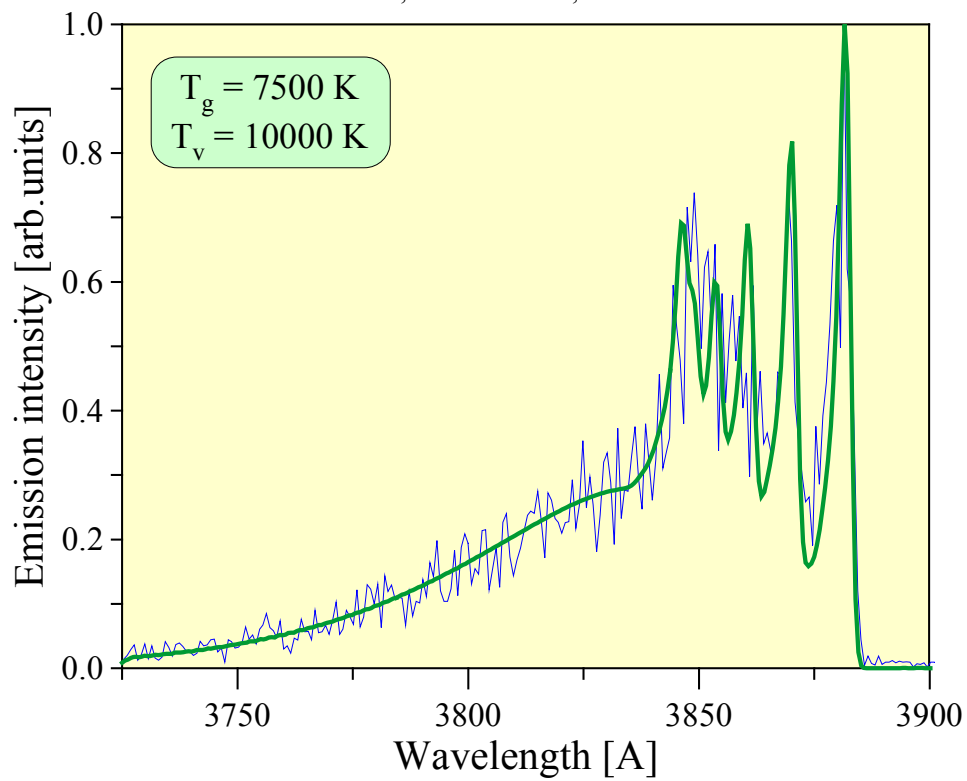


Fig.4.2. CN violet system, 0-sequence, P = 100 Tor, s ≈ 16 kW/cm²,
instrumental broadening ≈ 2 Å

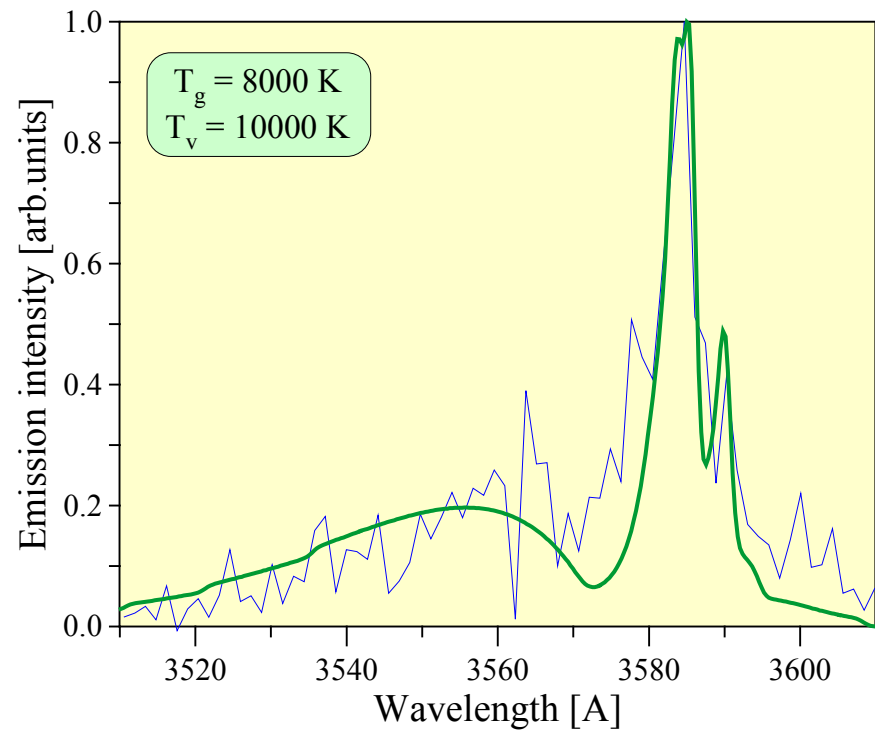


Fig.4.3. CN violet system, +1-sequence, $P = 100$ Torr, $s \approx 16$ kW/cm², instrumental broadening ≈ 2 Å

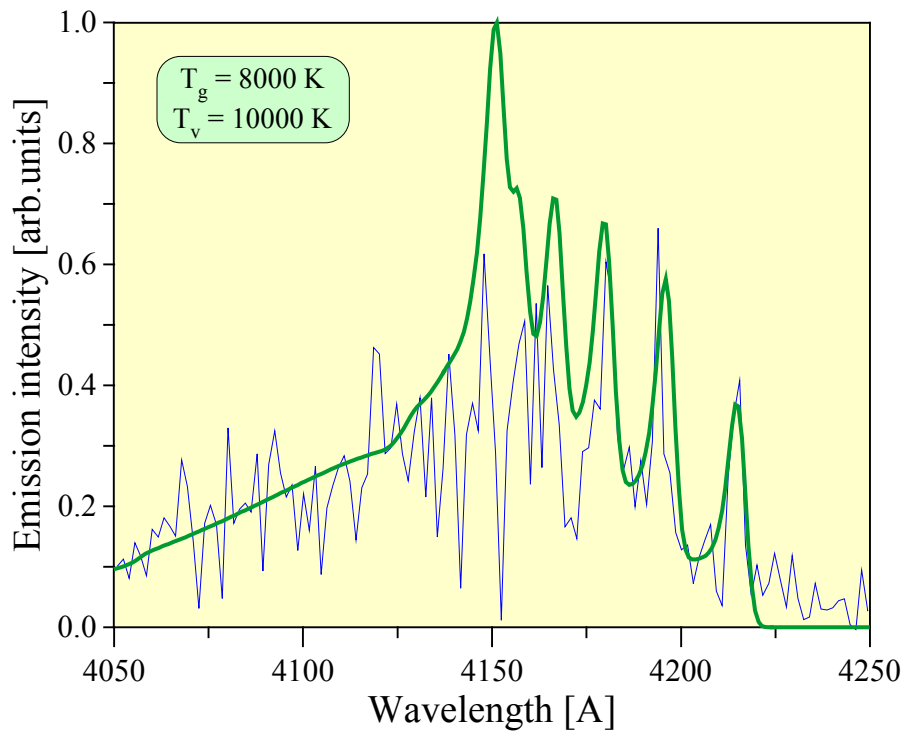


Fig.4.4. CN violet system, -1-sequence, $P = 100$ Torr, $s \approx 16$ kW/cm², instrumental broadening ≈ 2 Å

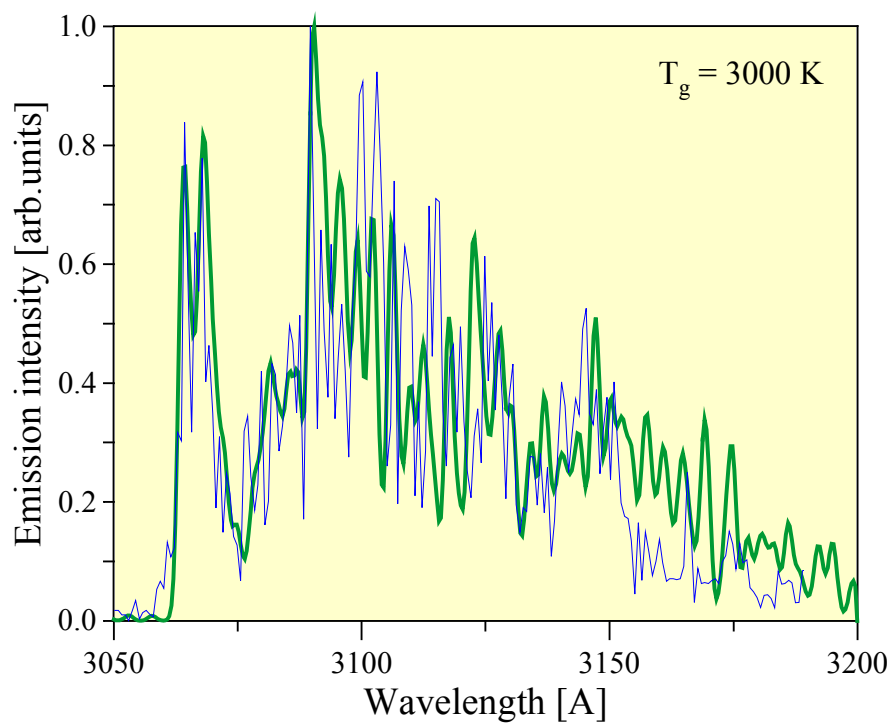


Fig.4.5. Emission of OH($A^2\Sigma^+ - X^2\Pi_i$) 0-0 band. $P = 50$ Torr, $s \approx 4$ kW/cm², instrumental broadening ≈ 2 Å

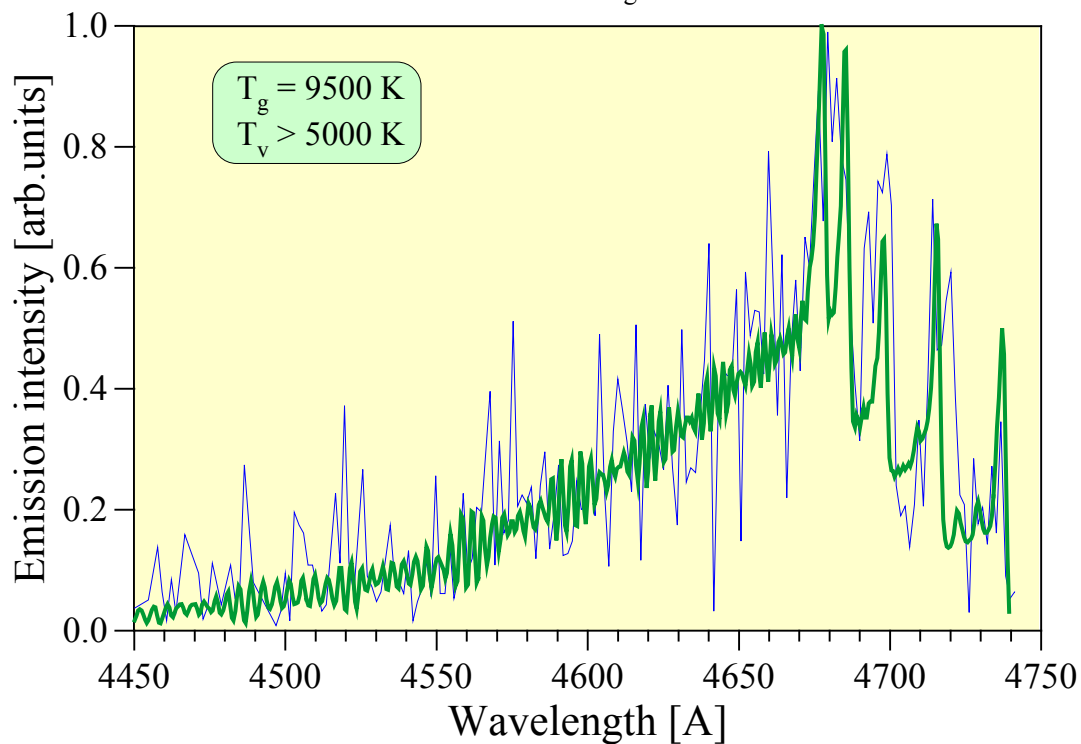


Fig.4.6. Comparison of experimental and calculated spectra of C₂ Swan +1 sequence in commercial CO₂ at 100 Torr, instrumental broadening ≈ 2 Å

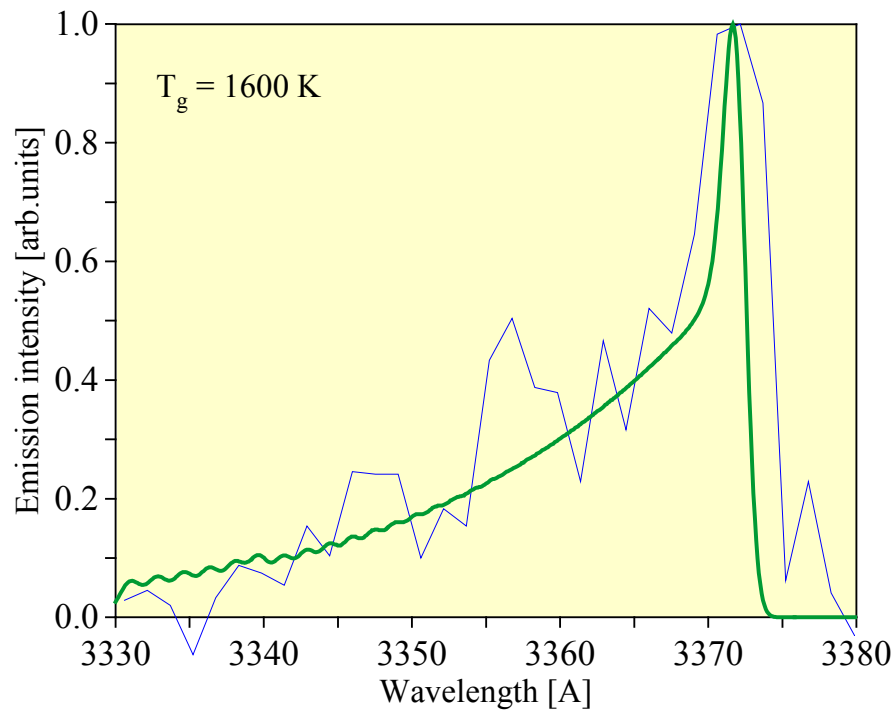


Fig.4.7. Emission of $\text{N}_2(\text{C}^3\Pi_u - \text{B}^3\Pi_g)$ 0-0 band. $P = 100 \text{ Torr}$, $s \approx 16 \text{ kW/cm}^2$, instrumental broadening $\approx 2 \text{ Å}$

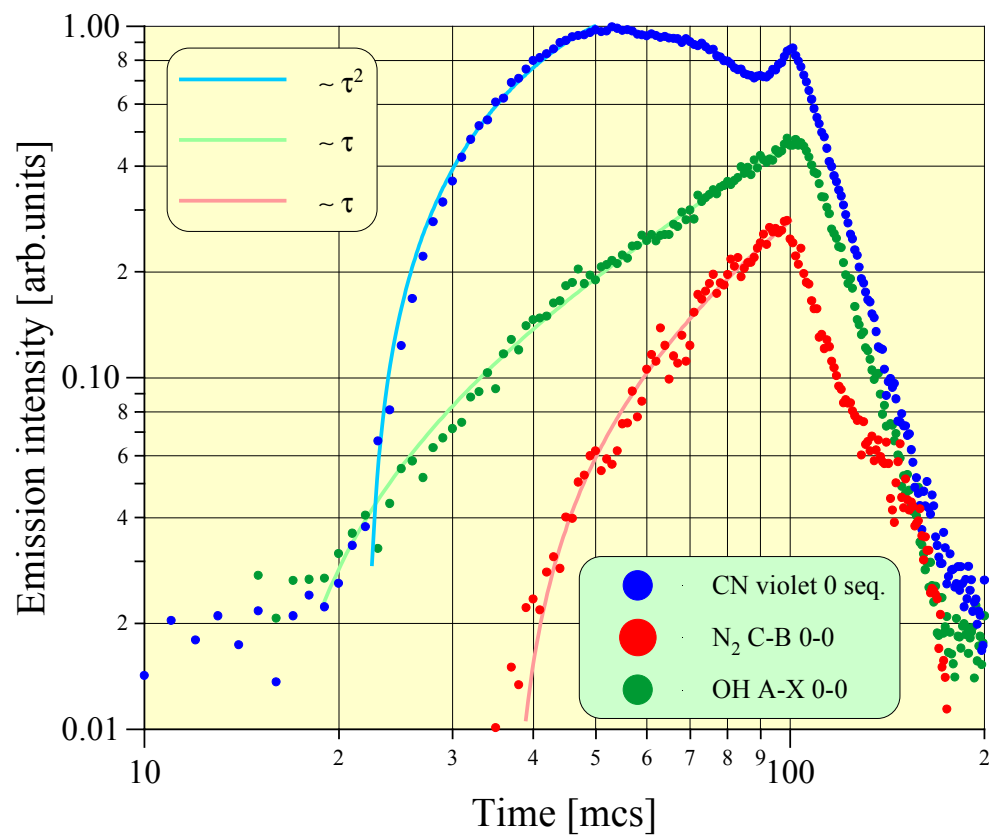


Fig.4.8. Emission temporal dependences $P = 100 \text{ Torr}$, $s \approx 8 \text{ kW/cm}^2$

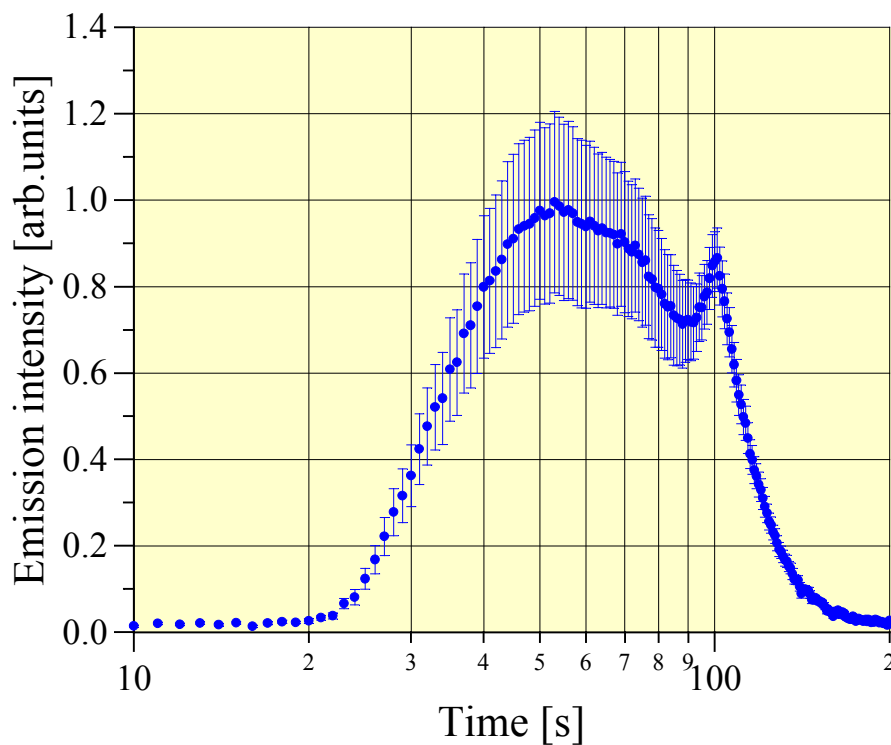


Fig.4.9. CN B-X 0-sequence emission temporal dependence. Averaging and scattering by 10 measurements.
 $P = 100 \text{ Torr}$, $s \approx 8 \text{ kW/cm}^2$

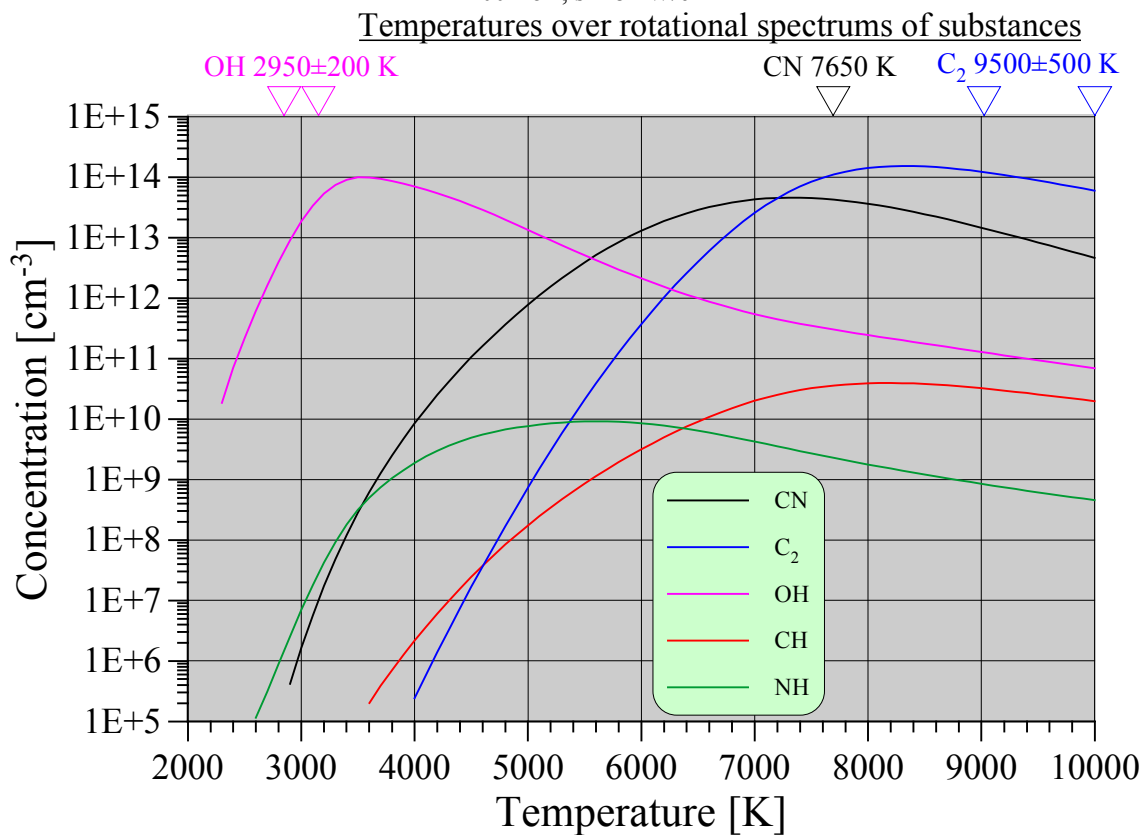


Fig.4.10. Equilibrium concentrations of emission radicals were observed in experiments and some others are possible for observation in “commercial CO₂”

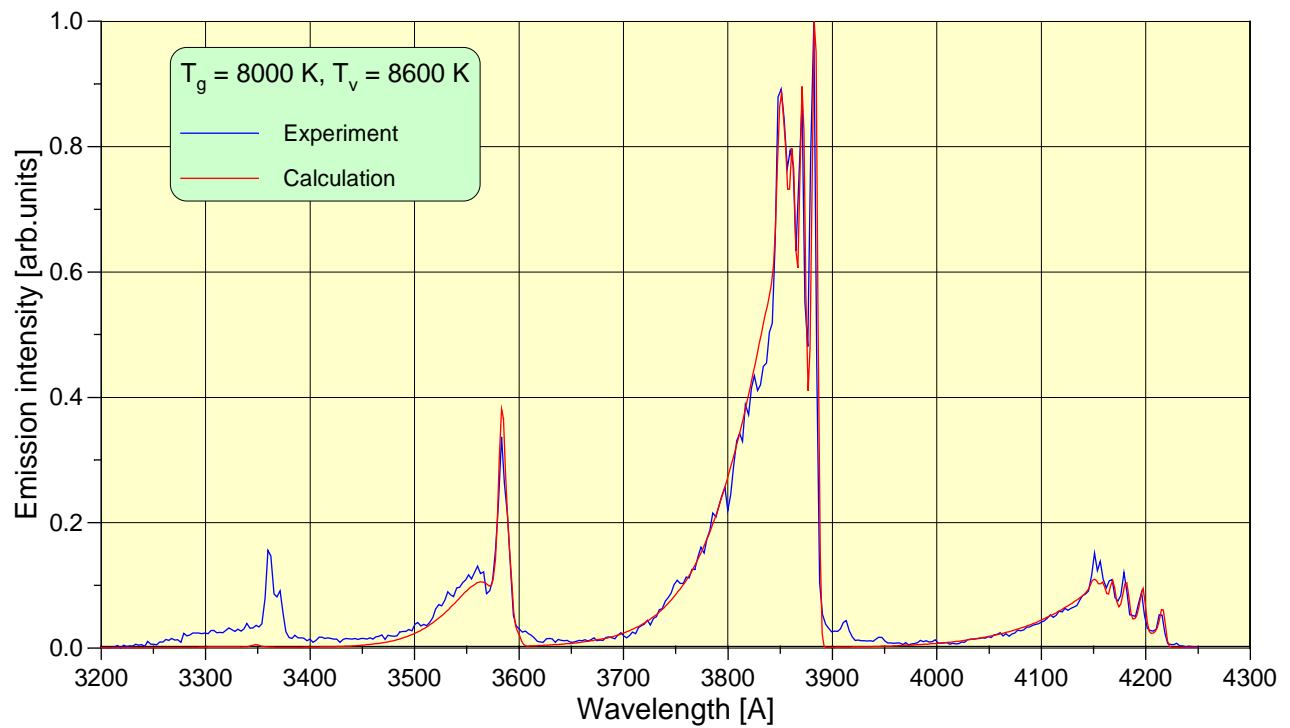


Fig.4.11. Overview of CN emission spectrum of MW discharge along dielectric plate

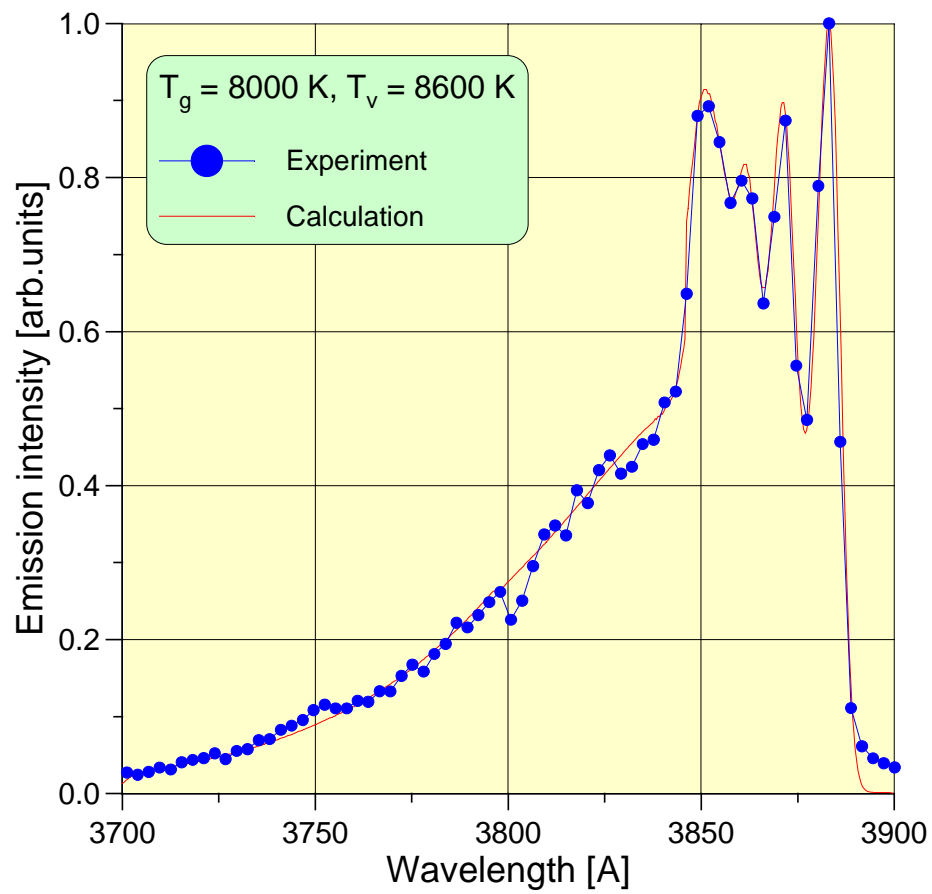


Fig.4.12. Emission spectrum of CN 0-sequence

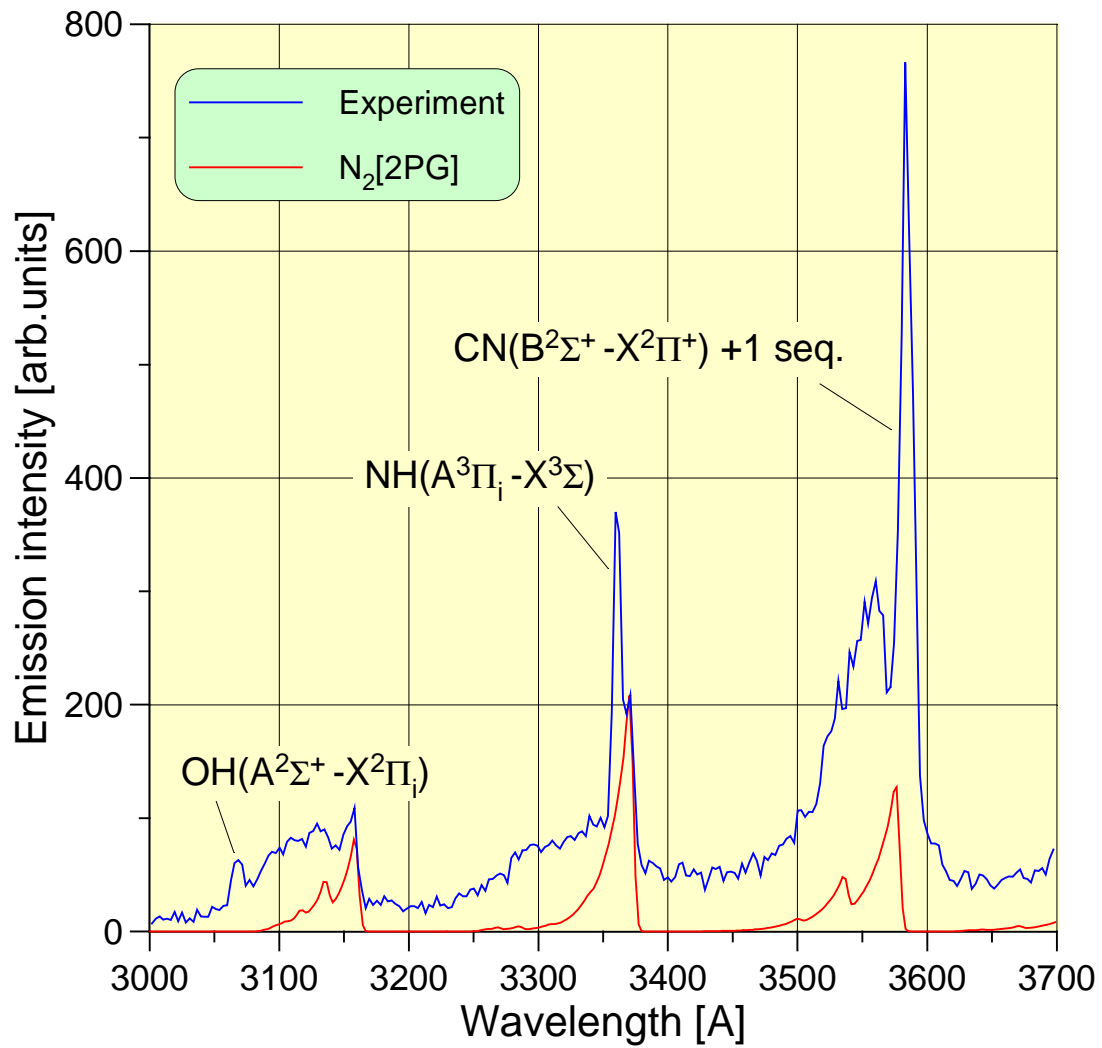


Fig.4.13. Short-wave part of emission spectrum

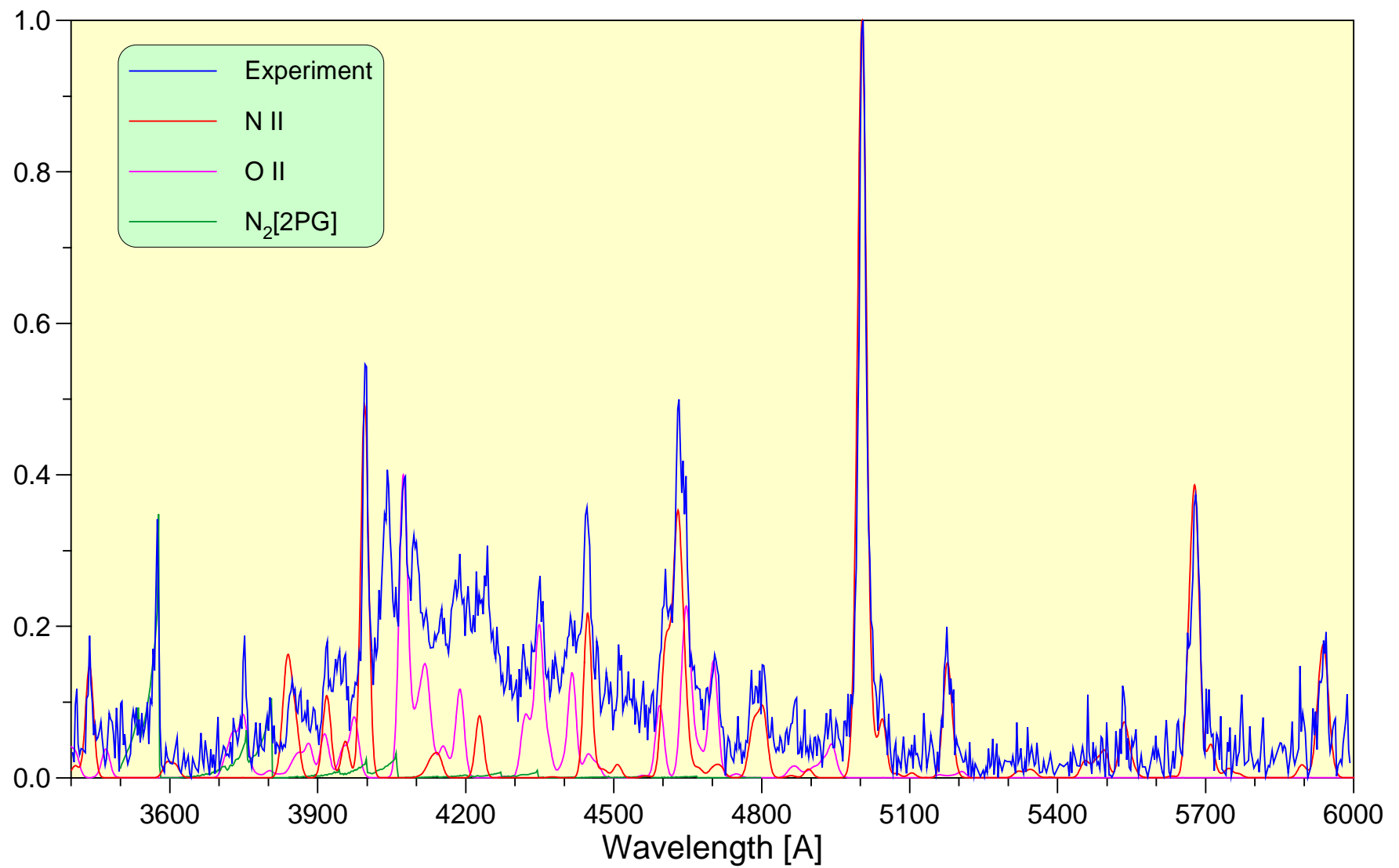


Fig.4.14. Review spectrum of DC spark channel

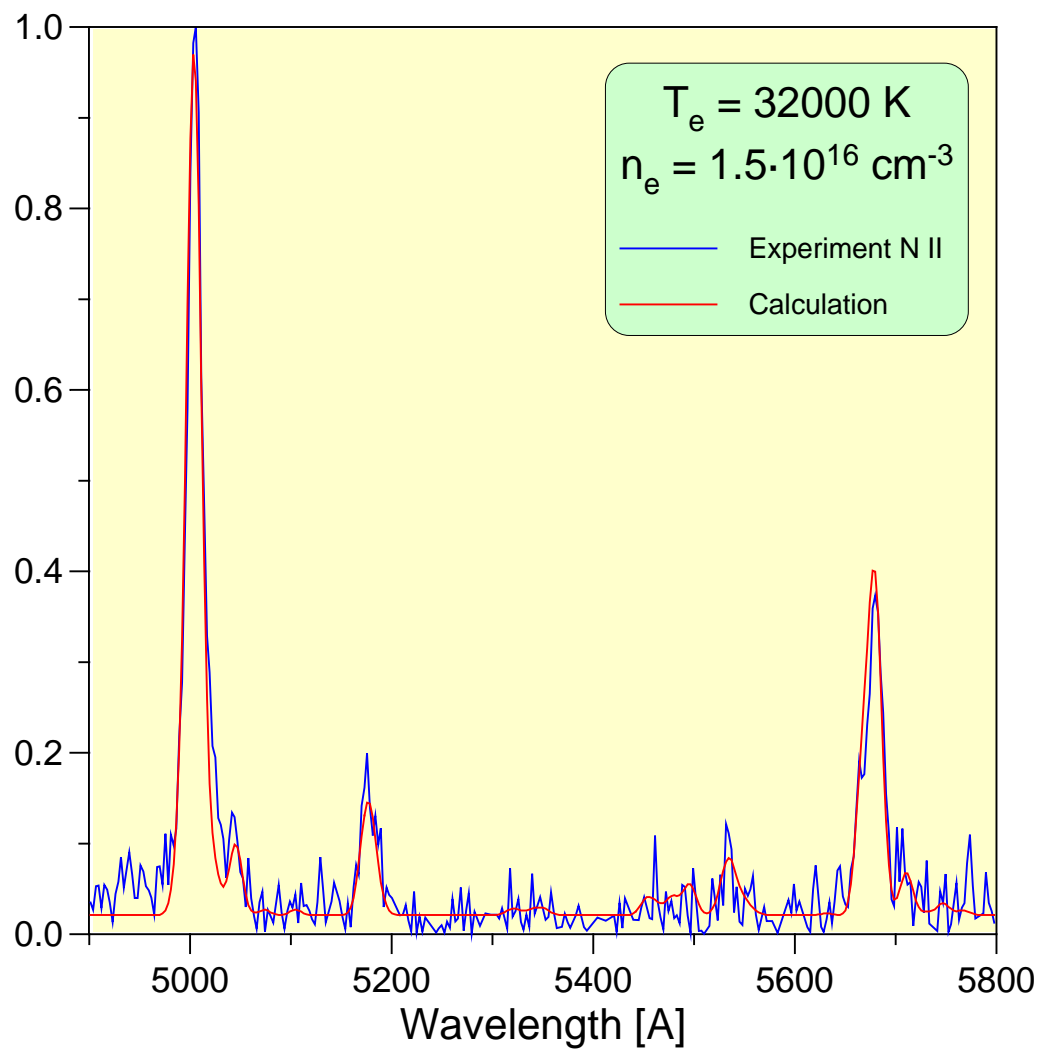


Fig.4.15. Emission spectrum of N II lines and fit of this spectrum

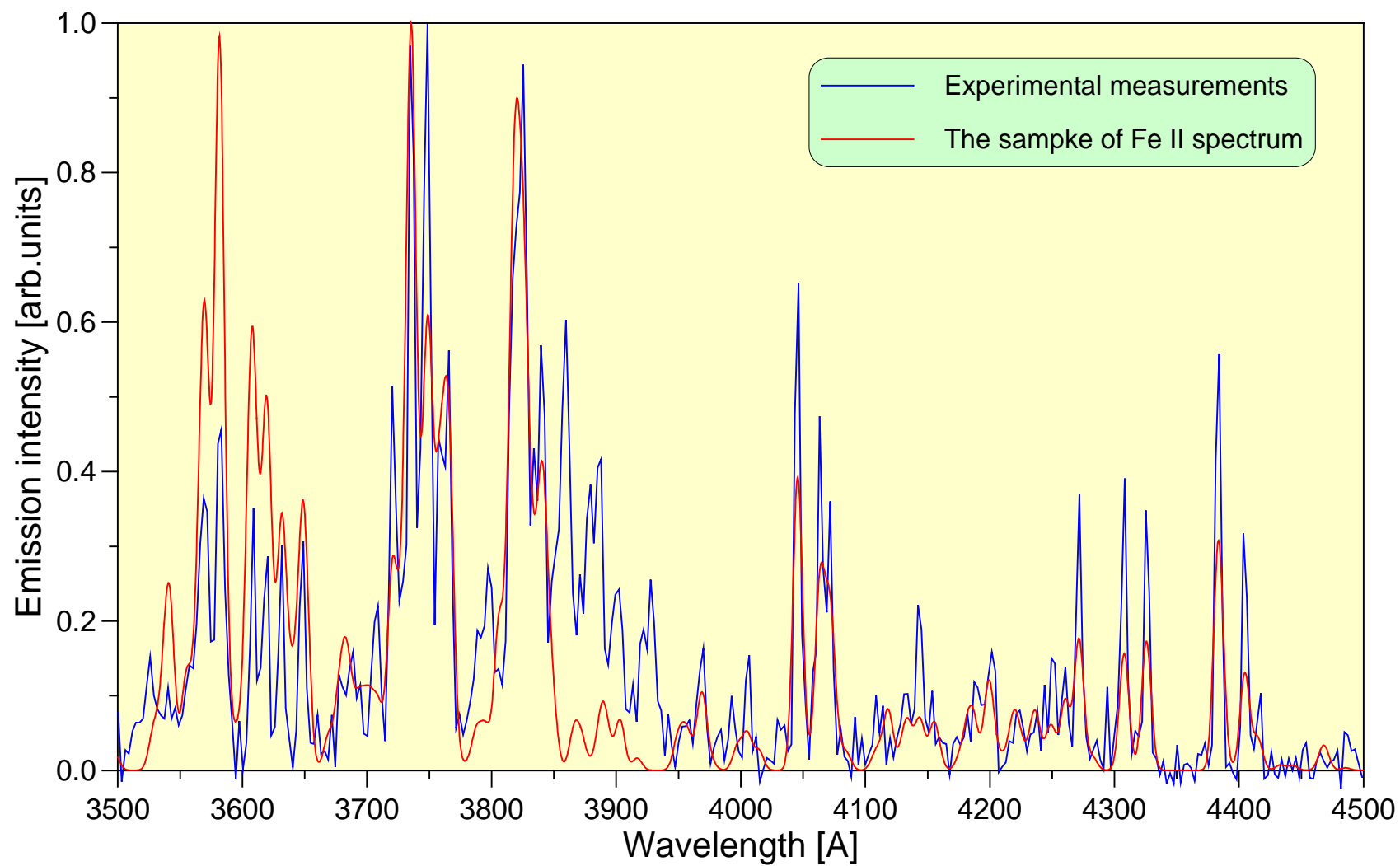


Fig.4.16. The overview of emission spectrum from the volume near initiator tip

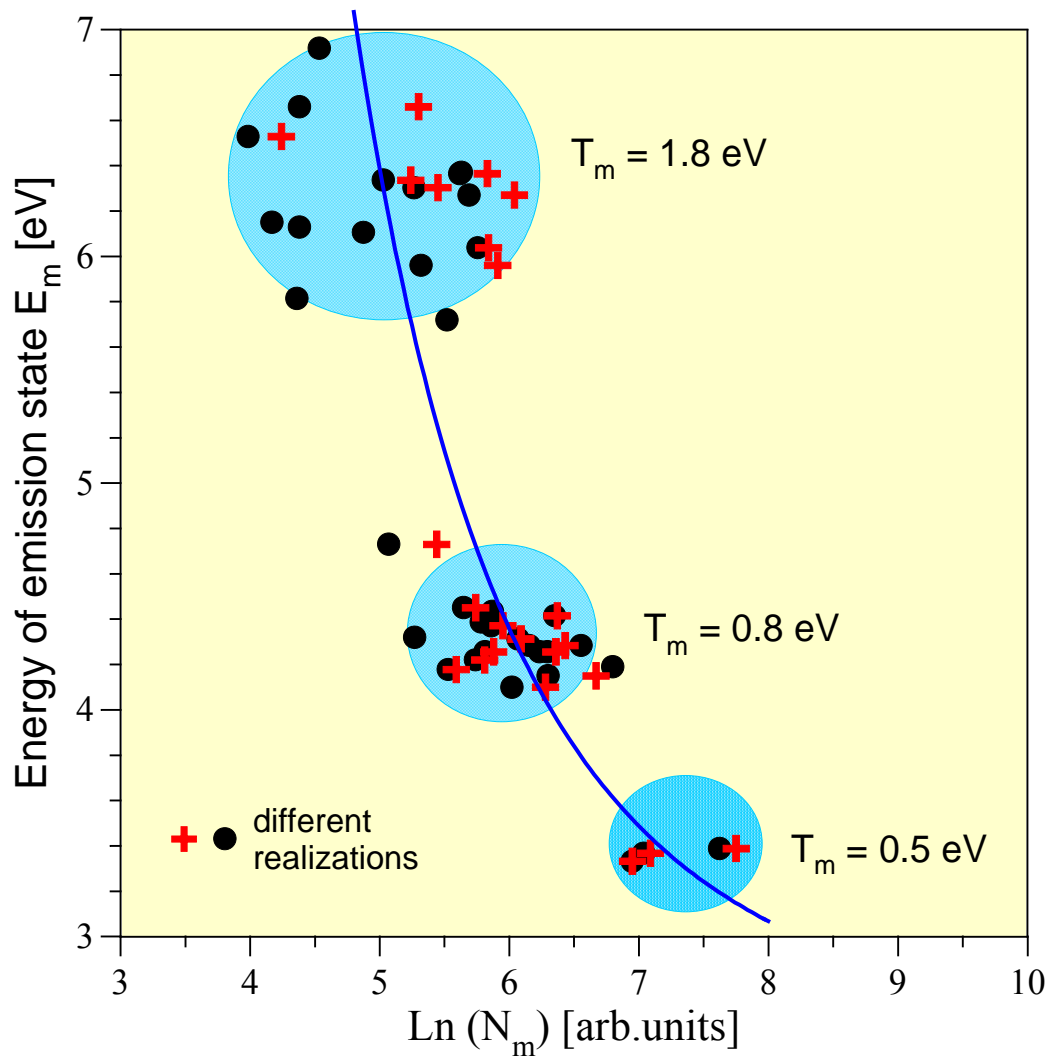


Fig.4.17. The dependence $E_m - \ln(N_m)$ over Fe I emission spectrum

5. Experimental investigations of AD-bodies drag under MW energy deposition in supersonic flow

The detailed experimental investigations are implemented for better understanding of phenomena taking place under interaction of microwave discharge in supersonic flow with aerodynamic bodies.

In the previous reports the basic understanding of streamlining of a blunt body by a supersonic flow with a finite thin heated channel on the axis of it was given. It was carried out by computation mainly. The sense of the non-stationary interaction of discharge region with bow shock wave is *vortex* generation inside the perturbed area between the bow shock wave and the body. The vortex is forming during thermal discontinuity absorption by the shock layer and starts its movement towards the model after the back fronts of discontinuity and vortex coincidence. Diminishing of transverse dimension of discontinuity leads to noticeable increase of interaction efficiency even under the same gas temperature of discontinuity (i.e. under the total energy input decrease). The value of the effect remains practically the same. Increase of longitudinal dimension (length) of discontinuity does not affect efficiency (it remains constant in the area of parameters considered), but leads to the more pronounced decrease of mean pressure reduction.

Comparison with experimental values manifests in favor of highly non-uniform structure of microwave plasmoid. We've formulated also for the proposed method the universal physical mechanism, its application range and ultimate efficiency, as well as the requirements for the performance of microwave discharge for efficient method application.

The purpose of current activity is to bring microwave experiment at a new level of supersonic flow quality. Investigation under enhanced-quality flow conditions by the full spectrum of modern methods can open new possibilities of plasma technology in fundamentals of plasma-airflow interaction area.

5.1. Results of exploration of aerodynamic characteristics of a body in supersonic flow with X-polarized MW discharge

5.1.1. Interaction of blunt body with central-axis-positioned microwave plasmoid

Blunt cylinder of 20mm diameter was placed in such a way that it's central axis coincided with the axis of symmetry of the main microwave plasmoid. Fig.5.1 represents several frames of plasmoid interaction with shock wave of cylinder, left column is Schlieren, right –

chemiluminescence. Figures on each image indicate time interval (in microseconds) after microwave discharge termination.

The nearest to aerodynamic body tip of plasmoid was disposed at the moment of its creation in about several millimeters upstream from the bow shock wave. It is seen that at 20thmcs interaction already started – it is especially well seen from chemiluminescent image due to light emission intensification after the shock (emission intensity is proportional to density squared). On Schlieren image one can see the blast wave originated from plasmoid and propagating away from it.

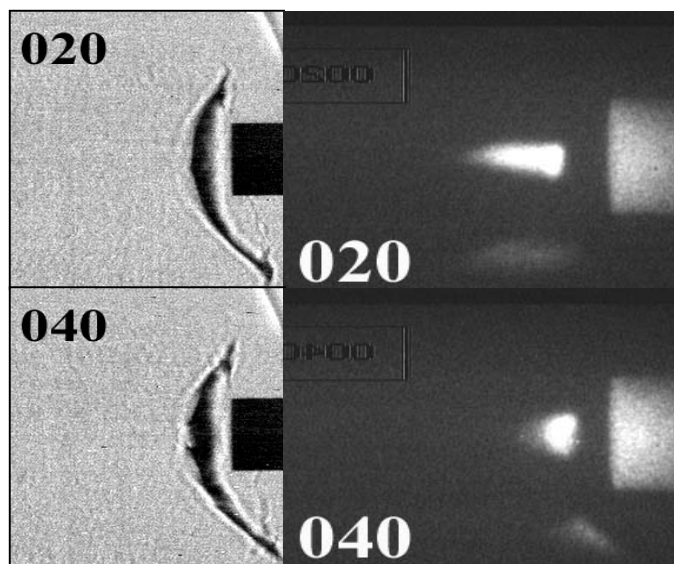


Fig.5.1. Early phase of interaction of microwave channel with blunt body

The next images (Fig.5.2) refer to the moment just preceding the complete “absorption” of plasmoid by the shock layer. By this moment the emitting agent has already fulfilled the entire structure volume. These images represent vortex formation inside shock layer also. This process is especially distinct at chemiluminescent images, from which even the rotation direction is seen. But Schlieren images also deliver information of the vortex development and reflect the vortex growth process.

Unfortunately, chemiluminescent imaging is informative only for about one hundred microseconds, after that its luminosity becomes too weak and can not be registered by our tools. Thus, only Schlieren images represent the latest stages of interaction.

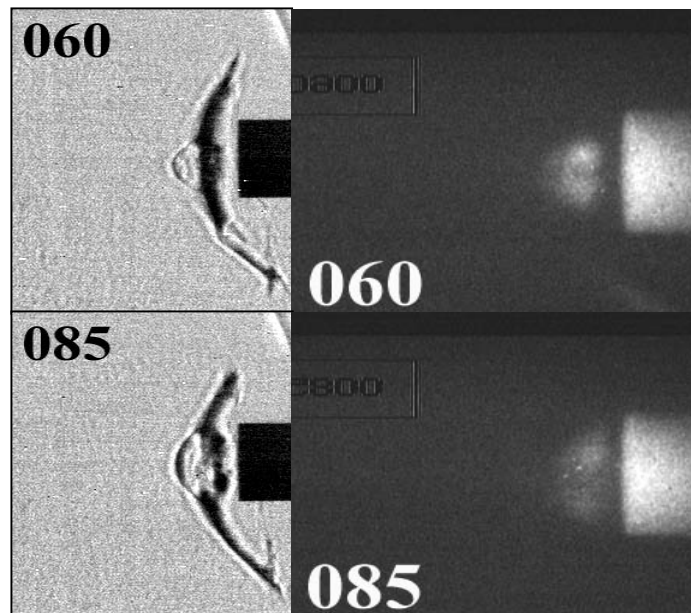


Fig.5.2. Middle stage of interaction of microwave channel with blunt body

Images on Fig.5.3 deliver imagination about the process of shock layer evolution in time interval from 110 to 190mcs. Vortex growth in size is represented by first three images. Relaxation of the bow shock position is not seen even at 180mcs. The most intriguing is a fact that the stand-off practically has not changed its value during previous 100mcs. Relaxation starts only after 200mcs.

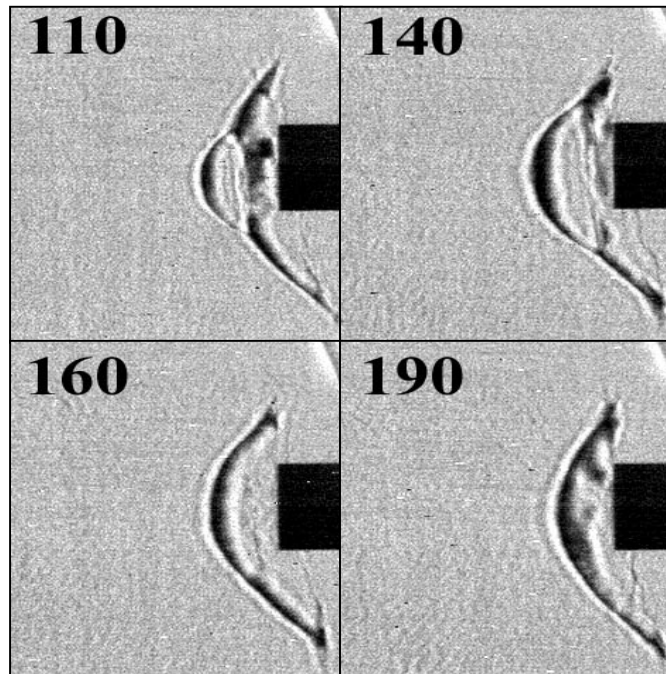


Fig.5.3. Bow shock wave evolution

So several main stages of the process can be marked:

- moment of microwave discharge. At the moment about 20mcs the discharge region touches the bow shock wave;
- discontinuity decay, shock wave moves along the heated channel. Upstream velocity of shock movement (in the laboratory frame) is about 0.22-0.25mm/mcs, or 0.45-0.5 of the flow (bow shock) velocity;
- vortex creation and it's extension (this process seems to start even earlier, at 35mcs, but it is not well distinguished due to main part of the bow shock screening);
- decay of the vortex, vortex disintegration;
- reconstruction of primary streamlining. The process of the bow shock wave relaxation to stationary state takes 100mcs more and represents gradual movement (with oscillations) to a nominal position.

Below the time-resolved signal from pressure sensor obtained in this experiment is shown on Fig.5.4.

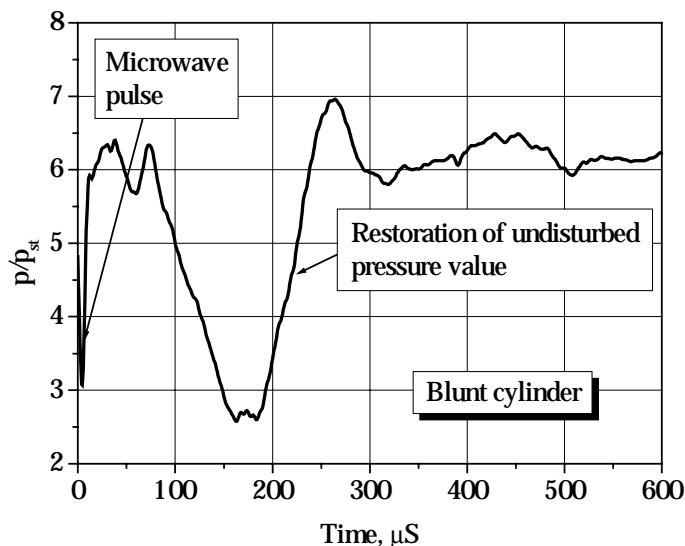


Fig.5.4. Stagnation pressure signal during interaction of microwave (MW) channel with aerodynamic body

It is seen that intensive pressure fall down takes start at about 70mcs. This is the moment when vortex has already occupied the area in shock layer just in the vicinity of front surface and begins to interact with it. The process of interaction and gradual vortex blow-down occupies about 150mcs. During this phase, stagnation pressure drops down from 215Torr (its nominal value) to about 70Torr, or 3 times. This lowest value is attained at about 160mcs. The undisturbed value of stagnation pressure is attained after about 300mcs.

5.1.2. Interaction of blunt body with off-axis-positioned microwave plasmoid

One of the options through which the flow parameters could be controlled is the control of discharge region position relatively the aerodynamic body. Beam position control is inherent to microwave technique. In our case we changed the mutual position of discharge channel and body by its displacement. Blunt cylinder of 20mm diameter was placed now in such a way that its central axis was shifted for different distance away from the axis of symmetry of the main microwave plasmoid.

Experiments showed that in contrast with the symmetric interaction, only one asymmetric vortex originates in shock layer and its rotation takes place in such a manner that increases the pressure at stagnation point.

Investigated was also the pressure signal structure under the consecutive displacement of the discharge region in respect of body symmetry axis. Results are presented at Fig.5.5. It is seen that displacement of discharge channel leads to dramatic change in pressure signal character. The behavior of it becomes different from 70mcs, when the vortex starts its interaction with body front surface. When $y=0$ stagnation pressure at time delay 150mcs falls up to 40% from it's initial level. Radial displacement of discharge channel at distance of 2mm, i.e. $0.1D$, where D is model diameter, diminishes the effect of drag reduction. Further displacement over 2mm, i.e. from 2mm to 5mm, delivers increase of drag with maximum effect at $0.25D$. In this case measuring pressure is more than 20% higher than stagnation one p_o' (black dash line). Some recovery of total pressure p_o is observed. Also it means drag increase in contrary to drag reduction for the case of symmetric geometry of discharge – aerodynamic body interaction. Thus, plasmoid position can control the value of the stagnation pressure on the blunt cylinder.

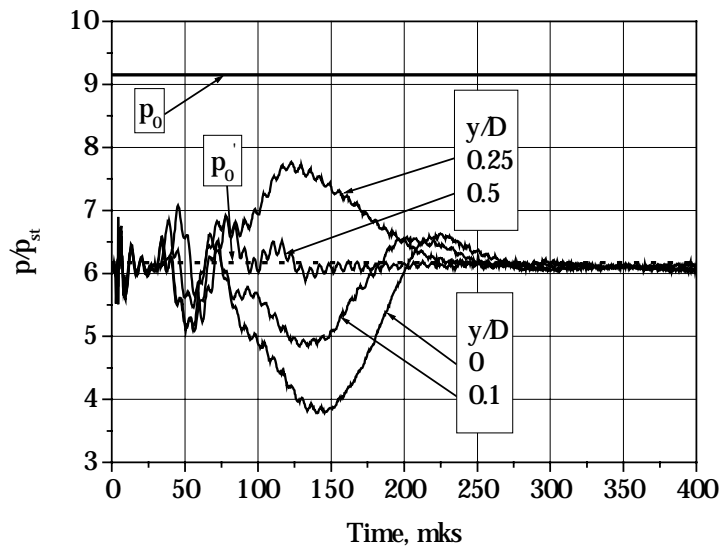


Fig.5.5. Interaction of off-axis-positioned microwave channel with blunt body.

Integral is calculated on the whole investigated time period. The results are shown on Fig.5.6.

It is seen that impulse changes it's sign via increasing misalignment from minus to plus and maximum positive impulse has value twice less than negative one.

Also experiments showed that pressure distribution on the front surface of the blunt cylinder was sufficiently uniform while model interacted with plasmoid. So measured stagnation pressure can be considered to be an indicator of drag changing.

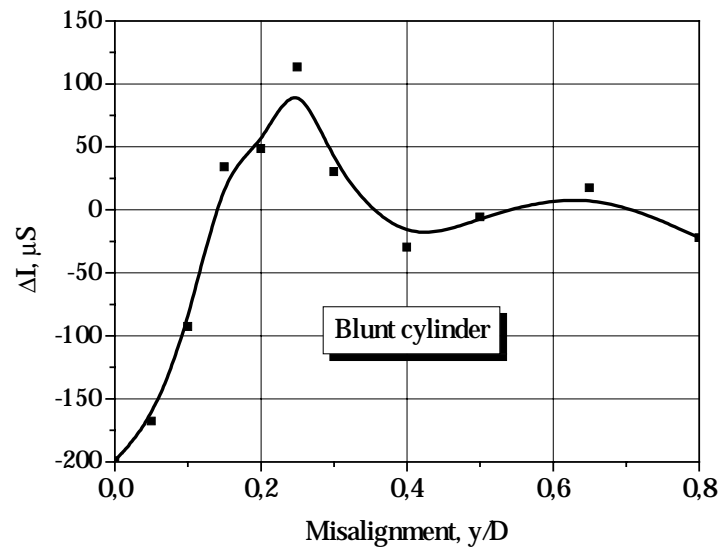


Fig.5.6. Quantity proportionate to impulse, which is imparted to the blunt cylinder during plasma – shock layer interaction via misalignment

5.1.3. Interaction of sphere with central-axis-positioned microwave plasmoid

The sequence of Schlieren photos and chemiluminescent imaging Fig.5.7 presents interaction dynamics in time interval about 120mcs.

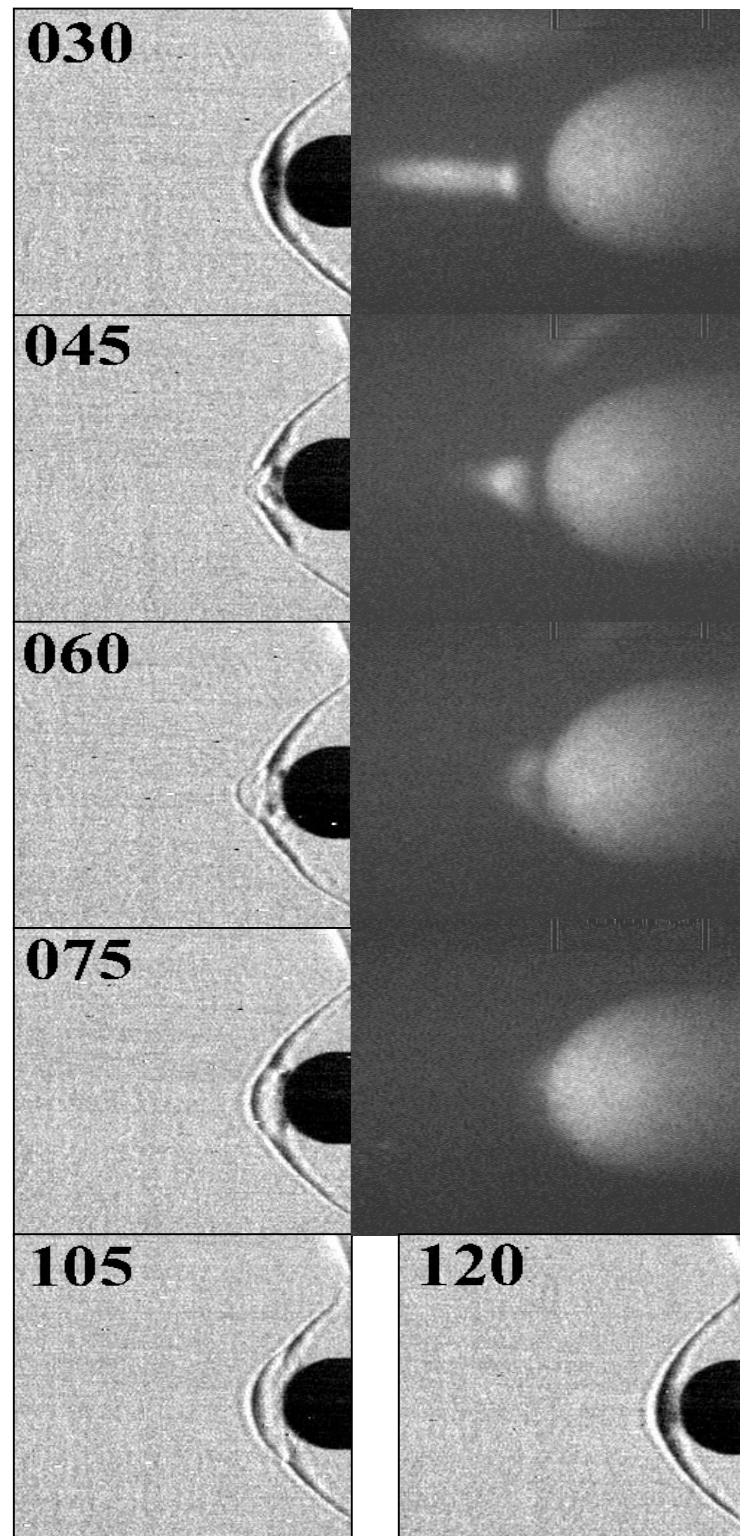


Fig.5.7. Sphere in supersonic flow with microwave discharge

Several stages can be remarked. At about 30mcs heated domain begins to interact with shock layer on the sphere. Bow shock wave moves upstream, rarefaction goes downstream (45mcs). The velocity of shock upstream propagation is somewhat about 0.15-0.17mm/mcs and is approximately 1.5 times less than in the case of blunt cylinder of the same diameter. Disturbed area becomes broader (60 – 105mcs). A vortex appears in the shock layer. Then reconstruction of undisturbed streamlining begins.

It is likely that all the process of plasma body interaction on the sphere elapses faster then in the case of blunt cylinder. Probably it is connected with better sphere streamlining. Conclusion can be made that the better is the body aerodynamics, the faster are the processes of interaction of the bow shock wave with energy deposition region. Pressure measurements on sphere confirms this consideration (see Fig.5.8).

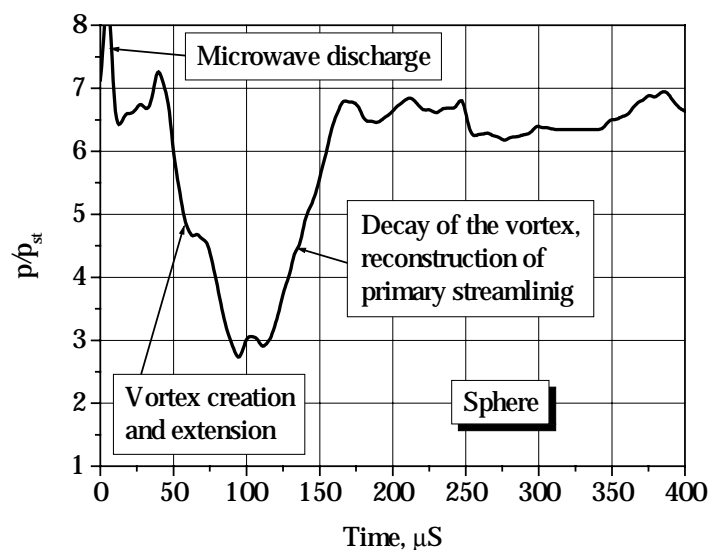


Fig.5.8. Pressure changing on a sphere with diameter 20 mm

Noticeable changing in stagnation pressure on sphere begins at about 30mcs. The main pressure takes a fall from level of full pressure behind the bow shock wave up to 50% from this pressure. This process finishes to 100mcs from microwave discharge. From that time on restoration of stagnation pressure begins on the sphere.

5.2. Results of exploration of aerodynamic characteristics of a body in supersonic flow with Y-polarized MW discharge

5.2.1. MW discharge in the working flow

Experimental setup gives opportunity to change static pressure of the working flow. So pressure in the test section was chosen of high enough level in order to realize MW discharge in the flow and to get appreciably big signal from Kulite sensor and high quality Schlieren images. Tests were carried out at static pressure of 30 – 50 Torr.

On Fig.5.9 typical Schlieren image of AD model in the working flow at the moment of MW discharge is shown (000 mcs delay).

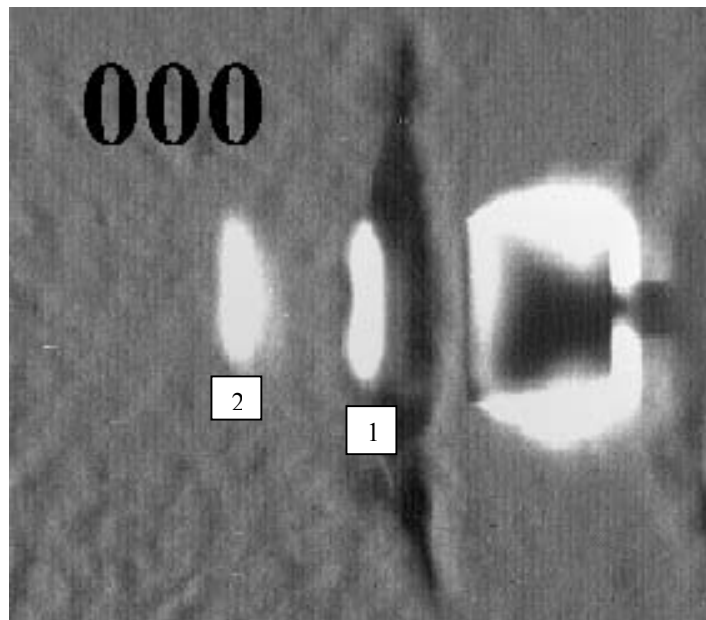


Fig.5.9. AD model in the supersonic flow with MW discharge

The model was blunt cylinder of 20 mm diameter. It can be seen that there are two filaments of the discharge in the flow. A glow can be seen around AD model. The experiments showed that the model was an initiator of MW discharge. In all experiment a glow around the model exists. The first filament is situated in half wavelength (13 mm) upstream from the model. In the case of 20 mm cylinder when bow shock wave standby is 11 mm for Mach number 1,52, shock wave disposition practically coincides with discharge location. The second filament is

situated on 26 mm distant upstream from the front surface of the model. The length of filaments is about 16 mm.

5.2.2. Temporary and spatial evolution of Y-polarized plasmoid near the model

Weak Luminescent technique

Moving of heated domain of air after MW discharge was observed by means of intensified CCD camera. The camera records position of chemiluminescence area arising in afterglow of MW discharge in the air. Time resolution of the camera is better than 2 mcs. Method of registration of weak luminescence was described in Section 1.2.5. Temporary evolution of two thermal wells is shown on Fig.5.10. These wells are generated by MW plasmoids 1 and 2 (see on Fig.5.9.) Numeral in the left upper corner of image shows time delay after MW discharge.

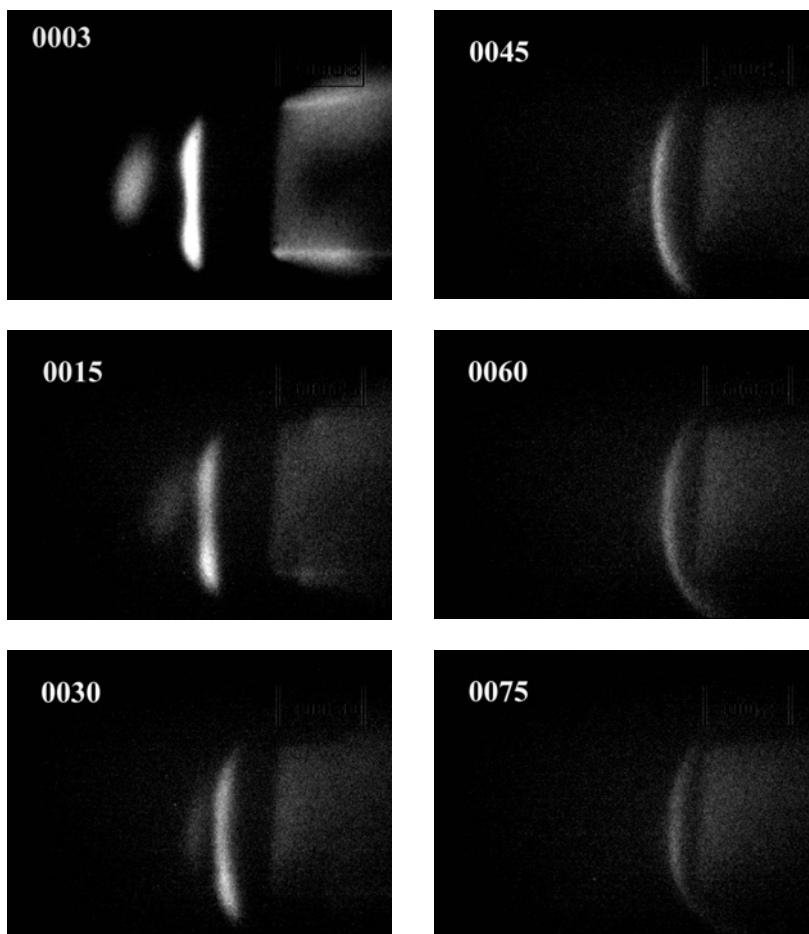


Fig.5.10. Chemiluminescence evolution of afterglow near the model

The well 1 gets to the shock layer immediately after arising and begins to move towards the model with initial velocity 226 m/s. It becomes slower then and spreads around the model. The well 2 is arising in the supersonic flow and moves downstream to the bow shock wave with the velocity 425 m/s. When it achieves to the shock layer it slightly compresses and begins to move with the velocity as plasmoid 1 does.

Schlieren investigation

For investigation of temporary and spatial evolution of gas density field around the model digital synchronous Schlieren system was used (Section 1.2.3). Time resolution of the system is 0.5 mcs. On Fig.5.11 Schlieren images are presented for time delay 15, 45 and 75 mcs. The digit 1 marks the position the first thermal well. The digit 2 denotes the second well. At the time delay 15 mcs it is clearly seen a divergent quasi-cylindrical shock wave from the second plasmoid. The left side of the shock wave flows downstream with velocity 140 m/s in laboratory coordinate system. The right side of the shock wave has the velocity 710 m/s. Tracks from shock wave become negligible at the 45 mcs of the process and thermal well images are observed only. Schlieren images (Fig.5.11) confirm the results of investigation presented on Fig.5.10. It should be marked that both methods show the absence of any vortex processes in the shock layer.

Stagnation pressure evolution on the blunt cylinder

Pressure sensor Kulite XCQ-093 was used for investigation of temporal behavior of stagnation pressure. The sensor was situated in the center of the front surface of the model. The natural frequency of the sensor is about 160 kHz. On Fig.5.12 typical signal of the sensor is presented. The ordinate axis is relative stagnation pressure (stagnation pressure divided on static pressure in the flow). The curve 1 on Fig.5.12 is real experimental signal that contains the strong oscillations on the sensor natural frequency. The curve 2 is the result of filtering of the real signal with frequency band passes 110 kHz. The line 3 corresponds to the relative stagnation pressure in the undisturbed flow.

The oscillations are arising from two reasons. The first one is electromagnet shock from MW discharge (mark C), the second one is air shock waves coming to the sensor (mark A from the first plasmoid and B from the second one).

Pressure decreasing from plasma-body interaction in this case is not great. The pressure falls is not more then 20%. It is essential less then in the case of X polarized interaction.

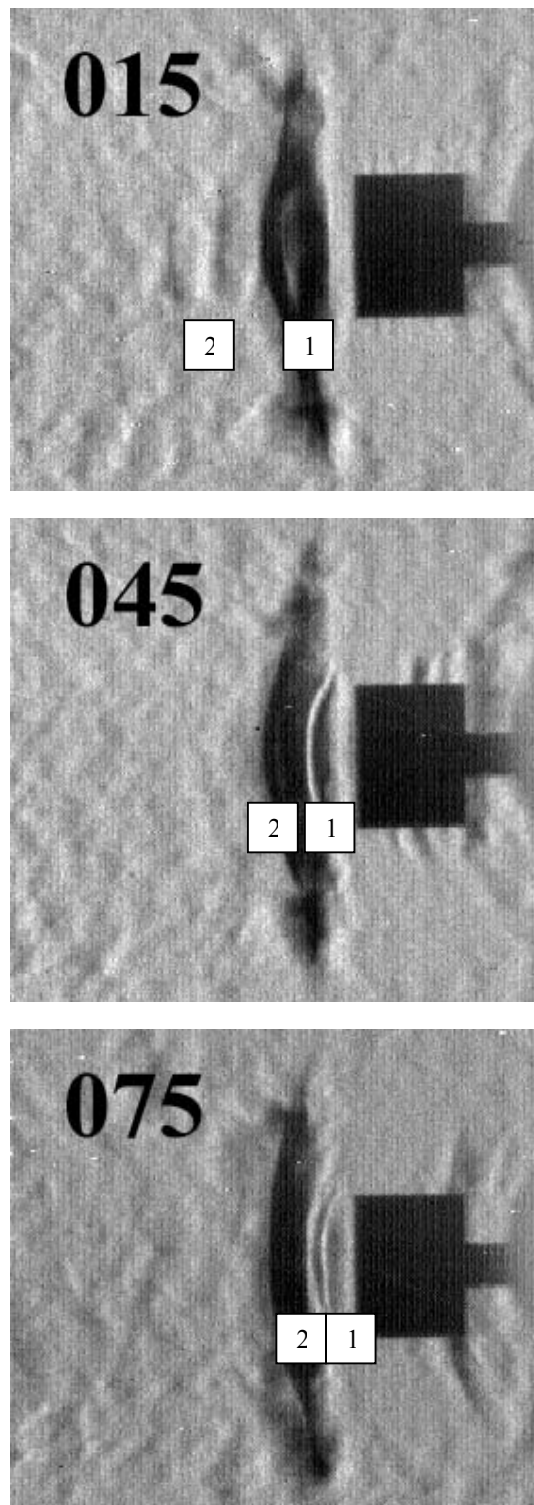


Fig.5.11. Schlieren images of plasma – body interaction

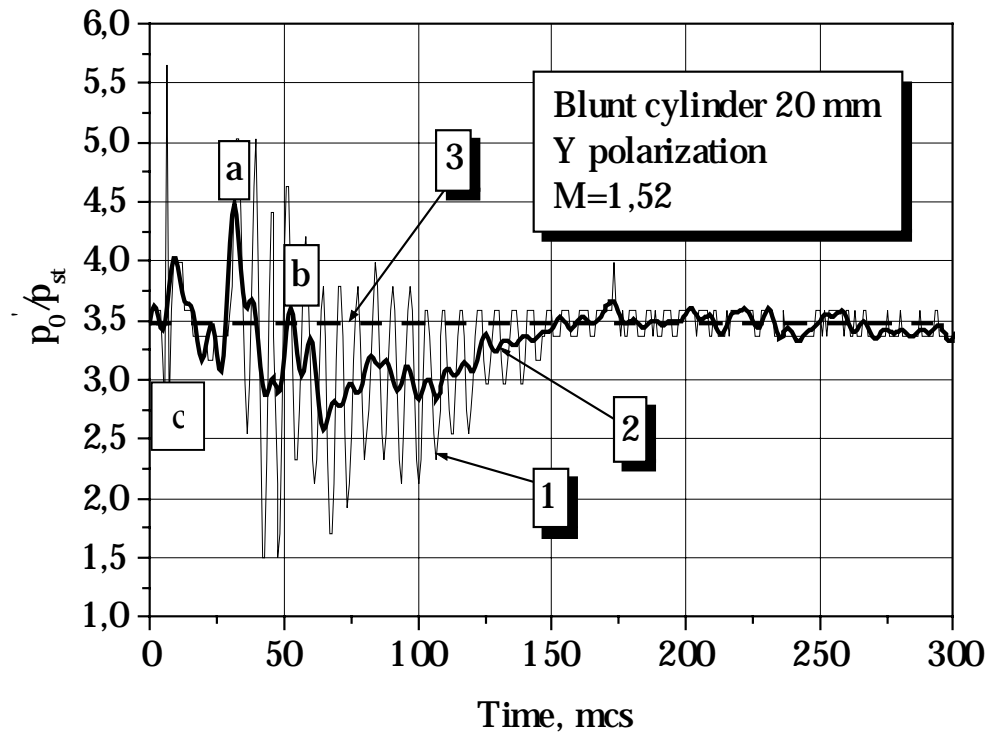


Fig.5.12. Stagnation pressure measurements on the blunt cylinder

5.3. Interaction of plasmoid with a spike-tipped body

5.3.1. Sphere with a spike. Schlieren

A model of sphere with a spike was investigated in supersonic flow with microwave discharge of X-polarization. Diameter of the sphere was 20 mm, the spike was 15 mm long. On Fig.5.13 (left) usual streamlining of the sphere with the spike can be seen. Boundary layer separation on the spike, caused by a positive pressure gradient, leads to the circulation zone creation. Outside the circulation zone there is a supersonic cone-like flow.

Usual Schlieren image of sphere with needle in supersonic flow without discharge is presented at the left of Fig.5.13. Moment of microwave discharge in the flow is seen at Fig.5.13 (right). Microwave discharge touches the left end of the needle.

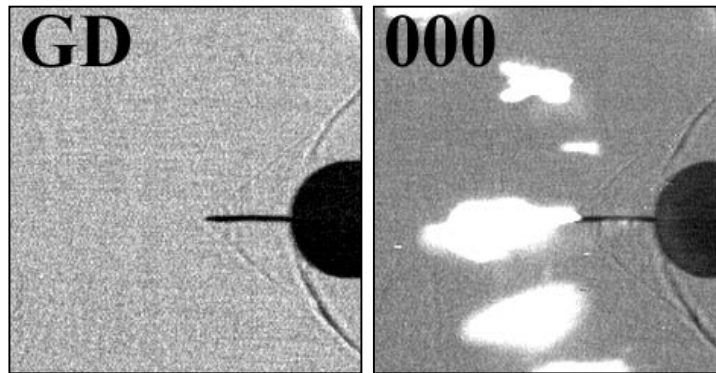


Fig.5.13. The initial phase of the interaction

Beginning of interaction heated domain with shock structure on the needle-sphere model. The shock wave on the tip of the spike becomes curvilinear one. It increases the pressure after the shock wave and decreases the pressure gradient on the needle (Fig.5.14).

Oblique shock wave on the needle nose disappear (see Fig.5.15), it transforms into straight shock wave. Straight shock wave moves downstream along the needle to the sphere.

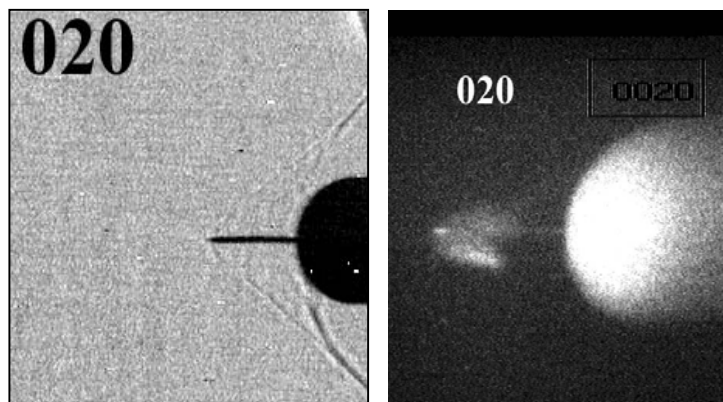


Fig.5.14. The 20-mcs phase of the process

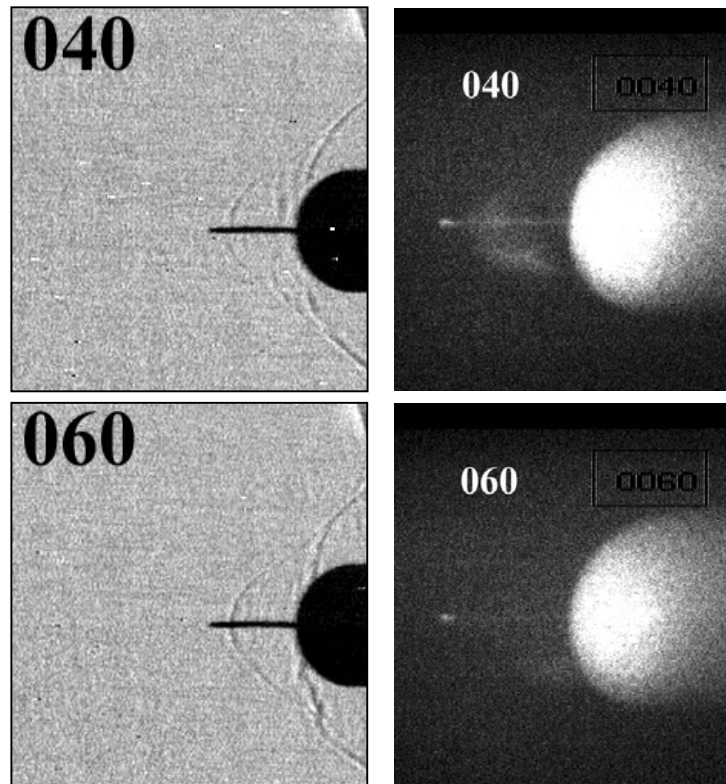


Fig.5.15. Active phase of the interaction

Shock wave interacts with boundary layer on the needle. The recirculation zone is destroyed (see Fig.5.16). Shock wave structure on the needle-sphere model is similar to the bow shock wave on the sphere.

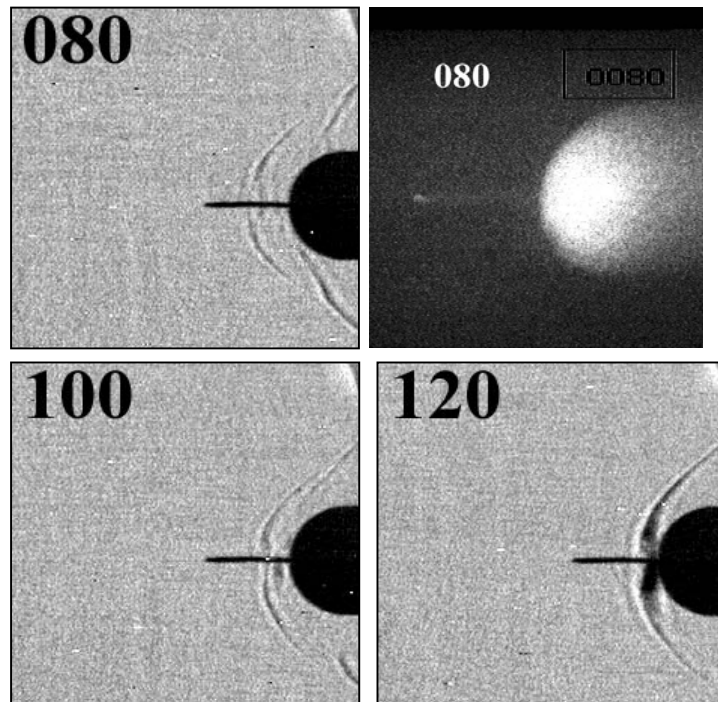


Fig.5.16. Transformation of the shock wave on the sphere with spike

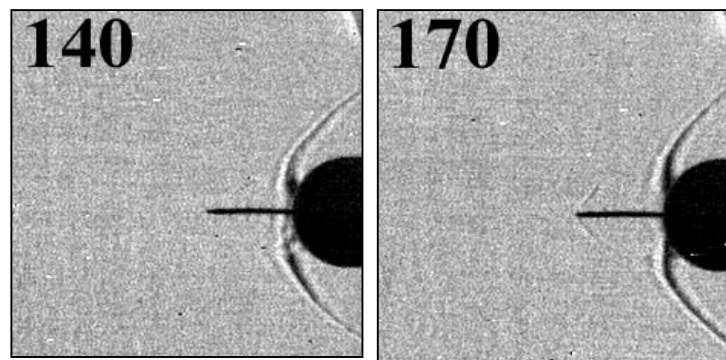


Fig.5.17. Restoring of initial shock wave configuration

After 120-mcs the process of separation zone restoring begins (Fig.5.17). Separation point of the flow on the needle moves upstream. Shock wave structure on the needle-sphere model is restoring.

5.3.2. Sphere with a spike. Kulite

Interaction of the model with plasmoid causes a dramatic stagnation pressure changing. The results of stagnation pressure measurement on the sphere with a spike are shown on Fig.5.18.

It can be seen on the Fig.5.18: the dash line is stagnation pressure after bow shock wave in the air flow (stagnation pressure on the sphere without microwave discharge); the short dot line is stagnation pressure on the sphere with the spike in the flow without microwave discharge; the solid line is stagnation pressure evolution on the sphere with the spike in the flow with microwave discharge.

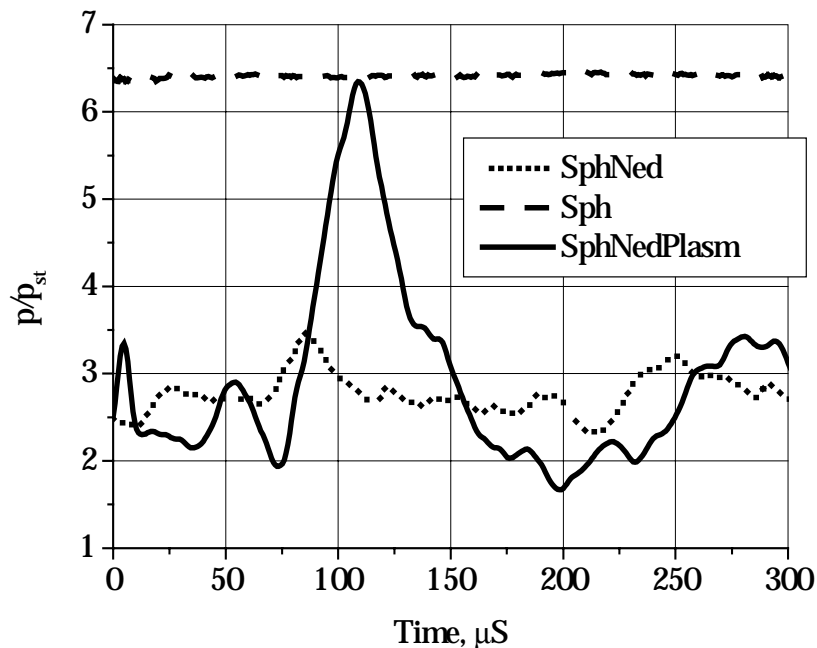


Fig.5.18. Stagnation pressure evolution on the sphere with a spike

So mounting the spike on the sphere leads to stagnation pressure decreasing from 6.16 relative units to about 2.5. Evidently drag of the body does so. The 1,5-mcs microwave discharge is restoring stagnation pressure on the sphere with the spike up to pressure level on the simple sphere. The pressure is increasing about 2.5 times. The process of pressure increasing lasts for 70 mcs. This is expectable that both the drag of the body and the convective heat transfer rate from the flow to the body are increasing sharply during the plasma-sphere with the spike interaction.

5.4. Interaction of thin bodies with central-axis positioned microwave plasmoid.

X polarization.

As in the case of cylinder, both Schlieren and chemiluminescent imaging were applied for investigation of thin bodies – cone and wedge. The effect of discharge on gas dynamics around a wedge or a cone is not so visible. Nevertheless, such interaction is seen on the obtained images.

For example a wedge with half-angle about 22 degrees is performed on Fig.5.19. The moment of interaction is better detected by chemiluminescent image. The angle of the modified oblique shock wave is diminished and there is a small stand-off of new configuration. At 75mcs these processes are near their maximum. It is immediately seen that the velocity of detachment motion is at least 3-4 times less than that for blunt-nosed cylinder. About 100mcs the oblique shock wave is already attached again, but its angle is still larger than the nominal one.

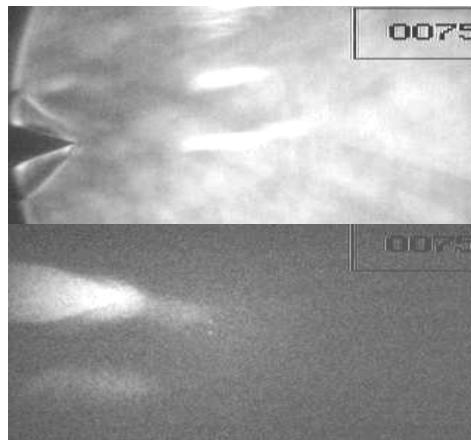


Fig.5.19. Images of wedge interaction with microwave discharge channel
(symmetric geometry)

Thus, the scenario of discharge region interaction with a wedge is not so rich physically as that for a blunt body. No vortices appear in this interaction, shock detachment velocity is much less, as well as its ultimate stand-off.

5.5. Scaling in discharge channel – blunt body interaction

5.5.1. X polarization

Modernization of gas dynamic stand has sufficiently widened possibilities in testing aerodynamic bodies of different dimension. We've conducted special set of experiments to eliminate the scaling law in discharge channel – blunt aerodynamic body interaction. The lower limit for cylinder dimension was determined by conditions for Kulite installation inside the model and turned out to be 8mm. The upper limit is defined by the flow diameter. As the last is now 60mm, the upper limit of aerodynamic body diameter is 20-24mm. Thus, we are able to test aerodynamic bodies in half-of-order range – from 8mm to 24mm.

On Fig.5.20 stagnation pressure evolution is shown for the blunt cylinders of different diameter. It is immediately seen that time of plasma – body interaction becomes larger with diameter of cylinder increasing. Such a result can be seen on the model – sphere too.

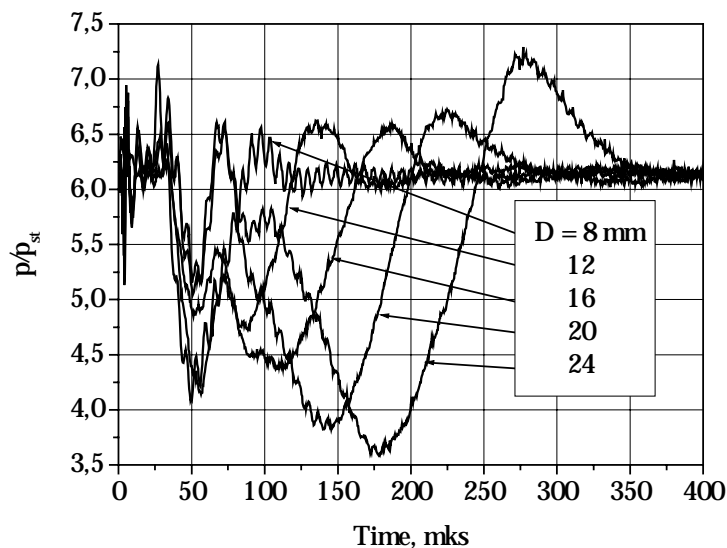


Fig.5.20. Stagnation pressure evolution on blunt cylinder of different diameter

Quantity proportionate to impulse ΔI is defined as integral over time from pressure change. Integral is calculated over the entire investigated time period.

The result of integration is shown on Fig.5.21. We can conclude that actual effect grows linearly with body diameter! Moreover, the total drag effect (for blunt cylinder) integrated over front surface is to be proportional to D^3 .

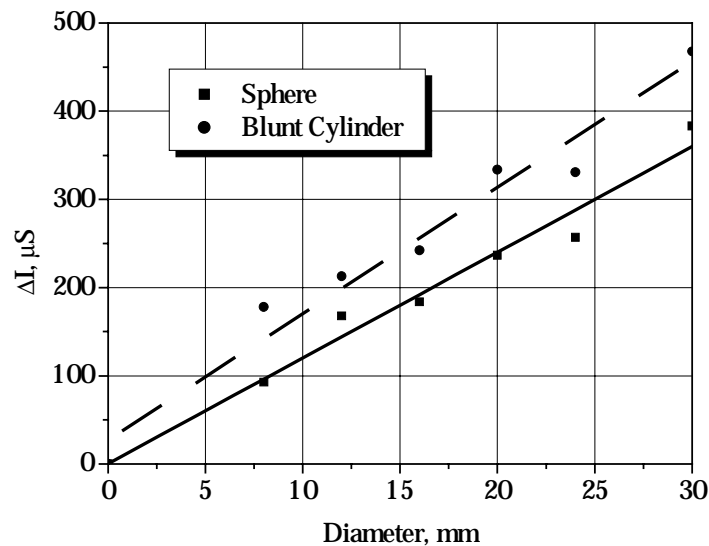


Fig.5.21. Effectiveness of microwave discharge for drag reduction over diameter of blunt cylinder and sphere

The result obtained seems amazing as theoretical considerations evidence for integral effect ΔI as being independent of body diameter under the condition of fixed channel length. Thus, in experiment we have additional (in comparison of what we could expect from theory) rise of efficiency with body diameter increase – linear rise except of constant one.

5.5.2. Drag reduction efficiency

It is also seen from Fig.5.20 that the structure of pressure signal changes significantly if compare signals from 8mm and 24mm bodies. The case of smaller body is closer to the situation of relatively long discontinuity – $L/D=2.5$, whereas for large body - to transient one ($L/D=0.83$). It should be kept in mind that probably not all details in pressure evolution in the case of 8mm body are resolved because of temporal resolution limitations of the pressure sensor.

According to our investigation of non-stationary interaction of channel with blunt body, stagnation pressure fall consists of two portions. The first – it is also the first in time – is due to rarefaction wave, arising from contact of leading tip of discontinuity with bow shock wave. The depth of this fall is governed by D/d parameter, where d is the diameter of discontinuity. The closer is this parameter to the unity, the more pronounced pressure fall is observed. In the case of $D=d$ we have situation of body streamlining by a uniform heated region. This regime of interaction in this case can be treated as decay of discontinuity and was investigated analytically. No vortex

formation in a shock layer can be observed in this case. Obviously, this regime does not lead to any gas dynamic structure transformation and is not effective.

Under the diminishing d over D ratio the impact of the first mechanism goes down and the role of vortex formation mechanism grows up. This is reflected by the second - more pronounced and vast region of pressure fall in stagnation pressure dynamics. The structure of a flow exerts a significant change - bifurcation. This is the most effective mechanism of drag reduction. Indeed, the obtained efficiency value for 24mm diameter blunt body under $M=2.1$ flow conditions is about 10. This means that having deposited of about 30mJ in specific microwave plasmoid we've saved 300mJ in body drag during interaction with it.

5.5.3. Y polarization

Integral ΔI was defined for the case of Y polarized microwave discharge too. The result of investigation is presented on Fig.5.22.

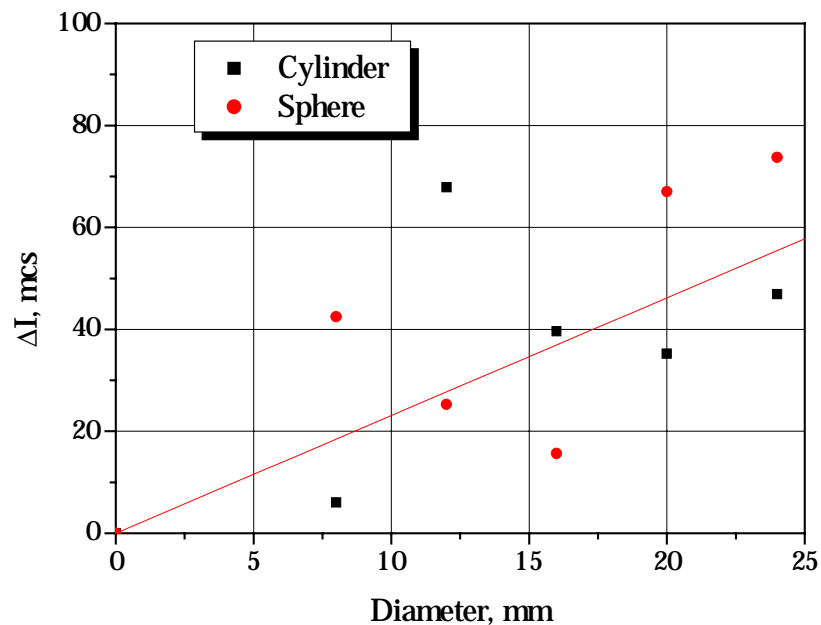


Fig.5.22. Effectiveness of microwave discharge for drag reduction over diameter of blunt cylinder and sphere. Y polarization

Effectiveness of discharge in the case of Y polarized discharge is sufficiently less than in the case of X polarization. These two cases differ from each other in order. So the discharge elongated in the direction of the axis of the model (X polarization) is most preferable for drag reduction.

6. Modeling of energy deposition effects in supersonic flow

Finding out of conditions for efficient influence on AD characteristics can be divided in two general trends. The first is aimed at specifying of desirable parameters of disturbance in airflow, which effects in a defined manner on AD-body characteristic. The second one defines how to create this disturbance in a flow by means of electric discharge. The first trend is mostly gas dynamic one, the second – electrodynamic and kinetic. In present Section modeling of energy deposition in supersonic flow for drag reduction of a blunt and streamlined body is given. Modeling is aimed at getting answer at the following questions: what are the optimal geometry (shape) of disturbance and parameters inside it; what type of energy deposition rate – quasi-static or explosive – is more efficient; what are scaling laws for the incoming parameters. Modeling – numeric and analytic – deals with both non-stationary and stationary interaction of gas dynamic discontinuity with AD body in supersonic flow. Numerical modeling of discharge domain interaction with spike-tipped body is also presented.

Thermal component is present in any type of energy deposition system, being useful or parasite in dependence of its intend. Thus, careful and complex investigation of conditions for thermal mechanism application for flight control seems to be topical. Two limiting regimes of energy deposition are quasi-static isobaric heating and very fast (explosive-like) isohoric heating. In the first case as a result of energy deposition a density well appears. In the second case shock (or sound) wave is formed along with density decrease in a heated region. In neglecting of dissipative processes, the result of interaction of density well with the shock layer is independent of its initial position upstream the body. On the contrary, disposition of the energy injection domain in respect of the body is essential parameter for the explosive heating. We start our investigation with treatment of non-linear stage of energy deposition process.

6.1. Non-linear stage of explosive-type energy deposition in MW discharge

It is shown below, energy deposition in breakdown field goes through several phases in MW discharge development. The phase of energy injection itself is final one. The earlier phases prepare conditions for high concentration of deposited energy. The final stage is characterized by interconnection of electrodynamic, gas dynamic, kinetic processes and is strongly non-linear.

Below we've made an attempt to construct analytic solution for this stage, taking into account in simplified way all the mentioned above processes.

6.1.1. Scenario of MW discharge breakdown evolution

Let us remind briefly the scenario of initial phases in discharge development, keeping in mind that they form the initial conditions for the last one. The shape of high field region in the area of focus is estimated by inspection of the surface of constant field intensity. It looks like a prolate ellipsoid of revolution - "lens". In zero approximation the distribution of electric field intensity along k-direction can be taken as $E = E_0 \cos kx$. Assuming the distribution of initial electron concentration as constant over space one obtain the electron concentration and its distribution in avalanche for a moment t

$$n_e(x,t) = n_e(0,t) \cdot \exp[\tau \exp((1 - \cos kx) \cdot BN/E_0) - \tau],$$

where $\tau = \nu_i t$ and ionization frequency $\nu_i = A \exp(-BN/E_0)$, $n_e(0,t)$ – electron concentration in the central point of avalanche, the point of the maximal concentration in it.

Due to high sensitivity of ionization coefficient to electric field intensity ($BN/E_0 \sim 10$) initially uniform spatial distribution of electrons very soon becomes extremely non-uniform. Its form is gaussian with equivalent "radius"

$$R_x = k^{-1} \cdot (2E_0/\tau BN)^{1/2}.$$

It is seen that formally equivalent "radius" may reach zero value at infinity, diminishing with time as $t^{-1/2}$. But before it several limiting factors take force. For values of $\tau \sim 15-20$ the longitudinal dimension of structure is about $\lambda/(57-60)$. It saturates at this value at least until new ionization processes begin to contribute in the total ionization flux. Analogous consideration can be applied for the transverse distribution with obtaining of the same result, except the characteristic dimension is several times larger, according to the initial field distribution parameters.

The next (second) phase in plasma creation development is connected with the process of EM field polarization inside the structure. As plasma becomes conductive, it strives to "push out" the electric field from inside. Simultaneously, the amplification of electric field at the poles of ellipsoid begins, which lead to fast elongation of conductive polar domains in the direction of electric field vector. This is well known mechanism of streamer propagation. Thus, the wave of

breakdown spreads in the area of less intensive field until the amplified field on the poles will drop to that in the center of structure. Elongation in E-direction prevents external field screening and provides conditions for better penetration of it inside structure. Depolarization coefficient of plasma structure becomes smaller and smaller. Another consequence is that the shape of plasma volume changes – it exerts transition from prolated to elongated one. The process of elongation increases the dimension in E-direction in 3 - 4 times. It means that depolarization coefficient drops to the value about 1/20.

The third and last phase manifests the onset of some kind of ionization instability in already conductive media, which is also highly non-equilibrium. Exactly this phase we are intended to investigate below. The most fundamental is ionization-thermal instability, which possesses the amplification of ionization due to rarefaction of gas along the center axis of the channel. The chain of events can be presented as follows: $T \uparrow \rho \downarrow T_e \uparrow \sigma \uparrow \sigma E^2 \uparrow T \uparrow \uparrow$. Under the constant pressure increasing of gas temperature due to energy dissipation leads to decreasing of density, that, in turn, to increase of electron temperature, conductivity and, finally, new grow up of gas temperature. The positive feedback in this chain is known as ionization-thermal instability. The most important in it is supposition about constant pressure during the process development. It means neglecting of gas movement, arising due to energy deposition. One of the aims of the present investigation is to include gas movement in the frame of scenario.

6.1.2. Problem formulation and solution for general case

For more clear formulation of the problem, let us consider characteristic features of it. The specific energy deposition rate is highly non-uniform function in space. It can be presented as bell-shaped, or, with some approximation, as turned over parabola. Due to gas heating process, one can expect that the pressure spatial distribution will repeat that of the specific energy deposition rate. It means that pressure gradient forces gas to move away from the point of pressure maximum, thus, rarefying the medium. This, in turn, strongly intensifies the process of energy deposition and it receives new acceleration. It is seen that in spite of the problem of instant energy deposition, in our case the process is inherently linked with the gas density evolution. The problem is strongly non-linear.

Well-defined formulation includes equations for conservation of mass, momentum and energy of gas, along with equation(s) for ionization production in media and electric field. Here

we'll limit ourselves by simplified ionization kinetics and electric field geometry. The problem is treated as one-dimensional. Therefore, equations for gas density ρ , velocity v and specific energy ε look as

$$\rho_t + (\rho v)_x = 0 \quad (1)$$

$$\rho (v_t + v v_x) = -p_x \quad (2)$$

$$(\rho \varepsilon + \rho v^2/2)_t + (\rho v(\varepsilon + v^2/2) + p v)_x = \rho Q. \quad (3)$$

Here p is pressure, Q – dissipated power per unit mass. These equations are to be added by the gas state equation. The term ρQ in our case is equal to σE^2 . Below we'll consider electric field distribution as time independent and having maximum at zero spatial point, which is a center of symmetry in the problem. We'll also consider the conductivity of medium as a function of E/ρ value. This supposition means omitting of time partial derivative in electron concentration equation, i.e. at every time moment electron number density is balanced by ionization and recombination processes. This is true for characteristic ionization time much less than that of the process under consideration and relatively high electron concentrations. We also suppose ionization rate as being a power function of E/ρ value, $v_i \sim (E/\rho)^\theta$, $\theta \gg 1$. This approximation is valid in some vicinity of the breakdown threshold and is often used in discharge problematic.

Our problem belongs to the class of non-stationary symmetric problems for which velocity distribution can be presented as $v = x f(t)$. The solutions for the adiabatic motions are given in well-known monograph [1]. The peculiarity of the problem under consideration is that it is non-adiabatic. Due to the symmetry in geometry, all incoming parameters except velocity have extremum at $x=0$. For simplicity, we'll find solution for the spatial region around zero point. In this approximation the set of equations (1) – (3) takes form

$$\rho_t + \rho v_x = 0 \quad (4)$$

$$\rho (v_t + v v_x) = -p_x \quad (5)$$

$$p_t + p v_x = 0.4 \cdot \eta \sigma E^2. \quad (6)$$

The spatial distribution of parameters is forced by dissipative term $\eta \sigma E^2$, in which electric field intensity is the primary source of inhomogeneity (η is the portion of dissipated energy which immediately transforms in gas heating). Substituting $v = x f(t)$ in this system, one obtain

$$\rho_t + \rho f = 0 \quad (7)$$

$$\rho \cdot (f_t + f^2) = -p_x/x \quad (8)$$

$$p_t + \gamma p f = 0.4 \cdot \sigma E^2. \quad (9)$$

As $p = p_0(t) \cdot (1 - \alpha x^2)$ the term $-p_x/x = 2\alpha p_0$. It is seen from (8), that density has next order of flatness, therefore, can be treated as depending only over time. As $E \approx E_0 \cdot (1 - k^2 x^2/2)$, one can obtain from (9) that $2\alpha = (\theta+2) \cdot k^2$.

Finally we have

$$\rho_t + \rho f = 0 \quad (10)$$

$$\rho \cdot (f_t + f^2) = (\theta+2) \cdot k^2 \cdot p_0 \quad (11)$$

$$p_{0t} + \gamma p_0 f = 0.4 \cdot A / \rho^\theta. \quad (12)$$

Substituting p_0 from (11) in (12) allow reduce the set from 3 to 2 equations:

$$\rho_t + \rho f = 0 \quad (13)$$

$$f_t + (\gamma+1)f_t f + (\gamma-1) \cdot f^3 = 0.4 \cdot (\theta+2) \cdot k^2 A / \rho^{\theta+1}. \quad (14)$$

Let us find solution for ρ as $\rho = a \cdot (t_* - t)^\beta$. From (13) it immediately follows that f has time dependence as $(t_* - t)^{-1}$, or in complete form $f(t) = \beta / (t_* - t)$. Substituting dependencies for ρ and f in (14), one obtains the linkage: $\beta = 3/(\theta+1)$. As at $t=0$ $\rho = \rho_0$, characteristic time t_* is determined by $\rho_0 = a \cdot t_*^\beta$, factor a can be find from (14):

$$2\beta + (\gamma+1) \cdot \beta^2 + (\gamma-1) \cdot \beta^3 = (a^{\theta+1} \cdot T_*^3)^{-1}, \quad (15)$$

or

$$t_* = T_* \cdot (2\beta + (\gamma+1) \cdot \beta^2 + (\gamma-1) \cdot \beta^3)^{1/3}, \quad (16)$$

where

$$T_* = (0.4 \cdot (\theta+2) \cdot k^2 \cdot \eta \sigma_0 E_0^2 / \rho_0)^{-1/3}. \quad (17)$$

Unifying (16) and (17), obtain finally

$$t_* = (1.5 \cdot k^2 \cdot \eta \sigma_0 E_0^2 / \rho_0)^{-1/3} \quad (18)$$

We used also $\theta \gg 1$ ($\theta \approx 5$). The quantity σ_0 defines conductivity, which would establish stationary under the action of electric field of E_0 intensity. This value does not depend on pressure when $v_m \gg \omega$ and is about $10 \text{ Ohm}^{-1}/\text{cm}$ for the breakdown electric field intensity. For $p=0.1 \text{ atm}$, $\lambda=3 \text{ cm}$ and $E_0=3 \text{ kV/cm}$ the characteristic time t_* is about $1 \mu\text{s}$. This time depends as $2/3$ power of radiation wavelength (or a scale of spatial inhomogeneity) and $-(2+\theta)/3$ of the electric field intensity (approximately as E_0^{-2}) under the same initial pressure.

6.1.3. Comparison with the constant pressure case

Thus, we obtained the finite-time explosive self-similar solution. If arrange the incoming characteristics in a line with increasing growth rates the picture is as follows:

$$1/\rho \rightarrow v \rightarrow p \rightarrow T \rightarrow \sigma \quad (19)$$

with an appropriate negative powers

$$3/(\theta+1) \rightarrow 1 \rightarrow (2\theta-1)/(\theta+1) \rightarrow 2 \rightarrow 3\theta/(\theta+1). \quad (20)$$

Let us compare the results obtained above with those for ionization-thermal instability under the constant pressure. Under the same suppositions for ionization process we have only one equation

$$\rho_t = -D/\rho^{\theta-1}. \quad (21)$$

Integration delivers the following dependencies

$$\rho = \rho_0 \cdot (1 - t/t_*)^{1/\theta}, \quad \sigma \sim (1 - t/t_*)^{-1}, \quad (22)$$

with

$$t_*^{-1} = 0.4 \cdot \theta \cdot \eta \sigma_0 E_0^2 / p_0. \quad (23)$$

For the similar external conditions characteristic time (23) is sufficiently (about two orders) less than (18), whereas the dependence on time is much weaker. The last can be stated also for conductivity dependence. As for other characteristics, temperature has the same behavior as density, whereas pressure and velocity each have zero power.

The last item, which is important to discuss, is the behavior of the channel transverse dimension during instability evolution. As it is seen from above, the dissipative factors, such as thermal conductivity, diffusion, etc., which demand introducing second order spatial derivatives were not taken into account. Usually exactly these processes define the limiting spatial scale of the structure at the final stage. But at earlier (also non-linear) stages these factors may not play sufficient role and the spatial structure be determined by other inherent properties. Let us estimate evolution of characteristic transverse dimension of conductivity σ while instability development and begin with the constant pressure case. We are to introduce the scale of electric field spatial distribution and let consider it as above, $E \approx E_0 (1 - k^2 x^2 / 2)$. Now characteristic time of instability (23) is a function over spatial coordinate. Then let us normalize the conductivity curve on its maximum value at time moment t , it means that conductivity value $\underline{\sigma}$ is unity at zero x-point. Expanding of (23) for $k^2 x^2 \ll 1$ and substituting in conductivity expression, obtain

$$\underline{\sigma}(x,t) = 1 / [1 + (\theta/2 + 1) \cdot k^2 x^2 \cdot t / (t_* - t)] \quad (24)$$

or, characteristic dimension x_*

$$x_*(t) = (\theta/2+1)^{-1/2} \cdot k^{-1} \cdot ((t_* - t)/t)^{1/2} \quad (25)$$

It is seen that characteristic dimension collapses and becomes zero at time moment equal t_* . Expression (25) is generalization of that for avalanche size evolution presented at the beginning of this section.

Application of such approach for the case of instability with gas dynamic effects leads to expression, which differs from (25) by some factor, depending on θ , that is not of importance, taking into account the estimation character of expressions. Thus, all the collapsing parameters can be subjected this procedure, delivering the same result. This seems to be not true for some cases, therefore demands further investigation.

Briefly concluding this investigation one can state, that scenario of plasma structure evolution in breakdown field is a consecutive diminishing of transverse dimension, that allows for better penetration of the external field and results in some collapse-like creation of very thin channel(s) with high electron and energy concentration.

6.2. Energy injection in SS flow for drag reduction - modeling

Historically the first phenomenon discovered in the area of plasma aerodynamics was elimination of a shock wave during its passage through discharge plasma area or – in another formulation – drag reduction of a body moving through discharge plasma. As an introduction to the problem let us consider the most evident situation, specifying simultaneously an inherent important parameters. An aerodynamic body with cross-section S is streamlined by supersonic flow, and quasi-static isobaric heating of a flow in front of the BSW provides drag reduction. If cross-section of the heated region S_h is about S and, therefore c_x is weakly dependent on M -number, one can easily obtain the efficiency η of such method,

$$\eta = c_x \cdot \rho_0 v^2 S / 2 c_p p_0 S_h .$$

Efficiency means the ratio of saved power over deposited in the form of heat in a discontinuity, ρ_0 and p_0 – density and static pressure in the undisturbed part of the flow, c_p – specific heat at constant pressure per unit molecule, and v – flow velocity. For $S \sim S_h$ and $\gamma = 1.4$ this formula can be rewritten in another form, using Mach number M_0 of the flow

$$\eta = 0.2 \cdot c_x \cdot M_0^2 .$$

This simple formula shows the most important influential parameters and dependency between them. Two main parameters quantify efficiency in this case – the quality of aerodynamic shape (c_x) and the Mach number. The better shape the body has, the more difficult is to enhance it. Situation dramatically depends on the Mach number, so for every AD body shape there exist a critical M-number, over which the efficiency becomes greater unity. But if take into account that the efficiency of direct gas heating generally is not high, in practice this way, demanding very high level of total power, is not perspective. Therefore external action should be more localized in order to launch both more delicate mechanism of gas dynamic interaction and deliberate those kinetic processes, which lead to more efficient gas heating.

6.2.1. General relations

To formulate the aim of modeling more definitely, we write in a dimensionless form the expression for the energy E_s saved (or spent) due to modification of the flow. If u is the flow velocity at infinity, p and p_0 – pressure over the front (plane) surface of the body for the disturbed and non-disturbed flow, correspondingly

$$E_s = u \cdot \int dt \iint (p - p_0) dS.$$

Introducing the longitudinal dimension of disturbance (along the flow) L , characteristic time $\tau_* = L/u$, cross-section square of the body S and stagnation pressure p_0^{sg} , which is proportional to M_0^2 for Mach numbers not very close to the unity, one obtain

$$E_s = L \cdot S \cdot p_0^{sg} \cdot \int d\tau \iint (p - p_0) ds.$$

Thus, the aim of numeric modeling is to obtain the dependencies of ΔI

$$\Delta I = \int d\tau \iint (p - p_0) ds$$

on the main incoming parameters of the problem. For 2D plane geometry E_s has dimension of energy per unit length, and S means the transverse dimension D of a body.

Two limiting regimes of energy deposition are quasi-static isobaric heating and very fast (explosive-like) isohoric heating. In the first case as a result of energy deposition a density well appears. In the second case shock (or sound) wave is formed along with density decrease in a heated region. In neglecting of dissipative processes, the result of interaction of density well with

the shock layer is independent of its initial position upstream the body. On the contrary, disposition of the energy injection domain in respect of the body is essential parameter for the explosive heating.

Efficiency of interaction is defined as the ratio of saved energy over deposited into a discontinuity. For the case of density well the energy for its production E_h is

$$E_h = L \cdot d \cdot p_{static} \cdot (1 - \alpha) \cdot c_p / R,$$

where d is transverse dimension of discontinuity, p_{static} – static pressure of the flow, gas density ρ in discontinuity $\rho = \alpha \cdot \rho_0$ ($\alpha < 1$). Therefore, expression for efficiency is given by

$$\eta = M_0^2 \cdot (D/d) \cdot R / c_p \cdot |\Delta I| / (1 - \alpha).$$

Thus, the aim of our investigation was to eliminate and systemize the fundamental regularities of non-stationary interaction of gas dynamic discontinuity with AD body in supersonic flow under different energy injection regimes, dimensions of energy dissipation domain and their position, Mach number, etc. Two-dimensional plane geometry was chosen both for its simplicity and all characteristic features being seen especially distinct. Therefore, the present investigation should be treated as more qualitative one, reflecting general peculiarities of actual situation under consideration.

6.2.2. Numeric procedure

The modeling approach is based on numerical analysis of the Euler equations for inviscid gas flow:

$$\frac{\partial \bar{U}}{\partial t} + \frac{\partial \bar{F}}{\partial x} + \frac{\partial \bar{G}}{\partial y} = 0$$

$$\bar{U} = \begin{pmatrix} \rho \\ \rho u \\ \rho v \\ E_S \end{pmatrix}, \bar{F} = \begin{pmatrix} \rho u \\ p + \rho u^2 \\ \rho uv \\ u(E_S + p) \end{pmatrix}, \bar{G} = \begin{pmatrix} \rho v \\ \rho uv \\ p + \rho v^2 \\ v(E_S + p) \end{pmatrix},$$

ρ , p , u and v are the density, pressure, and the x - and y - components of the gas velocity, $E_S = \rho(\epsilon + 0.5(u^2 + v^2))$, ϵ is the specific internal energy; and the ratio of specific heats $\gamma = 1.4$.

A second order of accuracy conservative difference scheme on the minimal stencil was applied in the computations. The scheme is based on the method for constructing difference schemes with arbitrary order of approximation [2] and appears to be the two-dimensional difference analogue of the method [3] for orthogonal grids. The grid is orthogonal the stencil having only four grid points on the previous time layer. The spatial grid steps were equal to 0.005 and the largest grid contained 800×600 points.

The streamlined body was a rectangular in a supersonic flow with typical Mach number equal to 1.9. Energy injection was assumed to occur in a rectangular spatial area, the latter was symmetrical in respect to the flow central axis. Two limiting types of the energy injection areas were under consideration: a rectangle placed “along” the flow and another one – disposed “across” it. The density in the area of discontinuity was supposed to be constant and equal to $\rho = \alpha \cdot \rho_0$ ($\alpha < 1$), the static pressure and velocity be equal to those of the initial flow. Thus, interaction of a density well with AD-body was modeled. The effects of gas dynamic disturbances, which take place during fast energy deposition in a gas, were also investigated, but variation of position was not wide at this stage of investigation.

6.2.3. Description of interaction mechanism

In almost all cases the *vortex* is being generated inside the perturbed area between the bow shock wave and the body. It is well seen at Fig.6.1a, where Schlieren-like set of images is presented. This phenomenon is accompanied by the temporary increase of the bow shock wave standoff. It can be seen that this increase is greater for the case of the longitudinal energy area shape and the maximum increase corresponds to the greatest length of the energy deposition area. The vortex flow moves to the right boundary and leaves the area of calculation. At the same time the second, weaker shock wave is shown to arise between the body and the bow shock wave, later on it is catching up with the first one. At this time the bow shock wave returns to its previous position and the second shock wave has practically no effect upon the position.

In the case of energy injection area across the flow the standoff increase is considerably less but the shock front deformation takes place on the greater part of the front.

These pictures are in qualitative agreement with Schlieren images, obtained in experiment.

6.2.4. Principle features of interaction

The following distinctive features can characterize non-stationary interaction of thermal discontinuity with a blunt body (blunt-nosed “cylinder”) in SS airflow.

Pressure evolution at stagnation point can be conditionally divided in four stages (Fig.6.1b):

- arrival of shock and/or rarefaction wave
- phase of relatively constant pressure (vortex formation in front of body surface)
- interaction with vortex
- post -vortex relaxation (temperature rise at stagnation point).

Pressure evolution at the *first* stage depends upon the regime of energy input in discontinuity and includes the pressure splash-downfall in the case of adiabatic regime and pressure downfall in the case of quasi-static regime (Fig.6.2). The *second* stage is characterized by approximately constant reduction of stagnation pressure this reduction being the more pronounced, the wider discontinuity is. This time interval corresponds to vortex formation in a shock layer and is directly proportional to the length of discontinuity. The *third* stage is interaction with a vortex drifting towards the model. If the length of discontinuity is not too large (about model “diameter” or less), the splash of pressure may precede the vortex-body interaction phase oncoming. This effect takes place due to the return back of the wave that falls at the body surface (stage 1), reflects from it and then reflects from the boundary of cold gas – back front of discontinuity, which comes by that time to the BSW position. In the case of long discontinuity this peak is not distinguished, as a reflection from the hot region is not effective. The *last* stage, which is characterized by increasing of stagnation pressure over its unperturbed value, corresponds to relaxation of gas dynamic parameters to normal values. This is the only stage where gas temperature is higher, than stagnation temperature for unperturbed flow. *The most effective is the phase of vortex interaction with the front surface of a model.*

The vortex is forming during thermal discontinuity absorption by the shock layer and starts its movement towards the model after the back fronts of discontinuity and vortex coincidence. Vortex appearance demands satisfying some conditions for the length and width of discontinuity and density inside it. Vortex intensity increases with diminishing of transverse dimension of discontinuity.

Diminishing of transverse dimension of discontinuity leads to noticeable increase of interaction efficiency ($\eta \sim r^{-1}$) even under the same gas temperature of discontinuity (i.e. under the total energy input decrease). *The value of the effect remains practically the same, it even slightly increases with decrease of transversal dimension* (Fig.6.3, 6.6) in the area of parameters considered. Increase of longitudinal dimension (length) of discontinuity does not affect efficiency (it remains constant in the area of parameters considered), but leads to the more pronounced decrease of mean pressure reduction.

On the contrary, diminishing of longitudinal length and increasing of the transverse one leads to the sufficient fall down of the value of the effect. This fact is illustrated in Fig.6.4, where also the effect from two transverse wells is presented. The first curve corresponds to a single well (length one forth of model diameter, width – diameter). The second corresponds to two wells of half diameter length and one and a half width at a distance between them equal to model diameter. Density inside well is twice less than in the undisturbed medium.

From the viewpoint of efficiency, quasi-static energy deposition (i.e. under a constant pressure in discontinuity, which is equal to that in a medium) is more efficient than explosive (i.e. fast heating under a constant density) one (Fig.6.2). For the adiabatic regime of energy input the distance of the domain from the body also becomes an influential parameter. Efficiency dramatically increases with Mach-number increase.

It should be noted that temperature evolution curve for stagnation point repeats in general that for pressure or density, therefore, its mean value during interaction is *less* in comparison with steady one.

Symmetric off-line shift of each half of discontinuity at a distance equal its width leads to a qualitative change in stagnation pressure evolution (Fig.6.5). The pressure difference at third stage changes the sign and the overall effect, as well as interaction efficiency becomes equal to zero.

Thus, in non-stationary interaction of channel with blunt body, stagnation pressure fall consists of two portions. The first – it is also comes first in time – is due to rarefaction wave, arising from the contact of leading tip of discontinuity with BSW. The depth of this fall is governed by d/D parameter, where d is the diameter of discontinuity. The closer is this parameter to the unity, the more pronounced pressure fall is observed. In the case of $D=d$ we have situation of body streamlining by a uniform heated region. No vortex formation in a shock layer can be observed in this case. Obviously, this regime does not lead to any gas dynamic structure

transformation and is not effective. Under the diminishing d over D ratio the impact of the first mechanism goes down and the role of vortex formation mechanism grows up. This is reflected by the second - more pronounced and vast region of pressure fall in stagnation pressure dynamics. The structure of a flow exerts a significant change - bifurcation. This is the most effective mechanism of drag reduction.

6.2.5. Scaling

Most of the cited above conclusions are the consequence of ΔI -function behavior. This function turned out to be independent or weakly dependent of 3 from 4 of the incoming parameters – L , d and M_0 . For $\alpha=0.5$ variation of these parameters in a wide range led to $|\Delta I|$ change in an interval 0.43 – 0.50. The unique parameter of influence is α - the relative density in the well. Thus, the efficiency of density well effect for drag reduction in the area of parameters considered is

$$\eta \approx M_0^2 \cdot (D/d) \cdot R/c_p \cdot |\Delta I(\alpha)| / (1 - \alpha).$$

$|\Delta I|$ is a monotonous function of density in the well. The depth in stagnation pressure evolution depends only on this parameter.

High efficiency of interaction can be explained by the fact that vortex formation consumes energy of a flow and less of this energy is dissipated as a heat. In another words, streamlining by a structured flow is more regular motion than non-structured one. Cooling of the region around stagnation point during interaction phase confirms this.

It is surprising, but formula (1) in its complete form,

$$\eta = 0.2 \cdot c_x \cdot M_0^2 \cdot S/S_h,$$

describes the efficiency value (with a satisfactory precision!) even for $S_h \ll S$, where generally speaking it is not valid.

Further investigation will be aimed at quantifying of the local parameters of discontinuity by fitting of the calculated pictures to experimental ones in an actual cylindrical geometry. More careful investigation of “instant” energy deposition leading to shock waves origination from the discharge region and optimizing of discharge channel position in respect to AD-body will be also provided.

6.2.6. Asymmetric disturbances

It is important to estimate the sensitivity of effect scale to breaking of symmetry, i.e. off-line shift of a disturbance. This is rather common situation for experimental conditions, as it is difficult to realize exactly symmetric geometry.

Thermal disturbance off-line shift inserts visible changes in the third and forth phases of its interaction with AD body. The stagnation pressure drop become less and less pronounced, as the pressure splash at the back front of disturbance grow up. After reaching its maximum, the amplitude of overpressure goes down. When the disturbance is shifted far from symmetry axis, it exerts no effect on the body streamlining. The described effects are illustrated by Fig.6.7.

As for drag force behavior, shifting of the centerline of disturbance from the symmetry axis of the body (and flow) at a distance of about half “radius” of AD body leads to vanishing of the integral drag force.

It is natural that along with diminishing of the drag, discontinuity displacement leads to integral lift force arising, as exactly compensating each other pressure distributions on the upper and lower planes now become different. For this problem treatment we considered supersonic streamlining of a rectangular body. First the *symmetrical* problem was under investigation, i.e. the area of energy deposition was assumed to be symmetrical versus the central axis of the flow (Fig.6.8). As it was already discussed above, arising vortex structure causes decrease of the pressure in the stagnation point to the value of 30%, the same value having the drag reduction of the body. Besides, flow transformation effects on the areas near the lateral sides of the body (Fig.6.8c, 1d). The value of the back pressure is sufficiently smaller than that on the front surface of the body and is close to 0.02-0.03 of stagnation pressure.

Then the effect of *non-symmetrical* situation of the energy deposition area versus the body was considered. This influence was found to be maximal when the heat channel “lies” on the axis of symmetry of the body. The flow dynamics for this case at the same time moments as in the Fig.6.8 is presented in the Fig.6.9. It is well seen the considerable difference between the arising vortices. It causes asymmetrical deformation of the bow shock wave front (Fig.6.9 2b, 2c). The vortex structure effects differently on the lateral surfaces too. Calculations showed the difference between maximal values of the drag forces on the lateral surfaces to be close to 6% from their value for symmetrical case (Fig.6.10). This effect represents several stages during the disturbed flow domains convecting downstream, changing the sign of the instant resultant force (Fig.6.10).

But the integral (over time) force is non-zero and smoothly varies under the displacement of the discontinuity position, attaining maximum when the disturbance is shifted at its own “radius”. The lift force arises under the zero angle of attack.

Thus, existence of the longitudinal heat channel inside the supersonic flow considerably changes the whole picture of the flow. The arising vortex structures decrease the drag force and effect on the drag forces of the lateral surfaces of the body. In the case of non-symmetrical situation of the energy deposition area versus the body it is possible to change considerably the lift force acting on the body.

6.2.7. Velocity of SW detachment and comparison with experiment

Velocity of the SW movement upstream the flow is essential parameter, which characterizes the density-drop in discontinuity. Investigations have revealed several important features of this movement:

- The upstream movement takes place under the constant velocity practically by the moment of attaining the maximum stand-off position or meeting the end (back-front) of the discontinuity for $L < L_*$
- The velocity depends mainly upon the density drop in the well and in less extent on the Mach number
- The movement can be characterized as being self-similar. It means that the velocity, shape and other parameters do not depend upon initial conditions and the transverse dimension of discontinuity
- Detachment of the SW is a threshold phenomenon, it occurs when the density in discontinuity falls below some critical value (for $\gamma=1.4$ this value is equal to 0.67 [4])

The last statement is a consequence of detachment criterion. The dependence of detachment velocity on the dimensionless density in the well both for the plane and cylindrical geometry (the last is taken from [4]) is presented at Fig.6.11. Under the same conditions the velocity in plane geometry is higher than in cylindrical one.

The values of dimensionless velocity of the BSW detachment were obtained in experiment and turned out to be about 0.5. Comparison with curves calculated numerically immediately leads to the conclusion that the density drop in a channel should be from 7 to 10 times in carbon dioxide and more than 10 times in air. It means that gas temperature in MW discharge channel in CO₂

varies from $1500K$ to $2000K$, whereas in air it even exceeds $2000K$. At any case it is dramatically far from that obtained from registered optic spectra (second positive Nitrogen system), where temperature turned out to be about $300K$. Evidence at existing of fine hot filament inside relatively bulk volume of channel delivers our data, based on registering of nitrogen positive ion spectrum. Treatment of discharge spectra from nitrogen flow revealed that rotational temperature of nitrogen ion is sufficiently higher than that of neutrals. This result is also confirmed by discharge kinetics modeling (see Sections 3 and 4).

6.2.8. Bifurcation – self-organization – effectiveness

The problem under consideration is an excellent example of bifurcation in a complex system. Small disturbance in initial conditions leads to dramatic changes in resultant flow-field. Primarily gradient potential streamlining of a blunt body completely changes its structure becoming vortical and taking shape of an edge or cone in dependence of geometry. Thus, processes of self-organization make the effective shape of the streamlined region as better adopted to the conditions of supersonic flow, dramatically reducing the drag. If the relative density in the well is ρ ($\rho < 1$), the drag force diminishes as ρ^{-1} independently of the transverse dimension of the well. Thus, in neglecting of dissipative processes, the local efficiency of such interference can be made as high as desired.

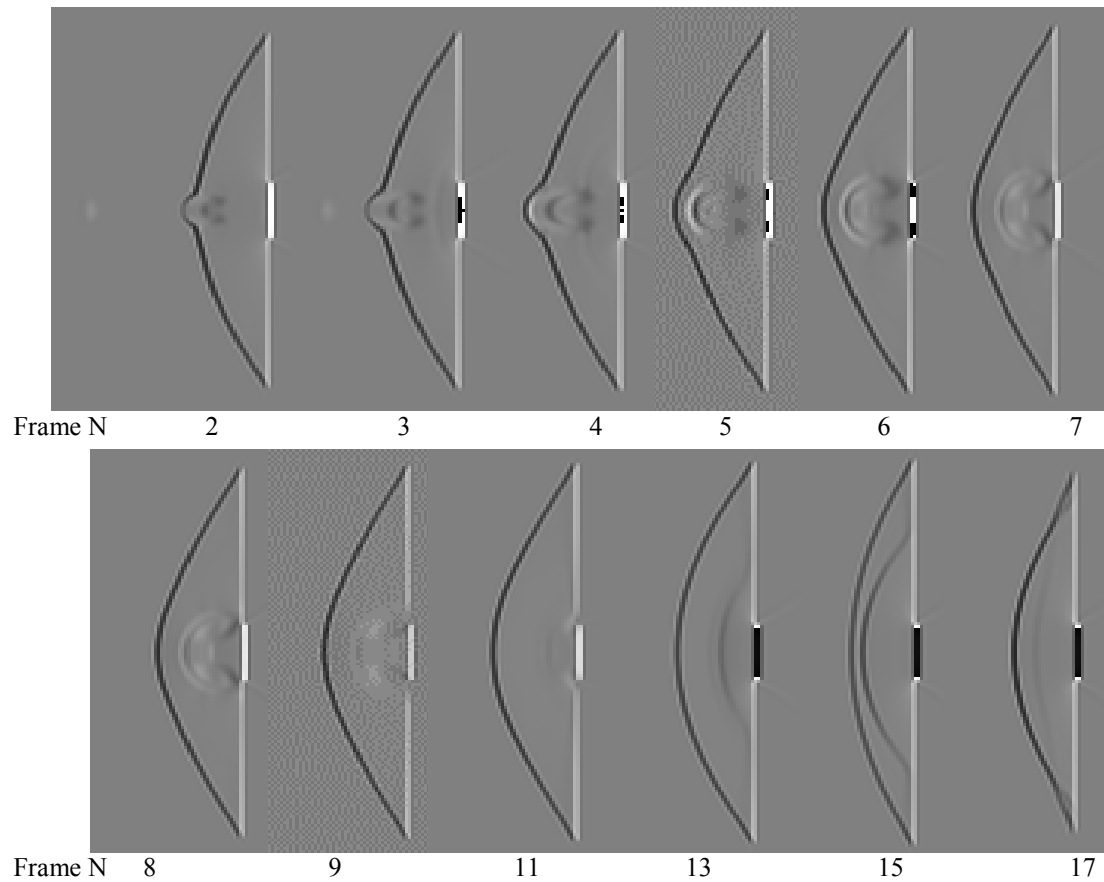


Fig.6.1a. Schlieren-like images of density well interaction with body in SS flow ($M=1.9$, $L=3D$)

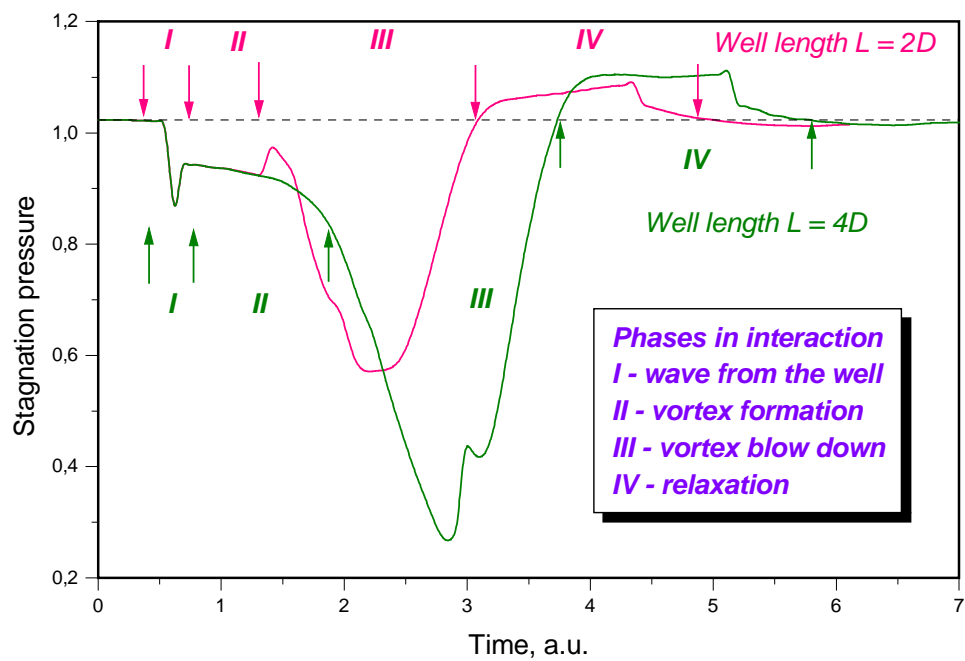


Fig.6.1b. Stages of interaction: I – frames 1,2; II – 2-4; III – 4-11; IV – 12 –18

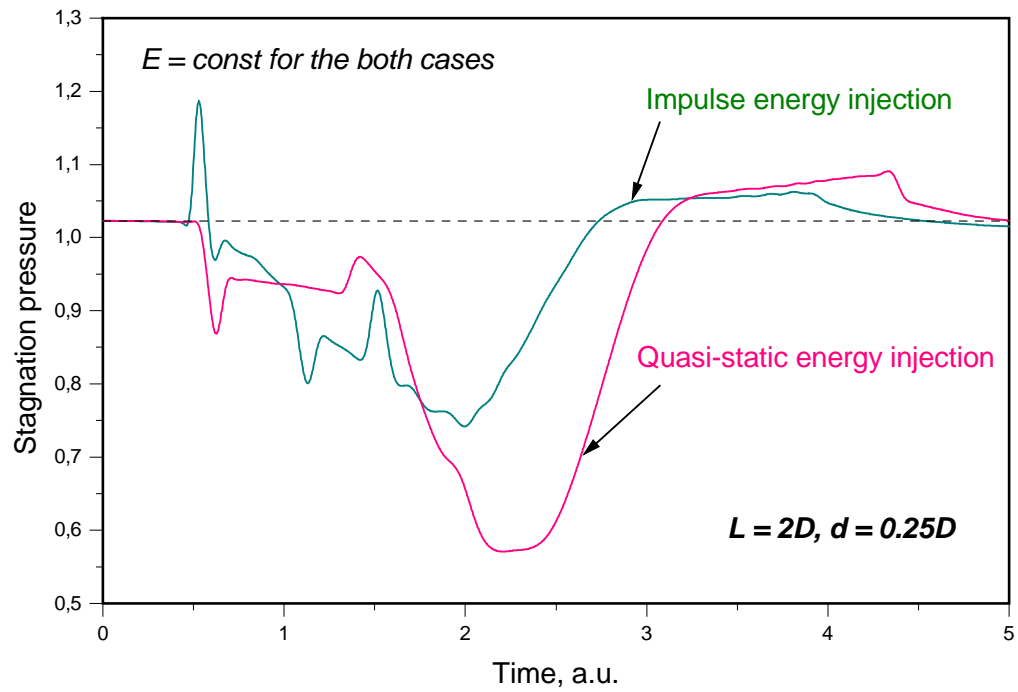


Fig.6.2. Evolution of stagnation pressure for quasi-static and impulse energy deposition. Total injected energy is the same for both cases. Discontinuity with length equal to two model diameters and width to one fourth of model diameter is placed in front of the BSW

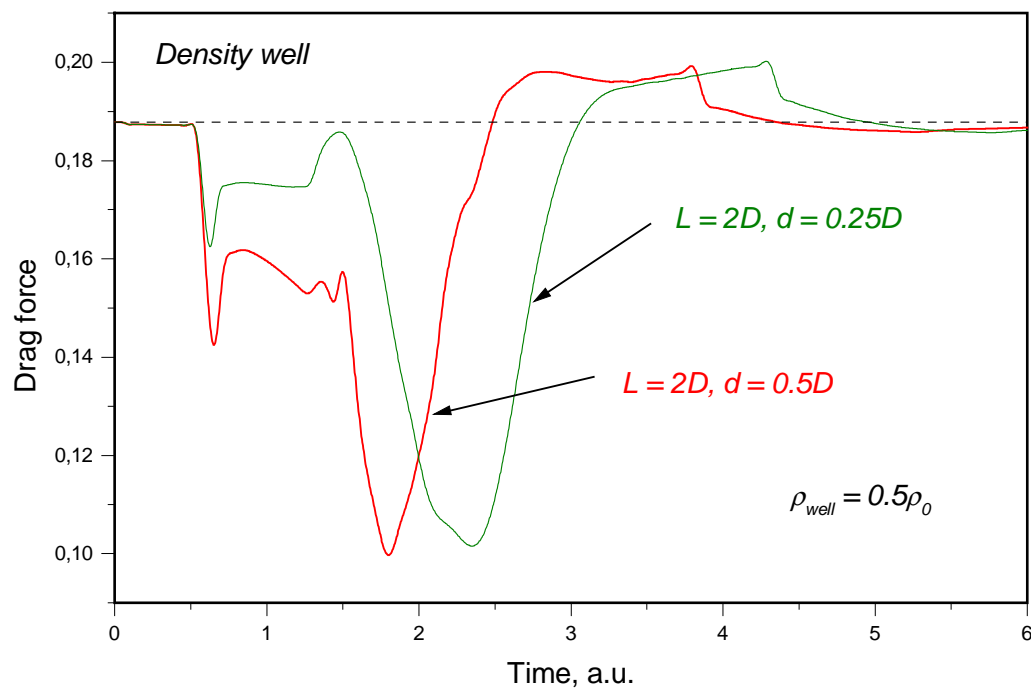


Fig.6.3. Evolution of stagnation pressure for density wells with equal length, but different width

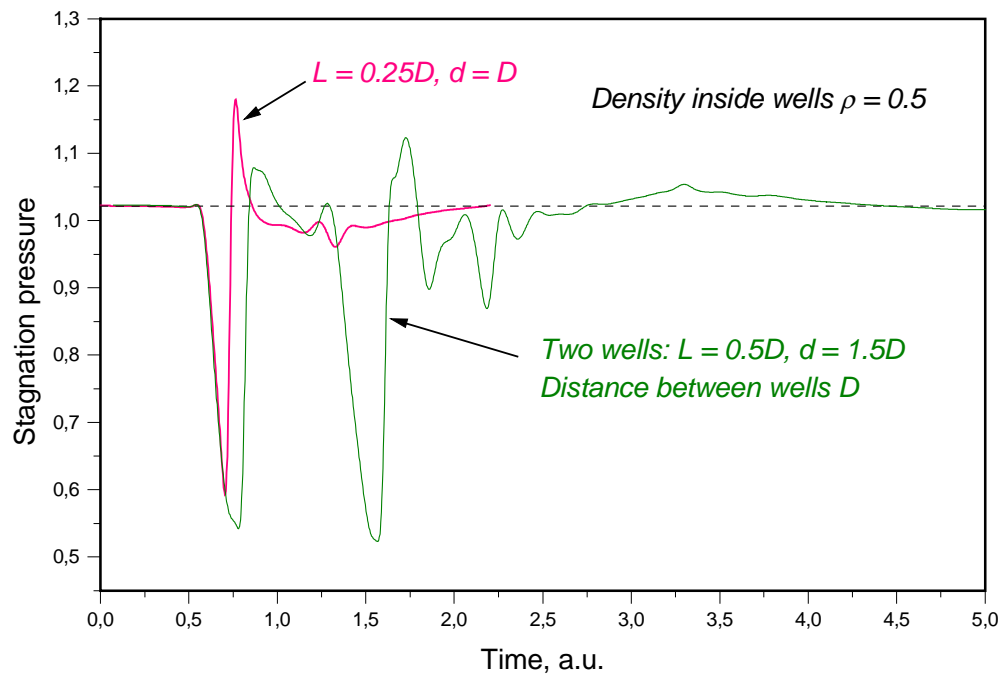


Fig.6.4. Evolution of stagnation pressure for transversely elongated wells.

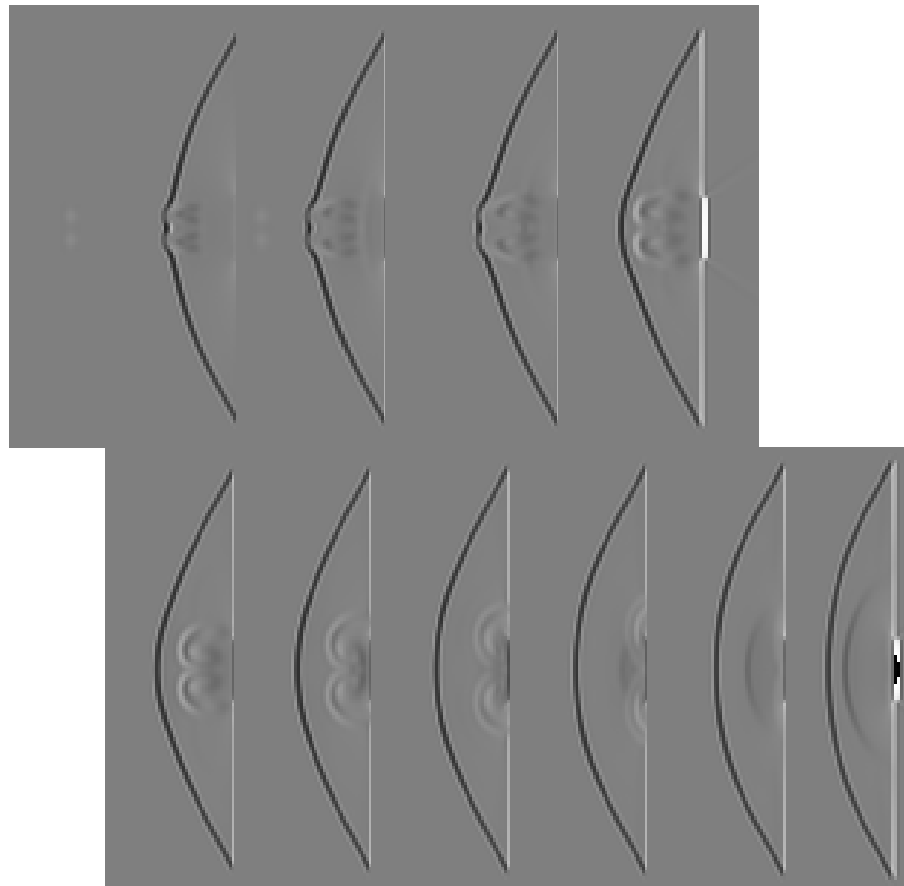


Fig.6.5. Schlieren-like images for two symmetric wells interaction with body

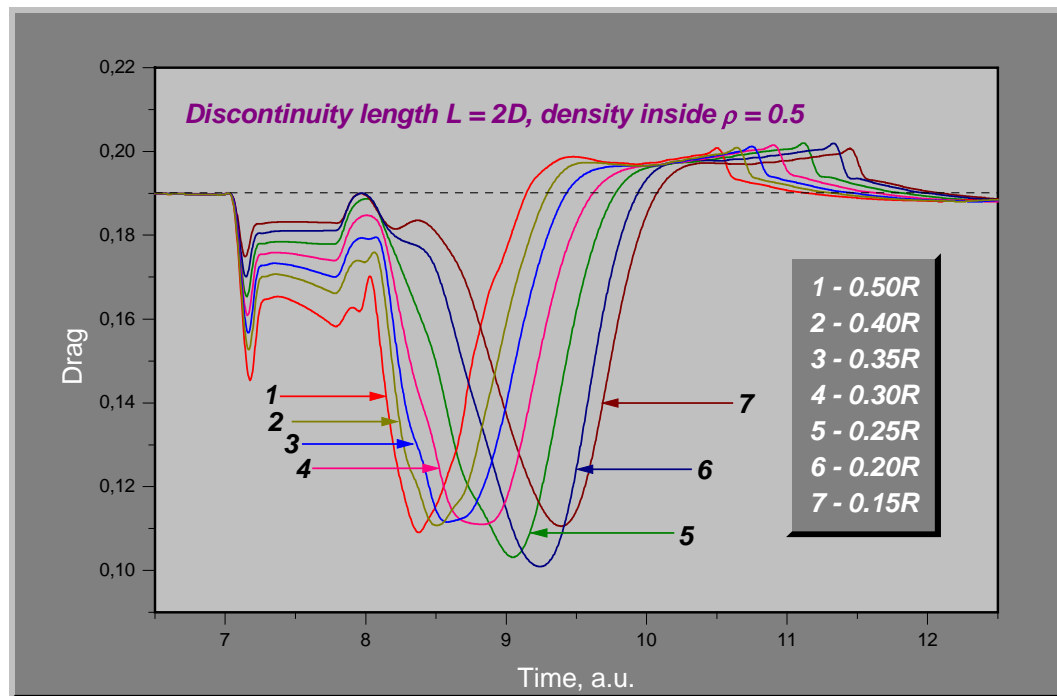


Fig.6.6. Influence of the transverse dimension of disturbance on drag evolution

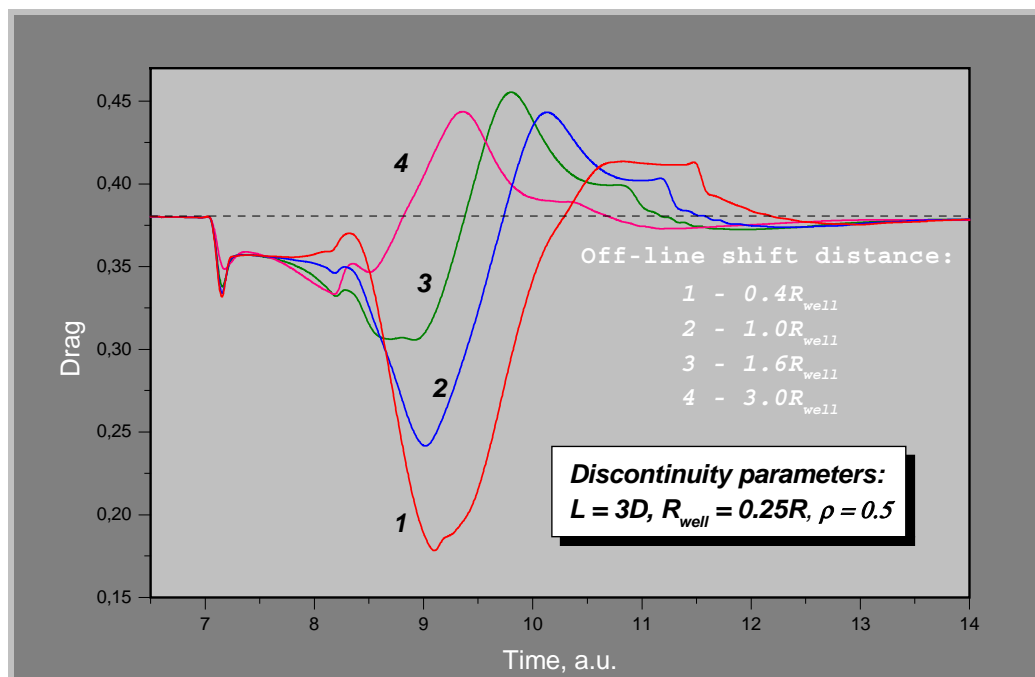
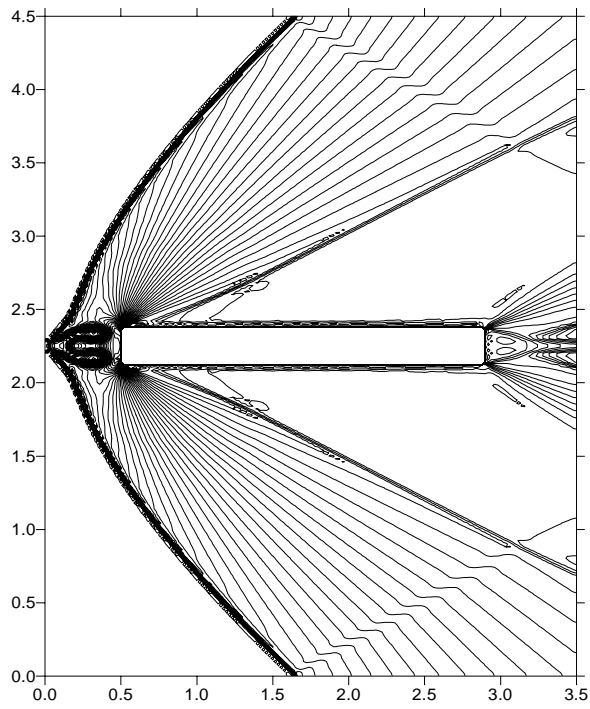
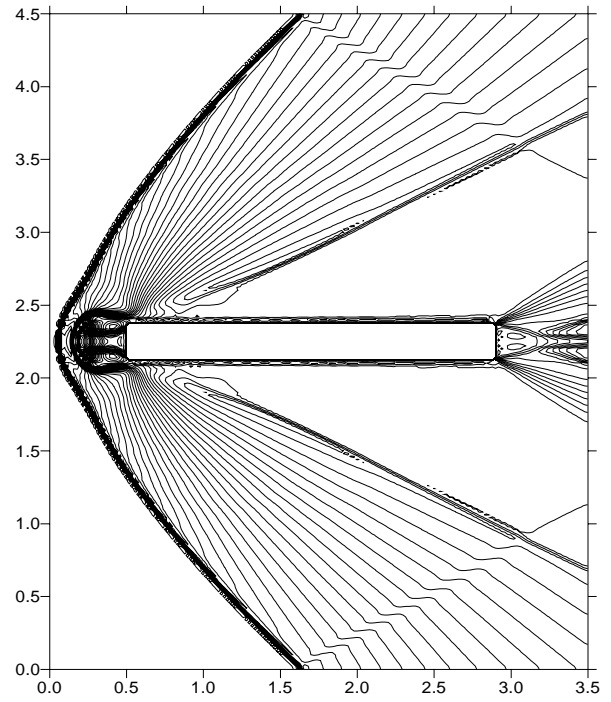


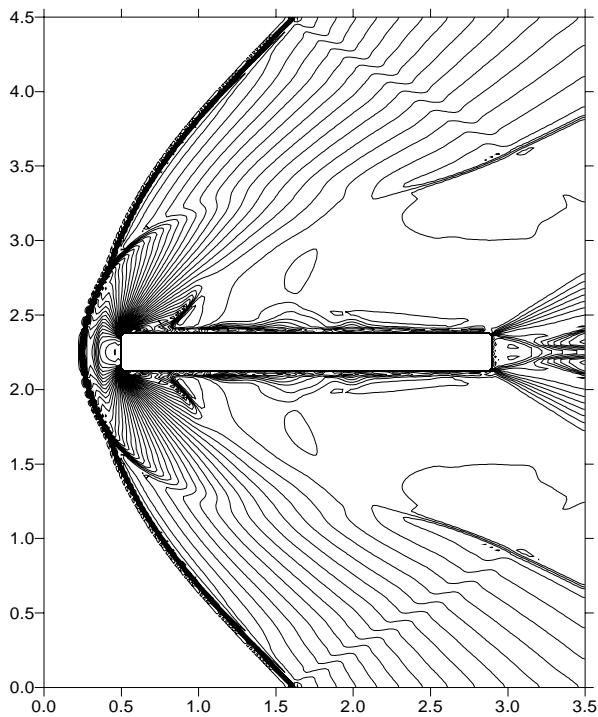
Fig.6.7. Asymmetric discontinuity disposition and its effect on drag



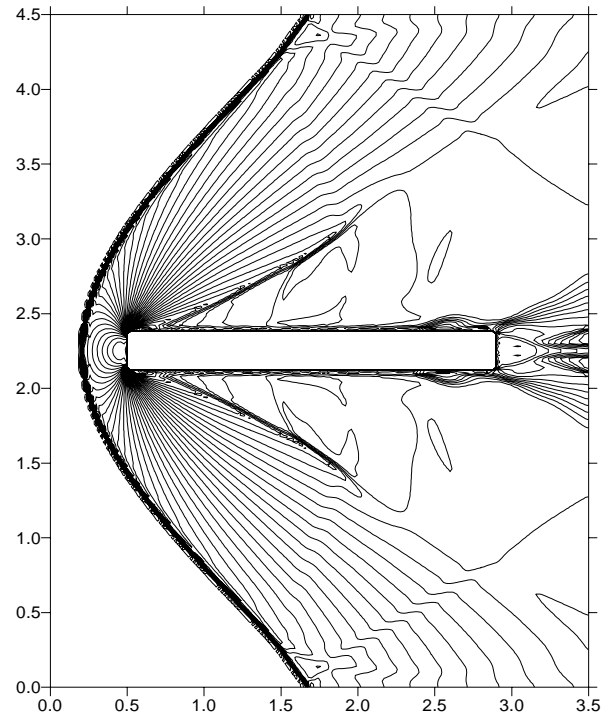
a)



b)



c)



d)

Fig.6.8. Symmetrical disposition of the heat channel versus the body.

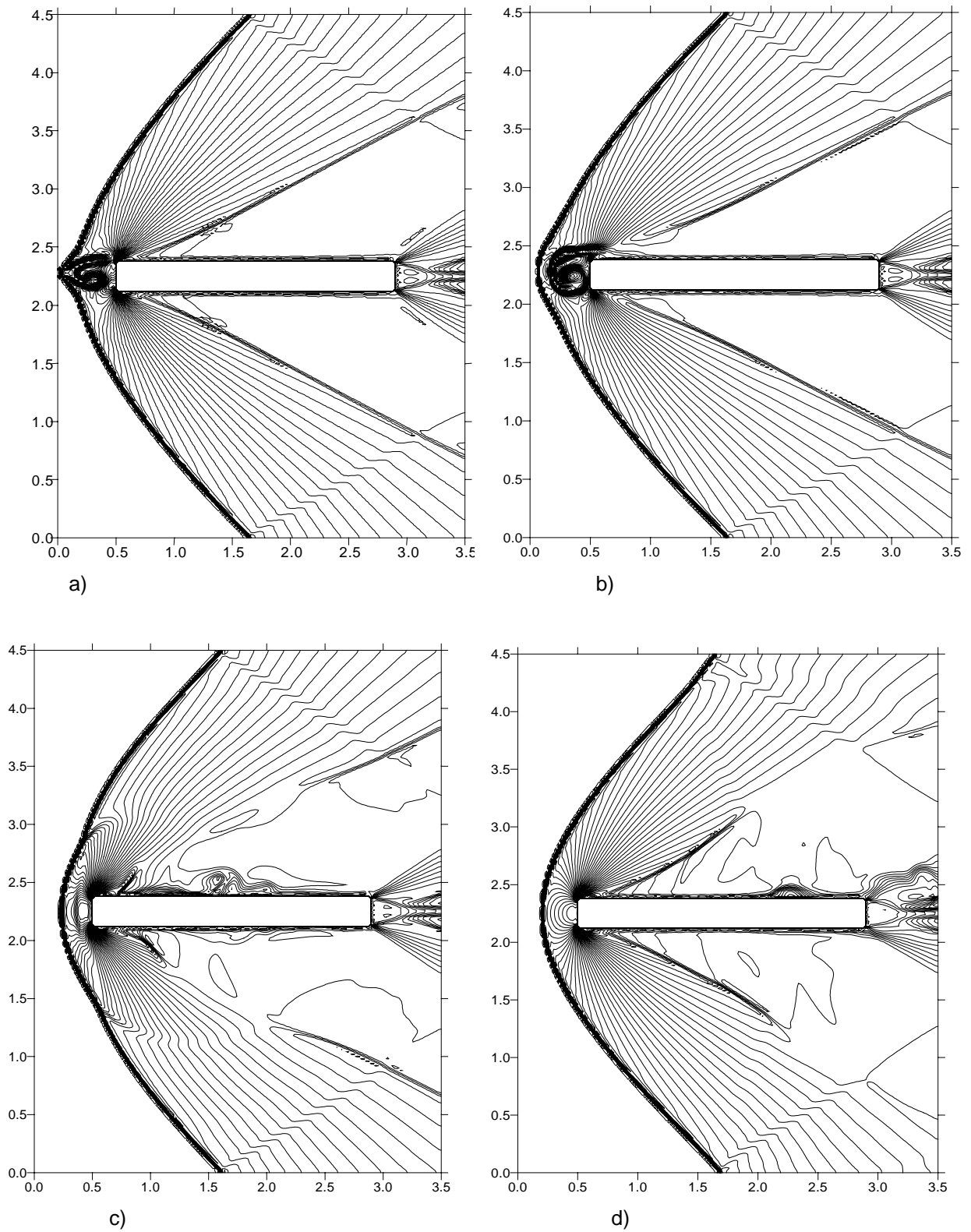


Fig.6.9. Non-symmetrical disposition of the heat channel versus the body.

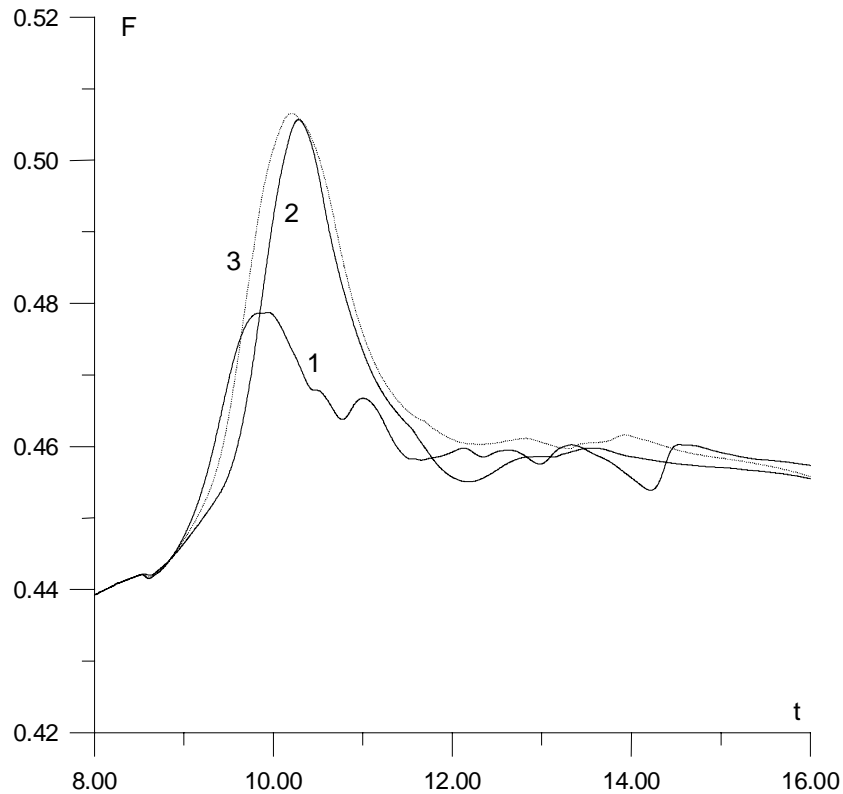


Fig.6.10. Dynamics of the forces on the lateral surfaces of the body for non-symmetrical case (curve1 - the force on the upper surface, curve2 - the force on the lower surface) and for symmetrical case (curve 3).

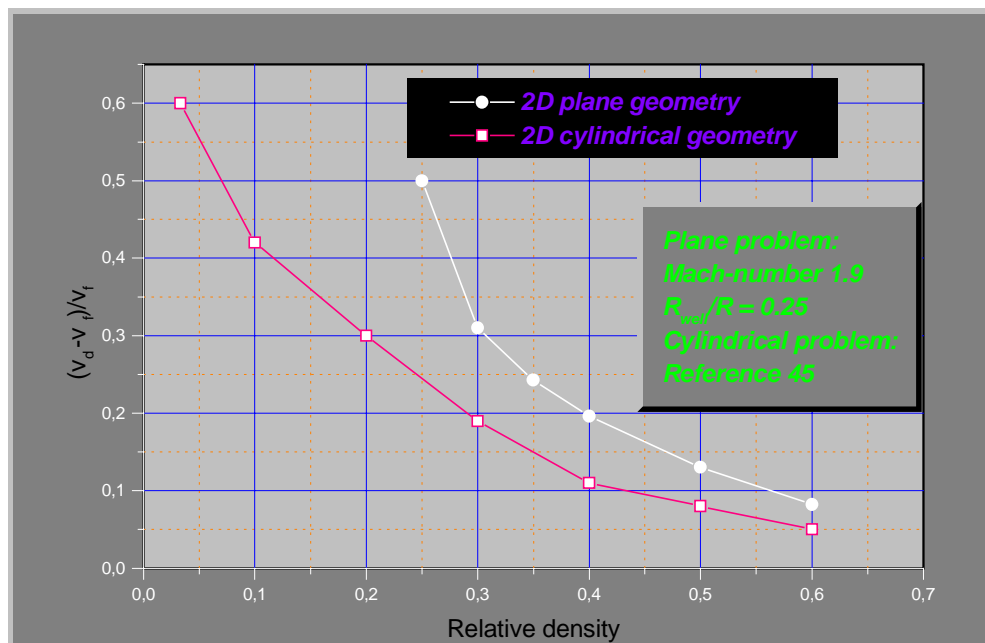


Fig.6.11. Normalized velocity of BSW detachment vs density in discontinuity

6.3. Modeling of non-stationary interaction of cone-shaped bodies with discontinuity

The problem under consideration is the influence of MW release on non-stationary streamlining of bodies with conic ledges. Numerical modeling is based on the Euler equations for ideal gas:

$$\frac{\partial \bar{U}}{\partial t} + \frac{\partial \bar{F}}{\partial x} + \frac{\partial \bar{G}}{\partial y} = 0$$

$$\bar{U} = \begin{pmatrix} \rho \\ \rho u \\ \rho v \\ E_S \end{pmatrix}, \bar{F} = \begin{pmatrix} \rho u \\ p + \rho u^2 \\ \rho uv \\ u(E_S + p) \end{pmatrix}, \bar{G} = \begin{pmatrix} \rho v \\ \rho uv \\ p + \rho v^2 \\ v(E_S + p) \end{pmatrix},$$

ρ , p , u and v are the density, pressure, and the x - and y - velocity components of the gas, $E_S = \rho(\epsilon + 0.5(u^2 + v^2))$, ϵ is specific internal energy, and the ratio of specific heats $\gamma = 1.4$. At the initial time moment and on the entrance boundary the flow parameters were defined as $\rho_0 = 1$, $p_0 = 0.2$, $u_0 = 1$ and $v_0 = 0$. As the units of measure the value of air density in the normal conditions $\rho_H = 1.29 \text{ kg/m}^3$ and the pressure value $p_H = 5 \text{ atm}$ were used. If the unit of length measure is $l_H = 10^{-2} \text{ m}$ the time and velocity units of measure are, respectively, $t_H = 5 \times 10^{-5} \text{ s}$ and $u_H = 1.98 \times 10^2 \text{ m/s}$. The original numerical method based on the second approximation order conservative difference scheme on a minimal stencil was employed in the computations [2].

6.3.1. Qualitative results

1.1. Non-stationary streamlining with detached bow shock wave

We consider the cases of bodies geometry presented in Fig.6.12. For the case I $\text{tg}\beta = \infty$ (rectangular body); for the case II $\text{tg}\beta = 1$; for the case III $\text{tg}\beta = 0.5$; for the case IV $\text{tg}\beta = 2$, β is the angle at the top of the conic ledge.

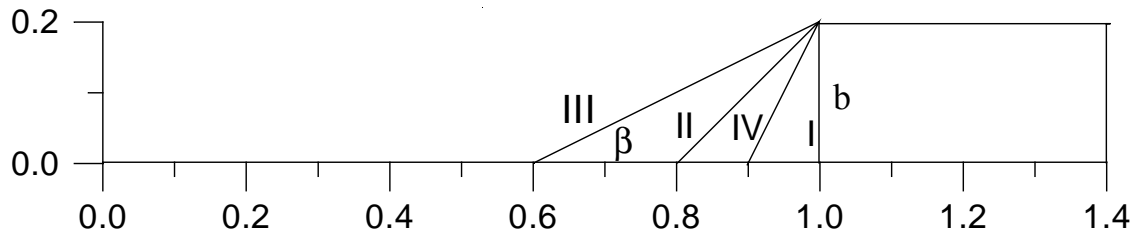


Fig.6.12. Considered bodies geometry.

Modeling the MW release was accomplished via formation an isobaric hot channel with the use of the boundary conditions for an incoming flow. From the time moment $t_i = 6.43$ when the

stationary regime has been already achieved the density on the boundary was supposed to be $\rho(0,y,t)=\rho_i=\alpha_p\rho_0$, $\alpha_p=0.4$ for $0\leq y\leq R_i$ and $t_i\leq t\leq t_i+\Delta t$, where R_i is the channel radius, $R_i=0.05$, $\Delta t=0.8$. The other parameters were applied to be equal to ones of an initial flow. These conditions generated the longitudinal rectangular heat channel with the width of R_i extending from the left boundary to the body. In the calculations the channel has been restricted on time by the value of $\Delta t=0.8$.

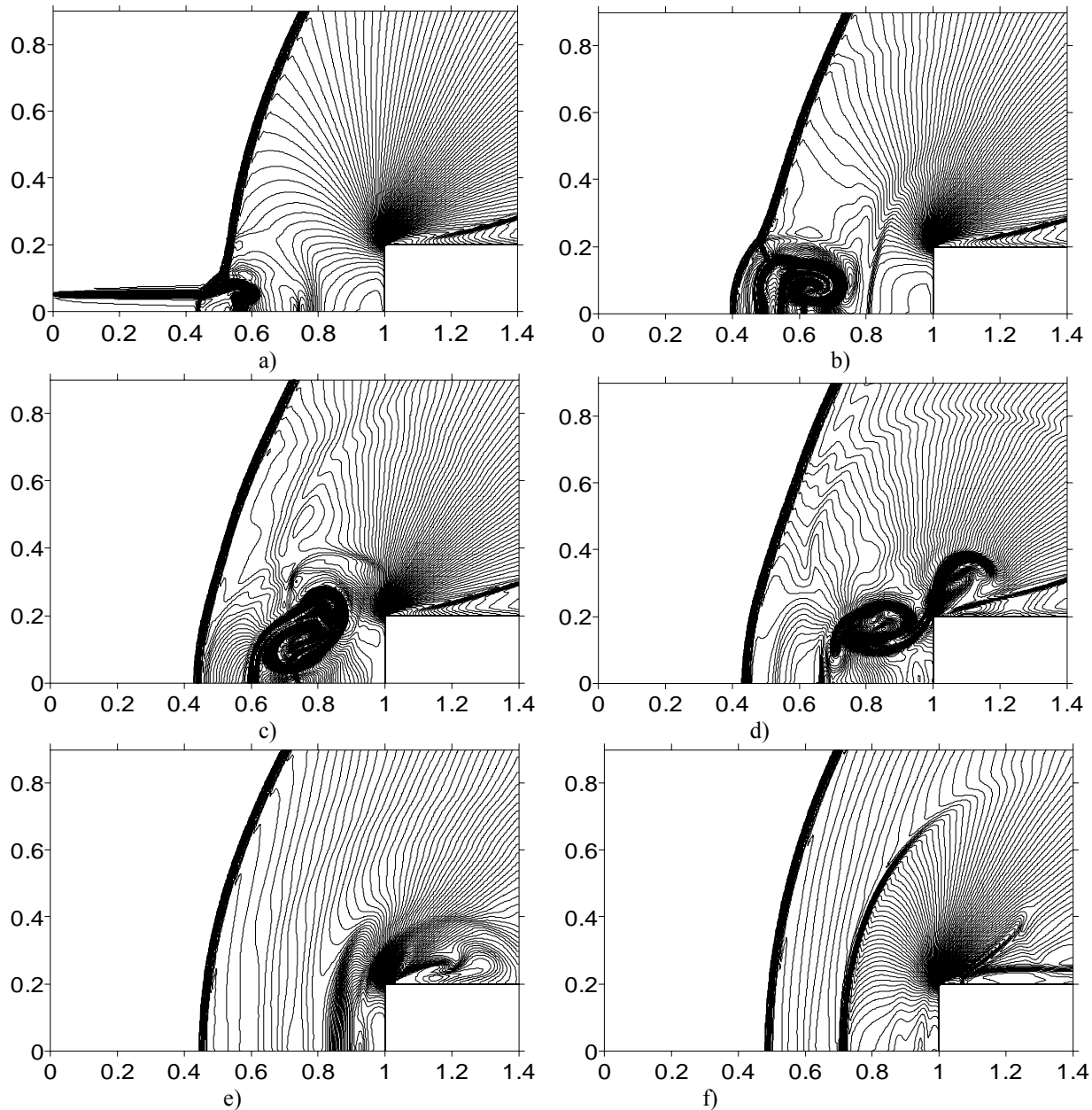


Fig.6.13. The effect of MW release on the non-stationary streamlining a rectangular body: a) $t=7.2$, b) $t=7.9$, c) $t=8.5$, d) $t=9.0$, e) $t=10.0$, f) $t=10.5$.

Density fields for different time moments for the case I are presented in Fig.6.13. As it has been shown in Section 6.2 the hot channel interacts with the stationary shock wave generating a vortex structure (Fig.6.13a). It is seen the vortex moving to the body (Fig.6.13.b, c). Later the vortex structure is divided near the upper corner of the body (Fig.6.13.d). After an interaction of the vortex with a rarefaction wave with a center in the body's corner a strong shock wave arises and moves to the bow wave (Fig.6.13d, e, f). In an area near the top surface of the body it is also seen a weak shock wave moving right after the vortex structure.

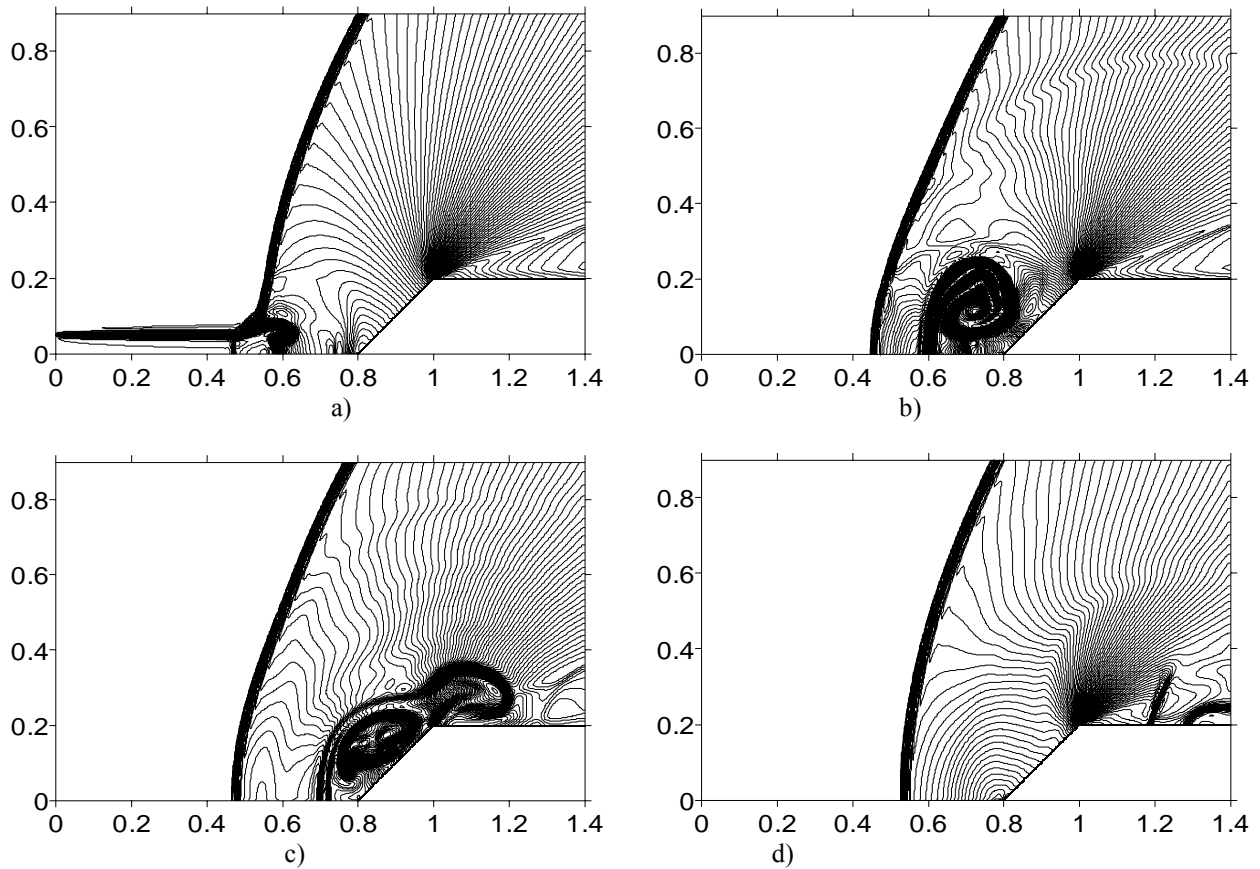


Fig.6.14. The effect of MW release on the non-stationary streamlining a body with a conic ledge for the case II ($\text{tg}\beta=1$): a) $t=7.2$, b) $t=8.3$, c) $t=8.9$, d) $t=10.0$.

Density fields for different time moments for the case II ($\text{tg}\beta=1$) are presented in Fig.6.14. It is seen that the effects are the same, but the reflected shock wave does not arise. Instead of it one can see an acoustic wave near the corner of the body (Fig.6.14d). Density fields for different time moments for the case III ($\text{tg}\beta=0.5$) are presented in Fig.6.15. It is seen that in this case the vortex structure isn't divided near the upper corner of the body (Fig.6.15c).

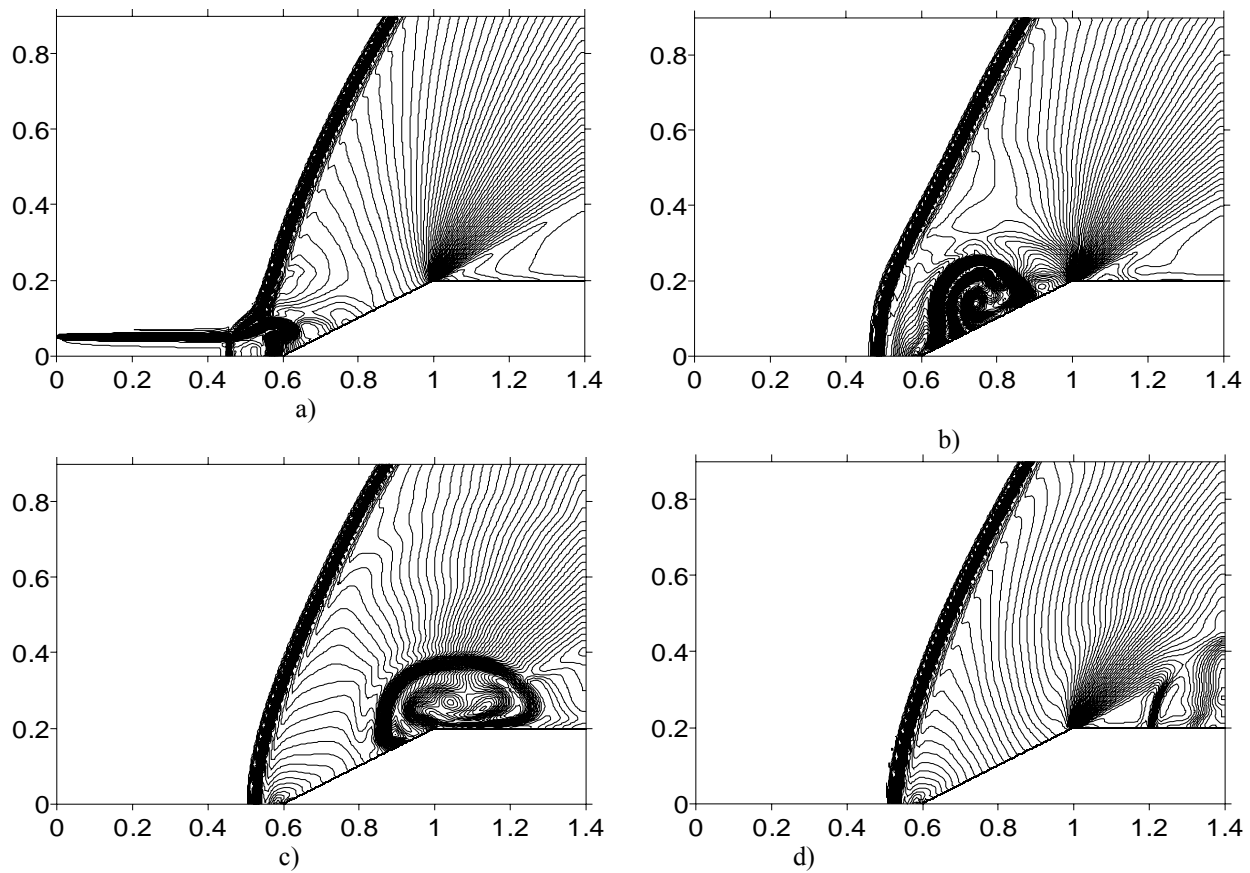


Fig.6.15. The effect of MW release on the non-stationary streamlining a body with a conic ledge for the case III ($\text{tg}\beta=0.5$): a) $t=7.2$, b) $t=8.2$, c) $t=8.8$, d) $t=9.4$.

6.3.2. Non-stationary streamlining with attached bow shock wave

Also we consider the body geometry with attached bow shock wave for the supersonic streamlining the body with $\text{tg}\beta=1/3$ (case V). The stages of the process in isochores are presented in Fig.6.16. Note that in this case the rectangular part of the body is situated from $x=0.9$ to $x=1.32$. It is seen that all effects of the MW release on the stationary streamlining can be observed in this case, too.

We can conclude that MW release qualitative effects on a supersonic flow past a body with a conic ledge are:

- generation of the vortex structure;
- motion of the bow shock wave and deformation of its front;
- splitting the vortex structure near the upper corner of the body (for $\text{tg}\beta \geq 1$);
- arising the additional shock waves with different mechanisms of generation;
- arising acoustic waves near the upper corner of the body.

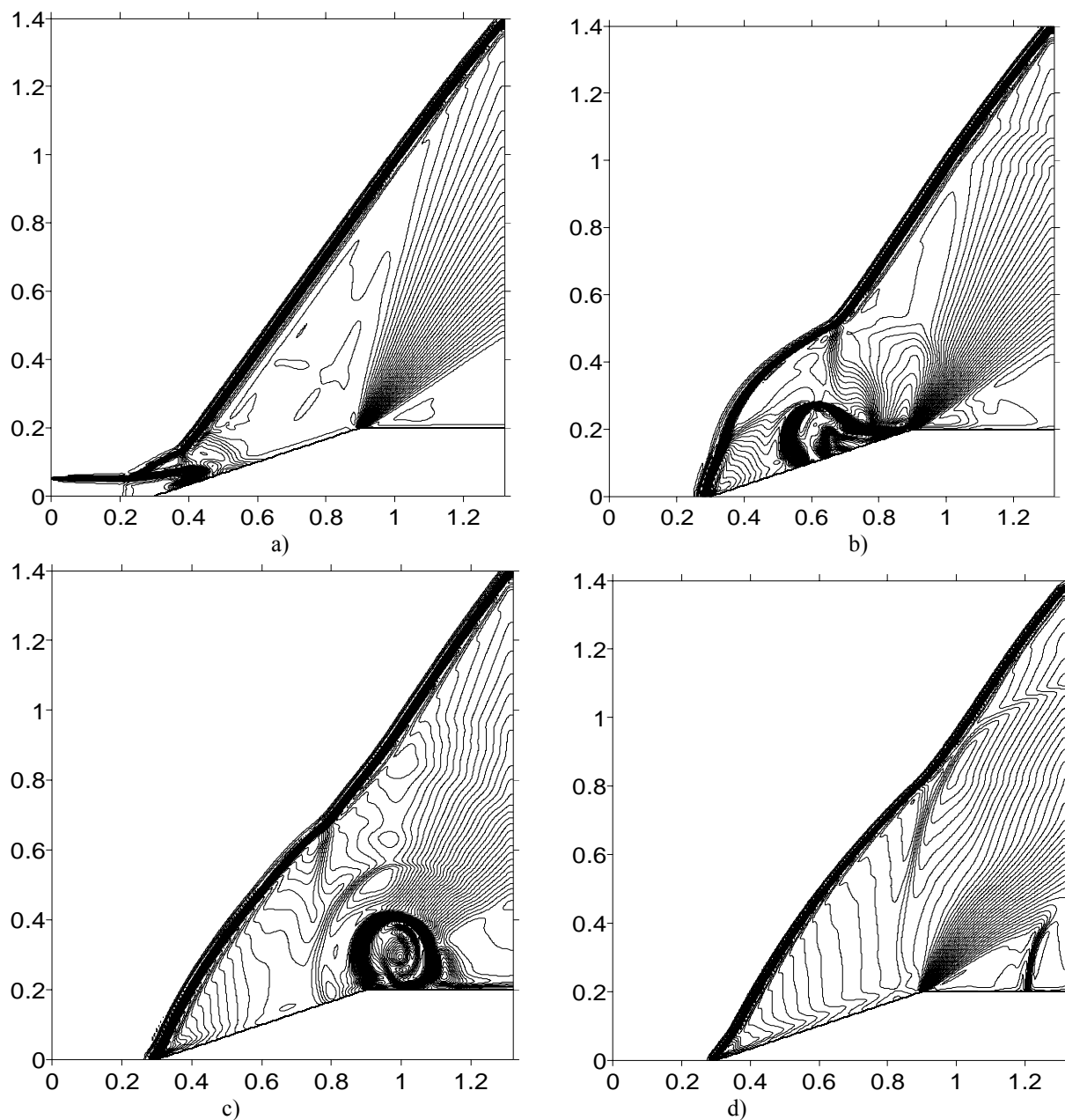


Fig.6.16. The effect of MW release on the non-stationary streamlining a body with a conic ledge for the case of attached bow shock wave ($\text{tg}\beta=1/3$): a) $t=6.9$, b) $t=8.0$, c) $t=8.5$, d) $t=9.2$.

6.3.3. Quantitative results

We consider the cases of bodies geometry described in section 1. For one of the quantitative criteria of the MW effect on the stationary streamlining bodies with conic ledge we use the drag force of the unit of length of the conic surface F :

$$F = \left(\int_0^l p dl \right) / l$$

Here l is the length of the wedge. Evolution of F in time for the considered cases of bodies geometry is presented in Fig.6.17.

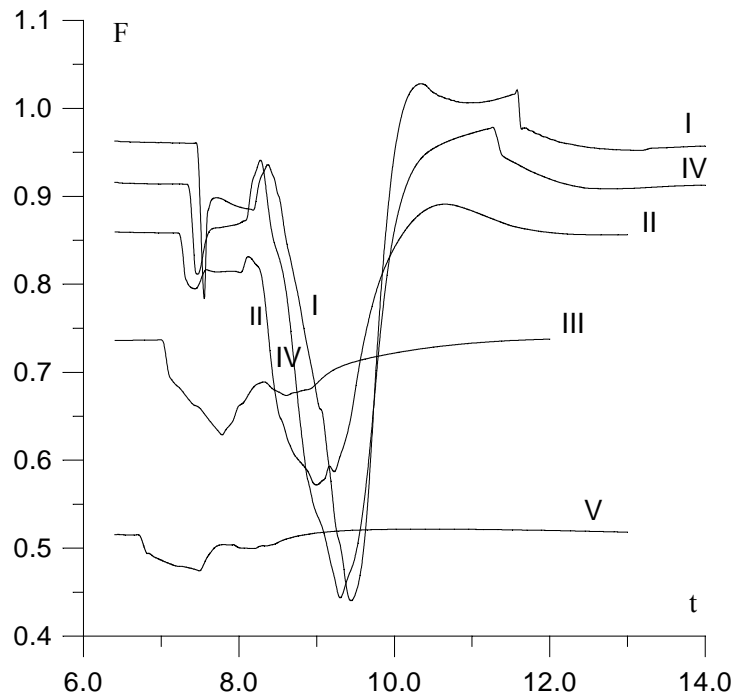


Fig.6.17. Evolution of drag force in time for the cases I – V, $\alpha_p=0.4$.

It is seen that the values of drag reduction for the case I (rectangular body) and for the case IV ($\text{tg}\beta=2$) are practically the same and are equal approximately 50% to initial values for stationary streamlining. We investigated the behavior of the value of a relative drag reduction $\delta=(F_{st}-F_{min})/F_{st}$ in the dependence upon $\sin\beta$ (Fig.6.18). Here F_{st} is the value of drag force for stationary streamlining.

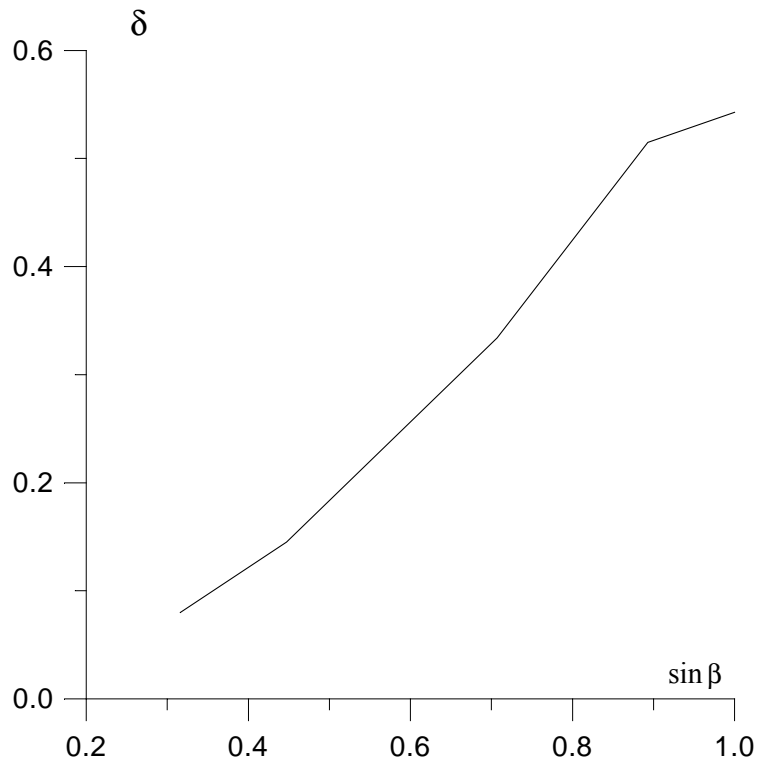


Fig.6.18. Dependence of the relative drag reduction δ upon the angle in the top of the ledge, $\alpha_p=0.4$.

It is seen that the dependence of the relative drag reduction δ upon $\sin \beta$ is close to linear. The drag reduction has the minimal value for the case V of attached bow shock wave ($\tan \beta = 1/3$). However it should be noted that the effects are stronger for the smaller values of α_p . Evolution of the drag force $F(t)$ in this case for different α_p is presented in Fig.6.19.

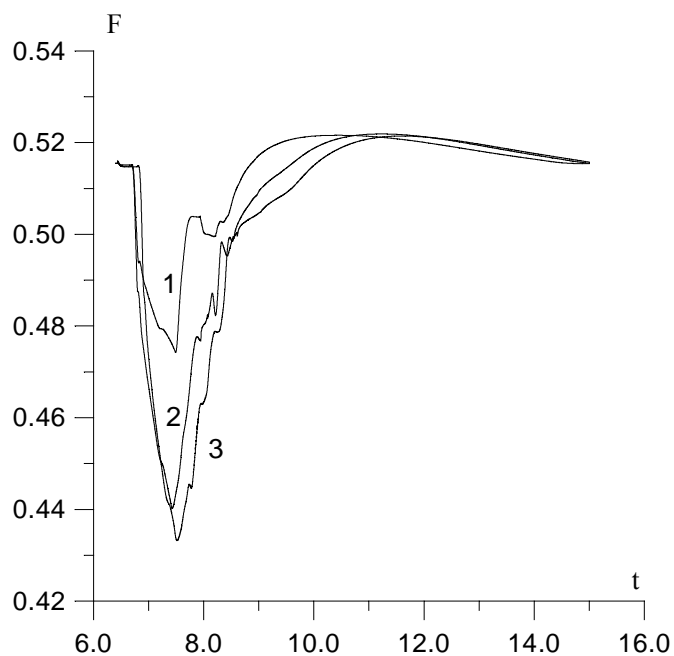


Fig.6.19. Behavior of $F(t)$ in the case V ($\tan \beta = 1/3$) for different α_p : *curve 1* - $\alpha_p=0.4$; *curve 2* - $\alpha_p=0.2$; *curve 3* - $\alpha_p=0.15$.

As a criterion of the vortex strength near the conic surface we use the value of circulation in a rectangular area restricted by the boundaries of calculation area and the straight-line b (see Fig.6.3.1):

$$C_b = \iint_S (v_x - u_y) ds$$

Evolution of the circulation C_b for the cases I – III and V is presented in Fig.6.20. Also we investigated the dynamics of the bow shock wave standoff (Fig.6.21). For the cases I – IV (detached bow shock wave) the rate of changing the standoff and the rate of changing the circulation C_b turned to be equal. As it is shown below in 6.5 the value of the rate is defined by the decision of the Riemann problem described the interaction of a shock wave and a contact discontinuity (a boundary of the heat channel). This rate is constant in time on the stage of drag reduction and it does not depend neither on the angle β nor on the radius of channel R_i . This conclusion is precise for the flat front of the shock wave. In the calculations we consider the shock front coordinate on the axe of symmetry where the shock front is close to flat. Thus the claim is valid with good accuracy for the cases I – IV. Note that in the case V (attached bow shock wave) these rates are constant in time, too. However, the values of the rates distinguish from the value defined by the Riemann problem because in this case the shock front is not flat.

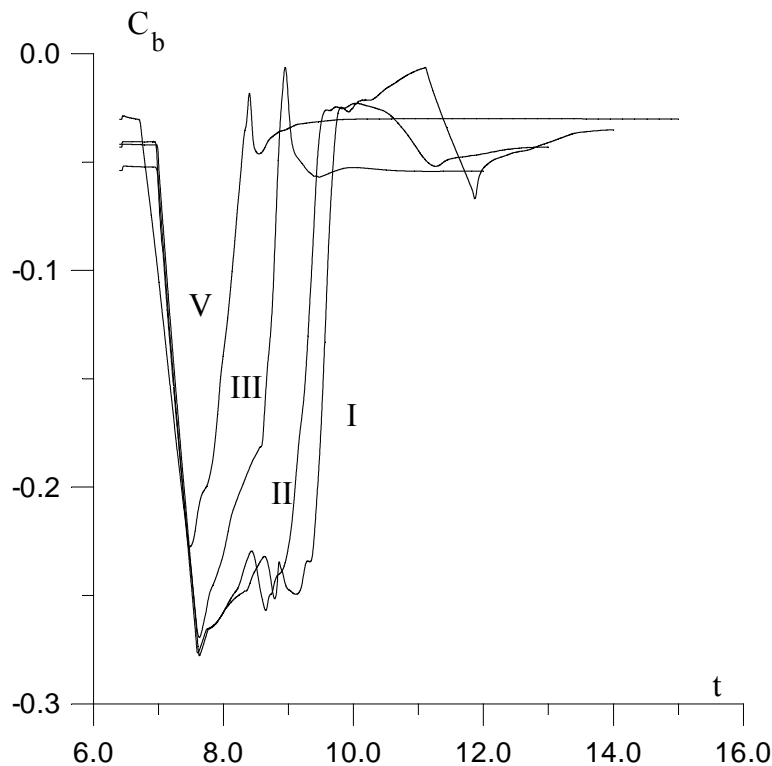
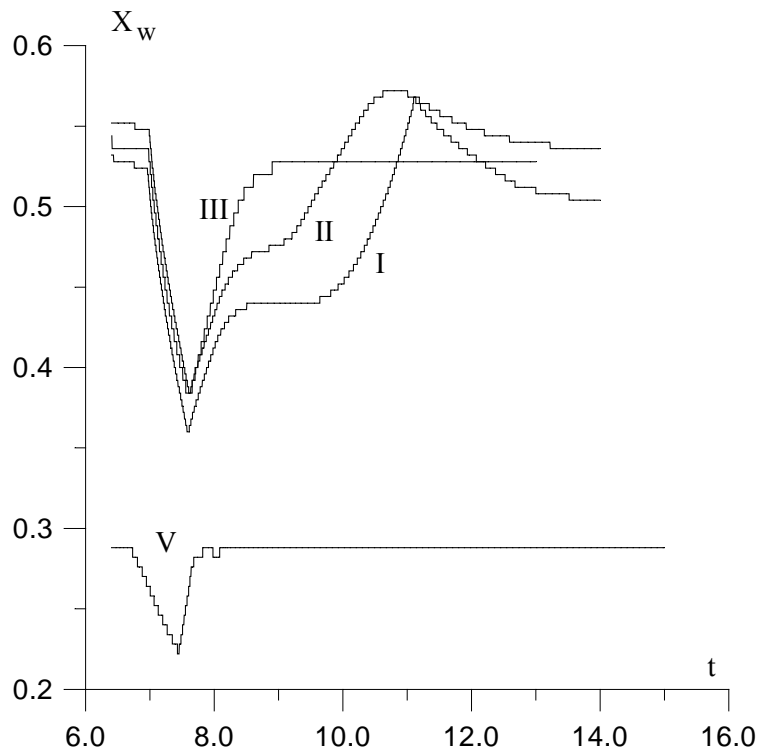


Fig.6.20. Evolution of the circulation C_b for the cases I – III, V; $\alpha_p=0.4$.



Note that in the cases I and II the bow shock wave coordinate makes a few oscillations under it comes back into the stationary state (see Fig.6.0).

Fig.6.21. Dynamics of the bow shock wave coordinate X_w for the cases I – III, V; $\alpha_p=0.4$.

The conclusions on MW release quantitative effects on a supersonic flow past a body with a conic ledge are:

- considerable reduction (up to 50%) of the drag force of the conic surface;
- the dependence of drag reduction upon $\sin\beta$ is close to linear;
- the effects of MW release are stronger for the smaller values of α_p ;
- for the cases I – IV (detached bow shock wave) the values of the rate of changing the standoff and of the rate of changing the circulation C_b are equal;
- the values of the rates are defined from the decision of the Riemann problem, described the interaction of the shock wave and contact discontinuity (boundary of the heat channel);
- the values of the rates practically do not depend on the angle β and the radius of channel R_i ;
- these rates are constant in time on the stage of the drag reduction for all considered cases of bodies geometry I - V.

6.4. Energy deposition in supersonic flow for blunt and sharpen bodies drag reduction

In the previous Section 6.2 streamlining of a blunt body by a supersonic flow with a finite thin heated channel on the axis of it was given. It was carried out by computation mainly. The case of infinite (stationary) discontinuity interaction admits analytic treatment. Both supersonic and subsonic flow conditions inside a channel are considered below. Thus, all cases of discontinuity interaction with a blunt body are described in unique approach. Moreover, this approach is successfully applied also for the description of a sharpen body (wedge as the simplest representative) interaction with such type of infinite discontinuity. Numeric modeling confirms the validity of assumptions accepted in analytic treatment. Under some assumptions this treatment is valid for AD body with an arbitrary shape.

6.4.1. Stationary streamlining of a blunt body by SS flow with thin infinite discontinuity

Let us remind in general the characteristic features of the established flow structure. A blunt body is streamlined by SS flow with on-axis thin heated channel. The conditions inside channel can be either supersonic or subsonic.

The stationary wave structure consists of the direct shock, moving through the heated gas, and the oblique shock, propagating in a cold flow (Fig.6.22). The contact surface composes a wedge structure, outside which, the relatively cold gas moves with supersonic speed after its passing through the oblique shock. Inside the “wedge” there exist the subsonic hot flow, which is maintained by the gas flow coming from the discontinuity.

The angle of the oblique shock and flow axis α can be obtained by considering the conditions after direct and oblique shocks.

In the simplest treatment the following considerations for determination of these conditions can be applied. The static pressure values after these shocks were equated. The static pressure p_2 after the oblique shock is

$$p_2/p_0 = 2\gamma/(\gamma+1) \cdot \sin^2 \alpha M_0^2 - (\gamma-1)/(\gamma+1), \quad (1)$$

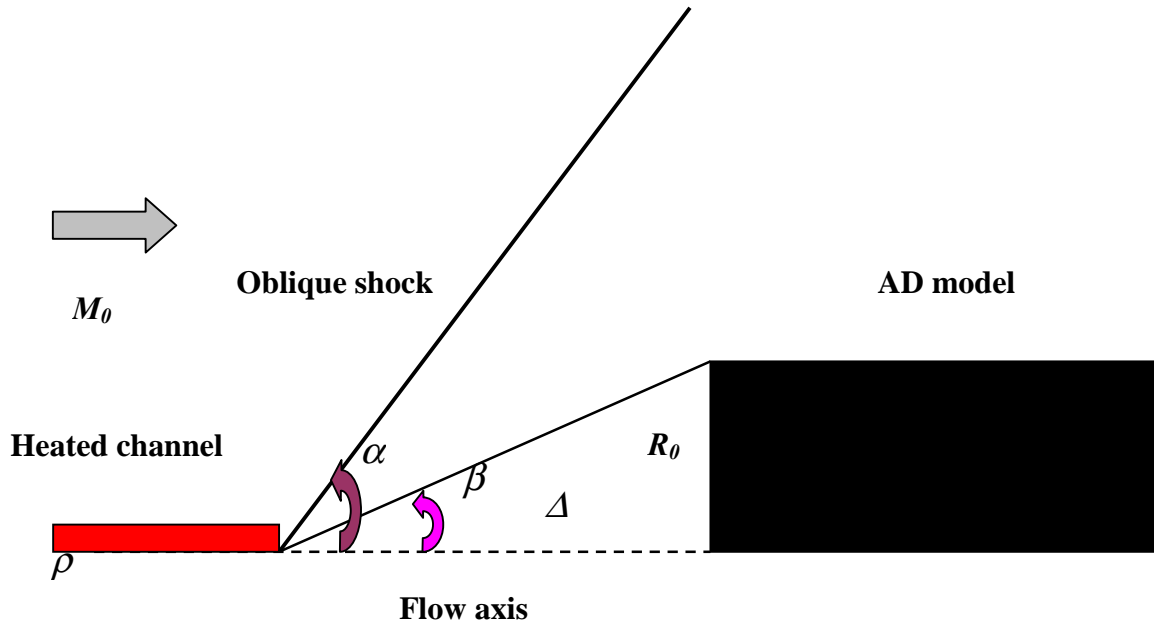
where as p_1 after the direct shock is

$$p_1/p_0 = 2\gamma/(\gamma+1) \cdot M_0^2 - (\gamma-1)/(\gamma+1). \quad (2)$$

Equating (1) and (2), one obtain simple relation:

$$\sin^2 \alpha = \rho. \quad (3)$$

The stationary stand-off Δ can be determined from formula connecting the angle of the attached oblique shock α with wedge angle β [5]



$$\text{ctg} \beta = \text{tg} \alpha \cdot [(\gamma+1) M_0^2 / 2 (M_0^2 \sin^2 \alpha - 1) - 1]. \quad (4)$$

Fig.6.22. The scheme for stationary stand-off determination

The scheme is shown in Fig.6.22 (compare with Fig.6.23, where calculated stationary structure is shown). Substituting $\sin^2 \alpha = \rho$, obtain,

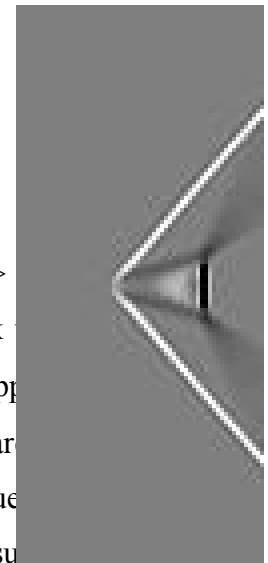
$$\text{ctg} \beta = (\rho / 1 - \rho)^{1/2} \cdot [(\gamma+1) M_0^2 / 2 (\rho \cdot M_0^2 - 1) - 1] \quad (5)$$

or,

$$\Delta = R \cdot (\rho / 1 - \rho)^{1/2} \cdot [(\gamma+1) M_0^2 / 2 (\rho \cdot M_0^2 - 1) - 1]. \quad (6)$$

It can be readily seen that this relationship is valid only for $\rho \cdot M_0^2 > 1$, which is the character of the flow in heated region, delivering the infinite value of shock angle at sonic condition inside discontinuity $\rho \cdot M_0^2 = 1$. This is indicative of rough application of the above for the stationary condition determination. Therefore, these conditions are not suitable for the stationary condition determination.

In corrected approach we imply that the static pressure after the oblique shock is equal to the stagnation pressure of the hot flow in the internal region. The use of such approach is shown in Fig.6.23.



based in [6] as a result of numeric calculations analysis. This condition allows taking into account both supersonic and subsonic conditions in discontinuity.

Firstly, let us make the expression for oblique shock wave angle α dependence on the relative density ρ inside the heated channel for the case $\rho \cdot M_0^2 > 1$ more precise. Equating the expressions for the static pressure after the oblique shock and the stagnation pressure of the flow inside the discontinuity, and expanding the last expression over large $\rho \cdot M_0^2$ parameter, obtain

$$\sin^2 \alpha = (\gamma - 1) / 2 \gamma M_0^2 + \psi(\gamma) \cdot (\rho + 1 / \rho), \quad (7)$$

where $\psi(\gamma)$ is a function of the specific gas heats ratio only and which is practically equal to the unity for all physically realized gas compositions. Thus, in neglecting of the difference between actual meaning of $\psi(\gamma)$ and unity, expression (7) takes very simple form

$$\sin^2 \alpha = \rho + 1 / 2 M_0^2. \quad (8)$$

Comparing (8) and (3) one can obviously see that we've obtained the next approximation in $\sin^2 \alpha$ expansion over large $\rho \cdot M_0^2$ parameter.

In the opposite case, when $\rho \cdot M_0^2$ parameter is small (subsonic flow in a discontinuity) application of the above-cited procedure leads to the expression

$$M_0^2 \cdot \sin^2 \alpha = 1 + (\gamma + 1) \rho M_0^2 / 4, \quad (9)$$

or

$$\sin^2 \alpha = (\gamma + 1) \rho / 4 + 1 / M_0^2. \quad (9')$$

It is seen from the expressions (8) and (9) that influence of such factors as density inside discontinuity and Mach number of the oncoming undisturbed flow on the established oblique shock wave angle is separate, the Mach number being only the small addition to the density factor in supersonic region. In the case of transient condition $\rho \cdot M_0^2 = 1$ the exact expression, which is obviously the same for both super- and subsonic flows in discontinuity, differs not so large from the values, obtained by substituting $\rho \cdot M_0^2 = 1$ in (8) and (9):

$$M_0^2 \cdot \sin^2 \alpha = 1.76 \text{ (exact value)}$$

against 1.6 from (9) for $\gamma = 1.4$.

The limiting cases $\rho \cdot M_0^2 \rightarrow 0$ and $\rho \cdot M_0^2 \rightarrow \infty$ (the last is hypersonic region) are also transparent. In the first case the angle tends to its Mach value and corresponding intensity of the oblique shock is determined by the value of $M_0 \beta$ -parameter (see below). This case implies $\rho \rightarrow 0$, as Mach number of the undisturbed flow exceeds unity. In the second case, which not

necessarily implies $\rho \rightarrow 0$, the shock position is entirely determined by the density value in discontinuity (expression (3)).

Let us also give corrected formulas for the relative pressure drop down at stagnation point for $\rho \cdot M_0^2 > 1$

$$p_d^{stagn}/p_0^{stagn} = \rho \cdot [1 + (1 - \rho)/2 \gamma \rho M_0^2] \quad (10)$$

and $\rho \cdot M_0^2 < 1$

$$p_d^{stagn}/p_0^{stagn} = (1 + \gamma \rho M_0^2/2) \cdot p_0^{static}/p_0^{stagn}. \quad (11)$$

The last expression reflects the evident fact that in stationary streamlining the pressure at the front surface can not be made less than the static pressure in the oncoming flow. It means also that non-effective is to rarefy the channel below the value $\rho^* = 1/M_0^2$, as it is the region of saturation of pressure drop down.

Finally, let us obtain the corrected expression for the angle β and the stationary standoff Δ . Substituting (8) and (9) in (4), obtain for $\rho \cdot M_0^2 > 1$

$$ctg\beta = tg\alpha \cdot [(\gamma + 1)M_0^2/(2\rho M_0^2 - 1) - 1] \quad (12)$$

$$\Delta = R \cdot [(\rho + 1/2 M_0^2)/(1 - \rho - 1/2 M_0^2)]^{1/2} \cdot [(\gamma + 1)M_0^2/(2\rho M_0^2 - 1) - 1] \quad (13)$$

and for $\rho \cdot M_0^2 < 1$

$$ctg\beta = tg\alpha \cdot (2/\rho - 1) \quad (14)$$

$$\Delta = R \cdot [((\gamma + 1)\rho/4 + 1/M_0^2)/(1 - (\gamma + 1)\rho/4 - 1/M_0^2)]^{1/2} \cdot (2/\rho - 1) \quad (15)$$

It is clearly seen that for $\rho \cdot M_0^2 = 1$ ($\rho = \rho^*$) the standoff is about

$$\Delta_l = k \cdot 2R M_0, \quad (16)$$

where factor k is about 1.5 and weakly depends on M_0 .

For the case $\rho \cdot M_0^2 \rightarrow 0$ expressions (14) and (15) deliver

$$ctg\beta = [1/(M_0^2 - 1)]^{1/2} \cdot 2/\rho, \quad (17)$$

or

$$ctg\beta = 2/\rho M_0. \quad (18)$$

It means that the angle β is small and one can rewrite (18) as

$$\beta = \rho M_0/2. \quad (19)$$

Whereas the angle α saturates at the value of Mach angle ($\sin\alpha = 1/M_0$) the angle β successively tends to zero value under the condition $\rho \cdot M_0^2 \rightarrow 0$. Thus, only the case $M_0\beta < 1$ is realized if angle α satisfies additionally the above mentioned condition. This is the consequence of self-

organizing character of the flow structure system. Physically it means that for the case of subsonic conditions inside discontinuity the intensity of the oblique shock wave becomes weak while the density in discontinuity tends to zero value.

For the case $\rho \cdot M_0^2 \rightarrow \infty$ expressions (12) and (13) deliver

$$\operatorname{ctg} \beta = [\rho/(1-\rho)]^{1/2} \cdot [(\gamma+1)/2\rho - 1], \quad (17)$$

or, under $\rho \rightarrow 0$

$$\operatorname{ctg} \beta = (\gamma+1)/2\rho^{1/2}. \quad (18)$$

Thus, in this case angle α diminishes as $\alpha = \rho^{1/2}$, as well as $\beta = 2\rho^{1/2}/(\gamma+1)$, i.e. $\beta = 2\alpha/(\gamma+1)$, and therefore $M_0\beta \gg 1$. Physically it means that for the case of supersonic conditions inside discontinuity the intensity of the oblique shock wave remains strong even if the density in discontinuity and therefore the oblique shock angle tends to zero value.

6.4.2. Stationary streamlining of a wedge by SS flow with thin infinite discontinuity

Expanding of physical understanding of energy deposition in SS flows on drag reduction of AD bodies demands consideration another class of such bodies – sharpen ones. The simplest representative of such class is a wedge. Therefore, we started both numeric and analytic investigation of wedge streamlining by supersonic flow with thin heated channel disposed on its axis.

Numeric modeling was carried out for undisturbed Mach number 1.9 and wedge angle $\chi = 18.4^\circ$ (this corresponds to $\operatorname{ctg} \chi = 3$). In undisturbed flow the oblique shock is attached to the wedge. The ratio of the transverse dimension of discontinuity to the maximal transverse dimension of the wedge was taken equal to 0.25. Relative density inside discontinuity ρ was varied from 0.3 to 0.7.

Typical sequence of Schlieren-type pictures of wedge interaction with infinite discontinuity with $\rho = 0.4$ is presented at Fig.6.24. It is readily seen that the basic features of the interaction process are qualitatively similar to those demonstrated under interaction with a blunt body. Moreover, the oblique shock angle α at stationary detached position turned out to be the same as for the case of blunt body interacting with discontinuity of the same density. It means

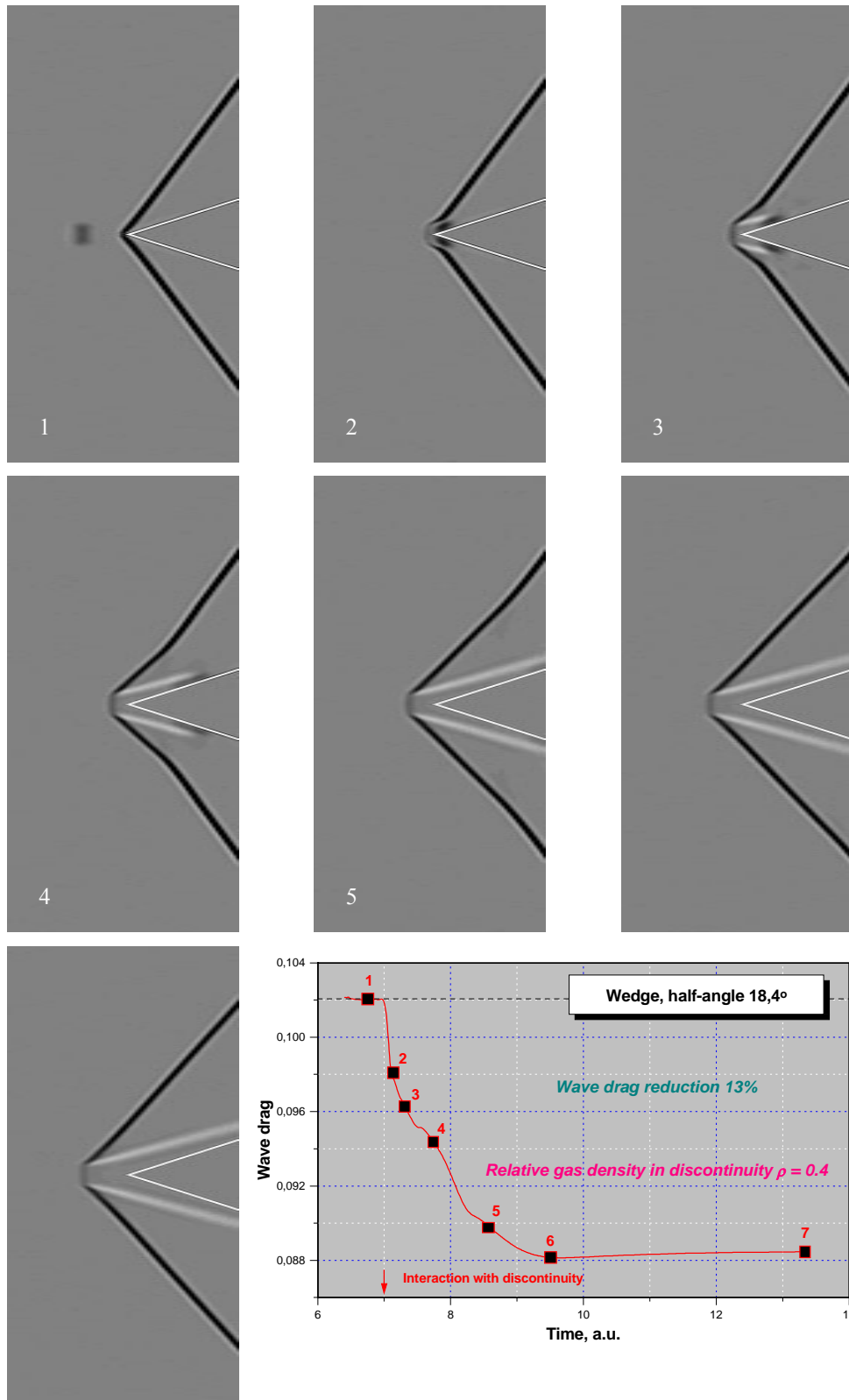


Fig.6.24. Wedge interaction with discontinuity (detached regime)

that stationary geometry does not depend on the body shape and satisfies the same relations as were obtained above in subsection 5.1. This fact greatly simplifies analytic treatment of wedge stationary interaction with thermal discontinuity in supersonic flow.

Before presenting of such treatment, let us consider those peculiarities of interaction, which distinguish this case from the blunt one. These differences refer to non-stationary phase of interaction, phase of establishing of stationary gas dynamic geometry. It is seen that in contrary with blunt body case, the detachment shock movement occurs monotonously (Fig.6.25), with gradual diminishing of speed. Thus, the phase of reverse movement is absent. Also drag force falls monotonously (Fig.6.26), its relative drop down being less in comparison with blunt body. The values of upstream shock movement velocity are sufficiently less than those under the same flow parameters for blunt body cases (Fig.6.27). It is seen that there appears a threshold for shock detachment, i.e. the upstream shock movement does not occur if the relative density in discontinuity exceeds some critical value (see also below).

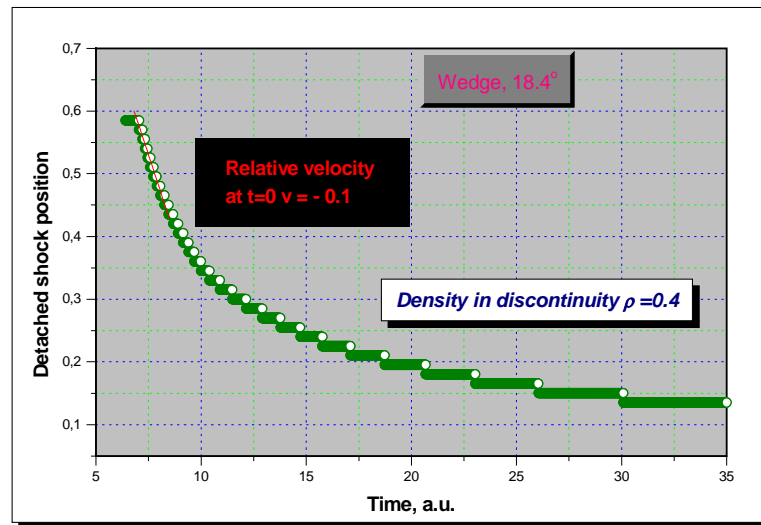


Fig.6.25. Evolution of detached shock position

Now let us obtain analytic expressions for shock detachment threshold and wedge drag reduction. For this we are to convert expression (4) and express oblique shock angle α over wedge angle χ . Considering $M_0^2 \gg 1$, neglecting of the difference between $(\gamma+1)/2$ and unity, and finally, M_0^{-2} in comparison with $2\sin^2 \alpha$ (the most strong assumption), one obtain

$$\sin^2 \alpha = \sin^2 \chi + 2 \cos^2 \chi / M_0^2. \quad (19)$$

This formula gives satisfactory precision and due to the last assumption delivers under $\chi \rightarrow 0$ the limiting value of $\sin \alpha$ greater its actual value in 1.41 times. This fact is to be kept in mind.

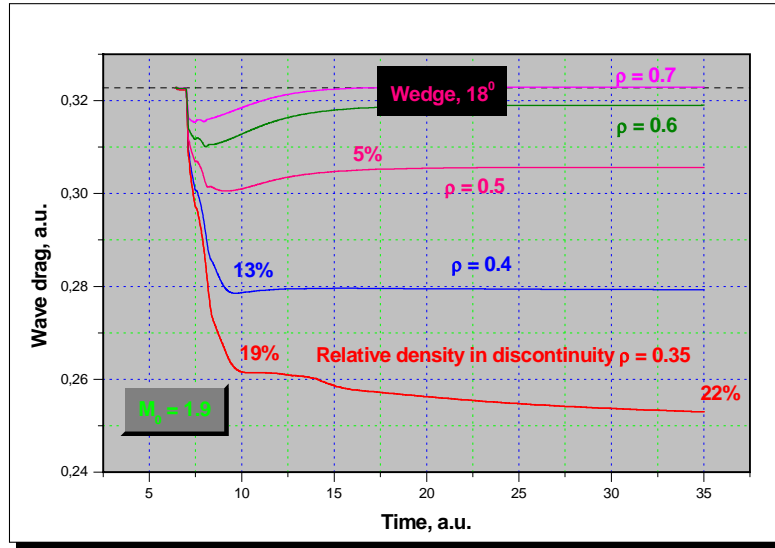


Fig.6.26. Wave drag evolution for different relative densities in discontinuity

The shock detachment threshold for a wedge can be obtained if suppose that $\sin \alpha$ in the undisturbed flow should be not be less than $\sin \alpha$ established in interaction with discontinuity (see expressions (8) and (9')). Non-detached regime of streamlining is presented at Fig.6.28. In other words, if interaction with discontinuity can potentially diminish the α angle, simultaneously diminishing the pressure after the oblique shock, detachment will occur (Fig.6.29). Foundation for such assumption is confirmed by numeric calculations (see above).

Thus, the detachment criterion can be formulated as $\sin^2 \alpha_1 \leq \sin^2 \alpha_0$, or in another form

$$\rho \leq \rho_{det}, \quad (20)$$

where ρ_{det} is determined as

$$\rho_{det} = (1 - 2/M_0^2) \cdot \sin^2 \chi + 1.5/M_0^2 \quad (21)$$

for supersonic conditions in discontinuity and

$$\rho_{det} = 4 [(1 - 2/M_0^2) \cdot \sin^2 \chi + 1/M_0^2] / (\gamma + 1) \quad (22)$$

for subsonic ones. The difference between these expressions is not large, especially taking into account all assumptions that were made previously. Below we'll use expression (8) for drag reduction expression obtaining. Thus, ρ_{det} is function of wedge angle and Mach number.

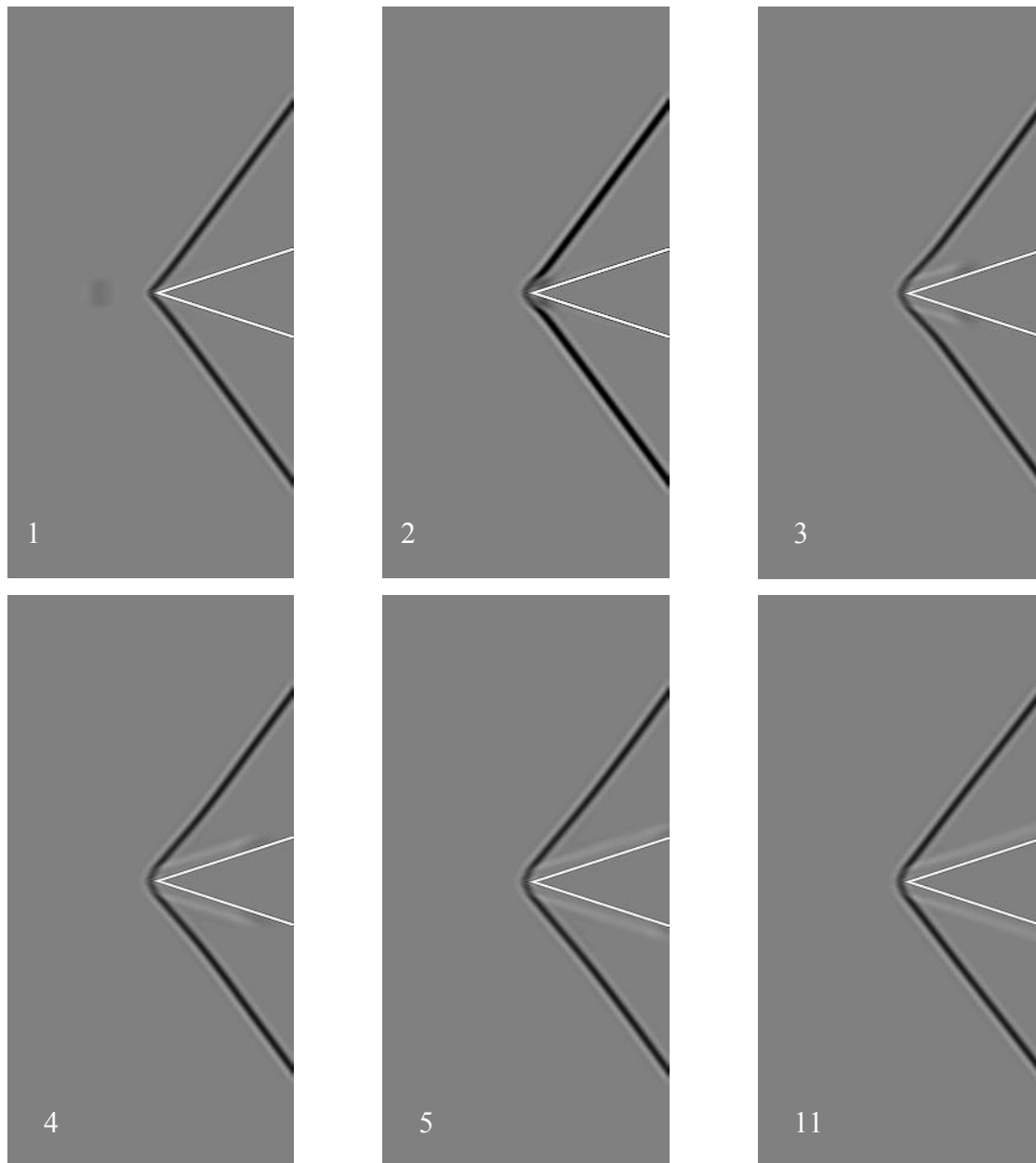


Fig.6.28. Wedge interaction with discontinuity (attached regime)

The stationary standoff for the wedge for $\rho \leq \rho_{det}$ obeys the same relation (6) as for the blunt (rectangular) body. In this case the “radius” R means the half of the maximal transverse dimension of a wedge.

Drag reduction in the case of a wedge has a transparent physical basis. The action of thermal discontinuity leads under the condition $\rho \leq \rho_{det}$ to formation of a new “wedge” in front

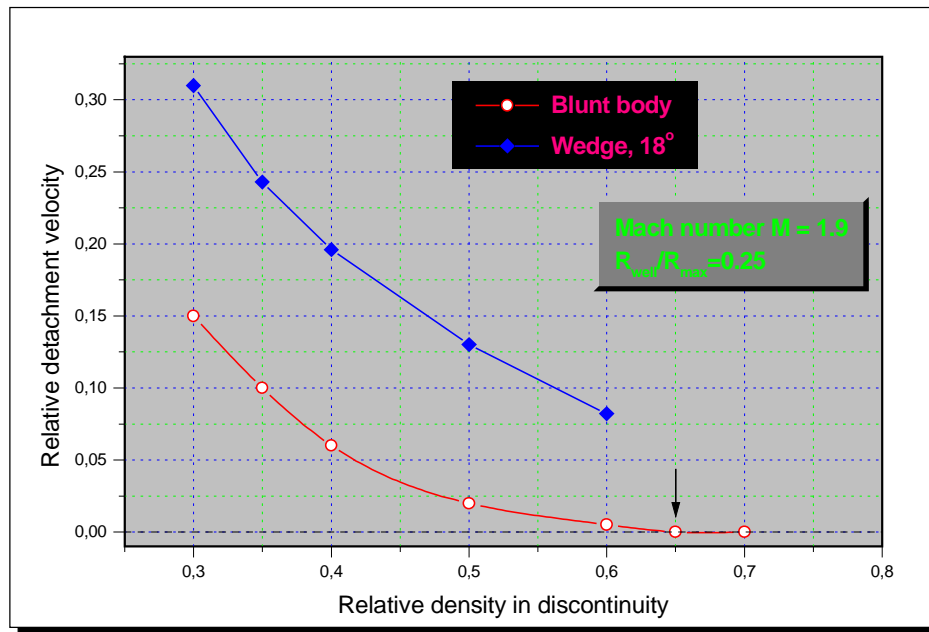


Fig.6.27. Start detachment velocity of shock wave over relative density in discontinuity

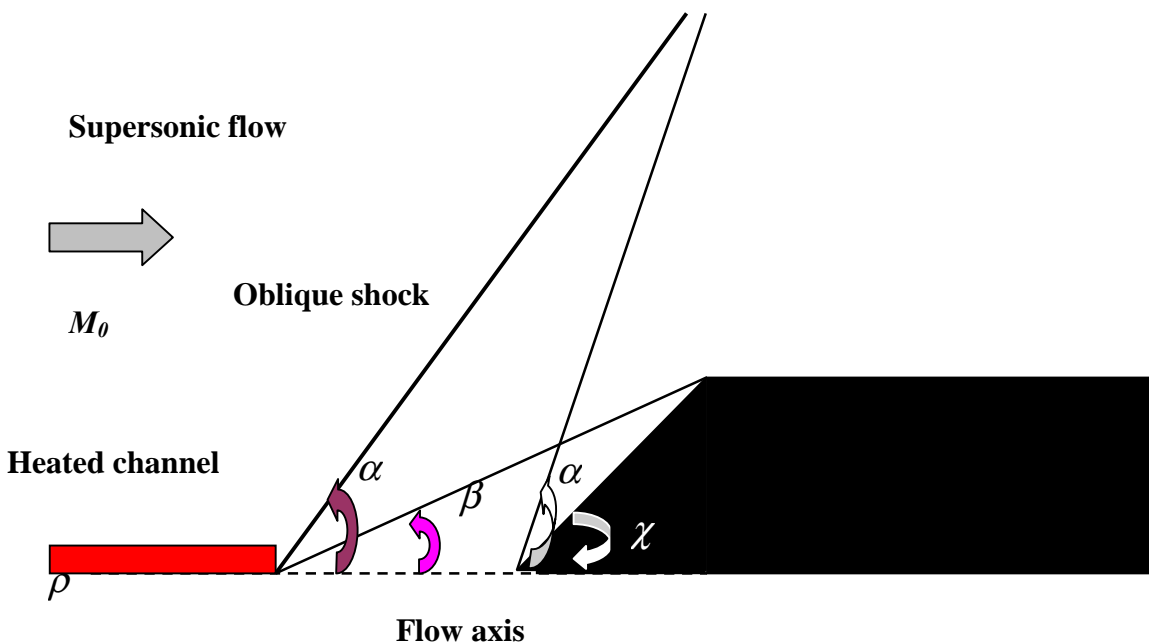


Fig.6.29. The scheme for determination of stationary parameters streamlining of a wedge

of the real one with an angle that is less than the actual. This fact obviously leads to pressure diminishing both after the new oblique shock and on the surface of the wedge (the same pressures). Therefore, one can write for the total wave drag change ΔF

$$\Delta F = - \Delta p D, \quad (23)$$

where Δp is the difference between the initial and new stationary pressures after oblique shocks, notice that $L \cdot \sin \chi = R$, L is the length of the wedge along contact with gas flow. Finally,

$$\Delta F = p_0 M_0^2 D \cdot (\rho - \rho_{det}) \cdot 2\gamma / (\gamma + 1). \quad (24)$$

Here p_0 is a static pressure in the oncoming flow. For the relative drag reduction $\Delta F/F_0$

$$\Delta F/F_0 = (\rho - \rho_{det}) / (\rho_{det} + 1/2 M_0^2). \quad (25)$$

Substituting (21) in (25) gives the dependence of the relative drag reduction value upon ρ , χ and M_0 :

$$\Delta F/F_0 = [\rho M_0^2 - (M_0^2 - 2) \cdot \sin^2 \chi - 1.5] / [(M_0^2 - 2) \cdot \sin^2 \chi + 2]. \quad (26)$$

Remind that $\rho \leq \rho_{det}$, i.e. the sign of the expression in numerator is negative. For $M_0^2 \sin^2 \chi \gg 1$ (and, hence, $M_0^2 \gg 1$) expression can be simplified

$$\Delta F/F_0 = (\rho - \sin^2 \chi) / \sin^2 \chi. \quad (27)$$

This limiting case corresponds to hypersonic conditions.

Thus, reduction at a fixed portion of a sharpen body drag demands deeper rarefaction of gas in a channel than in the case of blunt body.

6.4.3. Efficiency of stationary interaction

Now it is not difficult to derive an expression for stationary interaction efficiency. As it was shown above, the pressure on the front surface of the body under the stationary interaction with density well constitutes value ρ part of the undisturbed pressure. Therefore, the saved power is given by

$$W_s = p_{stagn}^0 \nu D (\rho_0 - \rho_1) / \rho_0.$$

Thus, interaction efficiency takes form

$$\eta \approx M_0^2 \cdot (D/d) \cdot R / C_p,$$

which is very close to that obtained for non-stationary interaction. It should be noticed that high efficiency is attained along with noticeable diminishing in drag. Explanation of this fact lies in self-similarity of the problem. The transverse dimension of discontinuity has no affect on the established stationary parameters of a flow around model.

6.5. Shock wave interaction with a wide long hot region

Let us examine analytically interaction of a shock wave in air with a long heated region. This phenomenon for example can be observed while interaction of the bow shock wave nearby the axis of a blunt cylinder with the area of energy release, which follows MW discharge in supersonic flow. Let us formulate the Riemann problem. At the very beginning when the heated area gets in touch with the bow shock wave there is the problem of a shock wave interaction with a contact discontinuity. Decay of discontinuity and shock wave behavior, while it interacts with a heated region were examined.

6.5.1. Normal shock interaction

The solution of the problem consists of the shock wave (SW) moving to the right direction, the contact discontinuity (CD) and the rarefaction wave (RW) moving to the left direction from the point 0 for $t \geq 0$, see Fig.6.30. Denote the right set of gas parameters outside the hot region upstream the shock wave (SW) – pressure, density and velocity as P_1 , ρ_1 , and v_1 . They are initial gas parameters. Gas parameters inside the hot area before the shock wave are P_2 , ρ_2 and v_2 . Let $\rho_2 = \alpha \times \rho_1$, where α is a degree of gas heating.

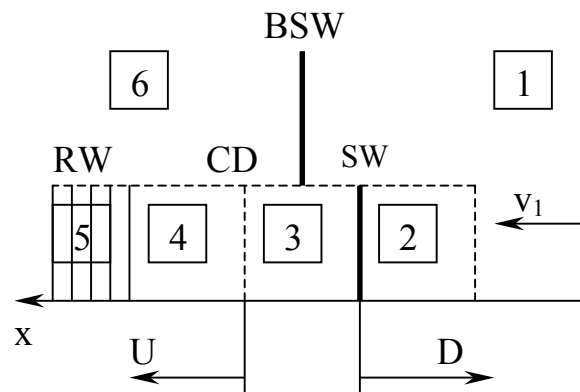


Fig.6.30. Diagram for the construction of the solution for the Riemann problem.

The values behind the bow shock wave front are the left set of gas parameters P_6 , ρ_6 and v_6 . Velocity of the shock wave is marked D. There are areas of the constant gas parameters between these components of the solution.

Using the pressure and velocity continuity on the contact discontinuity

$$v_3 = v_4 = U, \quad P_4 = P_3,$$

the expressions for the parameters on the shock wave

$$P_3 = P_2 \left(\frac{2k}{k+1} M_D^2 - \frac{k-1}{k+1} \right), \quad U = v_1 - \frac{2a_2}{k+1} \left(M_D - \frac{1}{M_D} \right)$$

and in the rarefaction wave area

$$P_6 = P_4 \left(\frac{a_6}{a_4} \right)^{\frac{2k}{k-1}}, \quad \frac{2}{k-1} a_6 - v_6 = \frac{2}{k-1} a_4 - v_4$$

and taking into consideration $P_1 = P_2$ it can be concluded that

$$P_1 \left(\frac{2k}{k+1} M_D^2 - \frac{k-1}{k+1} \right) = P_6 \left\{ 1 + \frac{k-1}{2a_6} \left[v_1 - \frac{2a_2}{k+1} \left(M_D - \frac{1}{M_D} \right) - v_6 \right] \right\}^{\frac{2k}{k-1}}$$

Here a – velocity of sound;

$$M_D = \frac{|D| + v_1}{a_2} - \text{Mach number of the shock wave;}$$

k – exponent of adiabat.

If to take into account that

$$\frac{P_6}{P_1} = \frac{2k}{k+1} M_o^2 - \frac{k-1}{k+1},$$

$$M_6 = \sqrt{\frac{1 + \frac{k-1}{2} M_o^2}{k M_o^2 - \frac{k-1}{2}}} \quad \text{and}$$

$$\frac{a_1}{a_6} = \left[1 + \frac{2(k-1)}{(k+1)^2 M_o^2} (M_o^2 - 1) (1 + k M_o^2) \right]^{-0.5},$$

where M_o – Mach number of the bow shock wave, finally it can be obtained that

$$\left(\frac{\frac{2k}{k+1} M_D^2 - \frac{k-1}{k+1}}{\frac{2k}{k+1} M_o^2 - \frac{k-1}{k+1}} \right)^{\frac{k-1}{2k}} - 1 = \frac{k-1}{2} \left\{ \frac{M_o - \frac{2 \left(M_D - \frac{1}{M_D} \right)}{\sqrt{\alpha}(k+1)}}{\sqrt{1 + \frac{2(k-1)}{(k+1)^2 M_o^2} (M_o^2 - 1)(1 + k M_o^2)}} - \sqrt{\frac{1 + \frac{k-1}{2} M_o^2}{k M_o^2 - \frac{k-1}{2}}} \right\}$$

So Mach number of the shock wave M_D is implicit function of two independent parameters – Mach number of the flow M_o and heating degree α

$$M_D = f(M_o, \alpha).$$

The computational values of D and the values of U obtained via solution of this equation are shown in Fig.6.31 and Fig.6.32 (stagnation temperature in region 1 is $290K^0$).

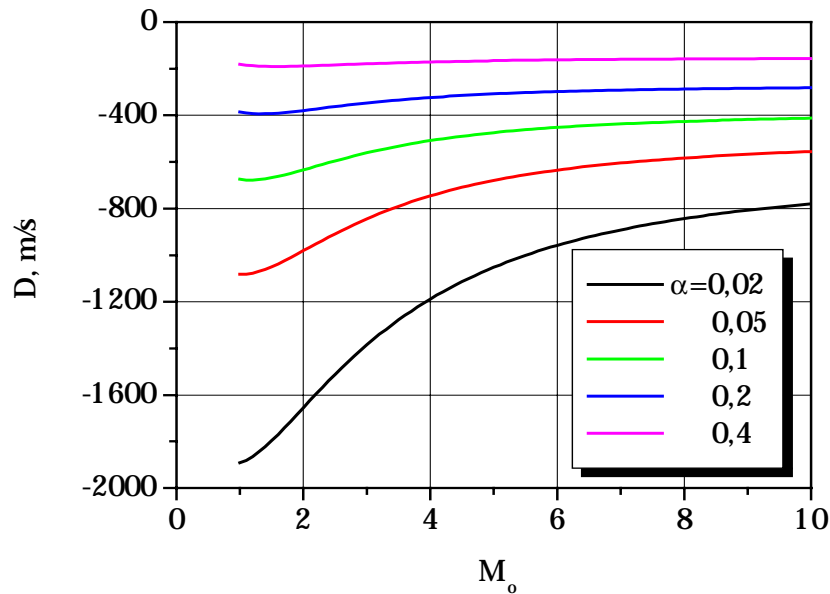


Fig.6.31. Velocity of shock wave via Mach number of the flow for different parameters α .

Velocity of shock wave D is increasing with rise of heating degree. It's value can reach of high enough magnitude (up to several thousand meters per second at $\alpha=0.02$).

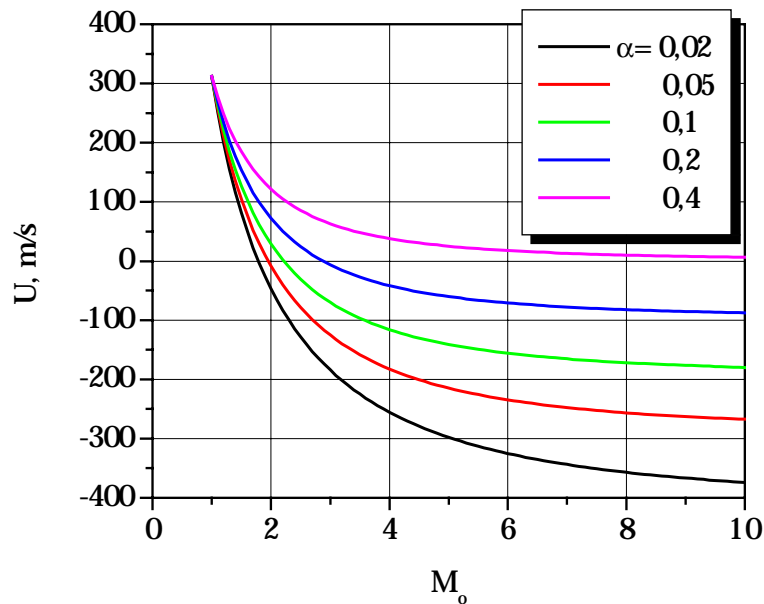


Fig.6.32. Velocity of the flow in the wake of shock wave.

Velocity U is decreasing via Mach number of the flow. It should be marked that at parameter α less than 0,4 the value U can change it's sign. When parameter α is falling, the value of velocity U is decreasing and can reach of several hundreds of meters per second.

It was revealed that velocity of shock wave moving in the heated area could reach of high magnitude. The gas after the shock wave can move both upstream and downstream. In the first case energy of pressed gas in shock layer can be realized in counter flow. The regime of the flow is determined with Mach number of the undisturbed flow and degree of gas heating. Next interesting feature of the interaction is that shear layers can lead to creating of vortex motion. Obviously intensity of the vortex depends on heating degree α .

6.5.2. Shock wave on the nose of wedge

Let us formulate the Riemann problem. Suppose that straight shock wave is forming at once when the heated area gets in touch with the shock wave. The straight shock wave is moving along the thin heated channel, Fig.6.33.

The solution of the problem consists of the shock wave (SW1) moving to the right direction, the contact discontinuity (CD) and the rarefaction wave (RW) moving to the left

direction from the point 0 for $t \geq 0$. Denote the write set of gas parameters outside the hot region upstream the shock wave (SW) – pressure, density and velocity as P_1 , ρ_1 , and v_1 . They are initial gas parameters. Gas parameters inside the hot area before the shock wave are P_2 , ρ_2 and v_2 . Let $\rho_2 = \alpha \rho_1$, where α is a degree of gas heating.

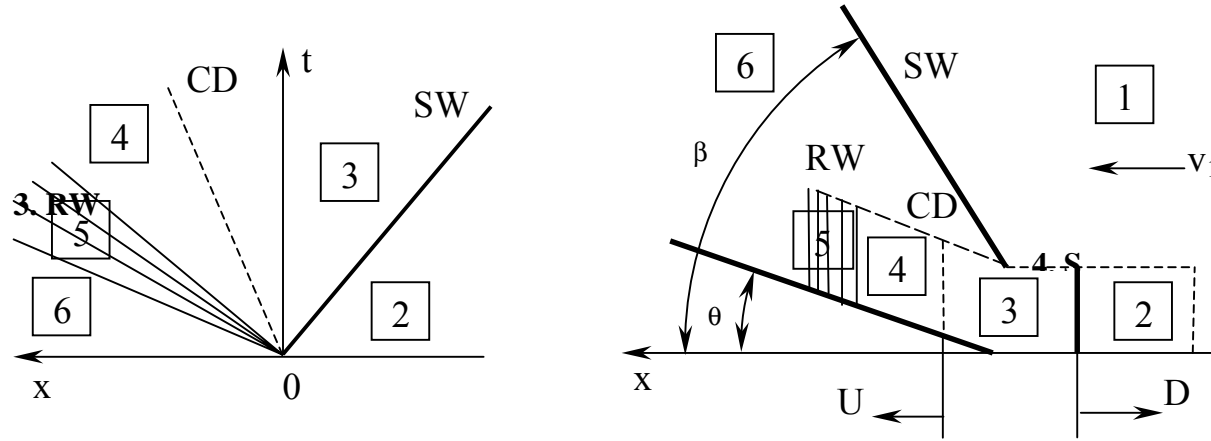


Fig.6.33. Diagram for the construction of the solution for the Riemann problem.

The values behind the shock wave front are the left set of gas parameters P_6 , ρ_6 and v_6 . Velocity of the shock wave is marked D. There are the areas of the constant gas parameters between these components of the solution.

Using the pressure and velocity continuity on the contact discontinuity

$$v_3 = v_4 = \frac{U}{\cos(\theta)}, \quad P_4 = P_3,$$

the expressions for the parameters on the shock wave

$$P_3 = P_2 \left(\frac{2k}{k+1} M_1^2 - \frac{k-1}{k+1} \right), \quad U = v_1 - \frac{2a_2}{k+1} \left(M_1 - \frac{1}{M_1} \right)$$

and in the rarefaction wave area

$$P_6 = P_4 \left(\frac{a_6}{a_4} \right)^{\frac{2k}{k-1}}, \quad \frac{2}{k-1} a_6 - v_6 = \frac{2}{k-1} a_4 - v_4$$

and taking into consideration $P_1 = P_2$ it can be concluded that

$$P_2 \left(\frac{2k}{k+1} M_1^2 - \frac{k-1}{k+1} \right) = P_6 \left\{ 1 + \frac{k-1}{2a_6} \left[\frac{v_1}{\cos(\theta)} - \frac{2a_2}{(k+1)\cos(\theta)} \left(M_1 - \frac{1}{M_1} \right) - v_6 \right] \right\}^{\frac{2k}{k-1}}$$

Here a – velocity of sound;

$$M_1 = \frac{-D + v_1}{a_2} \text{ – Mach number of the shock wave;}$$

k – exponent of adiabat.

If to take into account that

$$\frac{P_6}{P_1} = \frac{2k}{k+1} M_o^2 \sin^2(\beta) - \frac{k-1}{k+1}, \quad M_6 = \sqrt{\frac{1 + \frac{k-1}{2} M_o^2 \sin^2(\beta)}{k M_o^2 \sin^2(\beta) - \frac{k-1}{2} \sin(\beta - \theta)}} \quad \text{and}$$

$$\frac{a_1}{a_6} = \left[1 + \frac{2(k-1)}{(k+1)^2 M_o^2 \sin^2(\beta)} (M_o^2 \sin^2(\beta) - 1) (1 + k M_o^2 \sin^2(\beta)) \right]^{-0.5},$$

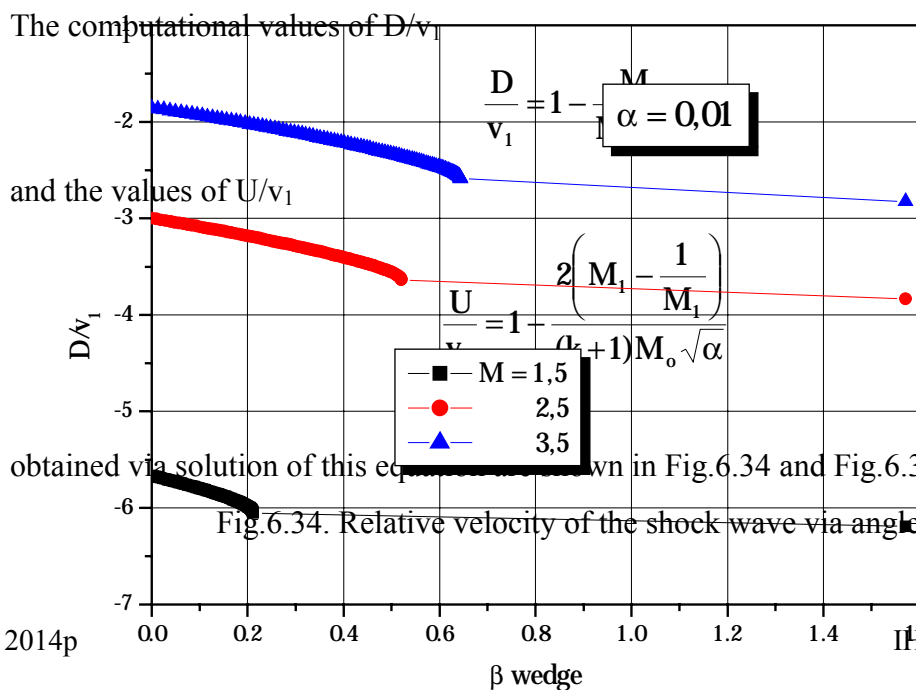
where M_o – Mach number of the basic shock wave,

finally it can be obtained that

$$= \frac{k-1}{2} \left\{ \frac{\frac{M_o}{\cos(\theta)} - \frac{2 \left(M_1 - \frac{1}{M_1} \right)}{\sqrt{\alpha(k+1)\cos(\theta)}}}{\sqrt{1 + \frac{2(k-1)}{(k+1)^2 M_o^2 \sin^2(\beta)} (M_o^2 \sin^2(\beta) - 1)(1 + k M_o^2 \sin^2(\beta))}} - \sqrt{\frac{1 + \frac{k-1}{2} M_o^2 \sin^2(\beta)}{k M_o^2 \sin^2(\beta) - \frac{k-1}{2} \sin(\beta - \theta)}} \cdot \frac{1}{\sin(\beta - \theta)} \right\}$$

So Mach number of the shock wave M_1 is implicit function of four independent parameters – Mach number of the flow M_o , heating degree α and two angles β and θ

$$M_1 = f(M_o, \alpha, \beta, \theta).$$



Absolute value of the relative velocity is decreasing with rise of Mach number of the flow and increase of parameter α . It is increasing with rise of angle β . The thick lines on the Fig. 6. 3 show the case when original oblique shock wave is attached to the wedge. The points at $\beta=1,57$ are result for straight shock wave.

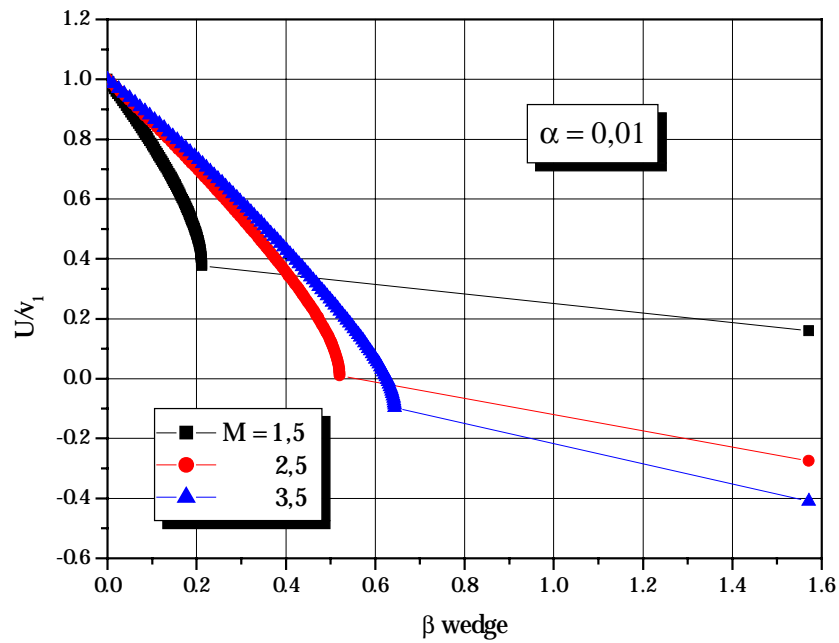


Fig.6.35. Relative velocity of gas flow after the shock wave via angle β .

Velocity of gas flow is decreasing with rise angle β . At some condition velocity U can be less zero, so gas flows upstream. This flow can be a powerful source of vortex motion of gas before the body.

6.6. Spike-tipped body streamlining with energy addition

The problem under consideration is the influence of MW energy release on a supersonic flow past blunt body with a spike. Numerical modeling is based on the Euler equations:

$$\frac{\partial \bar{U}}{\partial t} + \frac{\partial \bar{F}}{\partial x} + \frac{\partial \bar{G}}{\partial y} = 0$$

$$\bar{U} = \begin{pmatrix} \rho \\ \rho u \\ \rho v \\ E_S \end{pmatrix}, \bar{F} = \begin{pmatrix} \rho u \\ p + \rho u^2 \\ \rho uv \\ u(E_S + p) \end{pmatrix}, \bar{G} = \begin{pmatrix} \rho v \\ \rho uv \\ p + \rho v^2 \\ v(E_S + p) \end{pmatrix},$$

ρ , p , u and v are the density, pressure, and the x - and y - velocity components of the gas, $E_S = \rho(\epsilon + 0.5(u^2 + v^2))$, ϵ is specific internal energy, and the ratio of specific heats of perfect gas is $\gamma = 1.4$. At the initial time moment and on the entrance boundary the flow parameters were defined as $\rho_0 = 1$, $p_0 = 0.2$, $u_0 = 1$ and $v_0 = 0$. Thus, Mach number of a flow was $M_0 = 1.89$. As the units of measure the value of air density in the normal conditions $\rho_H = 1.29 \text{ kg/m}^3$ and the pressure value $p_H = 5 \text{ atm}$ were used. The original numerical method based on the second approximation order conservative difference scheme on a minimal stencil was employed in the computations [2].

The structure of a supersonic flow past bodies with spikes is well known and spikes are widely applied for drag force reducing [7]. We consider the cases of MW energy deposition effects on a supersonic flow past blunt body with spike when the system of shock waves is changed and the addition shock waves arise.

Case 1. The body radius $R_b = 0.176$, the spike length $L_s = 0.48$, the spike radius $R_s = 0.04$. The stationary flow picture in isochors is presented in Fig.6.36a. Here $\tan \alpha_s = 1/3$, where α_s is the top angle of the spike. Modeling the MW release was accomplished via formation an isobaric hot channel with the use of the boundary conditions for an incoming flow. From the time moment $t_i = 8.43$ when the stationary regime has been already achieved the density on the boundary was supposed to be $\rho(0, y, t) = \rho_i = \alpha_p \rho_0$, $\alpha_p = 0.4$ for $0 \leq y \leq R_i$ and $t_i \leq t \leq t_i + \Delta t$, where R_i is the channel radius, $R_i = 0.04$, $\Delta t = 0.4$. The other parameters were applied to be equal to ones of an initial flow. These conditions generated the longitudinal rectangular heat channel with the width of R_i extending from the boundary to the body.

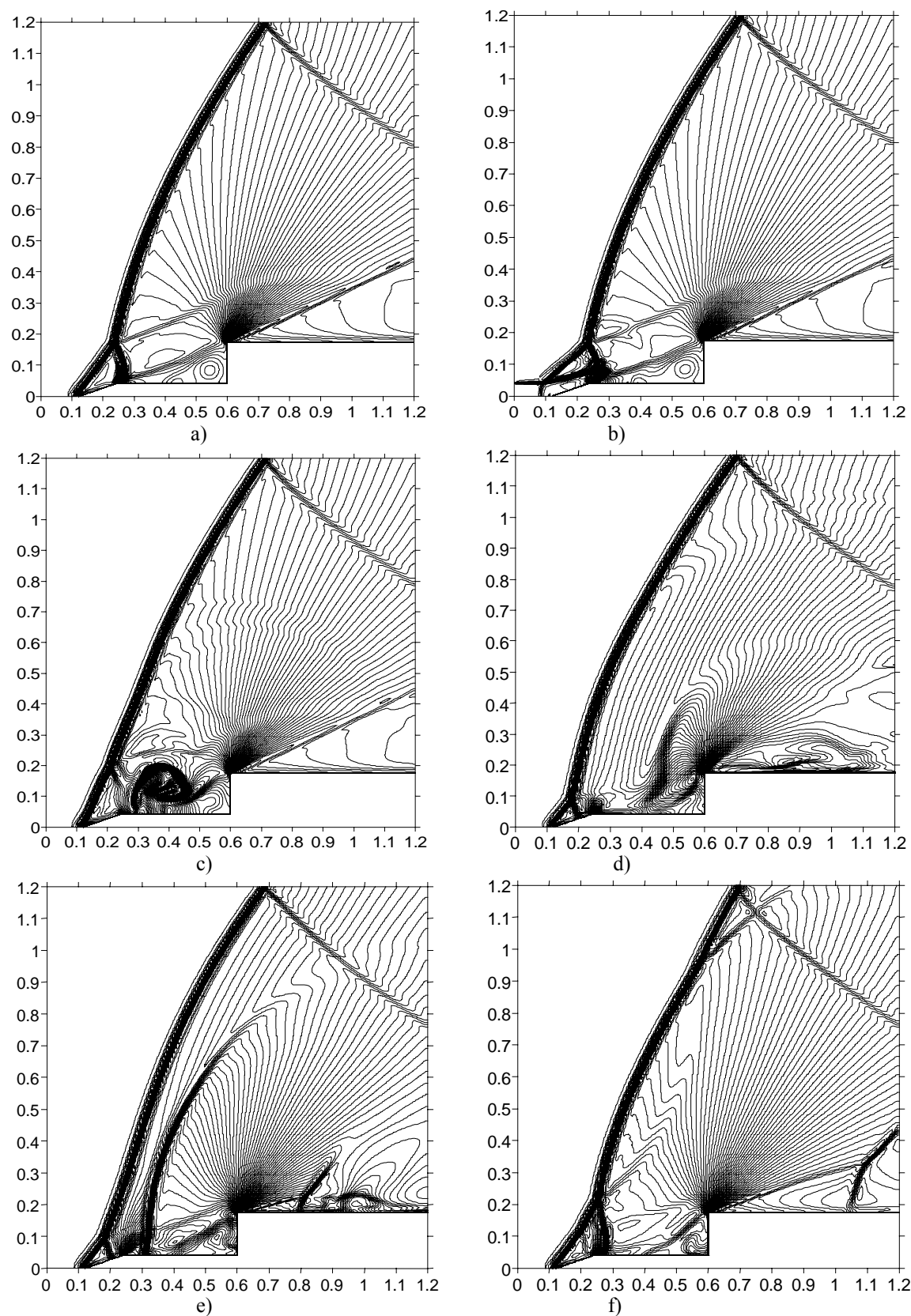


Fig.6.36. Effect of a short MW energy release domain on a stationary streamlining of a blunt body with a short sharp spike: a) $t=8.4$, b) $t=8.8$, c) $t=9.4$, d) $t=10.6$, e) $t=11.2$, f) $t=11.8$.

In the calculations the channel has been restricted on time by the value of $\Delta t=0.4$.

The density fields for different time moments are presented in Fig.6.36. In this case the triple point is situated near the top of the spike. The hot channel interacts with the right shock wave generating a vortex structure in an area near the top of the spike. It is seen the destruction of the right shock wave as the result of the interaction (Fig.6.36c). After an interaction of the vortex with the rarefaction wave with a center in the body's corner a strong shock wave arises and moves to the bow wave (Fig.6.36d, e). In an area near the top surface of the body it is also seen a weak shock wave moving right after the vortex structure.

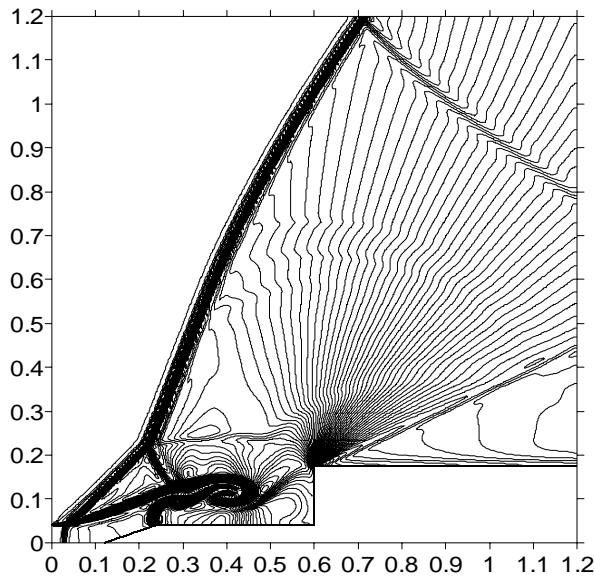


Fig.6.37. Effect of a long MW energy release domain on stationary streamlining of a blunt body with a short sharp spike, $t=9.4$, $\Delta t=1.0$

The aroused shock wave catches up with the bow wave. At the same time the vortex structure leaves the calculation area and the stationary flow re-establishes (Fig.6.36f).

Note that the longer on time hot channel generates a detached conic shock wave and more complicated vortex structure in an area near the spike (Fig.6.37).

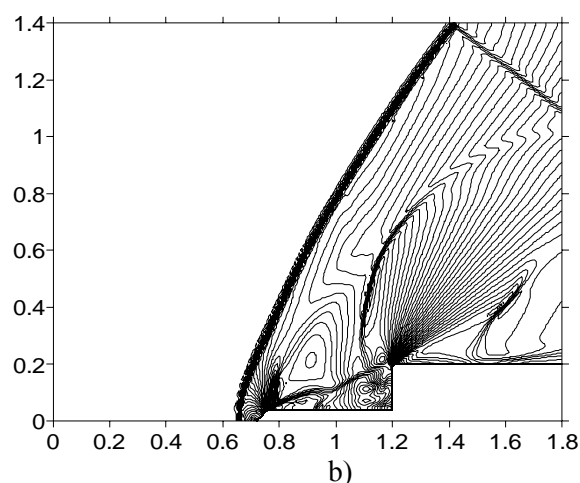
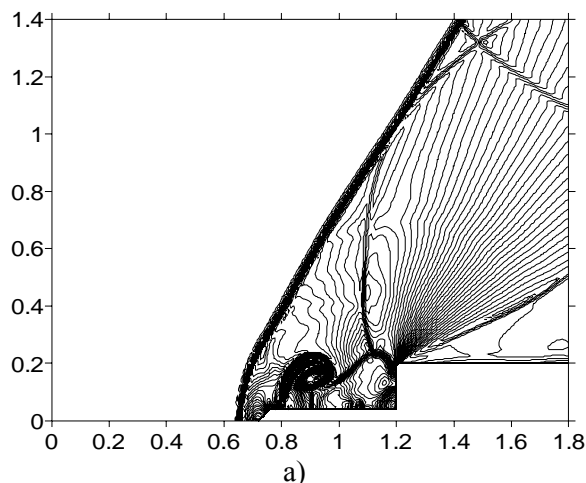


Fig.6.38. Effect of a short MW energy release domain on stationary streamlining of a blunt body with a short blunt spike: a) $t=8.4$, b) $t=9.4$

Case 2. The body radius $R_b=0.2$, the spike length $L_s=0.48$, the spike radius $R_s=0.04$, $\tan\alpha_s=1$. The stationary flow picture in isochors is presented in Fig.6.38a. Here a detached shock wave arises and it is seen a weaker shock wave near the corner of the body. The release parameters were the same as in the *Case 1*. The generated vortex structure is shown in Fig.6.38b.

Case 3. The body radius $R_b=0.2$, the spike length $L_s=1.68$, the spike radius $R_s=0.08$, $\tan\alpha_s=1/3$. The release parameters were: $t_i=10.03$, $\alpha_p=0.3$, $R_i=0.08$, $\Delta t=0.4$. The stationary flow picture is presented in Fig.6.39a. As one can see the triple point in this case is considerably far from the spike. The results of the release effect on the supersonic flow are shown in Fig.6.39b, 39c, 39d. It is seen a shock wave generation during the interaction of the aroused vortex structure and the right boundary of the rarefaction wave with a center in the spike “corner” (Fig.6.39b). It is shown this wave to blow off after the vortex structure (Fig.6.39c, 39d).

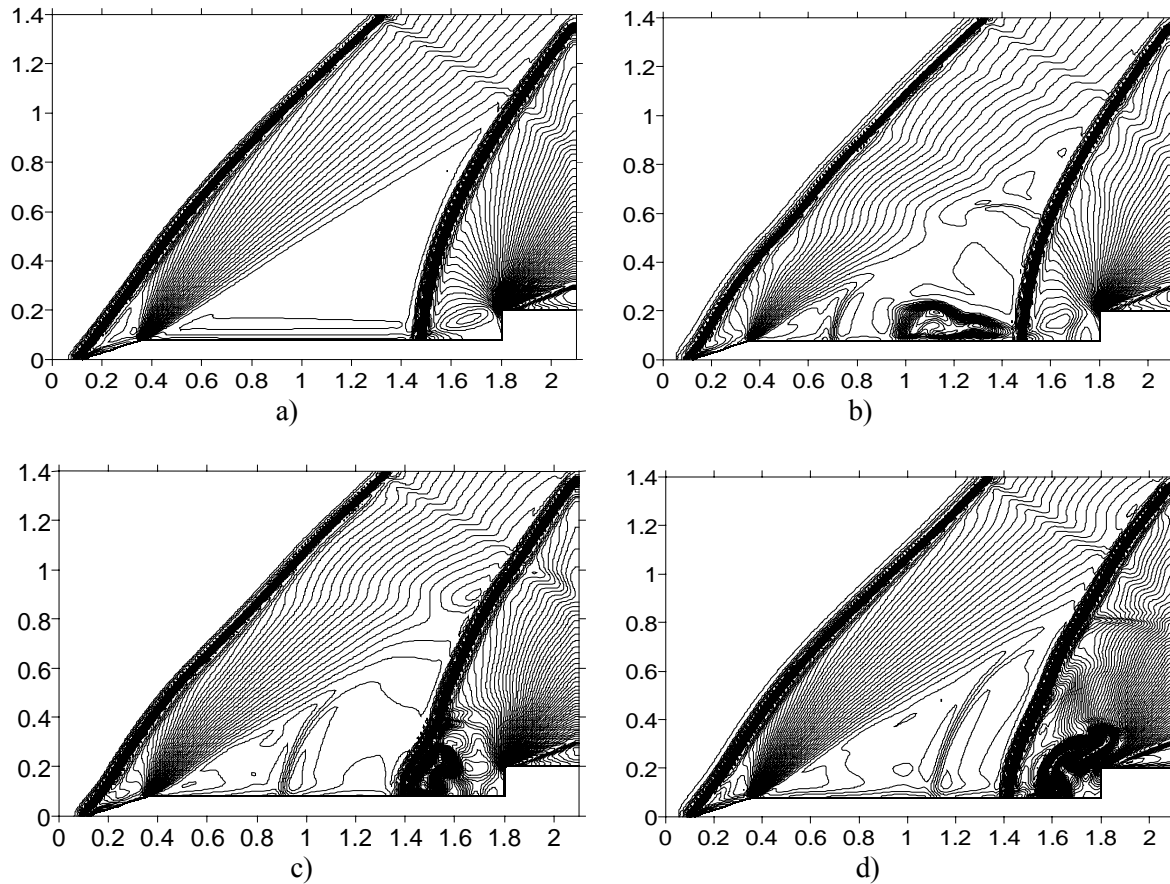


Fig.6.39. Effect of a short MW energy release domain on stationary streamlining of a blunt body with a long sharp spike: a) $t=10$, b) $t=11.6$, c) $t=12.1$, d) $t=12.6$

Conclusions

In spite we understand that the basic processes underlie the phenomenon of spike-tipped body streamlining are deeper and include separation, our qualitative modeling is aimed at highlighting of those general regularities which were revealed in our previous investigations.

The observed in our Euler approximated modeling effects of MW energy deposition on a supersonic flow past blunt body with a spike are as follows:

- generation of the vortex structure;
- changing the stationary shock waves system;
- arising of the additional shock waves with different mechanisms of generation.

Not all features of the experimentally observed phenomenon of MW energy deposition action on spike-tipped body streamlining (see Section 5.4) are well explained by this modeling, but we hope to achieve better understanding via step-by-step comparison of modeling and enhanced-quality experiment.

7. General view on Beamed Energy Deposition method abilities and efficiency

In this Section we summarize the most important physical results, which deliver the general understanding for beamed energy deposition method in application to drag/flow control in supersonic flow. Different examples – already presented in previous Sections and new ones - demonstrate abilities of flow control by proper choice of discharge structure in front of AD body, been realized in experiments. Very important topic – scaling in MW channel – AD body interaction – is investigated under the limited conditions of experiment. We also formulate for the proposed method the universal physical mechanism, its application range and ultimate efficiency, as well as the requirements for the performance of MW discharge for efficient method application.

7.1. Effect of channel off-axis position variation

Integral effect for the case of channel displacement in radial direction (see Section 4) is calculated. The results are shown on Fig.7.1. It is seen that impulse changes it's sign while increasing the distance from the axis and maximum positive impulse (at $y=0.25$) has value twice less than negative one (at $y=0$).

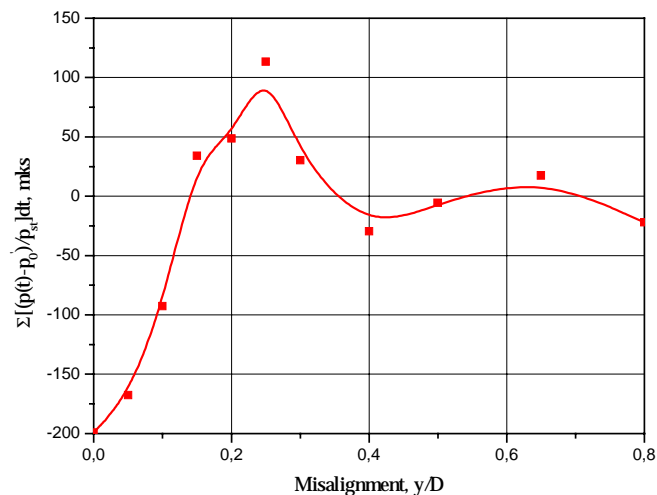


Fig.7.1. Quantity proportionate to impulse, which is imparted to the blunt cylinder during plasma – shock layer interaction via misalignment.

This also defines the scale of sensitivity of drag reduction to position of discharge channel.

7.2. Discharge structural factor for flow control

Variety of MW discharge structures made it possible to investigate experimentally the abilities of discharge structure for flow modification. Earlier we've treated numerically situation when instead of one discharge channel placed on the axis of symmetry of a blunt body, there appear two symmetrically off-line disposed channels. It was shown (Fig.7.2) that in this case two vortices originate in a shock layer, their rotation leading to pressure increase at stagnation point.

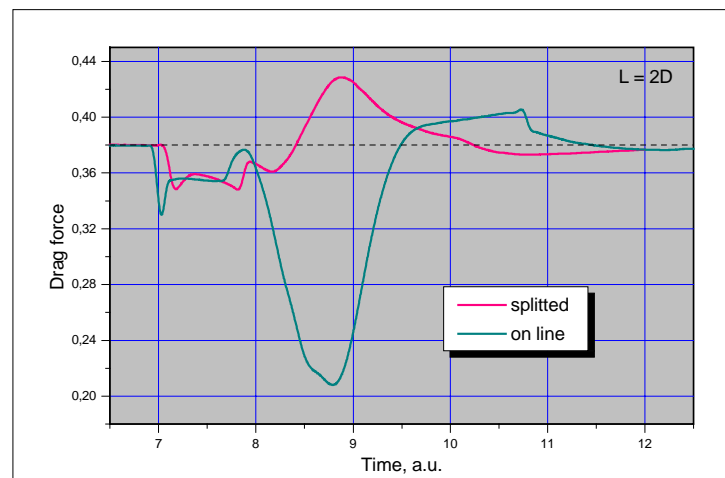
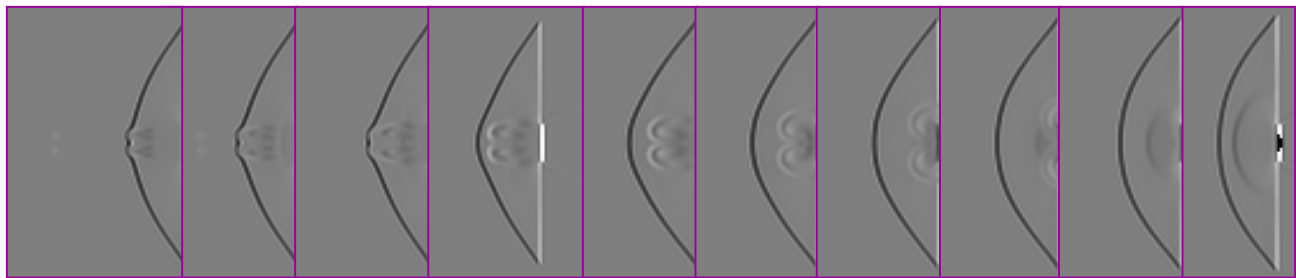


Fig.7.2. Computation of split-well action on blunt body, Shlieren-type (upper) and pressure

We've have realized this discharge geometry in experiment. Experimental conditions were similar to those mentioned above – Mach number of airflow 2.1, model diameter 20mm. Stagnation pressure evolution was registered by the Kulite sensor, which fixed single realization (non-averaged) of pressure signal.

Below are presented the instant photo of MW discharge structure and appropriate signal from pressure sensor.

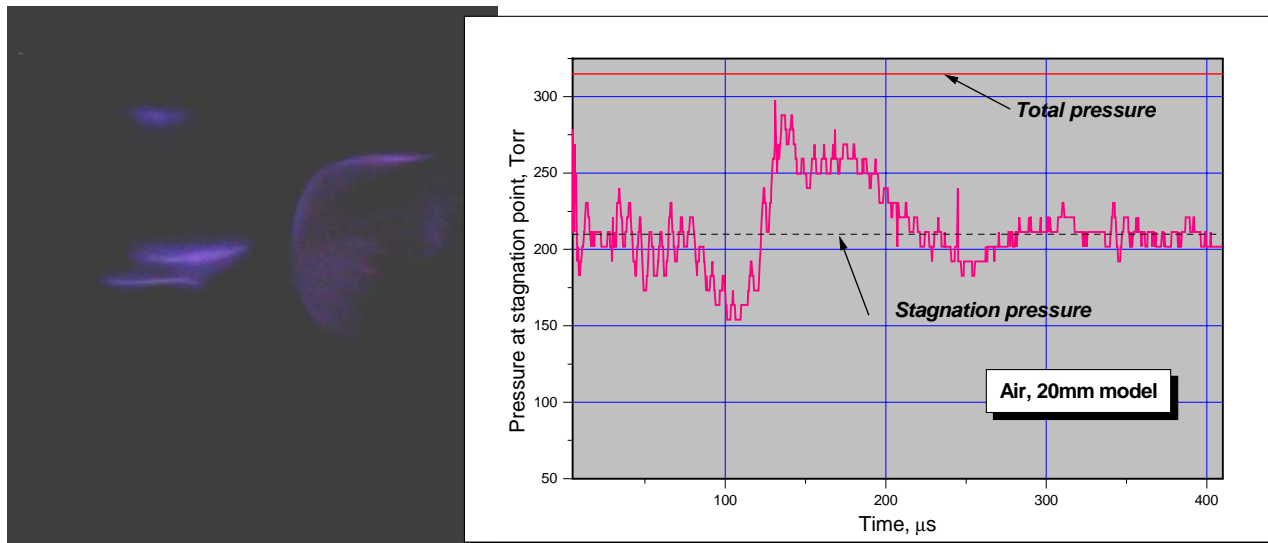


Fig.7.3. Instant photo of 2-channels discharge (left) and stagnation pressure signal (right)

It is seen that two MW plasmoids originate in front of AD body. They are not equal each other in luminosity, but are nevertheless, comparable in brightness (and, hence, in absorbed energy). Most probably, they appear one after another (not simultaneously). But due to short MW pulse (about 1.5mcs) energy deposition from plasmoids can be regarded as practically simultaneous. One can also see the luminosity on body surface due to MW surface discharge. But its input in pressure behavior is very limited. The distance between channels is of order several millimeters.

The pressure signal obtained as a result of two channels action dramatically differs from that obtained from the action of one channel. On the contrary to one centered channel action, when stagnation pressure dropped down about 3 times, in this geometry stagnation pressure grows up for more than 25% from its nominal value. This simple example demonstrates abilities of flow control by proper choice of discharge structure in front of AD body.

In spite the final result for flow control – pressure behavior – is very similar to that obtained by off-axis displacement of a single channel, these cases are quite different from point of view of processes inside shock layer. In the case of two channels there appear 2 symmetric vortices, whereas in asymmetric case only one vortex originates (see Section 4).

7.3. Scaling in discharge channel – blunt body interaction

Modernization of gas dynamic stand has sufficiently widened possibilities in testing AD bodies of different dimension. We've conducted special set of experiments to eliminate the scaling law in discharge channel – blunt AD body interaction. The lower limit for cylinder dimension was determined by conditions for Kulite installation inside the model and turned out to be 8mm. The upper limit is defined by the flow diameter. As the last is now 60mm, the upper limit of AD body diameter is 20-24mm. Thus, we are able to test AD bodies in half-of-order range – from 8mm to 24mm.

On Fig.7.4 stagnation pressure evolution is shown for the blunt cylinders of different diameter. It is immediately seen that time of plasma – body interaction becomes larger with diameter of cylinder increasing.

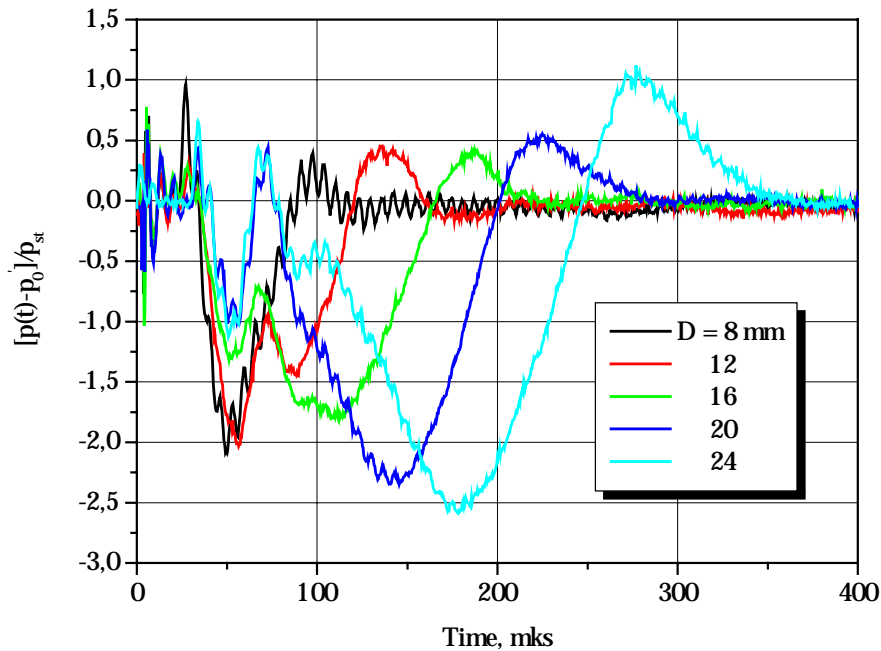


Fig.7.4. Stagnation pressure evolution on blunt cylinder of different diameter

Remind that stagnation dimensionless pressure change is defined as

$$\frac{p(t) - p_0}{p_{st}} = f(t).$$

$p(t)$ – stagnation pressure on the blunt cylinder in the flow with discharge,

t – time,

p_0 – stagnation pressure on the blunt cylinder in nominal condition (without discharge),

p_{st} – static pressure in the flow.

This function is needed to estimate impulse which is imparted to the blunt cylinder during plasma – shock layer interaction.

Quantity proportionate to impulse is defined as integral over time from pressure change:

$$\int_t \frac{p(t) - p_0}{p_{st}} dt.$$

Integral is calculated over the entire investigated time period.

It is also indicative to present the pressure signals in time-dimensionless manner, introducing time scale $t_* = D/u_0$, where D is model diameter and u_0 is flow velocity. The result of such procedure execution is given below (Fig.7.5).

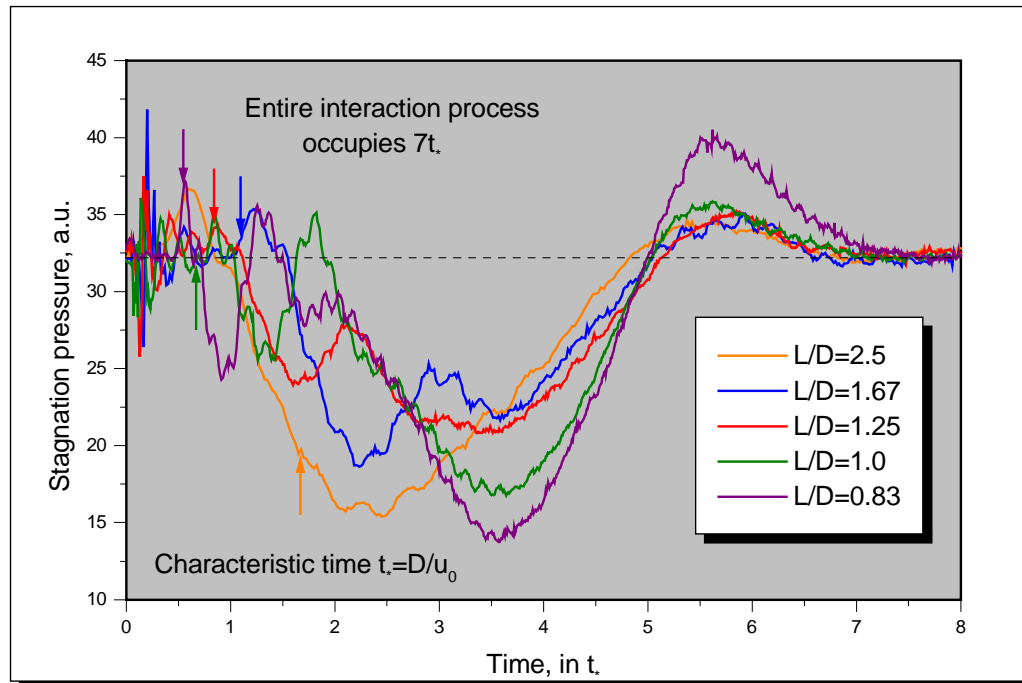


Fig.7.5. Pressure signals in natural time scale. Arrows show the moment of complete channel "absorption" by a shock layer

In these coordinates the entire process of interaction for each body occupies practically the same dimensionless time interval – about $7 \cdot D/u_0$. Calculation of integral of pressure change over time has led to the result presented on Fig. 6.6. Dashed line presents the mean effect value.

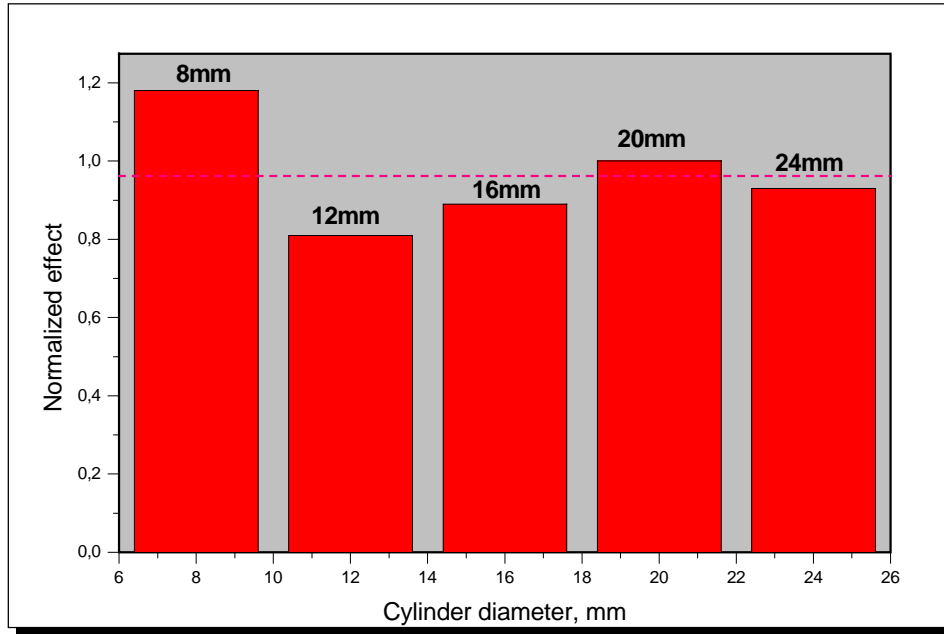


Fig.7.6. Integral effect normalized on that for 20mm body over body diameter

The result of integration is normalized on the value for 20mm body. We can conclude that in normalized (natural) time coordinates the integral effect is practically independent of blunt body diameter. ***This means that actual effect grows linearly with body diameter!*** Moreover, the total drag effect integrated over front surface is to be proportional to D^3 .

On Fig.7 the value proportional to the effectiveness of MW discharge for drag reduction is presented as a function of body diameter. This value was calculated as

$$D^2 \cdot \int_t \frac{p(t) - p_0}{p_{st}} dt,$$

where D – diameter of the cylinder.

It is seen that effectiveness of MW discharge using for drag reduction raises with body diameter increasing dramatically, actually near D^3 .

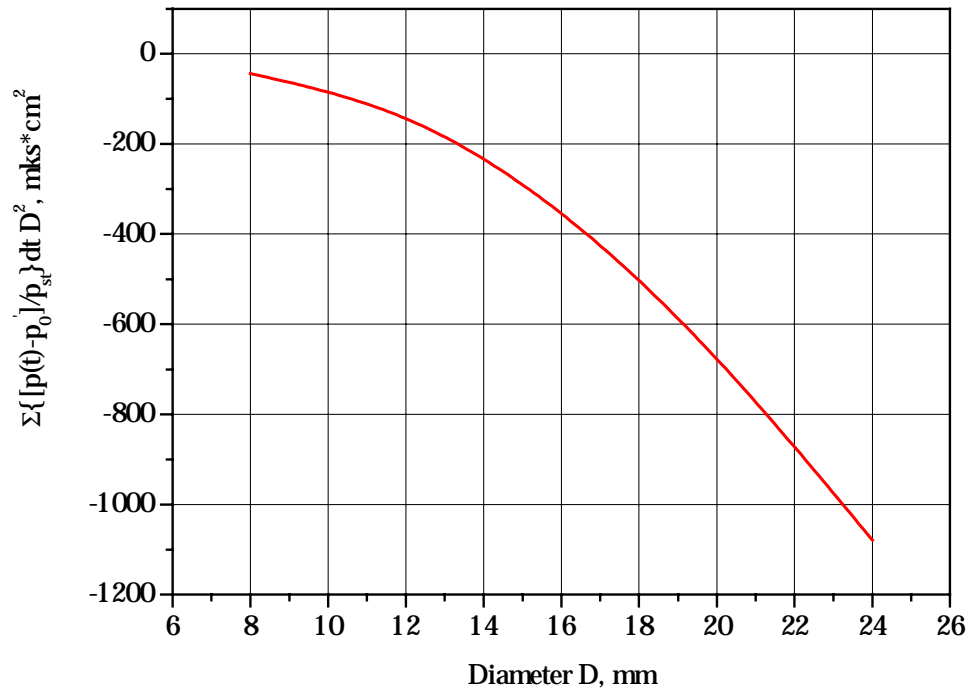


Fig.7.7. Relative effectiveness of MW discharge for drag reduction over diameter of blunt cylinder.

The result obtained seems amazing as theoretical considerations evidence for integral

effect $I = \int_t \frac{p(t) - p_0}{p_{st}} dt$ as being independent of body diameter under the condition of fixed

channel length. Indeed, let us imagine blunt body of fixed size and a channel in front of its BSW of length L . Now let us re-scale all the dimensions, say increase them in m times, keeping the flow parameters unchanged, i.e. Mach number the same. In this case all gas dynamic parameters will stay the same, but all dimensions (like standoff) will increase in m times. This means that the integral effect will increase in m times or it will be the same in natural time scale (in D/u_0 units). If we now diminish the length L in m times, I will also decreased in m times (this was previously confirmed by numeric calculations in some range of D/L values) and $I = m \cdot I/m$ will return to its initial value. But this is just situation when we increased the body diameter, keeping channel length constant. The transverse dimension plays practically no role in this interaction, as was also shown previously. Thus, in experiment we have additional (in comparison of what we

could expect from theory) rise of efficiency with body diameter increase – linear rise except of zero one.

It is also seen from Fig.7.4 that the structure of pressure signal changes significantly if compare signals from 8mm and 24mm bodies. The case of smaller body is closer to the situation of relatively long discontinuity – $L/D=2.5$, whereas for large body - to transient one ($L/D=0.83$). It should be kept in mind that probably not all details in pressure evolution in the case of 8mm body are resolved because of temporal resolution limitations of the pressure sensor.

According to our investigation of non-stationary interaction of channel with blunt body (see Section 6.2), stagnation pressure fall consists of two portions. The first – it is also the first in time – is due to rarefaction wave, arising from contact of leading tip of discontinuity with BSW. The depth of this fall is governed by D/d parameter, where d is the diameter of discontinuity. The closer is this parameter to the unity, the more pronounced pressure fall is observed. In the case of $D=d$ we have situation of body streamlining by a uniform heated region. No vortex formation in a shock layer can be observed in this case. Obviously, this regime does not lead to any gas dynamic structure transformation and is not effective.

Under the diminishing d over D ratio the impact of the first mechanism goes down and the role of vortex formation mechanism grows up. This is reflected by the second - more pronounced and vast region of pressure fall in stagnation pressure dynamics. The structure of a flow exerts a significant change - bifurcation. This is the most effective mechanism of drag reduction.

7.4. Physics of interaction

The sense of reformation of gas dynamic flow structure by energy addition can be formulated in simple manner. To reduce drag we are to substitute the normal shock by the oblique shocks. This is just the same what happens when we use wedge or cone, or spike instead of blunt body. Longitudinally disposed discharge channel serves as a virtual spike (this comparison is not complete!) and reform the flow around the model. In the case of relatively short discontinuity, the process of reformation is limited by phase of vortex formation and its interaction with blunt body. During this phase the temperature at stagnation point falls down in some cases practically to the static temperature of the oncoming flow. With elongation of discontinuity, the precursor shock structure goes further and further upstream until reaching the

ultimate standoff (this is described in details in Section 5). By this moment the pressure fall reaches its lower point and shock wave system gradually relaxes to its new stationary state. In the case of infinite discontinuity there appear new stationary gas dynamic structure, which resembles streamlining of a virtual cone (or wedge in 2D plane geometry), the last being defined by contact surfaces position. We are to strengthen that the transverse dimension of discontinuity plays no role! It is clearly seen that the drag of blunt body is significantly reduced, in about a coefficient of temperature rise in discontinuity. Generally speaking, this new pressure at stagnation point is now the static pressure after the oblique shock, which is much less than the pressure after the initial normal shock.

In the case of sharpen bodies as it was shown in Section 6.4, there appear a threshold in density depth for attaining drag reduction. It is clear from above description that to reduce pressure we are to reduce the angle of the oblique shock. It can be made only if we can detach the shocks from cone (wedge) tip. Thus, the detachment criterion is rather simple – it occurs if interaction with discontinuity can potentially diminish the angle of the oblique shock. The density in discontinuity, which results in wave structure of an actual cone, can be determined as critical, or threshold one. It can be shown that under some limitations this critical relative density can be defined as

$$\rho_* = (1/M_0 + \sin\chi)^2.$$

Therefore, it is more difficult to produce drag reduction for more perfect body from aerodynamic view. This expression can be generalized over greater nomenclature of AD body shapes if one can describe this body in respect of its c_{x0} by some effective angle χ .

Also it is readily seen that production of disturbance with subsonic conditions inside is excessive, as adds practically nothing to pressure decrease (see Section 6). On the base of stated above we can formulate for the proposed method universal physical mechanism, application range and ultimate efficiency.

7.4.1. Universal physical mechanism for AD body drag reduction

Formulations for unsteady and steady cases of interaction with *blunt* body:

- Unsteady: Creation of a counter-flow jet in a shock layer via vortex flow generation
- Steady: Bifurcation in the type of streamlining - from blunt to virtual sharpen

Formulations for unsteady and steady cases of interaction with *sharpen* body:

- Modification of streamlining towards virtual sharpen with less angle

For all cases:

- Decrease of the total entropy production

We believe that all other effective gas dynamic methods of drag reduction creation (for example, a counter-flow jet) also have very similar physical basis.

7.4.2. Method application range

The potential benefit of method application can be generally estimated by parameter $M_0^2 \sin^2 \chi$ (M_0 is cold flow Mach number, χ - is an angle, characterizing the body shape), which should be greater than unity for a strong effect. Nevertheless, effect of drag reduction can be achieved for practically any value of mentioned parameter.

The range of efficient rarefaction is defined as

$$1/M_0^2 < \rho < (1/M_0 + \sin \chi)^2,$$

which means that conditions inside the channel are sonic (left) and that the detached regime of interaction is to be realized.

7.4.3. Physical efficiency

Ultimate physical efficiency η (i.e. saved power over spent one) in respect of wave drag reduction by means of discontinuity interaction with aerodynamic body with AD performance characterized by c_{x0} can be expressed as

$$\eta \sim c_{x0} \cdot M_0^2 \cdot (D/d).$$

Here D - AD body diameter, d - transverse dimension of discontinuity. High efficiency can be attained along with noticeable diminishing in drag.

The physical sense of this expression can be understood from two considerations. The first reflects the fact that we spend a finite amount of energy to create a density well (for a perfect gas) in a quasi-static isobaric process, this amount entirely depending of its final diameter. The second is statement that the ultimate wave drag reduction is attained when this drag is eliminated completely. After this explanation the expression written above becomes trivial. We are to emphasize that this is the absolute limit for efficiency, which can be attained by this method. It can not be made higher whatever one can apply for discontinuity creation.

Experimental results for scaling. Experimentally obtained efficiency value for 30mm diameter blunt body under $M=2.1$ flow conditions is about 30. This means, that having deposited of about 30mJ in specific MW plasmoid we've saved 1J in body drag during interaction with it. The same result was obtained for 30mm hemisphere. It should be taken into account that only 10% of the absorbed energy go directly to heating of gas, i.e. 3mJ (this value is confirmed by estimation through shock wave dynamics from MW channel registration). This means physical efficiency 300. Moreover, the effect is caused by thin overheated filament inside the channel. We have no direct measurements of energy absorbed in it, but estimation made via combination of modeling of processes inside and experimental data delivers value of 0.3mJ (due to the fact that filament is very thin, see below). Thus, estimated efficiency exceeds 1000. This is in agreement with a concept developed, as efficiency formula includes D/d ratio (in our case this large parameter is about 1000, if assume filament diameter as $d=3 \cdot 10^{-3}$ cm). There are some evidences (heating rate value, for example) that manifest in favor of smaller size of filament.

Scaling curves for blunt cylinders and hemispheres of diameters 8-30mm are presented at Fig.7.8. We can conclude that actual effect (quantity I) grows linearly with body diameter and the total drag effect (for blunt cylinder) integrated over front surface is to be proportional to D^3 .

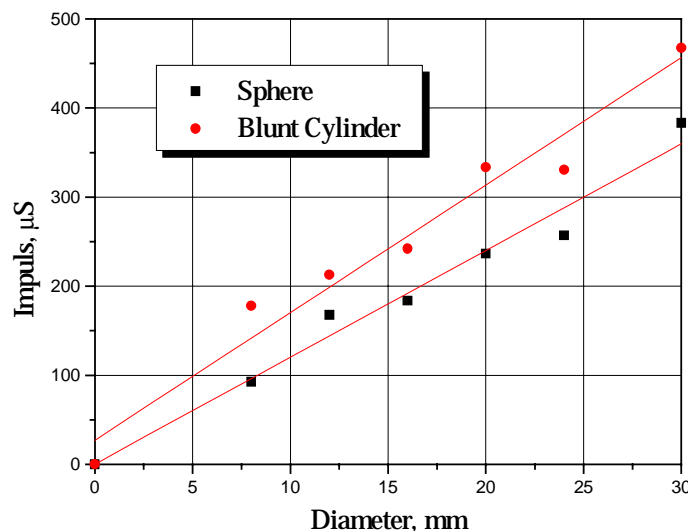


Fig.7.8. Effectiveness of MW discharge for drag reduction over diameter of blunt cylinder and hemisphere

The result obtained seems amazing as theoretical considerations evidence for integral effect ΔI as being independent of body diameter under the condition of fixed channel length (see

above). Thus, in experiment we have additional (in comparison of what we could expect from theory) rise of efficiency with body diameter increase – linear rise except of constant one.

Also scaling investigation was fulfilled for the case of Y polarized microwave discharge and ΔI was defined. The result of investigation is presented on Fig.7.9.

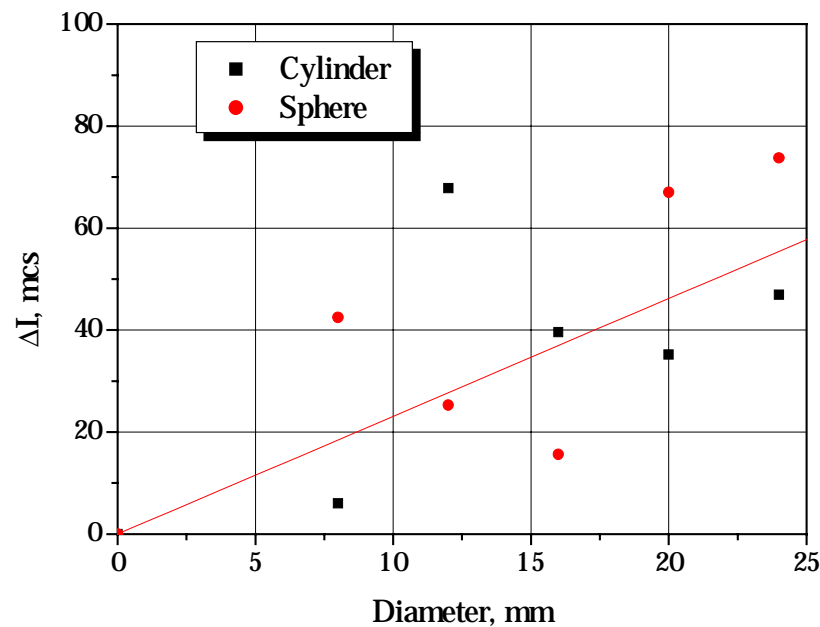


Fig.7.9. Effectiveness of microwave discharge for drag reduction over diameter of blunt cylinder and sphere. Y polarization.

Effectiveness of discharge in the case of Y polarized discharge is visibly less (in about 4 – 6 times) than in the case of X polarization. So, these two cases differ from each other significantly. The discharge elongated in the direction of the axis of the model (X polarization) is most preferable for drag reduction.

7.5. Structure of discharge and discharge performance requirements for efficient application

It is obviously seen from above that discharge structure, its fine structure and methods of discharge creation is of great importance. The challenges from gas dynamics dictate creation of strongly non-uniform discharges, containing thin filaments with high level of energy concentration and therefore, high rates of energy liberation from internal to translational degrees

of freedom and high temperature. All this under very modest total energy deposited for filament creation. The results of Section 2 and 3 show that every type of MW discharge can be conventionally referred to inhomogeneous ones. What is common between MW channel in self-breakdown field and the low-threshold stimulated ball discharge? They both have some condensed part - filament or electrode surface thin-film – and relatively bulk domain - halo or ball region itself.

For our specific application only basis in these structures are of benefit. But practically the entire discharge power is dissipated in outer domains of discharge structure i.e. is spent useless. Thus, the concept of “undressed” discharge becomes urgent. The last can be done either by gas flow (as is done with ball discharge, Section 2) or by application of special (combined) tools for selective creation of filaments with low-level energy expense. This is very perspective trend, which we’ve proposed for the future Project.

We can now summarize requirements for effective application of MW discharge to drag/flow control issue. So, the requirements to MW discharge include control of its location, structure, intensity, stability and reproducibility, length in some interval of Mach numbers of airflow. Precise alignment of discharge position to sharpen body axis is especially urgent. We can generalize the trend – the higher aerodynamic performance the body has, the higher requirements are to be guaranteed for method application.

In the case of positive solution for each of the enumerated positions the pre-technologic stage might be achieved.

Summary

Flow modification by means of EM coupling turned out to be both effective as a tool and exciting from scientific point of view. The most impressive characteristic features are flow modification in bifurcated manner, spatial dimension(s) compactification, thresholds in interaction dependent on body performance, and others. Three phenomena – drag reduction via discharge-induced vortex creation in a shock layer, regular-Mach discharge-induced transition in intersecting shocks, radical change in separation flow in streamlining of spike-tipped bodies through discharge-affecting of viscous interaction - cover the most impressive areas of plasma aerodynamics and at the same time form its basis. Alike the Bernard convection in liquid between two heated plates initiated Synergetics, such phenomena could form the basis of plasma

aerodynamics. Each of these phenomena demonstrates wide abilities of MW energy deposition method and presents the complicated physics, which is not fully understood yet. In our opinion the list of such phenomena is still open and looks far from been completed and future developments will sufficiently enlarge it. In spite all the observed phenomena can be attributed to classical plasma aerodynamics, the presence of chemically active flow can be naturally embedded in conception, as well as main approaches can be generalized for this case. Beamed energy deposition as a principle tool for realization of aerodynamic phenomena guided by energy control in selected critical points seems both claimed and inherent and in general demands application both MW and laser techniques.

Main results

As it was mentioned in Introduction, the sense of the Project #2014p “Physics and Chemistry of Microwave Discharge in Gas Flow” is obtaining and investigation of MW discharges under different conditions and application the most perspective of them to plasma aerodynamic purposes. The Project tasks were implementing hand by hand with deep modernization of installations, improvement of diagnostics and developing of new codes. Below brief description of the main investigation trends and obtained results are given.

MW discharge in magnetic field and under other conditions (experiment)

New type of MW discharge – directed MW discharge – was realized and investigated in magnetic field and airflow. The most convenient turned out the near-surface MW discharge. The stable MW discharges, traveling along dielectric plate, were received in experiments. By changing MW power parameters or by using the gas flow and magnetic field the control over such discharges was realized. The main results of this discharge experimental research are the following. The SMD structures are very sensitive even to not large levels – 10...50mT - of magnetic field. Experiments with dynamic magnetic field of rather low levels demonstrate the possibility of the discharge parameters and size controlling.

Let us note some discharge structure changing in magnetic field:

- the increasing of plasma channels in discharge area and at the channels tip ,
- the spiral and curling plasma channels form formation,
- the channels color changing occurring in magnetic field.
- The SMD may be ignited or stopped by external magnetic field switch off/on.
- Plasma channels volume density is increasing in airflow. Energy deposition also increases in this case.
- The use of directed systems favors to SMD control range widening. Rather large near-plate MW discharge can be created along dielectric plate.

MW discharge study under relatively high gas flow velocity ($V \sim 0.8-1M$) demonstrates the possibility of its structure significant modification. MW discharge may propagate along the gas flow or drift by the gas flow.

New RF unit was assembled and tuned. For the first time low threshold RF ball discharge was ignited. The similarity of ball RF and MW discharges is shown.

Experiments with MW and spark discharge were carried out. On our opinion we've selected the flexible model object - the pulse air spark, which is very similar to the separate MW plasma channel and may be used for its study in some cases. For the first time we revealed the effect of very strong interaction of free microwaves with an external plasma channel. At the early evolution phase the channel practically develops along the force electric line of convergent wave. This effect demands more experimental attention and may be of importance both for practical use and/or as fundamental trend for further research.

The results of experimental study of MWD interaction with magnetic field and directed systems demonstrate the possibility of MW energy expenditure optimization on creating of the demanding plasma structure, size and volume.

Measurements of discharge local parameters

The measurements of MW discharge and separated plasma channel parameters in air were carried out both by intrusive (probe) and non-intrusive (optic) methods. Optical emission spectra obtained from MW discharge in supersonic flows of air and nitrogen has shown that along with the second positive nitrogen system bands, the first negative system bands of the positive nitrogen molecule ion are definitely observed. Gas temperatures defined by processing of the rotational spectra bands of each system turned out to differ strongly. This fact let us suppose that light emission from nitrogen molecules and ions is coming from different spatial domains - the second positive nitrogen system is lightening from the relatively cold bulk halo, whereas the first negative – from the hot breakdown filament. Gas temperature in channel filament turned out to be about 3000K. Comparison of the results of kinetic modeling with experimental ones let us determine the minimal electron concentration in filament as 10^{16}cm^{-3} under 70Torr air pressure and its dimension as less than 10^{-2} cm. The results obtained by probe measurements under atmospheric pressure also gave the channel conductivity of the order of several Moh/cm. New diagnostic – Thomson scattering – is applied for direct non-intrusive measurements of electron temperature and concentration.

Modeling of discharge kinetics

Unification of optic information processing with discharge kinetic modeling sufficiently rises the validity of obtained results. Therefore, kinetic method for description of MW discharge in air was further developed. The updated kinetic model includes:

- the method for calculation of electron-neutral interacts rate constants concerted with specific character of vibration distribution function (VDF), which is formed in gas discharges in air;
- the formation of the adequate kinetic mechanism for description of both filament and halo of MW plasmoid including expert estimation for individual reactions rate constants;
- the selection of reliable kinetic channels of plasma heating.

Summarizing and updating of information about radiative and collisional processes of electronically excited nitrogen states was provided. This action was aimed at further validation of the used database.

Self-consisted numeric investigation of the active phase and relaxation in the main discharge domain (halo afterglow) is carried out with taking into account influence of energy deposition on the rate constants. This allowed both make more precise the parameters of discharge halo by the end of MW pulse and to investigate relaxation of the main components after pulse termination at $100\text{-}\mu\text{s}$ scale. In comparison with the previous calculations the specific energy input turned out to be 1.5 times higher and reached about 0.5eV/molecule . This fact has led to intensification of the super-elastic collisions and acceleration of high-threshold processes, as well as some deceleration of electron recombination process. During time interval from $30\mu\text{s}$ to $100\mu\text{s}$ concentration of negative ions is nearly constant and is about $2\cdot 10^{11}\text{cm}^{-3}$, which is rather large value. Electron temperature at the decay phase is equal nearly 0.3eV , being practically constant. The amount of oxygen atoms by the end of impulse reaches 4% of the total particles density number, it means that about 10% of oxygen molecules are dissociated in electron-neutral and electronically excited species reactions. In the conditions under consideration this fact does not affect greatly on temperature rise in VT-relaxation process, but in a warm flows it can be of remarkable importance.

Numeric investigation of kinetic processes in MW discharge halo and filament has been fulfilled. The parameters of MW plasmoid internal structure are quantified. Solving of the problem of gas heating rate in filament with taking into account the detailed information about partial probability of dissociative recombination channels was proposed. This approach leads to reasonable agreement with experiment. Thus, combination of experimental curves fitting and direct kinetic modeling let obtain verified information about the local discharge parameters. At 70 Torr air pressure and breakdown conditions for pulse duration $1.5\mu s$ the main domain (halo) can be characterized by specific energy input about $2J/cm^3 atm$, peak electron concentration about $6 \cdot 10^{13} cm^{-3}$ and temperature rise 80-100K. The rate of heating for the main domain of plasmoid is $\sim 100 K/\mu s$. Electron concentration in the filament exceeds $5 \cdot 10^{16} cm^{-3}$, the specific energy input being about $7eV/particle$. Rate of heating in the filament is sufficiently higher than in the halo attaining $\sim 2-3 kK/\mu s$. Gas temperature in the filament obtained for the moment of MW pulse termination turned out to be 2 800K.

Processing of discharge emission spectra

Method for decoding of optic spectra from strongly non-homogeneous object and extraction of optical information from highly non-homogeneous objects has been proposed. Emission of species with high-energy production threshold can deliver information about temperature distribution in strongly non-homogeneous discharge structures. Among such species radicals CN, OH, C₂, CH and others play an important role. Preliminary conclusion was made that optical emission from different species is coming from different spatial regions of discharge structure. Thermodynamic analysis has shown that emitting species manifest rotational temperatures, which are in a good agreement with the temperatures of maximal concentrations of these substances under equilibrium conditions. In other words, emission of each substance brings information from the plasmoid layer with the temperature not less and not much higher than this certain one. So, the most power-consuming substance observation allows to “penetrate” inside the most power-saturated layers of MW plasmoid. Special attention was paid on reduction of atomic lines. Stark broadening elimination has led to direct estimation of electron concentration in discharge channel. Also the work over molecular spectra of directed MW discharge was aimed at further characterization of its parameters. Optic data reduction has been applied for investigation of different discharge types, such as MW discharge in free space, MW plane-

directed discharge and impulse spark. As distinct lines of atomic nitrogen atom were seen in spark spectra, Stark broadening technique was applied. The channels of these discharges turned out rather similar in their characteristics, the fact, which confirmed our choice in model selection.

Gas dynamic experiments for drag/flow control

Experiments on longitudinally oriented (X-polarized) MW discharge filaments interaction with different types of AD bodies were conducted at the modernized gas dynamic stand equipped by sufficiently improved Schlieren facility, which now enables to receive instant images with time-gating. Also synchronized (with Schlieren) time-gated imaging in chemiluminescent emission was applied to better fixation of position and structure of MW discharge region. Typical types of AD bodies were blunt-nosed cylinder, hemisphere and wedge with half-angle about 22 degrees. Also important is that due to increased free-flow diameter (60mm) experiments could be made with better spatial resolution. The diameter of tested models was increased up to 24mm that is 3 times larger than what was available in previous experiments. For the first time vortex origination and evolution in the shock layer was registered. Also measurements of stagnation pressure evolution were conducted by Kulite sensor for a set of cylinder diameters – from 8mm up to 24mm, or in a half-order range. Improvements in diagnostics let us obtain for the first time synchronized Schlieren and Kulite data. The work for creation of data bank for realized MW discharge structure and its pressure signature in stagnation point has started. Another investigation trend concerned testing of ability to control flow parameters by displacing of discharge region away from the central axis. In such manner asymmetric interaction was realized and investigated by Schlieren and chemiluminescence (for cylinder and wedge), and Kulite (for cylinder).

Scaling curves for hemispheres and blunt cylinders in the range of diameters from 8mm to 30mm are obtained. They demonstrate linear growth of the module of mean stagnation pressure (over front surface) value decrease with body diameter increase. Experimentally obtained efficiency value for 24mm diameter blunt body under $M=2.1$ flow conditions is about 30. This means, that having deposited of about 30mJ in specific MW plasmoid we've saved 1J in body drag during interaction with it. The same result was obtained for 30mm hemisphere. It should be taken into

account that only 10% of the absorbed energy go directly to heating of gas, i.e. 3mJ (this value is confirmed by estimation through shock wave dynamics from MW channel registration). This means physical efficiency 300. Moreover, the effect is caused by thin overheated filament inside the channel. We have no direct measurements of energy absorbed in it, but estimation made via combination of modeling of processes inside and experimental data delivers value of 0.3mJ (due to the fact that filament is very thin). Thus, estimated efficiency exceeds 1000. This is in agreement with a concept developed, as efficiency formula includes D/d ratio (in our case this large parameter is about 1000, if assume filament diameter as $d=3\cdot 10^{-3}\text{cm}$). There are some evidences (heating rate value, for example) that manifest in favor of smaller size of filament.

Transversely oriented MW discharge (Y-polarized) was investigated in supersonic flow. The Schlieren and chemiluminescent methods show the absence of any vortex processes in the shock layer. The pressure fall is essentially less (in 5 times) than in the case of X polarized interaction. The scaling law demonstrates the same behavior.

Gas dynamic modeling and analytic treatment for conceptual purposes

Numeric modeling of streamlining of a blunt body by a supersonic flow with a finite thin heated channel on the axis of it was fulfilled. The modeling approach is based on numerical analysis of the Euler equations for inviscid gas flow. Energy injection was assumed to occur in a rectangular spatial area. If the transverse dimension of the heated region is less than that of the body, the *vortex* is being generated inside the perturbed area between the bow shock wave and the body during interaction. Diminishing of transverse dimension of discontinuity leads to noticeable increase of interaction efficiency even under the same gas temperature of discontinuity (i.e. under the total energy input decrease). *The value of the effect remains practically the same.* Increase of longitudinal dimension (length) of discontinuity does not affect efficiency (it remains constant in the area of parameters considered), but leads to the more pronounced decrease of mean pressure reduction. On the contrary, diminishing of longitudinal length and increasing of the transverse one leads to the sufficient fall down of the value of the effect. From the viewpoint of efficiency, quasi-static energy deposition (i.e. under a constant pressure in discontinuity, which is equal to that in a medium) is more efficient than explosive one. For the adiabatic regime

of energy input the distance of the domain from the body also becomes an influential parameter. Efficiency dramatically increases with Mach-number increase.

Also investigated was the case of infinite (stationary) discontinuity interaction, which admits analytic treatment. Both supersonic and subsonic flow conditions inside a channel were considered. Thus, all cases of discontinuity interaction with a blunt body were described in unique approach. Moreover, this approach was successfully applied also for the description of a sharpen body (wedge as the simplest representative) interaction with such type of infinite discontinuity. Numeric modeling confirmed the validity of assumptions accepted in analytic treatment. The stationary gas dynamic geometry turned out to be independent on the body shape. The shock detachment criterion was formulated - detachment occurs if interaction with discontinuity leads to diminishing of the shock angle, and simultaneously the pressure after the shock. Reduction of a sharpen body drag at a fixed portion demands deeper rarefaction of gas in a channel than in the case of blunt body. The dependencies of shock detachment velocity on the dimensionless density in the channel for blunt body and wedge were obtained. Comparison with experimental values manifests in favor of highly non-uniform structure of MW plasmoid.

The influence of MW release on non-stationary streamlining of wedges with varied angle was numerically investigated. Effects revealed are: the considerable reduction (up to 50%) of the drag force of the wedge surface, the effects of MW release are stronger for deeper rarefaction in discontinuity, the dependence of drag reduction upon body angle is close to linear. For the cases of detached bow shock wave the values of the rate of changing the SW standoff and of the rate of changing the circulation are equal. These values of the rates can be also defined from the solution of the Riemann problem, describing the interaction of the shock wave and contact discontinuity (boundary of the heat channel). The values of the rates practically do not depend on the body angle and the radius of channel, also these rates are constant in time on the stage of drag reduction for all the considered cases of bodies geometry. Analytic investigation of oblique shock decay under interaction with density well has shown that the maximum velocity of upstream shock movement is attained under the conditions of normal angle of incidence, any inclination leads to diminishing of this velocity. Thus, interaction of oblique shock with heated

region of finite length demonstrates less stand-off than in the case of normal one. This effect is observed in experiments.

Numeric modeling of supersonic spike-tipped body interaction with density well of planar geometry has been initiated. In spite we understand that the basic processes underlie the phenomenon of spike-tipped body streamlining are deeper and include separation, our qualitative modeling is aimed at highlighting of those general regularities which were revealed in our previous investigations. The observed in our Euler approximated modeling effects of MW energy deposition on a supersonic flow past blunt body with a spike are as follows: generation of the vortex structure; changing the stationary shock waves system; arising of the additional shock waves with different mechanisms of generation. Not all features of the experimentally observed phenomenon of MW energy deposition action on spike-tipped body streamlining are well explained by this modeling, but we hope to achieve better understanding via step-by-step comparison of modeling and enhanced-quality experiment.

Realistic physical basis in exploration of the challenging phenomenon in plasma aerodynamics – interference of MW discharge with gas dynamic structures in supersonic flow is formulated. Four basic phenomena, reflecting the main features of such interference can be distinguished. These phenomena – MW discharge filament formation, drag reduction via discharge-induced vortex creation in a shock layer, regular-Mach discharge-induced transition in intersecting shocks and radical change in flow separation in streamlining of spike-tipped bodies through discharge-affecting of viscous-inviscid interaction – cover the most impressive areas of plasma aerodynamics and at the same time form its basis. Each of these examples demonstrates wide abilities of MW energy deposition method and presents the complicated physics, which is not fully understood yet. Discharge structure plays a key role in effective interaction with gas dynamic discontinuities. MW discharge performance requirements are formulated. Beamed energy deposition as a principle tool for plasma aerodynamic phenomena realization seems both claimed and inherent and in general demands application combined MW and laser techniques.

Also summarized are the most important physical results, which deliver the general understanding for beamed energy deposition method in application to drag/flow control in supersonic flow. Different examples demonstrate abilities of flow control by proper choice of

discharge structure in front of AD body, been realized in experiments. Very important topic – scaling in MW channel – AD body interaction – was investigated under the limited conditions of experiment. High efficiency of drag reduction was obtained in experiments and this efficiency rises up with body diameter increase. We've formulated also for the proposed method the universal physical mechanism, its application range and ultimate efficiency, as well as the requirements for the performance of MW discharge for efficient method application.

The product of three parameters define the ultimate efficiency of interaction – the ratio of cross-sections of body and discontinuity, the square of undisturbed flow Mach number and the body aerodynamic performance. In spite of the last parameter can be small, the first two parameters are large, the fact that gives foundation to assume the method of drag/flow control by means of MW energy deposition in supersonic flow as beneficial.

Development of Laser + MW technique

Special activity was aimed at creation of Laser – MW setup, which was successfully developed (see Appendix D). The possibility of laser spark initiation of microwave discharge in quiescent air under the atmospheric pressure has been investigated. The complex Laser – MW setup was assembled. It consists of impulse Ruby laser (6943 Å, 0.22 J pulse energy and 25ns-pulse duration) and X-range impulse MW generator (output power 180 kW, pulse duration 1,2 μs). The results obtained show that semi-self-maintained MW discharge is arising during the time window, corresponding to decaying phase of laser-induced plasma. Contribution of MW energy in plasma luminosity has distinct maximum under the Laser-MW delays 80-110μs, duration of this discharge is defined by MW impulse. For the Laser-MW delay 85 μs the series of shock-wave pictures is recorded. They clearly show the weak quasi-spherical shock wave structure originating due to MW energy contribution.

Thus, the first important step for MW discharge position control by laser-ignited spark is made. The developing technique may become a promising way for creating of spatially compact MW discharges with predictable shape and position for plasmadynamic applications.

This shows the team abilities in realization of new proposals and put basis in the declared way of the discharge performance enhancement.

Acknowledgments

We are sincerely grateful to Dr. Joseph Shang (WSU) and Dr. Charbel Raffoul (WPAFB) for initiation and support of this work. We are also deeply acknowledged to Dr. Datta Gaitonde (WPAFB) and Mr. Wayne Donaldson (EOAED) for their interest and support.

Our deep gratitude is also addressed to the European Office of Aerospace Research and Development (EOARD).

We are especially grateful to Dr. Julian Tishkoff (AFRL/AFOSR), Dr. John Schmisser (AFRL/AFOSR), Dr. David Van Wie (JHU) and all the WIG group for the support of collaboration between Russian and United States scientists, as well as for the opportunity of interaction with the greatest American Universities.

References

Introduction

1. 1st – 5th Weakly Ionized Gases Workshops, USA, 1996 – 2003.
2. Magneto-plasma-aerodynamics in Aerospace Applications, 1st – 5th Workshops, Moscow, IVTAN, 1999-2003.
3. Thermochemical processes in plasma aerodynamics, 1st – 4th Workshops, St-Petersburg, Leninetz, 2000-2003.
4. W. Beaulieu, V. Brovkin, I. Goldberg, A. Klimov, Yu. Kolesnichenko, A. Krylov, V. Lashkov, S. Leonov, I. Mashek, M. Ryvkin, Yu. Serov, “Microwave Plasma Influence on Aerodynamic Characteristics of Body in Airflow”, Proceedings of the 2nd Weakly Ionized Gases Workshop, AIAA, Norfolk, VA, April 24-25, 1998, pp.193-198.
5. V.G. Brovkin, Yu. F. Kolesnichenko, S. B. Leonov et al. “Study of Microwave Plasma-Body Interaction in Supersonic Airflow”, 30th AIAA Plasmadynamics and Lasers Conference, June 28-July 1, 1999 / Norfolk, Virginia, AIAA 99-3740.

Section 2

1. P. Uhlig, J.C. Maan and P. Wyder, "Spatial Evolution of Filamentary Surface Discharges in High Magnetic Fields". Phys. Rev. Lett. **63**, No.18, p.1968 (1989).

Section 3

1. W. B. DeMore, D. M. Golden, R. F. Hampson, et al. “Chemical Kinetics and Photochemical Data for Use in Stratospheric Modeling”, Jet Propulsion Laboratory, NASA, Evaluation 12, 1997
2. S. P. Sander, R. R. Friedl, W. B. DeMore et al. Supplement to Evaluation 12, Jet Propulsion Laboratory, NASA, 2000
3. R. Atkinson, D. L. Baulch, R. A. Cox, et al. “Summary of Evaluated Kinetic and Photochemical Data for Atmospheric Chemistry”, IUPAC Subcommittee on Gas Kinetic Data Evaluation for Atmospheric Chemistry, Web version, 2003
4. A. V. Eletsky, B. M. Smirnov. Uspekhi Fizicheskikh Nauk, v.136, 1, 1982 (in Rus.)
5. L. I. Virin et al. Ion-molecular reactions in gases, Moscow, Nauka, 1979
6. A. Lofthus, P. H. Krupene. The Spectrum of Molecular Nitrogen, J.Phys.Chem.Ref.Data, v.6, 1, 1977
7. A. M. Pravilov. Photo-processes in Molecular Gases, Moscow, Energoatomizdat, 1992 (in Rus.)
8. N. L. Alexandrov, A.M.Konchakov, E.E.Son, Rus: “Fyzika plasmy” (Physics of plasma), 4, 5, 1978, p.1182
9. A. A. Devyatov, S.A.Dolenko, A.T.Rakhimov et al., Rus: “Zh.ETF” (Journal of experimental and theoretical physics), 90, 2, 1986, p.429
10. B. Massabieaux, G.Gousset, G.Lefebvre et al., J.Physique, 48, 1987, p.1939
11. T.G. Slanger, G. Black - J. Chem. Phys. 1974, v.60, p.468
12. Kella D., Johnson P.J., Pedersen H.B., Vejby-Christensen L., Andersen L.H. - Phys. Rev. Lett., 1996, v.77, p.2432

13. Peterson J.R., Le Padellec A., Danared H., Dunn G.H., Larsson M., Larson A., Peverall R., Strömholm C., Rosén S., af Ugglas M., van der Zande W.J. - J. Chem. Phys., 1998, v.108 p.1978
14. van der Zande W.J., Peverall R., Rosen S., Peterson J., Larsson M. - Van A tot Q, 1997/1998, No.12, p.73
15. Guberman S.L. - Amer. Phys. Soc. AAPT Joint Meeting April 19-21, 1997

Section 4

1. Gilmore F.R., Laher R.R., Espy P.E. Franck-Condon factors, r-centroids, electronic transition moments and Einstein Coefficients for many nitrogen and oxygen band systems - J. Phys. Chem. Ref. Data, 1992, v.21(5), p.1005
2. Laux Ch.O. Optical diagnostics and radiative emission of air plasmas - HTGL report No T-288 (Stanford Univ.), 1993
3. Laux C.O., Spence T.G., Kruger C.H., Zare R.N., Optical diagnostics of atmospheric pressure plasmas – Plasma Sources Sci. Technol., 2003, v.12, p.125-138
4. Thermodynamic properties of individual substances - Handbook issue in 4 volumes, Ed. by V.P. Glushko and L.V. Gurvich, Moscow, Nauka, 1978 (in Rus.)
5. NIST Atomic Spectra Database: http://physics.nist.gov/cgi-bin/AtData/lines_form
6. N. Konjevic, A. Lesage, J. R. Fuhra, W. L. Wiese - Experimental Stark Widths and Shifts for Spectral Lines of Neutral and Ionized Atoms (A Critical Review of Selected Data for the Period 1989 Through 2000) - J. Phys. Chem. Ref. Data, v.31, No.3, 2002, p.819

Section 6

1. L.I.Sedov. Methods of self-similarity and dimensions in mechanics, Moskva, Nauka, 1972, 440 p. (in Rus.)
2. V.G.Grudnitsky, Yu.A.Prokhorchuk. A method for constructing difference schemes with arbitrary order of approximation of partial differential equations // Dokl. Acad. Nauk SSSR. 1977. V.234. No.6. P.1249-1252.
3. O.A.Azarova, V.G.Grudnitsky. Front-tracking numerical methods for calculation of flows generated by a local energy injection in liquids and gases // Mathematical Modeling. 1992. V.4. No 12. Pp. 9-13.
4. V.Artem'ev, V.Bergel'son et al. Matematicheskoe Modelirovanie, V.1, No.8, 1989, pp. 1-11. (in Rus.)
5. L. D. Landau and E. M. Lifshits. Theoretical Physics, vol. VI. Hydrodynamics. Moscow, 1986 (in Rus.)
6. H. Mirels. Proc. 16th Intern. Symp. on Shock Waves and Shock Tubes, Aachen, 1987.
7. Snežana S. Miliev, Miloš D. Pavlovi, Slavica Risti, Aleksandar Viti. «ON THE INFLUENCE OF SPIKE SHAPE AT SUPERSONIC FLOW PAST BLUNT BODIES». FACTA UNIVERSITATIS. Series: Mechanics, Automatic Control and Robotics Vol.3, No. 12, 2002, pp. 371 - 382

List of main publications over the Project implementation period

1. Yu. F. Kolesnichenko, D.V. Khmara. Plasma-chemical composition of airflow in MW discharge, relaxation zone and under interaction with bow shock wave of AD body. Perspectives of MHD and Plasma Technologies in Aerospace Applications. 2nd Workshop, Moscow, IVTAN, April 16-17, 2000
2. Yu. F. Kolesnichenko. Multi-scale electric field structure in developing MW-HF discharge channels. Perspectives of MHD and Plasma Technologies in Aerospace Applications. 2nd Workshop, Moscow, IVTAN, April 16-17, 2000
3. Yu. Kolesnichenko, V. Brovkin, et al. Investigation of AD - Body Interaction with Microwave Discharge Region in Supersonic Flows (AIAA-2001-0345). 39th AIAA Aerospace Sciences Meeting & Exhibit, USA, Reno, NV, January 8-11, 2001
4. Yu. Kolesnichenko, V. Brovkin, et al. Influence of Differently Organized Microwave Discharge on AD-Body Characteristics in Supersonic Flow (AIAA-2001-3060). 32nd AIAA Plasmadynamics and Laser Conference and 4th Weakly Ionized Gases Workshop, USA, Anaheim, CA, June 11-14, 2001
5. Yu. Kolesnichenko, V. Brovkin, et al. Local Parameters of Microwave Discharge Determination in Plasma-Aerodynamic Experiment via Optic Information Processing. II Workshop "Thermochemical processes in plasma aerodynamics" St-Petersburg, September 10-12, 2001
6. Yu. Kolesnichenko, V. Brovkin, et al. Microwave Energy Release Regimes for Drag Reduction in Supersonic Flows (AIAA-2002-0353). 40th AIAA Aerospace Sciences Meeting & Exhibit, Reno, NV, 14-17 January, 2002.
7. Yu. Kolesnichenko, V. Brovkin, et al. Microwave Discharge Parameters in Supersonic Flow (AIAA-2002-0356). 40th AIAA Aerospace Sciences Meeting & Exhibit, Reno, NV, 14-17 January, 2002.
8. Yu. F. Kolesnichenko, D.V. Khmara. Influence of Energy Deposition into Discharge on Electron-Neutral Impact Rate Constants in Nitrogen and Air Plasmas. The 4th Workshop on Magneto-plasma-aerodynamics in Aerospace Applications. Moscow, IVTAN, 9-11 April, 2002
9. Yu. Kolesnichenko, V. Brovkin, et al. Microwave Technique for Hypersonics. International Workshop "Thermochemical plasma processes in aerodynamics" St-Petersburg, July 15-19, 2002
10. Yu. Kolesnichenko, V. Brovkin, et al. Microwave Energy Deposition for Aerodynamic Application (AIAA-2003-0361). 41st AIAA Aerospace Sciences Meeting & Exhibit, Reno, NV, 6-9 January, 2003.
11. Yu. Kolesnichenko, V. Brovkin, et al. Fine Structure of Microwave Discharge: Evolution Scenario (AIAA-2003-0362). 41st AIAA Aerospace Sciences Meeting & Exhibit, Reno, NV, 6-9 January, 2003.
12. Igor Ch. Mashek, Yuri I. Anisimov, Valery A. Lashkov and Yuri F. Kolesnichenko. "THOMPSON SCATTERING TECHNIQUE FOR SPATIAL DIAGNOSTIC OF MW DISCHARGE IN SUPERSONIC FLOWS"(AIAA-2003-1196). 41st AIAA Aerospace Sciences Meeting & Exhibit, Reno, NV, 6-9 January, 2003.
13. Yu. F. Kolesnichenko et al. Flow Control by MW Energy Deposition. // The 5-th International Workshop on Magneto-Plasma Aerodynamics for Aerospace Applications. 7 – 10 April 2003, Moscow.
14. V. A. Lashkov, I. Ch. Mashek, Yu. I. Anisimov, Yu. F. Kolesnichenko. Influence of Microwave Discharge Plasma on AD-body Characteristics in Supersonic Flow.// International Symposium "Thermochemical and Plasma Processes in Aerodynamics", 29-31 July 2003, St.-Petersburg.
15. Yuri F. Kolesnichenko, Dmitry V. Khmara, Vadim G. Brovkin, et al. "MW Filaments in Supersonic Flow – Diagnostics and Application"// International Symposium "Thermochemical and Plasma Processes in Aerodynamics", 29-31 July 2003, St.-Petersburg.
16. V.G. Brovkin, S. A. Afanas'ev, D. V. Khmara, Yu. F. Kolesnichenko. MW Discharge Control by Magnetic Field (AIAA-2004-0357). 42nd AIAA Aerospace Sciences Meeting&Exhibit, Reno, NV, 5-8 January, 2004
17. Igor Ch. Mashek, Yuri I. Anisimov, Valery A. Lashkov, Yuri F. Kolesnichenko, et al. MW Discharge Initiated by Laser Spark (AIAA-2004-0358). 42nd AIAA Aerospace Sciences Meeting & Exhibit, Reno, NV, 5-8 January, 2004
18. V. A. Lashkov, I. Ch. Mashek, Yu. I. Anisimov, Yu. F. Kolesnichenko. Gas Dynamic Effect of Microwave Discharge on Supersonic Cone-shaped Bodies (AIAA-2004-0671). 42nd AIAA Aerospace Sciences Meeting & Exhibit, Reno, NV, 5-8 January, 2004
19. Yu. Kolesnichenko, O. Azarova, V. Brovkin, D. Khmara, V. A. Lashkov, I. Ch. Mashek, and M. Rivkin. Basics in Beamed MW Energy Deposition for Flow/Flight Control. (AIAA-2004-0669). 42nd AIAA Aerospace Sciences Meeting & Exhibit, Reno, NV, 5-8 January, 2004
20. Yu. F. Kolesnichenko et al. Selected Topics of Physics and Diagnostics of MW Discharge. // All-Russian Workshop on Magneto-Plasma Aerodynamics for Aerospace Applications. April 2004, Moscow.

Appendixes

Appendix A for Section 3

Approximation coefficients for electron impact rate constants expression

Table 1. Approximation coefficients for K_0 expression in pure nitrogen. Relative error of the fit less than 1%.

Transition	Reference	A, cm ³ /s	q	E/N ₀ , Td	Note	Plot
Elastic collisions						
	[5]	$7.91 \cdot 10^{-9}$	0.573	0.538		
Rotational excitation						
<i>Sum of rotation</i>	[6]	$4.56 \cdot 10^{-5}$	-1.327	175.8	¹	fig.2
Vibrational excitation						
$0 \rightarrow 1$	[7,8,9]	$3.72 \cdot 10^{-6}$	-1.153	147.5	²	
$0 \rightarrow 2$	[8,9]	$1.10 \cdot 10^{-5}$	-1.446	182.6	²	
$0 \rightarrow 3$	[8,9]	$2.02 \cdot 10^{-5}$	-1.610	203.9	²	
$0 \rightarrow 4$	[8,9]	$3.44 \cdot 10^{-5}$	-1.755	249.3	²	
$0 \rightarrow 5$	[8,9]	$3.05 \cdot 10^{-5}$	-1.746	269.3	²	
$0 \rightarrow 6$	[8,9]	$1.12 \cdot 10^{-4}$	-1.971	334.3	²	
$0 \rightarrow 7$	[8,9]	$1.32 \cdot 10^{-4}$	-2.085	381.4	²	
$0 \rightarrow 8$	[8,9]	$1.73 \cdot 10^{-4}$	-2.248	428.8	²	
$0 \rightarrow 9$	[10,9]	$8.50 \cdot 10^{-5}$	-2.319	466.2		
$0 \rightarrow 10$	[10,9]	$6.56 \cdot 10^{-5}$	-2.406	491.1		
Electron states excitation						
$X^1\Sigma_g^+ \rightarrow A^3\Sigma_u^+$	[11]	$1.16 \cdot 10^{-6}$	-0.954	505.0		fig.3
$X^1\Sigma_g^+ \rightarrow B^3\Pi_g$	[11]	$5.31 \cdot 10^{-6}$	-1.196	544.0	³	
$X^1\Sigma_g^+ \rightarrow w^3\Delta_u$	[11]	$2.95 \cdot 10^{-7}$	-0.714	523.1	³	
$X^1\Sigma_g^+ \rightarrow B^3\Sigma_u$	[11]	$2.05 \cdot 10^{-7}$	-0.840	555.3	³	
$X^1\Sigma_g^+ \rightarrow a^1\Sigma_u$	[11]	$2.41 \cdot 10^{-7}$	-0.901	562.7	³	
$X^1\Sigma_g^+ \rightarrow a^1\Pi_g$	[11]	$8.48 \cdot 10^{-8}$	-0.547	542.5	³	
$X^1\Sigma_g^+ \rightarrow w^1\Delta_u$	[11]	$9.77 \cdot 10^{-7}$	-1.097	588.1	³	
$X^1\Sigma_g^+ \rightarrow C^3\Pi_u$	[11]	$2.76 \cdot 10^{-6}$	-0.958	700.9	⁴	fig.3
$X^1\Sigma_g^+ \rightarrow E^3\Sigma_g$	[11]	$1.18 \cdot 10^{-10}$	-0.093	657.9	³	
$X^1\Sigma_g^+ \rightarrow a''^1\Sigma_g$	[11]	$1.78 \cdot 10^{-9}$	-0.185	696.1	³	
<i>Sum of singlets</i>	[11]	$2.01 \cdot 10^{-9}$	0.295	722.8	³	
$X^2\Sigma_g \rightarrow b^2\Sigma_u$	[12]	$3.86 \cdot 10^{-3}$	-1.864	491.9	³	
Dissociation						
<i>Resonant dissociation</i>	[13]	$1.13 \cdot 10^{-5}$	-1.924	595.3	⁵	
<i>Sum dissociation</i>	[14]	$1.24 \cdot 10^{-12}$	1.452	527.4	⁶	
Ionization						
$A^3\Sigma_u^+ \rightarrow X^2\Sigma_g$	[15]	$4.72 \cdot 10^{-9}$	0.149	551.3	⁷	
$X^1\Sigma_g^+ \rightarrow X^2\Sigma_g$	[16,17]	$1.21 \cdot 10^{-9}$	0.325	916.2		fig.3
$X^1\Sigma_g^+ \rightarrow N^+ + N$	[16,17]	$1.01 \cdot 10^{-8}$	-0.282	2126.5		
Recombination						
$e + N_2^+$	[18]	$1.63 \cdot 10^{-5}$	-1.091	59.9		

Table 2. Approximation coefficients for K_0 expression in air. Relative error of the fit less than 2%.

<i>Reaction</i>	<i>reference</i>	<i>A, cm³/s</i>	<i>q</i>	<i>E/N₀, Td</i>	<i>Note</i>
e-N₂ reactions in air					
Elastic collisions					
	see table 1	$5.63 \cdot 10^{-8}$	0.232	29.6	
Rotational excitation					
<i>Sum of rotation</i>	see table 1	$6.84 \cdot 10^{-5}$	-1.422	163.0	¹
Vibrational excitation					
$0 \rightarrow 1$	see table 1	$4.81 \cdot 10^{-6}$	-1.219	136.0	²
$0 \rightarrow 2$	see table 1	$1.13 \cdot 10^{-5}$	-1.476	162.9	²
$0 \rightarrow 3$	see table 1	$1.42 \cdot 10^{-5}$	-1.578	174.8	²
$0 \rightarrow 4$	see table 1	$2.27 \cdot 10^{-5}$	-1.717	211.1	²
$0 \rightarrow 5$	see table 1	$2.28 \cdot 10^{-5}$	-1.731	229.2	²
$0 \rightarrow 6$	see table 1	$6.53 \cdot 10^{-5}$	-1.920	278.6	²
$0 \rightarrow 7$	see table 1	$6.67 \cdot 10^{-5}$	-2.014	314.6	²
$0 \rightarrow 8$	see table 1	$6.32 \cdot 10^{-5}$	-2.125	348.1	²
$0 \rightarrow 9$	see table 1	$2.83 \cdot 10^{-5}$	-2.186	377.6	²
$0 \rightarrow 10$	see table 1	$1.80 \cdot 10^{-5}$	-2.243	395.2	²
Electron states excitation					
$X^1\Sigma_g^+ \rightarrow A^3\Sigma_u^+$	see table 1	$1.78 \cdot 10^{-7}$	-0.678	412.6	
$X^1\Sigma_g^+ \rightarrow B^3\Pi_g$	see table 1	$8.70 \cdot 10^{-7}$	-0.928	456.0	³
$X^1\Sigma_g^+ \rightarrow w^3\Delta_u$	see table 1	$4.48 \cdot 10^{-8}$	-0.429	435.5	³
$X^1\Sigma_g^+ \rightarrow B^3\Sigma_u$	see table 1	$3.36 \cdot 10^{-8}$	-0.565	471.4	³
$X^1\Sigma_g^+ \rightarrow a'^1\Sigma_u$	see table 1	$4.25 \cdot 10^{-8}$	-0.639	480.6	³
$X^1\Sigma_g^+ \rightarrow a'^1\Pi_g$	see table 1	$1.80 \cdot 10^{-8}$	-0.315	464.6	³
$X^1\Sigma_g^+ \rightarrow w^1\Delta_u$	see table 1	$2.18 \cdot 10^{-7}$	-0.875	511.1	³
$X^1\Sigma_g^+ \rightarrow C^3\Pi_u$	see table 1	$1.04 \cdot 10^{-6}$	-0.819	636.2	⁴
$X^1\Sigma_g^+ \rightarrow E^3\Sigma_g$	see table 1	$5.52 \cdot 10^{-11}$	0.017	598.8	³
$X^1\Sigma_g^+ \rightarrow a''^1\Sigma_g$	see table 1	$7.36 \cdot 10^{-10}$	-0.052	633.9	³
<i>Sum of singlets</i>	see table 1	$1.08 \cdot 10^{-9}$	0.387	664.3	³
$X^2\Sigma_g \rightarrow b^2\Sigma_u$	see table 1	$8.67 \cdot 10^{-4}$	-1.668	393.6	³
Dissociation					
<i>Resonant dissociation</i>	see table 1	$3.45 \cdot 10^{-6}$	-1.768	520.0	⁵
<i>Sum dissociation</i>	see table 1	$4.03 \cdot 10^{-13}$	1.638	464.6	⁶
Ionization					
$A^3\Sigma_u^+ \rightarrow X^2\Sigma_g$	see table 1	$1.41 \cdot 10^{-9}$	0.334	483.9	⁷
$X^1\Sigma_g^+ \rightarrow X^2\Sigma_g$	see table 1	$9.95 \cdot 10^{-10}$	0.347	858.4	
$X^1\Sigma_g^+ \rightarrow N^+ + N$	see table 1	$2.70 \cdot 10^{-7}$	-0.831	2113.4	
Recombination					
$e + N_2^+$	see table 1	$6.04 \cdot 10^{-6}$	-0.935	40.1	

Table 2. Continue.

Reaction	Cross section reference	$A, \text{cm}^3/\text{s}$	q	$E/N_0, \text{Td}$	Note
e-O₂ reactions in air					
Elastic collisions					
	[19]	$6.41 \cdot 10^{-10}$	0.909	-32.9	
Rotational excitation					
Sum of rotation	[20]	$1.12 \cdot 10^{-9}$	0.666	80.8	
Vibrational excitation					
$0 \rightarrow 1$	[21,22]	$4.80 \cdot 10^{-13}$	1.504	-24.3	⁸
$0 \rightarrow 2$	[21,22]	$1.39 \cdot 10^{-13}$	1.575	-39.2	⁸
$0 \rightarrow 3$	[21,22]	$8.23 \cdot 10^{-14}$	1.593	-4.6	⁸
$0 \rightarrow 4$	[21,22]	$3.34 \cdot 10^{-12}$	0.888	109.9	⁸
Electron states excitation					
$X^3\Sigma_g^- \rightarrow a^1\Delta_g$	[6]	$8.69 \cdot 10^{-8}$	-0.650	259.5	
$X^3\Sigma_g^- \rightarrow b^1\Sigma_g^+$	[6]	$2.20 \cdot 10^{-7}$	-1.053	316.0	
$X^3\Sigma_g^- \rightarrow A^3\Sigma_u^+$	[23,24]	$2.23 \cdot 10^{-5}$	-1.629	422.0	⁹
$X^3\Sigma_g^- \rightarrow B^3\Sigma^-$	[6]	$1.15 \cdot 10^{-5}$	-1.346	427.2	
Dissociation					
$X^3\Sigma_g^- \rightarrow O(^3P)$	[25]	$4.02 \cdot 10^{-6}$	-1.182	405.5	¹⁰
$X^3\Sigma_g^- \rightarrow O(^1D)$	[6]	$3.97 \cdot 10^{-6}$	-0.921	469.5	
$X^3\Sigma_g^- \rightarrow O(^1S)$	[23,24]	$8.63 \cdot 10^{-11}$	0.068	486.1	¹¹
$O(^1D) + O(^1S)$	[6]	$4.07 \cdot 10^{-11}$	0.223	779.3	
Ionization					
$X^3\Sigma_g^- \rightarrow X^2\Pi_g$	[16]	$8.31 \cdot 10^{-11}$	0.647	592.9	
$X^3\Sigma_g^- \rightarrow O^+ + O^-$	[26]	$9.28 \cdot 10^{-13}$	0.616	946.0	¹²
$X^3\Sigma_g^- \rightarrow O^+ + O$	[16]	$1.84 \cdot 10^{-11}$	0.633	1071.5	
Attachment					
$X^3\Sigma_g^- \rightarrow O_2^-$	[6]	$2.07 \cdot 10^{-26}$	-2.248	110.9	¹³
$b^1\Sigma_g^+ \rightarrow O^-$		$1.34 \text{E} \cdot 10^{-4}$	-2.173	408.6	¹⁴
$a^1\Delta_g \rightarrow O^-$	[27]	$5.10 \cdot 10^{-5}$	-2.115	412.2	¹⁵
$X^3\Sigma_g^- \rightarrow O^-$	[26]	$9.27 \cdot 10^{-6}$	-1.968	420.2	¹⁶
Recombination					
$e + O_2^+$	[18]	$2.22 \cdot 10^{-6}$	-0.901	38.7	

Table.3. Approximation coefficients for η expression in pure nitrogen. Relative error of the fit less than 5%.

Transition	F-C factors	ϵ_0 , J/cm ³ atm	a	b	E/N ₁ , Td
Rotational excitation					
Sum of rotation		2.12	4.894	0.764	148
Vibrational excitation					
0 → 1		2.42	4.467	0.696	131
0 → 2		1.86	4.916	0.786	141
0 → 3		1.64	5.496	0.886	151
0 → 4		1.42	6.702	1.081	187
0 → 5		1.34	7.179	1.155	204
0 → 6		1.15	9.111	1.477	258
0 → 7		1.07	10.486	1.701	297
0 → 8		1.02	11.915	1.938	335
0 → 9		1.02	12.798	2.082	364
0 → 10		1.03	13.462	2.200	384
Electron states excitation					
$X^1\Sigma_g^+ \rightarrow A^3\Sigma_u^+$	[28]	1.08	14.242	2.312	392
$X^1\Sigma_g^+ \rightarrow B^3\Pi_g$	[28]	1.06	13.906	2.243	402
$X^1\Sigma_g^+ \rightarrow w^3\Delta_u$	[28]	1.07	14.356	2.326	405
$X^1\Sigma_g^+ \rightarrow B^3\Sigma_u$	[28]	1.07	14.422	2.338	409
$X^1\Sigma_g^+ \rightarrow a^1\Sigma_u$	[28]	1.07	14.447	2.340	410
$X^1\Sigma_g^+ \rightarrow a^1\Pi_g$	[28]	1.06	13.810	2.220	406
$X^1\Sigma_g^+ \rightarrow w^1\Delta_u$	[28]	1.08	15.059	2.460	423
$X^1\Sigma_g^+ \rightarrow C^3\Pi_u$	[28]	1.09	14.736	2.400	430
$X^1\Sigma_g^+ \rightarrow E^3\Sigma_g$	no data	1.05	13.465	2.138	407
$X^1\Sigma_g^+ \rightarrow a^1\Sigma_g$	no data	1.03	13.527	2.187	411
Sum of singlets	†	1.01	13.914	2.226	421
$X^2\Sigma_g \rightarrow b^2\Sigma_u$	[28]	1.06	13.586	2.193	394
Dissociation					
Resonant dissociation		1.05	13.799	2.219	403
Sum dissociation		0.98	12.259	1.976	381
Ionization					
$A^3\Sigma_u^+ \rightarrow X^2\Sigma_g$	†	1.04	13.035	2.090	394
$X^1\Sigma_g^+ \rightarrow X^2\Sigma_g$	[28]	1.07	14.527	2.316	448
$X^1\Sigma_g^+ \rightarrow N^+ + N$		1.11	15.820	2.522	540
Recombination					
$e + N_2^+$		1.92	2.821	0.533	42

Table.4. Approximation coefficients for η expression in air. Relative error of the fit less than 5%.

Transition	F-C factors	ϵ_0 , J/cm ³ atm	a	b	E/N ₁ , Td
e-N₂ reactions in air					
Rotational excitation					
Sum of rotation		1.29	4.688	0.771	119
Vibrational excitation					
0 → 1		1.30	3.856	0.630	97
0 → 2		1.28	4.705	0.775	117
0 → 3		1.23	5.111	0.839	126
0 → 4		1.15	6.428	1.064	161
0 → 5		1.13	7.076	1.169	182
0 → 6		1.04	8.872	1.465	230
0 → 7		1.02	10.157	1.676	264
0 → 8		1.00	11.320	1.868	295
0 → 9		0.98	12.223	2.018	319
0 → 10		0.99	12.820	2.123	335
Electron states excitation					
$X^1\Sigma_g^+ \rightarrow A^3\Sigma_u^+$	see table 3	1.05	13.894	2.323	354
$X^1\Sigma_g^+ \rightarrow B^3\Pi_g$	see table 3	1.03	13.433	2.237	353
$X^1\Sigma_g^+ \rightarrow w^3\Delta_u$	see table 3	1.05	13.960	2.332	359
$X^1\Sigma_g^+ \rightarrow B'^3\Sigma_u$	see table 3	1.06	14.001	2.323	362
$X^1\Sigma_g^+ \rightarrow a'^1\Sigma_u$	see table 3	1.05	14.024	2.326	363
$X^1\Sigma_g^+ \rightarrow a'^1\Pi_g$	see table 3	1.01	13.455	2.236	355
$X^1\Sigma_g^+ \rightarrow w'^1\Delta_u$	see table 3	1.07	14.638	2.443	375
$X^1\Sigma_g^+ \rightarrow C^3\Pi_u$	see table 3	1.02	14.252	2.368	379
$X^1\Sigma_g^+ \rightarrow E^3\Sigma_g$	no data	0.98	13.153	2.177	361
$X^1\Sigma_g^+ \rightarrow a''^1\Sigma_g$	no data	0.99	13.205	2.174	363
Sum of singlets	see table 3	0.97	13.671	2.267	372
$X^2\Sigma_g \rightarrow b^2\Sigma_u$	see table 3	0.98	13.119	2.180	343
Dissociation					
Resonant dissociation		1.00	13.223	2.200	352
Sum dissociation		0.94	12.036	1.982	337
Ionization					
$A^3\Sigma_u^+ \rightarrow X^2\Sigma_g$	see table 3	0.97	12.857	2.131	349
$X^1\Sigma_g^+ \rightarrow X^2\Sigma_g$	see table 3	0.99	14.658	2.428	403
$X^1\Sigma_g^+ \rightarrow N^+ + N$		1.06	15.796	2.605	527
Recombination					
$e + N_2^+$		0.90	1.401	0.244	14

Table 4. Continue.

Transition	F-C factors	ϵ_0 , J/cm ³ atm	a	b	E/N ₁ , Td
e-O₂ reactions in air					
Electron states excitation					
$X^3\Sigma_g^- \rightarrow a^1\Delta_g$	†	1.29	6.189	0.930	143
$X^3\Sigma_g^- \rightarrow b^1\Sigma_g^+$	†	1.11	8.361	1.299	205
$X^3\Sigma_g^- \rightarrow A^3\Sigma_u^+$	[29]	1.00	12.957	2.152	341
$X^3\Sigma_g^- \rightarrow B^3\Sigma^-$	†	1.00	12.918	2.149	343
Dissociation					
$X^3\Sigma_g^- \rightarrow O(^3P)$	†	0.99	12.935	2.153	342
$X^3\Sigma_g^- \rightarrow O(^1D)$		0.98	13.069	2.176	348
$X^3\Sigma_g^- \rightarrow O(^1S)$		0.96	12.934	2.150	350
$O(^1D) + O(^1S)$		0.98	13.856	2.298	387
Ionization					
$X^3\Sigma_g^- \rightarrow X^2\Pi_g$	†	0.97	13.091	2.168	361
$X^3\Sigma_g^- \rightarrow O^+ + O^-$		1.00	14.495	2.936	410
$X^3\Sigma_g^- \rightarrow O^+ + O$		1.01	14.934	2.466	425
Attachment					
$X^3\Sigma_g^- \rightarrow O_2^-$		1.02	2.904	0.486	31
$b^1\Sigma_g^+ \rightarrow O^-$		1.00	10.085	1.672	244
$a^1\Delta_g \rightarrow O^-$		1.00	13.082	2.170	324
$X^3\Sigma_g^- \rightarrow O^-$		1.00	13.019	2.164	344
Recombination					
$e + O_2^+$		0.89	1.348	0.234	24

† Own calculation in approach of harmonic oscillator according the method described in [29]

Notes to tables 1 and 2

¹ Below 1.25 eV – own calculation of sum none-resonant cross section of non-polar molecule excitation by electron impact based on method of Gerjoy E., Stein S. - Phys. Rev 1955, v.97, p.1671 and v.98, p.1848 for rotational distribution function at gas temperature 300 K, above 1.25 eV - resonant cross section - from [6].

² The form of cross section energy dependence taken from [7], the dependence near threshold taken from [8]. Renormalization according the results [9], so sum cross section for $v = 1-8$ levels is 8 Å^2 at 2.3 eV (scaled in 2.7 times).

³ Renormalized based on [6] (scaled in 0.67 times). The same normalization was used by Capitelli M. and Phelps A.V. in their cross sections sets.

⁴ Renormalized based on Phelps A.V. - Phys.Rev. 31, 1985, p.2932 (scaled in 1.5 times)

⁵ Dissociation through negative ion formation: $e + N_2 \rightarrow N_2[X^2\Pi_g] \rightarrow N[{}^4S] + N[{}^4S]$. This cross section was not included in cross sections set for electron energy distribution function calculation.

⁶ In opinion of Phelps A.V. a good estimate of dissociation is 0.7 times the rate constant of “Sum of singlets” excitation. This cross section was not included in cross sections set for electron energy distribution function calculation.

⁷ In approach of minute amount of $N_2[A^3\Sigma_u^+]$ in comparison with $N_2[X^1\Sigma_g^+]$, cross section of this process was not included in cross sections set for electron energy distribution function calculation.

⁸ Low-energy resonances taken from [21] and renormalized according Lawton, Phelps A.V. - Phys. Rev., 69, 1978, p.1055 (scaled in 2.5 times); resonances near 9 eV taken from [22] and renormalized to Trajmar

⁹ Excitation of $O_2[A^3\Sigma_u^+]$ bound vibrational levels

¹⁰ Excitation of predissociation vibrational levels of $O_2[A^3\Sigma_u^+]$, $O_2[c^3\Delta_u]$ and $O_2[c^1\Sigma_u^-]$ states

¹¹ Excitation of $O_2[a^1\Sigma_u]$ predissociation state

¹² Polar ionization

¹³ Three body attachment at $T_g = 300 \text{ K}$ in $[\text{cm}^6/\text{s}]$

¹⁴ The form and magnitude of cross section energy dependence estimated by A.V.Phelps

¹⁵ Renormalized by A.V.Phelps: scale factor 0.88. Peak at 7.5 eV taken into account

¹⁶ Dissociative attachment at $T_g = 300 \text{ K}$

References to Appendix A

1. N.L.Alexandrov, A.M.Konchakov, E.E.Son, Rus: "Fyzika plasmy" (Physics of plasma), 4, 5, 1978, p.1182
2. S.I.Valyansky, K.A.Vereshagin, V.Vernike et al., Rus: "Kvantovaya elektronika" (Quantum electronics), 11, 9, 1984, p.1833
3. A.A.Devyatov, S.A.Dolenko, A.T.Rakhimov et al., Rus: "Zh.ETF" (Journal of experimental and theoretical physics), 90, 2, 1986, p.429
4. B.Massabieaux, G.Gousset, G.Lefebvre et al., J.Physique, 48, 1987, p.1939
5. Itikawa Y, - Atomic Data and Nuclear Data Tables, 1974, v.14, No1
6. Morgan W.L. - Plasma Chemistry and Plasma Processes, 12, 1992, pp.449-493
7. Schulz G.J. - Phys. Rev., 1964, v.135, A988
8. Engelhardt A.G., Phelps A.V., Risk S.R. - Phys.Rev., 1964, v.135, A1566
9. Gordeev O.A., Khmara D.V. - Teplofizika Vysokikh Temperatur, 1991, v.32, No1, p.133 (in Russian)
10. Boness M.J.W., Schulz G.J. - Phys. Rev. 1973 v.A8 p.2883
11. Cartwright D.C. et al - Phys. Rev. A, 1977, v.16, No3
12. Orel A.E. - Phys. Rev. A, v.42, No9, 1990, p.5292
13. Spence D., Burrow P.D. - J. Phys. B, 1979, v.12, L.179
14. Cosby P.C. - J. Chem. Phys., 98, 1993, p.9544
15. Mark T.D. - J. Chem. Phys., 1975, v.63, p.3731
16. Straub H.C. Renault P. et al - Phys. Rev. A, 1996, v.54, p.2146
17. Krishnakumar E. Srivastava S.K. - J. Phys.B, 1990, v.23, p.1893
18. Mitchel J.B.A., McGowan P.W. - Physics of Ion-Ion and Electron-Ion Collisions, N.Y., Plenum Press, 1983
19. Hake R.D., Phelps A.V. - Phys. Rev., 1967, v.158, No1, p.70
20. Islamov R.Sh., Kochetov I.V., Pevgov V.G. - Preprint No169, Physical Institute of Academy of Science, Moscow, 1977
21. Linder F., Schmidt H. - Z.Naturforsch, 1971, Bd.2a, S.1603
22. Wong S.F., Schulz G.J. - Rhys. Rev. Lett., 1973, v.31, p.969
23. Trajmar S., Cartwrite D.C., Williams W. - Phys. Rev., A4, 1971, p.1482
24. Trajmar S., Williams W., Kuppermann A. - J. Chem. Phys., 1972, v.56, p.3759
25. Itikawa Y. et al, - J. Phys. Chem. Ref. Data, 1989, v.18, No1, p.23
26. Rapp D., Briglia D.D., - J. Chem. Phys., 1965, v.43, No5, p.1480
27. Jaffke, Meinke, Hashemi, Christophorou, Illenberger - Chem. Phys. Lett., 1992, 193, p.62
28. Lofthus A., Krupene P.H. - J. Phys. Chem. Ref. Data, 1977, v.6, No1, p.133
29. Kuzmenko N.E., Kuznetsova L.A., Kuzyanov Yu.Ya. - Franck-Condon factors of diatomic molecules, Moscow, Moscow State University Press, 1984 (in Russian)

Appendix B for Section 3

Table 1. Heat effects during collisional quenching of electron-excited atoms and molecules

M^*	Allowed M	Heat effect, eV
$M^* + O_2 \rightarrow M + O + O$		
$A^3\Sigma_u^+$	$X^1\Sigma_g^+$	0.29
$B^3\Pi_g$	$X^1\Sigma_g^+$	1.23
$a^1\Sigma_u^-$	$X^1\Sigma_g^+$	1.28
$C^3\Pi_u$	$X^1\Sigma_g^+$	3.58, 1.79 ^{††}
$M^* + N \rightarrow M + N(^2P)$		
$A^3\Sigma_u^+$	$X^1\Sigma_g^+$	0.61
$B^3\Pi_g$	$X^1\Sigma_g^+$	2.38
$a^1\Sigma_u^-$	$X^1\Sigma_g^+$	2.16

^{††} One or both oxygen atoms is in ¹D state correspondingly

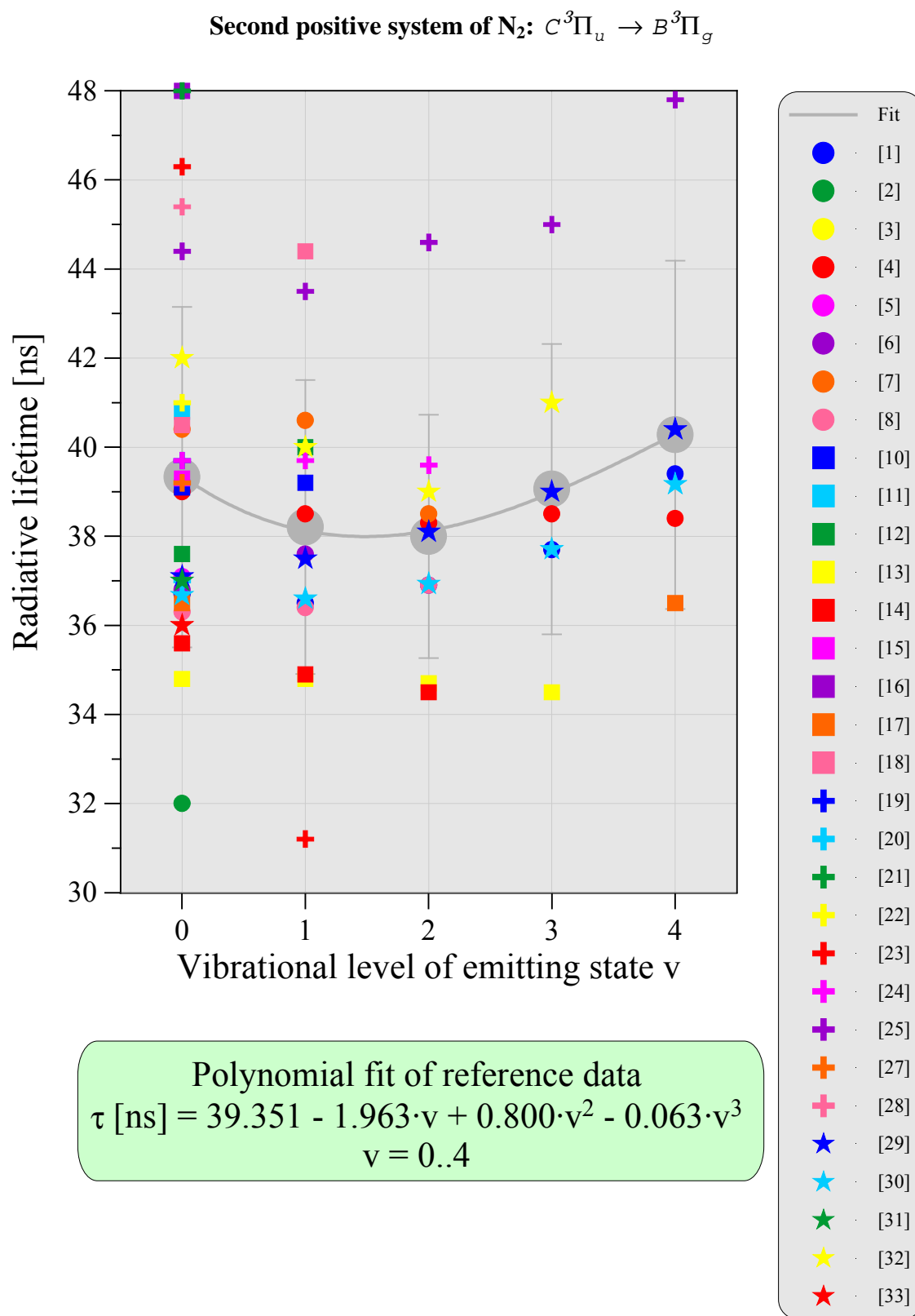
Table 2. Heat effects of dissociative recombination reactions

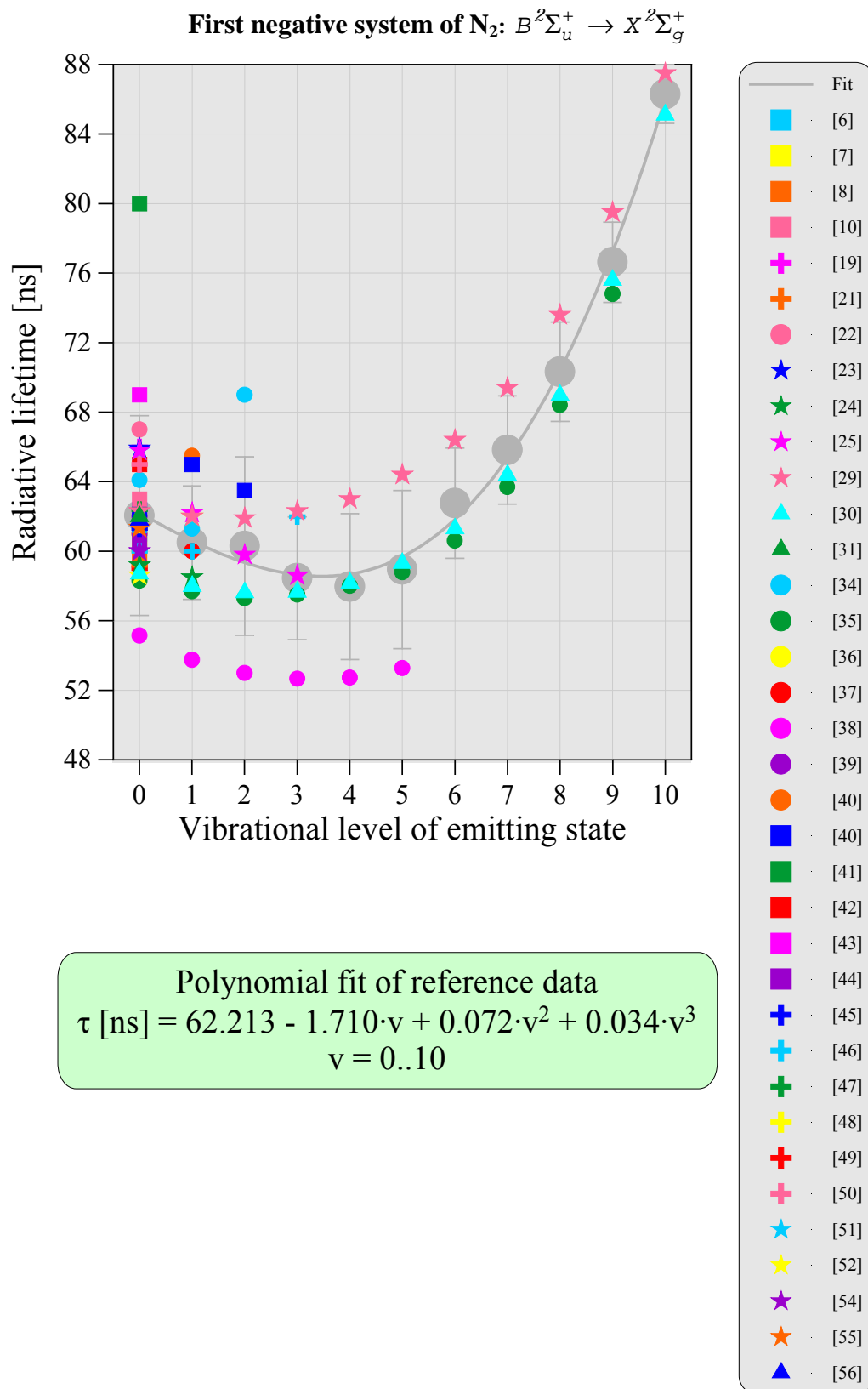
Products	Heat effect, eV
$e + N_2^+$	
$N(^2D) + N$	1.44
$N(^2P) + N$	0.2
$N(^2D) + N(^2D)$	0.51
$e + O_2^+$	
$O(^1D) + O$	3.73
$O(^1D) + O(^1D)$	0.6
$O(^1D) + O(^1S)$	0.04
$e + NO^+$	
$N + O$	1.38
$N(^2D) + O$	0.19

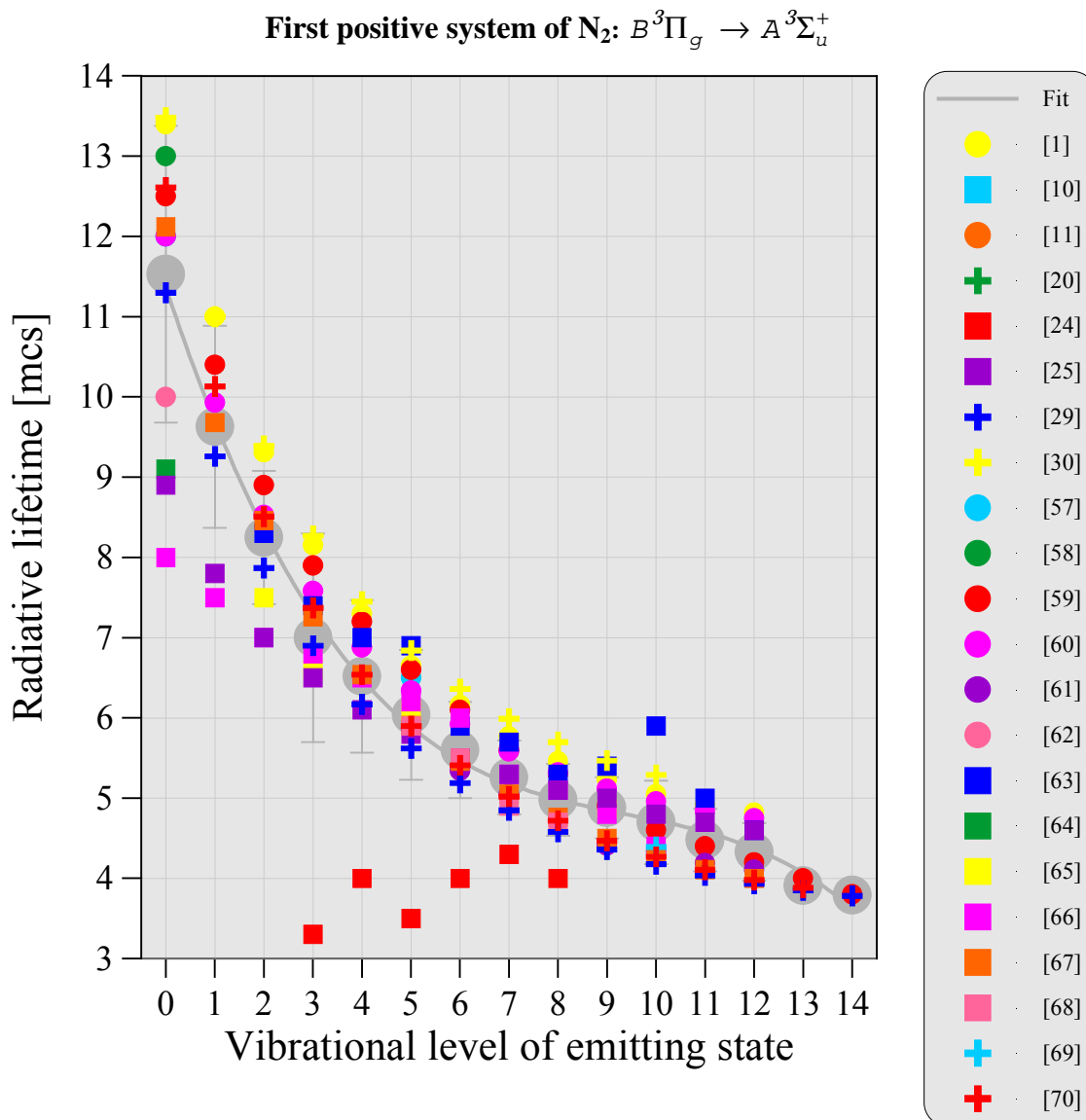
Appendix C

Significant radiative and non-radiative processes for gas discharge kinetic modeling
and processing of experimental spectra.

Survey of theoretical and experimental data for radiative lifetimes



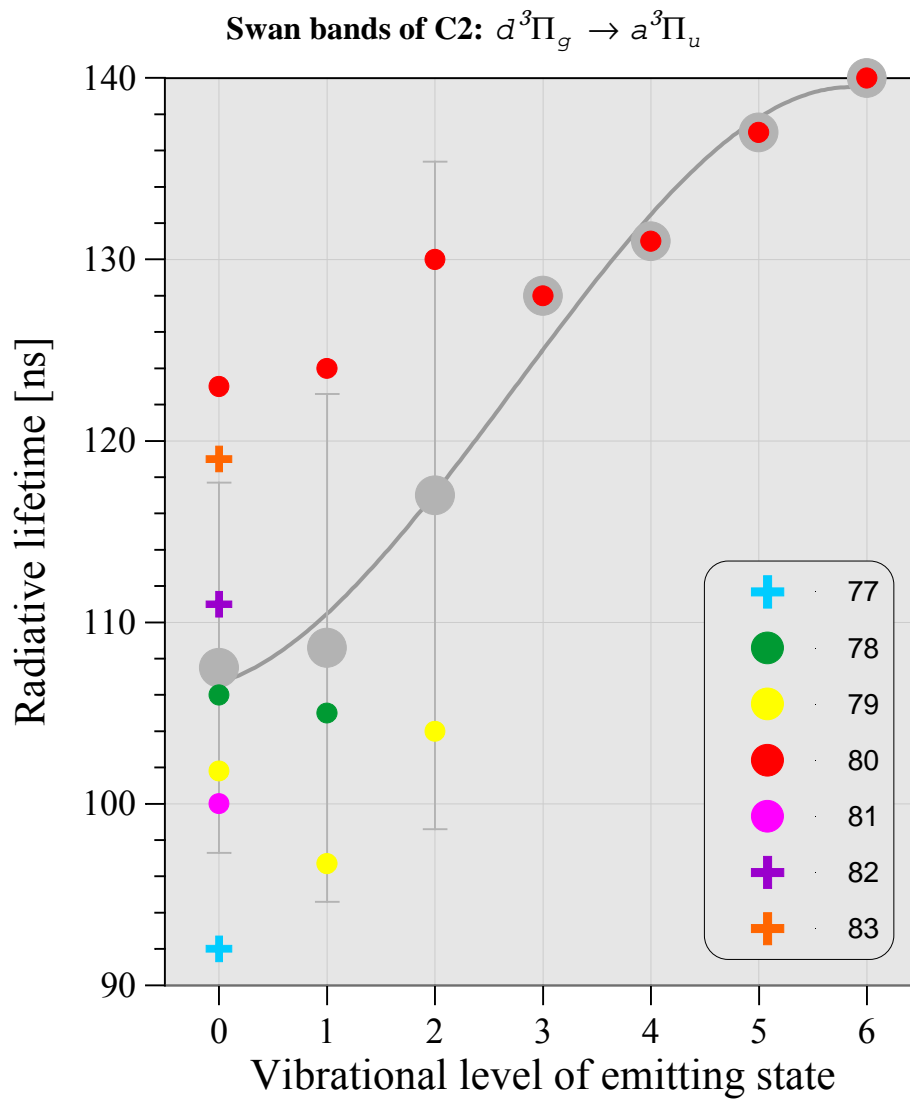




Polynomial fit of reference data

$$\tau \text{ [mcs]} = 10.367 - 1.852 \cdot v + 0.184 \cdot v^2 - 0.007 \cdot v^3$$

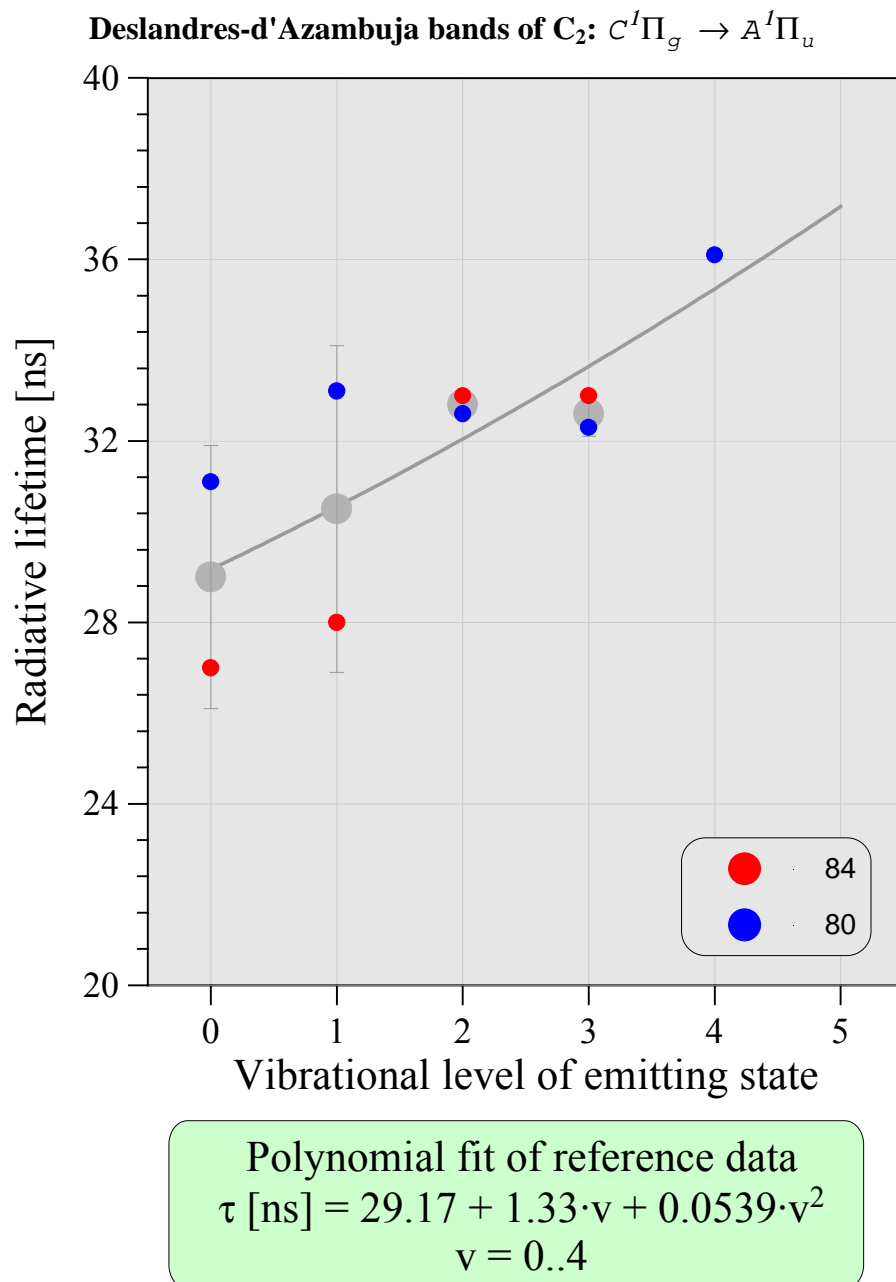
$v = 0..14$

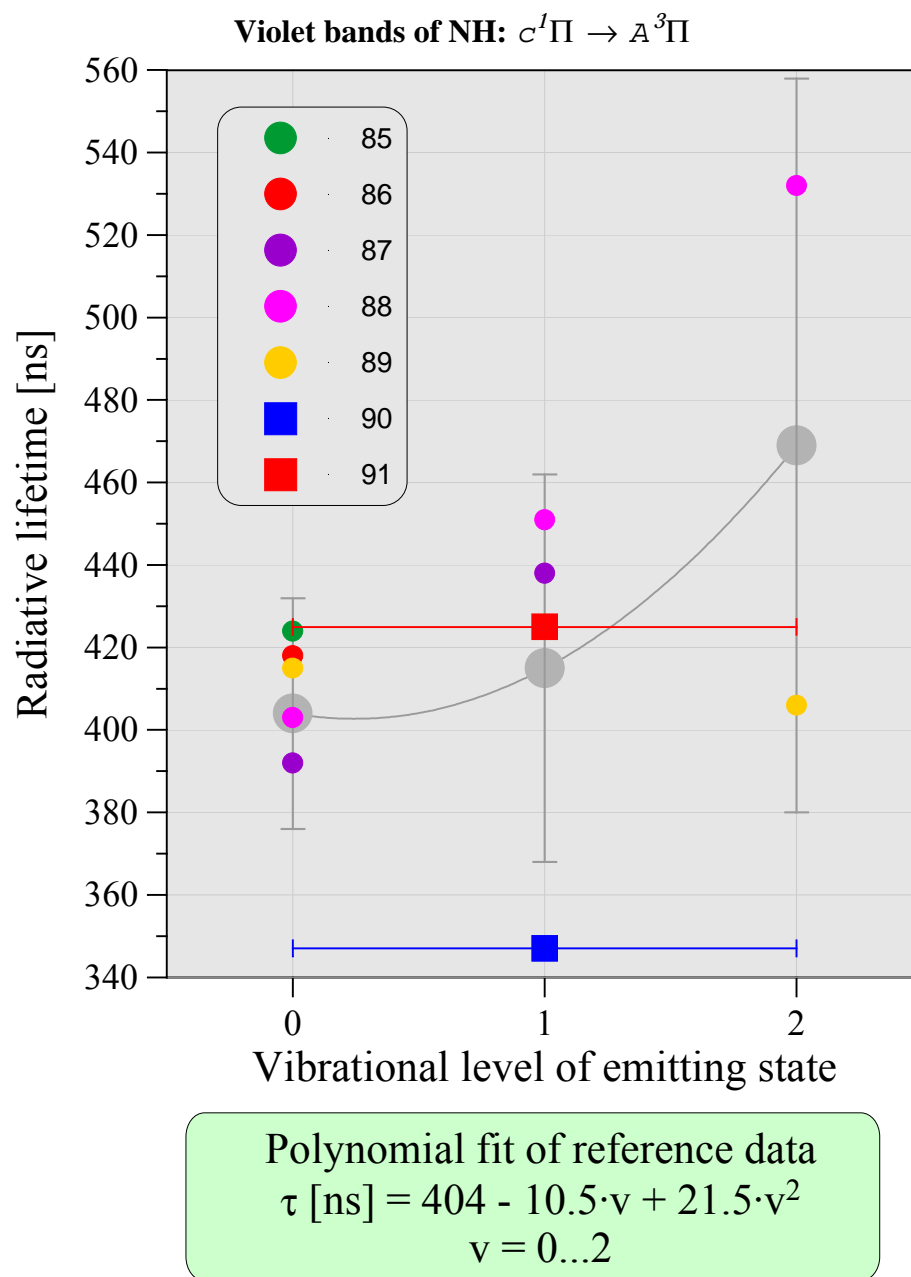


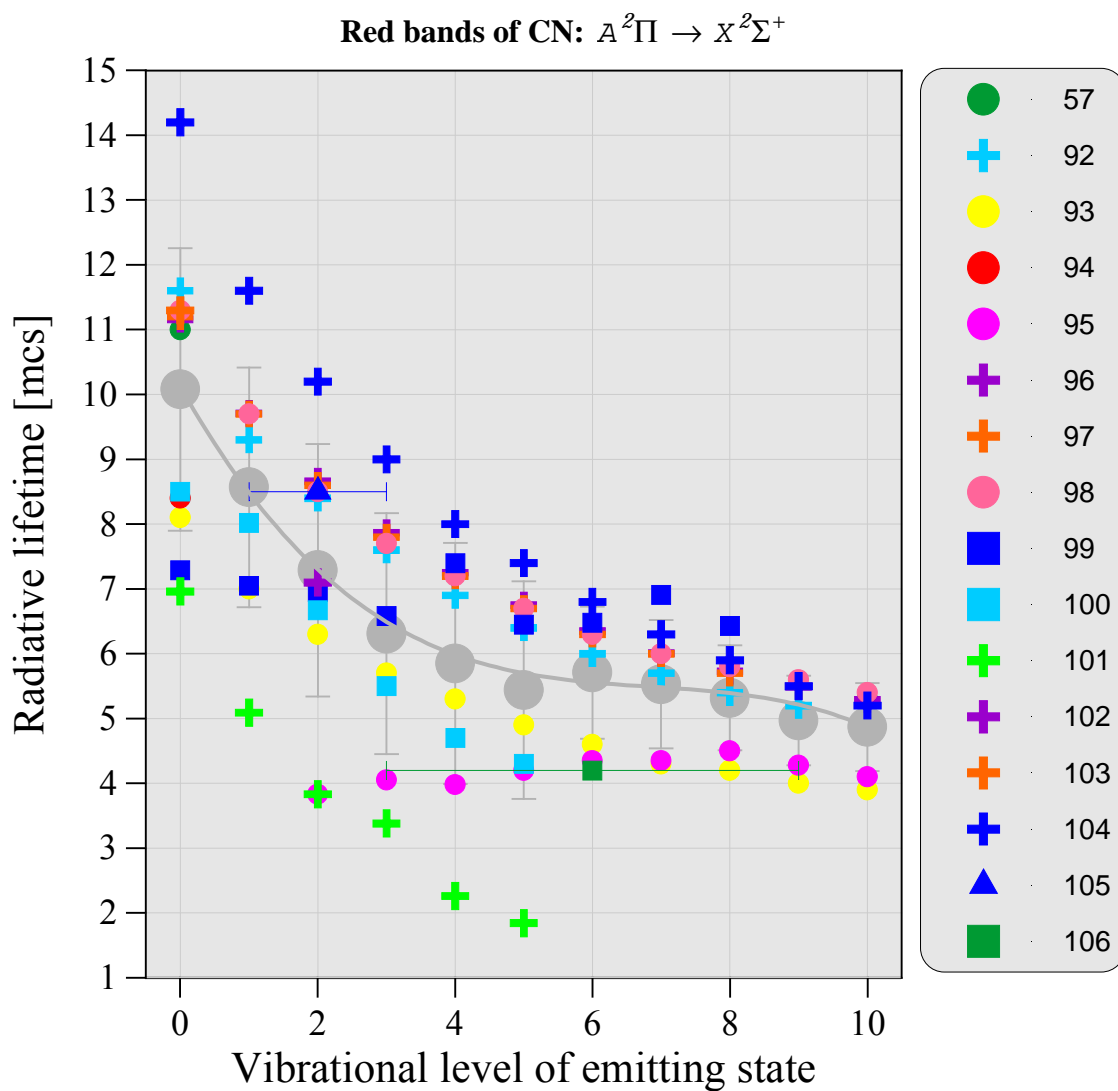
Polynomial fit of reference data

$$\tau \text{ [ns]} = 106.7 + 1.83 \cdot v + 2.25 \cdot v^2 - 0.28 \cdot v^3$$

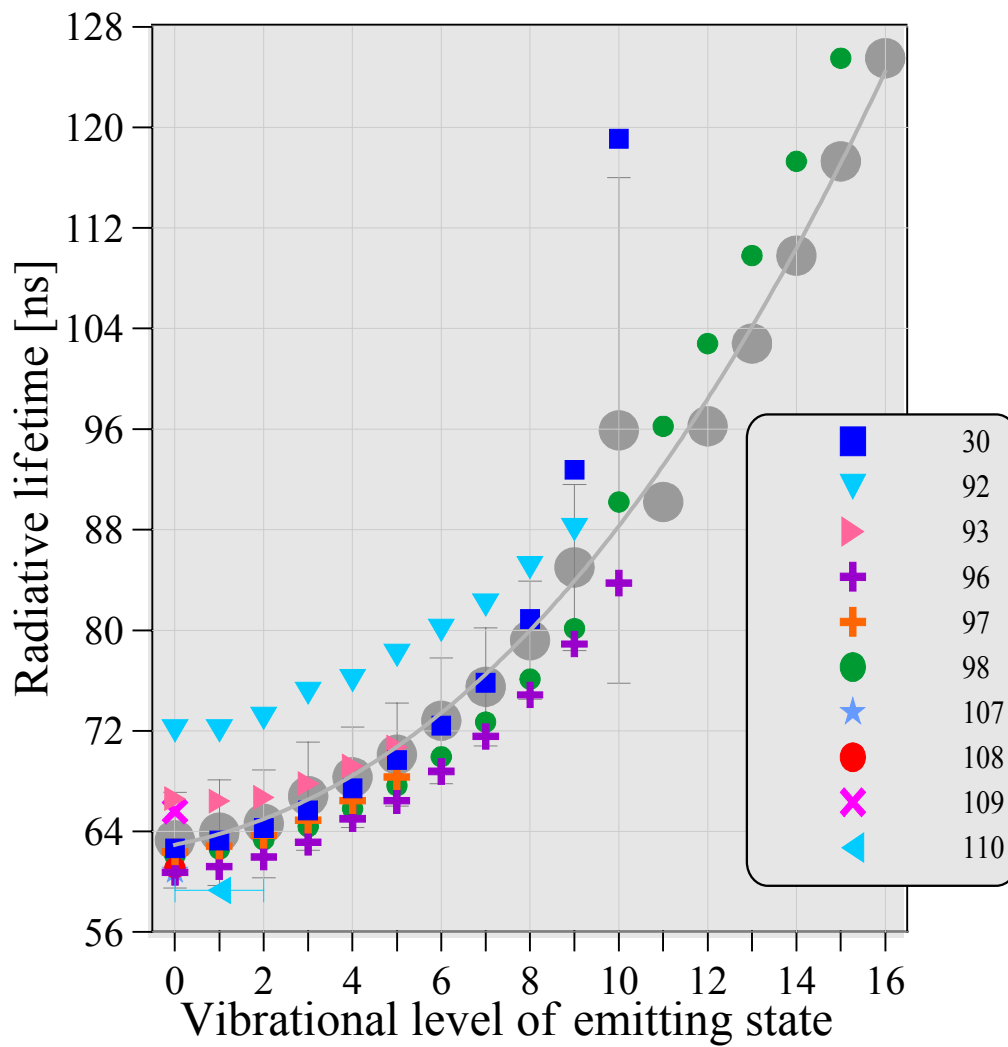
$v = 0 \dots 6$



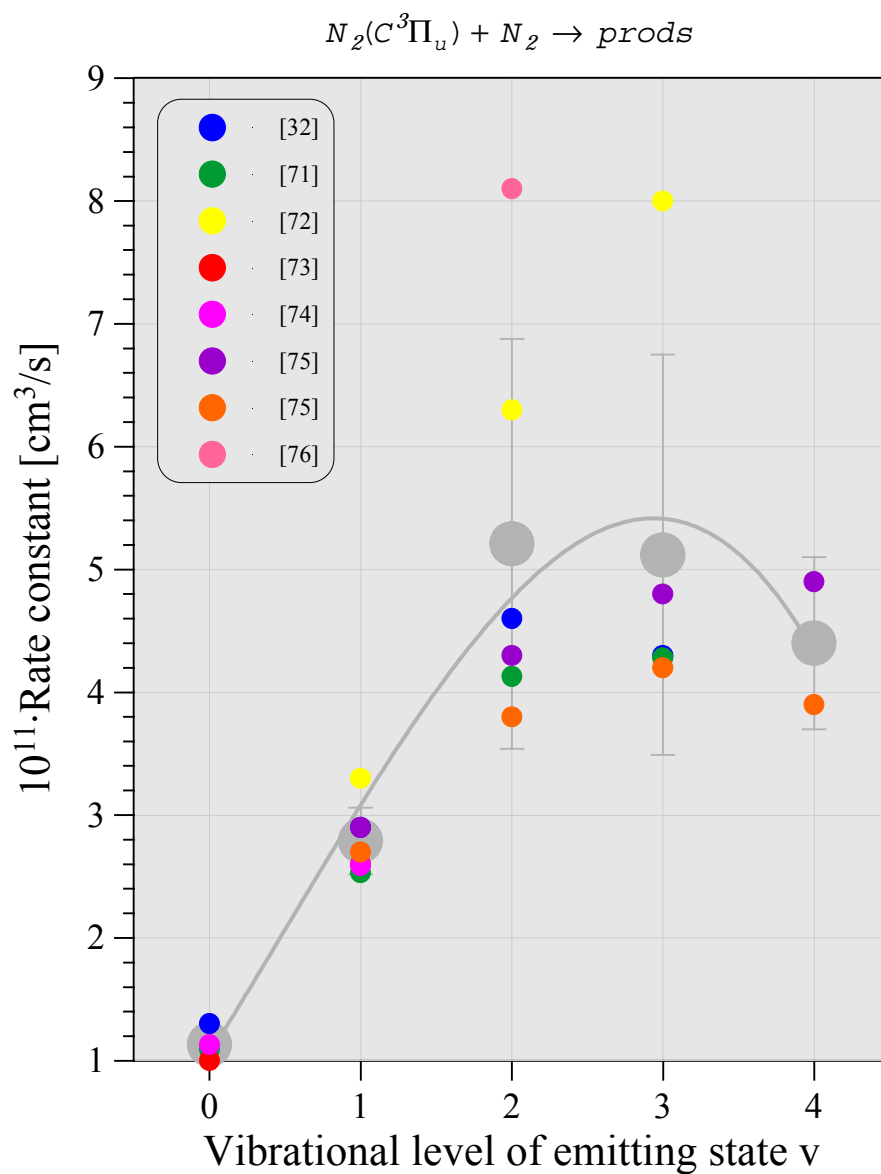




Violet bands of CN: $A^2\Pi \rightarrow X^2\Sigma^+$



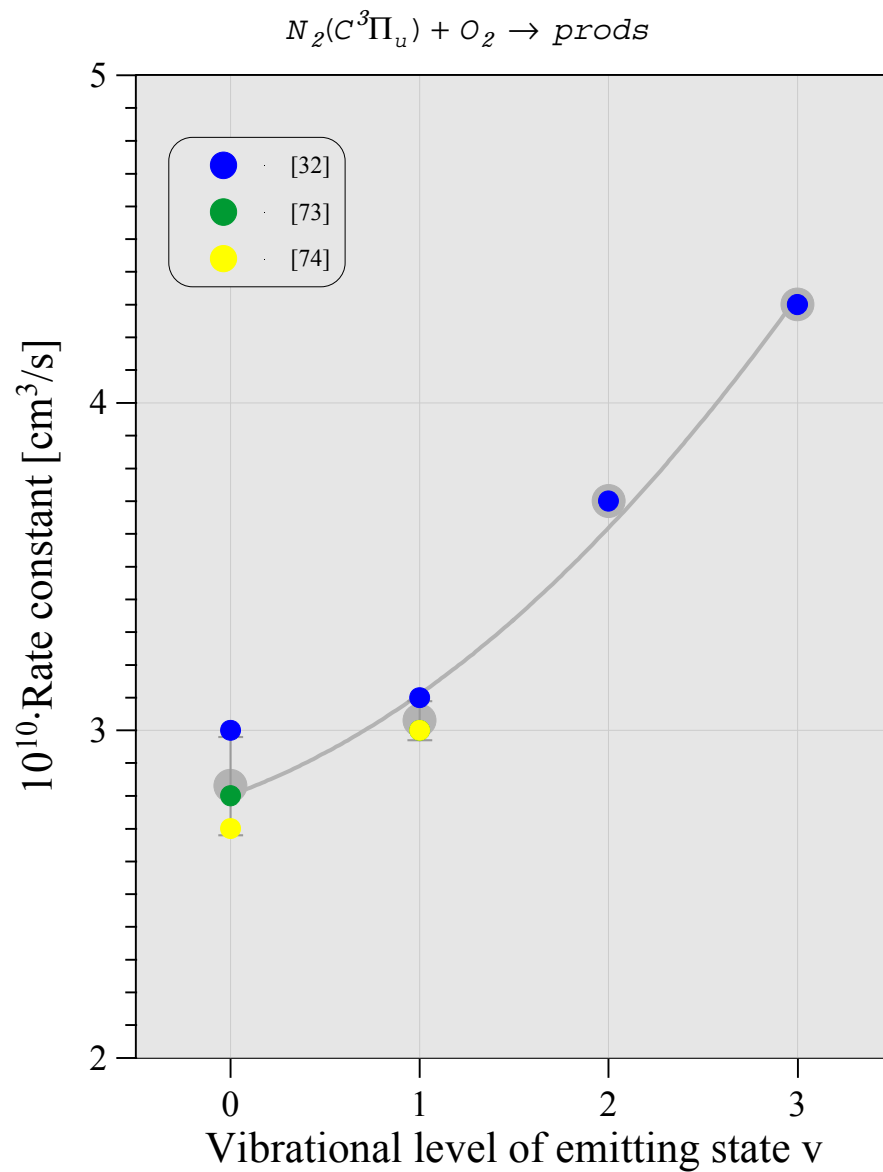
Collisional quenching of $N_2(C^3\Pi_u)$ state in air. Survey of experimental data for rate constants



Polynomial fit of reference data

$$10^{11} \cdot K [\text{cm}^3/\text{s}] = 1.056 + 1.968 \cdot v + 0.176 \cdot v^2 - 0.116 \cdot v^3$$

$v = 0..4$



Polynomial fit of reference data

$$10^{10} \cdot K[\text{cm}^3/\text{s}] = 2.803 + 0.208 \cdot v + 0.1 \cdot v^2$$

$v = 0..3$

References for Appendix C

1. Werner H.-J., Kalcher J., Reinsch E.-A. Accurate ab initio calculations of radiative transition probabilities between the $A^3\Sigma_u^+$, $B^3\Pi_g$, $w^3\Delta_u$, $B'^3\Sigma_u^-$ and $C^3\Pi_u$ states of N_2 - J. Chem. Phys., 1984, v81(5), pp.2420-2431
2. Buenker R.J., Peyerimhoff S.D. Ab initio calculations close to the full CI level of accuracy and their use for the interpretation of molecular spectra – New Hor. Q. Chem. Proc. 4 Int. Congr., 1983, p183
3. Khakoo M.A., Srivastava S.K. Measurement of the lifetime of the $C^3\Pi_u$ state of molecular nitrogen by the delayed coincidence method. - JQSRT, 1983, v30(1), pp.31-35
4. Larsson M., Radozycki T. Time resolved studies of perturbations in the $v'=1$ level and radiative properties of the $C^3\Pi_u$ state in N_2 . - Phys. Scr., 1982, v.25(5), pp.627-630
5. Asinowski E.I., Vasilyak L.M., Tokunov Yu.M. Measurement of the effective lifetime of $C^3\Pi_u$ $v=0$ state of N_2 in nitrogen and air.(in russian)" - Teplov. vys. temp., 1979, v.17(4), pp.858-860
6. Bingham F.W. Radiative lifetime measurements in N_2 , N_2^+ and CO^+ - Bull. Am. Phys. Soc., 1973, v.18(4), pp.609-610
7. Dotchin L.W., Chupp E.L., Pegg D.J. Radiative lifetimes and pressure dependence of the relaxation rates of some vibronic levels in N_2^+ , N_2 , CO^+ and CO - J. Chem. Phys., 1973, v.59(8), pp.3960-3967
8. Osherovich L.A., Gorshkov V.N. Radiative lifetimes of the $C^3\Pi_u$ state of N_2 and $B^2\Sigma_u^+$ state N_2^+ (in russian)" // Opt. i spektrosk., 1976, v.41, pp.158-160
- Erman P., Brzozowski J., Sigfridson B. Gas excitations using high frequency deflected electron beams: a convenient method for determinations of atomic and molecular lifetimes - Nucl. Instr. Meth., 1973, v.110, pp.471-476
11. Carr T.W., Dondes S. Direct measurement of the radiative lifetime and collisional quenching of the $C^3\Pi_u$ state of nitrogen as studied by pulse radiolysis - J. Phys. Chem., 1977, v.81(24), pp.2225-2228.
12. Bennett W.R., Jr, Flint J. $Ar(^3P_2)-N_2(C^3\Pi_u)$ excitation transfer cross section and radiative lifetimes of the nitrogen-molecular-laser transitions - Phys. Rev., 1978, v.A18(6), pp.2527-2532
13. Pochat A., Doritch M., Peresse J. Mesures absolues de durees de vie dans l'helium, le neon, l'azote moleculaire et l'oxyde de carbone" - J. ch. ph. et ph. ch. bio., 1973, v.70(6), pp.936-940
14. Imhof R.E., Read F.H. Measured lifetimes of the $C^3\Pi_u$ state of N_2 and the $a^3\Sigma_g^+$ state of H_2 - J. Phys., 1971, v.B4(8), pp.1063-1069
15. Chen S.T., Anderson R.J. Excitation of the $C^3\Pi_u$ state of N_2 by electron impact - J. Chem. Phys., 1975, v.63(3), pp.1250-1254
16. Sawada T., Kamada H. Radiative lifetime measurements of $N_2(C^3\Pi_u)$, $NH(A^3\Pi_i)$ and $NH(C^1\Pi)$ - Bull. Chem. Soc. Japan, 1970, v.43, pp.331-334
17. Becker K.H., Engels H., Tatarczyk T. Lifetime measurements of the $C^3\Pi_u$ state of nitrogen by laser-induced fluorescence - Chem. Phys. Lett., 1977, v.51(1), pp.111-115
18. Calo J.M., Axtmann R.C. Vibrational relaxation and electronic quenching of the $C^3\Pi_u$ $v'=1$ state of nitrogen - J. Chem. Phys., 1971, v.54(3), pp.1332-1341
19. Desesquelles J., Dufay M., Pulizac M.C. Lifetime measurement of molecular states with an accelerated ion beam - Phys. Lett., 1968, v.A27(2), pp.96-97
20. Anton H. Zur Lumineszenz einiger Moleculgase bei Angerung durch schnelle Electronen.II - Ann. Phys., 1966, v.18(3-4), pp.178-193
21. Hesser J.E. Absolute transition probabilities in ultraviolet molecular spectra - J. Chem. Phys., 1968, v.48(6), pp.2518-2535
22. Wuerker R.F., Schmitz L., Fukuchi T., Straus P. Lifetime measurement of the excited states of N_2 and N_2^+ by laser- induced fluorescence - Chem. Phys. Lett., 1988, v.150(3), pp.443-452

23. Nicholls L.L., Wilson W.E. Optical lifetime measurements using a positive ion Van De Graaff accelerator - Appl. Opt., 1968, v.7(1), pp.167-170
24. Johnson A.W., Fowler R.G. Measured lifetimes of rotational and vibrational levels of electronic states of N_2 - J. Chem. Phys., 1970, v.53(1), pp.65-72
25. Shemansky D.K., Broadfoot A.L. Excitation of N_2 and N_2^+ systems by electrons-I. Absolute transition probabilities - JQSRT, 1971, v.11, pp.1385-1400
26. Larsson M., Radozycki T. Time resolved studies of perturbations in the $v'=1$ level and radiative properties of the $C^3\Pi_u$ state in N_2 - Phys. Scr., 1982, v.25(5), pp.627-630
27. Dumont M.N., Remy F. The radiative lifetime of the $C^3\Pi_u$ state of N_2 - J. Chem. Phys., 1982, v.76(2), pp.1175-1176
28. Fukuchi T., Wuerker R.F., Wong A.Y. Lifetime and transition probability measurements of the second positive system of nitrogen by laser-induced fluorescence - J. Chem. Phys., 1992, v.97(12), pp.9490-9491
29. Gilmore F.R., Laher R.R., Espy P.E. Franck-Condon factors, r-centroids, electronic transition moments and Einstein Coefficients for many nitrogen and oxygen band systems - J. Phys. Chem. Ref. Data, 1992, v.21(5), p.1005
30. Laux Ch.O. Optical diagnostics and radiative emission of air plasmas - HTGL report No T-288 (Stanford Univ.), 1993
31. Pancheshnyi S.V., Starikovskaia S., Starikovskii A. "Measurements of rate constants of the $N_2(C^3\Pi_u, v=0)$ and $N_2^+(B^2\Sigma_u^+, v=0)$ deactivation by N_2 , O_2 , H_2 , CO , H_2O molecules in afterglow of the nanosecond discharge - Chem. Phys. Lett., 1998, v.294, pp.523-527
32. Pancheshnyi S.V., Starikovskaia S., Starikovskii A. Collisional deactivation of $N_2(C^3\Pi_u, v=0,1,2,3)$ states by N_2 , O_2 , H_2 and H_2O molecules - Chem. Phys., 2000, v.262, pp.349-357
33. Wagner K.H. Afterglow of Ar, N_2 and N_2 plus CH_4 after impact excitation by electron avalanches - Z. Naturforsch., 1964, v.19a, pp.716-721
34. Plain A., Jolly J. Quenching rate constants for $N_2^+(B^2\Sigma_u^+, v'=0,1,2)$ with N_2 and Ne - Chem. Phys. Lett., 1984, v.111(1-2), pp.133-135
35. Langhoff S.R., Bauschlicher Ch. Theoretical study of the first and second negative system of N_2^+ - J. Chem. Phys., 1988, v.88(1), pp.329-336
36. Mahan B.H., O'Keefe A. Rotational excitation and radiative lifetimes of N_2^+ - J. Chem. Phys., 1981, v.74, pp.5606-5612
37. Jolly J., Plain A. Determin. des coefficients de destruction collisionnelle des niveaux $N_2^+[B^2\Sigma_u^+, v'=0,1]$ par N_2 et Ne au moyen de fluorescence induite par laser - Collis. Et Rayonn. Colloq., 1983, p.9
38. Collins Lee A., Crtwright D.C., Wadt W.R. Electronic transitions in N_2^+ - J. Phys. B, 1980, v.13(20), pp.L613-L618
39. Mahan B.H., O'Keefe A. Radiative lifetimes of excited electronic states in molecular ions - Astrophys. J., 1981, v.248(3), p.1209-1216
40. Erman P., Larsson M. Time resolved studies of the interactions between the A and B states in N_2^+ - Phys. Scr., 1979, v.20(5-6), pp.582-586
41. Engelking P.C., Smith A.L. Tunable laser fluorescence spectroscopy of the molecular nitrogen cation at 390 nm - Chem. Phys. Lett., 1975, p.36(1), pp.21-22
42. Sawada T., Kamada H. Radiative lifetime measurements of some excited states of N_2^+ and CH - Bull. Chem. Soc. Japan, 1970, v.43(2), pp.325-330
43. Bloch M., Turner D.W. Radiative lifetimes of ions measured with the photoelectron spectrometer - Chem. Phys. Lett., 1975, v.30(3), pp.344-346
44. Smith A.J., Read F.H., Imhof R.E. Measurement of the lifetimes of ionic excited states using the inelastic electron-photon delayed coincidence technique - J. Phys. B: At. Mol. Phys., 1975, v.8(17), pp.2869-2879
45. Gray D., Morack J.L., Roberts T. Radiative lifetime of the $B^2\Sigma_u^+$ state of N_2 - Bull. Am. Phys. Soc., 1971, v.16(8), p.848, FB5
46. Dufayard J., Negre J.M., Nedelec O. Perturbation effects on lifetimes in N_2^+ - J. Chem. Phys., 1974, v.61(9), pp.3614-3618

47. Erman P. High resolution measurements of atomic and molecular lifetimes using the high frequency deflection technique - Phys. Scr., 1975, v.11, pp.65-78
48. Remy F., Dumont M.N. The radiative lifetime of the $B^2\Sigma_u^+$ state of N_2^+ : a new measurement and a discussion of previous results - JQSRT, 1978, v.20(2), pp.217-222
49. Hesser J.E., Dressler K. Radiative lifetime of ultraviolet molecular transitions - J. Chem. Phys., 1968, v.45, p.3149
50. Sebacher D.J. Study of collision effects between the constituents of a mixture of helium and nitrogen gases when excited by a 10 keV electron beam - J. Chem. Phys., 1965, v.42(4), pp.1368-1372
51. Bennett R.G., Dalby R.W. Experimental determination of the oscillator strength of the first negative band of N_2^+ - J. Chem. Phys., 1959, v.31(2), pp.434-441
52. Head C.E. Radiative lifetimes of the $B^2\Sigma_u^+$ $v'=0$ and $v'=1$ levels of N_2^+ - Phys. Lett., 1971, v.34A(2), pp.92-93
53. Jeunehomme M. Oscillator strengths of the first negative and second positive systems of nitrogen - J. Chem. Phys., 1966, v.44(7), pp.2672-2677
54. Fink E., Welge K.H. " Lifetime of the electronic states $N_2(C^3\Pi_u)$, $N_2^+(B^2\Sigma_u^+)$, $NH(A^3\Pi_i)$, $NH(C^1\Pi)$ and $PH(^3\Pi_i)$ - Z. Naturforsch., 1964, v.19a(10), pp.1193-1201
55. Schmoranz H., Hartmetz P., Marger D., Dudda J. Lifetime measurement of the $B^2\Sigma_u^+$ ($v=0$) state of $^{14}N_2^+$ by the beam-dye-laser method - J. Phys.B, 1989, v.22(11), pp.1761-1769
56. Scholl R.J., Cameron R., Rosner S.D., Holt R.A. Beam-laser measurements of lifetimes in SiO^+ and N_2^+ - Phys. Rev. A, 1995, v.51(3), pp.2014-2019
57. Werner H., Reinsch E. Internally contracted MCSCF-SCEP calculations - Adv. Theor.and Comput. Appr.to El. Struct. M
58. Ortiz M., Perez A., Campos J. Experimental lifetime for the $B^3\Pi_g$, $v=0$ level of N_2 - Physica, 1988, v.BC150(3), pp.440-444
59. Weiner B., Ohm Y. A note on the radiative lifetimes of the $B^3\Pi_g$ state of N_2 - J. Chem. Phys., 1984, v.80(11), pp.5866-5867
60. Yeager D.L., McKoy V. Transition moments between excited electronic states of N_2 - J. Chem. Phys., 1977, v.67(6), pp.2473-2477
61. Eyler E.E., Pipkin F.M. Lifetime measurements of the $B^3\Pi_g$ state of N_2 using laser excitation - J. Chem. Phys., 1983, v.79(8), pp.3654-3659
62. Heidner R.F.III, Sutton D.G., Suchard S.N. Kinetic study of $N_2(B^3\Pi_g, v)$ quenching by laser-induced fluorescence - Chem. Phys. Lett., 1976, v.37(2), pp.243-248
63. Carlson T.A., Duric N., Erman P., Larsson M. Collisional transfer to the B state in N_2 - Phys. Scr., 1979, v.19(1), pp.25-28
64. Jeunehomme M., Duncan A.B.F. Lifetime measurements of some excited states of nitrogen, nitric oxide and formaldehyde - J. Chem. Phys., 1964, v.41(6), pp.1692-1699
65. Hollstein M., Lorents D.C., Peterson J.R., Sheridan J.R. Time of flight measurement of N_2 and N_2^+ lifetimes - Can. J. Chem., 1969, v.47(10), pp.1858-1861
66. Jeunehomme M. Transition moment of the first positive band system of nitrogen - J. Chem. Phys., 1966, v.45(5), pp.1805-1811
67. Piper L.G., Holtzclaw K.W., Green B.D., Blumberg W.A.M. Experimental determination of the Einstein coefficients for the $N_2(B-A)$ transition - J. Chem. Phys., 1989, v.90 (10), pp.5337-5345
68. Ortiz M., Perez A., Campos J. Vidas medias de niveles vibracionales ($v=5, 6, 7, 8$) del estado $B^3\Pi_g$ de la molecula de N_2 - Real Soc. Esp. Fis. 1989, v.85(1), pp.28-32
69. Ottinger Ch., Vilesov A.F. Laser spectroscopy of perturbed levels in $N_2(B^3\Pi_g, v=10)$ and the first experimental determination of the $N_2(A^3\Sigma_u^+)$ term energy - J. Chem. Phys., 1994, v.100(7), pp.4862-4869

70. Thuemmel H.T., Partridge H., Huo W.M. The theoretical transition probabilities between the $B^3\Pi_g$ and the $A^3\Sigma_u^+$, $B'^3\Sigma_u^-$, $w^3\Delta_u$ states of N_2 - Chem. Phys. Lett., 1995, v.247, pp.366-372
71. Chen C.H., Payne M. G., Hurts J.P., Judish J. Kinetic studies of N_2 and N_2 -SF₆ following proton excitation - J. Chem. Phys., 1976, v.65, pp.3863-3868
72. Gat E., Gherardi N., Lemoing S., Massines F., Ricard A. Quenching rates of $N_2(C^3\Pi_u, v')$ vibrational states in N_2 and He glow silent discharges- Chem. Phys. Lett., 1999, v.306, pp.263-268
73. Millet P., Salamero Y., Brunet H., Galy J., Blanc D. and Teyssier J. I. De-excitation of $N_2(C^3\Pi_u, v'=0$ and 1) levels in mixtures of oxygen and nitrogen - J. Chem. Phys., 1973, v.58, pp.5839-5841
74. Albugues F., Birot A., Blanc D., Brunet H., Galy J., Millet P., Teyssier J. I. - J. Chem. Phys., 1974, v.61, p.2695
75. Shimec M., DeBenedictis S., Dilecce G., Babicky V., Clupac M., Sunka P. Time and space resolved analyses of $N_2(C^3\Pi_u)$ vibrational distributions in pulsed positive corona discharge - J. Phys. D: Appl. Phys., 2002, v.35, pp.1981-1990
76. Urosevic V.V., Bozin J.V. and Petrovic Y.L. Excitation of the $C^3\Pi_u$ state of N_2 by electron swarm - Zeitschrift fur Physik, 1983., v.309, pp.293-300
77. Stark G., Davis S.P. The oscillator strength of the C_2 Swan bands - Z. Phys., 1985, v.A321 (1), p.75-77
78. Bauer W., Becker K.H., Bielefeld M., Meuser R. Lifetime measurements on electronically excited $C_2(A^1\Pi_u)$ and $C_2(d^3\Pi_g)$ by laser-induced fluorescence - Chem. Phys. Lett., 1986, v.123 (1-2), p.33-36
79. Naulin C., Costes M., Dorth G. C_2 radicals in a supersonic molecular beam. Radiative lifetime of the $d^3\Pi_g$ state measured by laser-induced fluorescence - Chem. Phys. Lett., 1988, v.143 (5), p.496-500
80. Curtis L., Engman B., Erman P. High resolution lifetime studies of the $d^3\Pi_g, C^1\Pi_g$ and $D^1\Sigma_u^+$ states in C_2 with applications to estimates of the solar carbon abundance - Phys. scr., 1976, 13 (5), p.270-274
81. Bergstrom H., Hallstadius H., Lundberg H., Persson A. Detection of carbon using amplified laser-induced fluorescence - Chem. Phys. Lett. 1989, v.155 (1), p.27-31
82. Nishi N., Shinohara H., Hanazaki I. VUV laser photofragmentation of an acrylonitrile molecular beam: one-, two- and three-photon processes - J. Chem. Phys., 1982, v.77, p.246-251
83. McDonald J.R., Baronavski A.P., Donnelly V.M. Multiphoton-vacuum-ultraviolet laser photodissociation of acetylene: emission from electronically excited fragments - Chem. Phys., 1978, v.33, p.161-170
84. Chabalowski C.F., Peyerimhoff S.D., Buenker R.J. The Ballik-Ramsay, Mulliken, Deslandres-d'Azambuja and Phillips system in C_2 . A theoretical study of their electronic transition moments - Chem. Phys., 1983, v.81 (1-2), p.57-72
85. Fujita Iwao, Radiative lifetime measurement of NH radical produced by electron impact on ammonia and ammonia-argon mixture - Z. Phys. Chem. <BRD>, 1983, v.136, p.187-197
86. Garland N.L., Crosley D.R., Rotational level dependent quenching of the $A^3\Pi, v'=0$ state of NH - J. Chem. Phys., 1989, v.90 (7), p.3566-3573
87. Yarkony D.R. On the electron structure of NH radical: The fine structure splitting $X^3\Sigma$ state and spin-forbidden ($b^1\Sigma^+, a^1\Delta$) \rightarrow $X^3\Sigma$ and $c^1\Pi \rightarrow$ ($b^1\Sigma^+, a^1\Delta$) radiative transitions - J. Chem. Phys., 1989, v.91 (8), p.4745-4757
88. Seong J., Park J.K., Sun H., Transition dipole moments, transition probabilities, and radiative lifetimes for NH by ab initio effective valence shell Hamiltonian - Chem. Phys. Lett., 1994, v.228, p.443-450
89. Rohrer F., Stuhl F., Collision-induced intersystem crossing $NH(c^1\Pi)-NH(A^3\Pi)$ - J. Chem. Phys., 1987, v.86 (1), p.226-233
90. Cvejanovic D., Adams A., King G.C., Radiative lifetime measurements of NH and CH using the electron-photon delayed coincidence method - J. Phys., 1978, v.B11 (9), p.1653-1662
91. Bennet R.G., Dalby F.W., Experimental oscillator strengths of CH and NH - J. Chem. Phys., 1960, v.32 (6), p.1716-1719

92. Lavendy H., Gandara G., Robbe J.M., Oscillator strengths, radiative lifetimes, and photodissociation cross-sections for CN - J. Mol. Spectrosc., 1984, v.106 (2), p.395-410
93. Larsson M., Siegbahn P.E.M., Aagen H., A theoretical investigation of the radiative properties of the cyanogen red and violet system - Astrophys. J., 1983, v.272 (1), Pt.1, p.369-376
94. Conley C., Halpern J.B. "Laser excitation of the CN $B^2\Sigma^+ - A^2\Pi$ 0-0 and 1-0 bands, - Chem. Phys. Lett., 1980, v.73 (2), p.224-227
95. Duric N., Erman P., Larsson M., The influence of collisional transfers and perturbations in measured A and B state lifetimes in CN - Phys. Scr., 1978, v.18 (1), p.39-46
96. Knowles P.J., Werner H.-J., Hay P.J., Cartwright D.C., The $A^2\Pi - X^2\Sigma^+$ red and $B^2\Sigma^+ - X^2\Sigma^+$ violet systems of the CN radical. Accurate multireference CI calculations of the radiative transition probabilities, - J. Chem. Phys. 1988, v.89 (12), p.7334-7343
97. Bauschlicher C., Langhoff S.R., Taylor P.R., Theoretical study of the dissociation energy and the red and violet band systems of CN - Astrophys. J. 1988, v.332 (1), Pt1, p.531-538
98. Cartwright D.C., Hay J.J. "Radiative lifetimes for the $A^2\Pi$ and $B^2\Sigma^+$ electronic states of the CN molecule - Astrophys. J., 1982, v.257 (1), Pt1, p.383-387
99. Jeunehomme M., Oscillator strength of the CN red system - J. Chem. Phys., 1965, v.42 (12), p.4086-4088
100. Taherian M.R., Slinger T.G., C_2N_2 photodissociation at 1576 Å. I. CN($A^2\Pi$) radiative lifetimes, nascent vibrational distribution, and C_2N_2 quenching - J. Chem. Phys., 1984, v.81 (9), p.3814-3819
101. Lu R., Huang Y., Halpern J.B., Radiative lifetimes of the CN($A^2\Pi$) electronic state - Astrophys. J., 1992, v.395, p.710-714
102. Nishi N., Shinohara H., Hanazaki I., VUV laser photofragmentation of an acrylonitrile molecular beam: one-, two- and three-photon processes - J. Chem. Phys., 1982, v.77, p.246-251
103. Pradhan A.D., Partridge H., Bauschlicher C., The dissociation energy of CN and C_2 - J. Chem. Phys., 1994, v.101 (5), p.3857-3861
104. Sneden C., Lambert D.L. - Astrophys. J., 1982, v.259, p.381
105. Wentink T., Jsaacson L., Morreal J., Radiative lifetime of the $^2\Pi$ state of the CN red system - J. Chem. Phys., 1964, v.41(1), p.278-279
106. Katayma D.H., Miller T.A., Bondybey V.E., Radiative decay and radiationless deactivation in selectively excited CN - J. Chem. Phys., 1979, v.71 (4), p.1662-1669
107. Luk C.K., Bersohn R., Time dependence of the fluorescence of the B state of CN - J. Chem. Phys., 1973, v.58 (5), p.2153-2163
108. Mohamed K.A., King G.C., Read F.H., The use of electron impact dissociation and the photon-photon cascade technique to measure the lifetime of the $B^2\Sigma^+$ state of CN - J. Electr. Spectr. and Rel. Phen., 1977, v.12, p.229
109. Jackson W.M., Laser induced fluorescence of CN radicals - J. Chem. Phys., 1973, v.59 (2), p.960-961
110. Liszt H.S., Hesser J.E., Transition probabilities for the cyanogen $B^2\Sigma^+ - X^2\Sigma^+$ - transition - Astrophys. J., 1970, v.159 (3), p.1101-1105

Appendix D

Laser – MW technique development

1. MICROWAVE DISCHARGE INITIATED BY LASER SPARK IN AIR

Several problems are arising in practical applications of MW discharges, especially in pressure range 100-760 Torr. The most important of these – the difficulty of focusing MW radiation for getting the breakdown level of electric field in investigation flow. The complex periodic structure of MW field, arising in focus area of quasi-optic MW focusing systems, usually leads to arising of multi-plasmoid type of discharge. Typical space period of these structures is about quarter or half of wavelength. For example, more than 8-10 plasmoids arise in the focus of parabolic mirror system with aperture/wavelength ratio 25-30 and focal length/wavelength ratio 10-15 /1/. Usually only several plasmoids (1-3, as a rule) interact with AD body and its shock wave. In this case only small part of general MW impulse energy is deposited to useful plasmoids. The next problem is connected with great difficulties in managing of MW plasmoid shape. For example, for some plasmadynamic applications the spatial-elongated kind of plasmoids (air spike) is needed /2,4/. Unfortunately, the plasmoid geometry for self-maintained MW discharge is defined by the mentioned above electric field structure in the focal area of MW focusing system.

One of the possible ways to solve these problems is using of laser initiator /3,4/. The interaction of laser radiation exciting media may have either resonant /4/, or non-resonant /3/ character. In the first case the necessary conditions for semi-self maintained MW discharge can be reached without laser breakdown of the working media. But realization of resonant character of excitation in air leads to using either vacuum UV lasers, or excimer laser (ArF in /4/ for multi-photon ionization of O₂). For the second (non resonant) case wide class of Q-switched impulse lasers might be used (Ruby or Nd:YAG in present work, CO₂ in /3/). The both ways permit to manage the spatial shape of excitation area. It might be realized by varying parameters of focusing optical system (resonant excitation /4/), or creating multi-point type of laser breakdown /5/. We suppose that in aerodynamics applications the last way could be realized with using of acousto-optic technology. This technique might permit to organize the time-series of laser breakdowns in predictable area during the time interval, which is sufficiently less than characteristic time of excited area AD body interaction. It is well known, that plasma of laser spark has high temperature and electron density /5-12/. Investigations of temporal and spatial

parameters of plasma in laser breakdown, experimentally studied in /6, 8-9, 12/ and numerically simulated in /11/ show that typical lifetime of laser plasma at atmospheric pressure for 5-30 ns laser impulse and energy 100- 200 mJ is about 5-20 μ s, or more. The thermal action of laser plasma on the area near the breakdown point is usually observed during tens of milliseconds /12/. Thus, if laser plasma is created quasi –simultaneously with MW impulse and placed in the vicinity of an area of high MW electric field, it can initiate MW discharge for pressure conditions when the value of MW electric field is not sufficient for self-maintained breakdown. The developing technique may become a promising way for creating of spatially compact MW discharges with predictable shape and position for plasmadynamic applications.

1.1. Experimental facility

The scheme of experimental facility is presented on Fig.S.1. Gas-dynamic chamber (1x1x1m³) working regimes include both operations under atmospheric pressure and in vacuum regime (minimal pressure is less than 25 Torr). Inside the vacuum chamber the MW radiating and focusing system and the impulse Q-switched Ruby laser with optical system for laser beam focusing are arranged. X-range impulse MW generator with output power 180 kW and pulse duration 1,2 μ s via radiating system illuminates the parabolic mirror M1. It has the diameter 0,8 m and focal length about 0,3 m 1,2. In the focal area of this mirror the complex periodic structure of MW field is arising. This distribution has several maximums, one of these (the main maximum with a largest value of electric field) is used as working one. The center of this maximum is disposed 4 mm lower the central axis of installation. On this area, placed in the vicinity of the main MW maximum, the Ruby laser beam is focused. Laser is installed inside the chamber and can operate there only under the atmospheric pressure. For determination of the main MW maximum coordinates in the chamber, the last was pumped out to 30-40 Torr pressure and the position of self-maintaining MW discharge plasmoid was recorded. On Fig.S.2 the structure and dimensions of the working area are presented. For eliminating the influence of laser body to MW field distribution laser beam is introduced into this area through a comparatively long tube (lens holder). The focusing quartz lens has a focal length 12 mm. Ruby laser operates in Q-switched regime and generates the light impulse with 25 ns duration and output energy about 0,22 J.

Digital synchronous Schlieren system is used for visualization of shock wave structures arising in the working area and records the spatial distribution of the emitted discharge light. It has the focal length 2 m for the both telescopes, high-output power impulse LED as a source of light (visible range, 0,5 μ s pulse duration) and entirely computer-managed synchronous CCD camera for images recording. The minimal open-gate state for this camera is 12 μ s, but time resolution of the presented Schlieren system is determined by the LED characteristic (0,5 μ s). Time delays between laser impulse, MW impulse and impulse of Schlieren registration are fully managing by the CAMAC system. Time behavior of discharges luminosity in the working area is measured by fast PMT. Time resolution of this channel is better than 30 ns. Spectral range of this channel is defined by interference filter (IF) with wavelength for transmission maximum 450 nm and spectral width 10 nm. Output signal of this channel is recorded in the Flash-ADC in CAMAC system.

1.2. Results of experiments

On Fig.S.3 the shock wave structures, arising after laser breakdown in quiescent air are shown. Output energy of laser is about 220 mJ, the delays between laser and Schlieren impulses are varying from 18 to 118 μ s. Estimation of laser energy deposition for these conditions gives the value less than 40 mJ. It is necessary to note, that in spite of closed CCD camera gate for all investigating moments, very bright light from laser impulse (scattered on lens and its holder) and from laser-induced plasma, particularly passed through the gate. The shapes of these parasite signals on the presented pictures do not correspond to the shapes of radiating area. It defines only by CCD chip properties. Interesting moment on these pictures the behavior of shocks wave, reflecting from the focusing lens. After 50 μ s this wave begins to pass through quite thermally excited area of laser breakdown. As a result of interaction of this wave with heated area, the shock dramatically changes its shape. These changes have a qualitative correspondence with effects observed in our previous works [1,2]. Fig.S.4 shows the typical time diagram on the output of PMT registration channel. Optic signal from laser-induced plasma has a wide tail. The impulse of MW contribution in decaying plasma luminosity is standing out against a background for delays more than 15-20 μ s. It means that semi-self maintained MW discharge is arising during the time window corresponding to decaying phase of laser- induced plasma. On Fig.S.5 the amplitude of MW contribution vs. delay Laser -MW is presented. This signal has distinct

maximum under delays 80-100 μs . Signal duration is defined completely by the duration of MW impulse. Let us strengthen attention to the fact of time-extended phase of laser plasma decay, which exceeds 200 μs . MW field imposing in this situation may be used both for diagnostic purposes and for energy deposition in selected points of a flow. For the laser-MW delay 85 μs the series of shock wave pictures was recorded. They are presented on Fig.S.6. Left column corresponds to situation with MW contribution in wave structure, and right without MW. Delays between laser pulse and Schlieren diagnostic pulse are 108 μs for the first couple, 118 μs for second and 128 μs for the third. Delays between MW pulse and Schlieren are 23, 33 and 53 μs , correspondingly. The pictures in the left column clearly indicate the weak quasi-spherical shock wave structure, originating due to MW energy contribution. Quasi-spherical character of monitoring weak shock waves is probably connected with their propagation through strongly excited and inhomogeneous area arising after laser breakdown.

1.3. Conclusions

Concluding this topic, it should be noted that the new experimental facility for investigation of combined Laser-MW type discharge is created. The possibility of laser spark initiation of microwave discharge in quiescent air under the atmospheric pressure has been investigated. Our results show that semi-self-maintained MW discharge can arise during the time window, corresponding to decaying phase of laser-induced plasma. Contribution of MW energy in plasma luminosity has distinct maximum under the Laser-MW delays 80-110 μs , duration of this discharge is defined by MW impulse. For the Laser-MW delay 85 μs the series of shock-wave pictures is recorded. They clearly show the weak quasi-spherical shock wave structure originating due to MW energy contribution. Thus, the first important step for MW discharge position control by laser-ignited spark is made, in spite the results of this work have a preliminary character. The developing technique may become a promising way for creating of spatially compact MW discharges with predictable shape and position for plasmadynamic applications.

References to Appendix D

1. Yu.F. Kolesnichenko, A.A. Gorynya, V. G. Brovkin, et. al. Investigation of AD-Body Interaction with Microwave Discharge Region in Supersonic Flows, AIAA 2001-0345
2. Yu. F. Kolesnichenko, V.G. Brovkin, O. A. Azarova, V. G. Grudnitsky, V. A. Lashkov and I. Ch. Mashek MW energy deposition for aerodynamic application , AIAA 2003-0361
3. V. G. Brovkin, D. F. Bykov, I. A. Kossy, et. al. Gas discharge, exciting by MW radiation and CO₂ laser radiation Journal of Technical Physics, Vol. 61, N 2, 1991, p.153
4. R.B. Miles Flow control by energy addition in to high-speed air . AIAA 2000-2324
5. Yu. P. Raizer. Laser spark and discharge propagation, Moscow, Nauka, 1974
6. P. X. Tran, C. M. White Optical characterization of laser-induced spark in air AIAA 2002-0568
7. Y. L. Chen, J. W. L. Lewis and C. Parigger Spatial and temporal profiles of pulsed laser-induced air plasma emissions , Journal of Quantitative spectroscopy and radiative transfer, **67**, 91-103 (2000)
8. C. Parigger, J.W.L. Lewis, D. Plemmons Electron number density and temperature measurement in a laser-induced hydrogen plasma , Journal of Quantitative spectroscopy and radiative transfer, **53**, 249-255, 1995
9. C. Parigger, D. Plemmons, J.O.Hornkohl, J.W.L. Lewis Spectroscopic temperature measurements in a decaying laser-induced plasma using the C2 Swan system Journal of Quantitative spectroscopy and radiative transfer, **52**, 707-711, 1994
10. J. O. Hornkohl, C. Parigger, J.W.L. Lewis Temperature measurements from CN spectra in a laser-induced plasma Journal of Quantitative spectroscopy and radiative transfer, **46**, 405-411, 1991
11. R. Kandala, G. V. Candler Computation modeling of localized laser energy deposition in quiescent air AIAA 2002-2160
12. H. Yan, R. Adelgren, G. Elliott, D. Knight, M. Bogushko Laser-energy deposition in quiescent air AIAA 2003-1051.

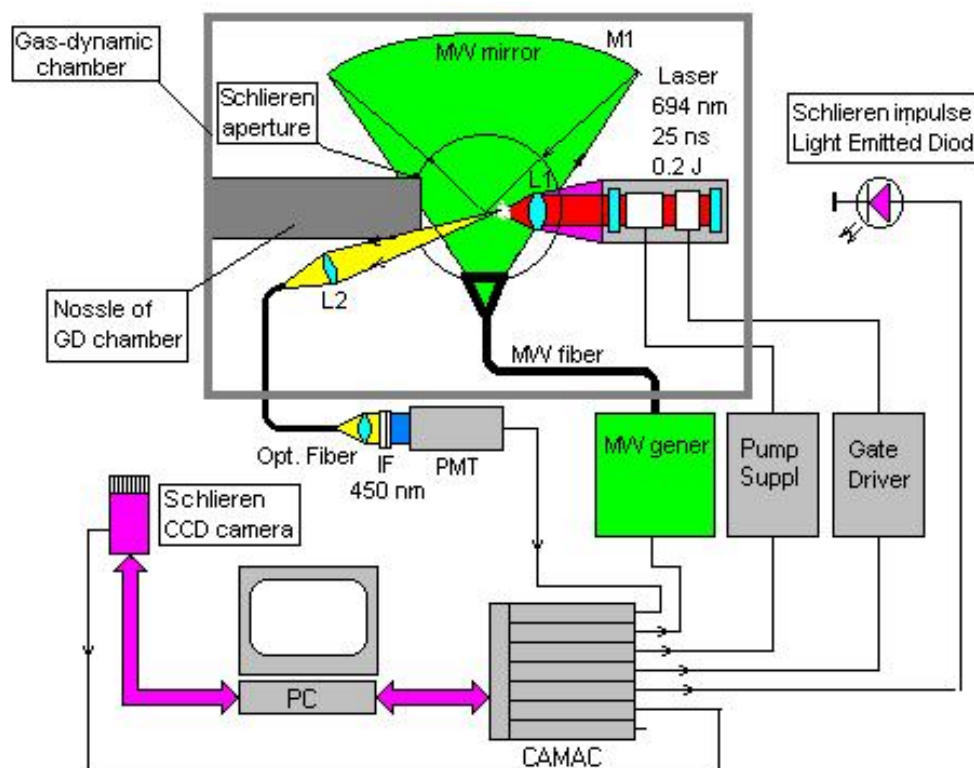


Fig.S.1. Scheme of experimental installation for investigation of combined Laser-MW discharge

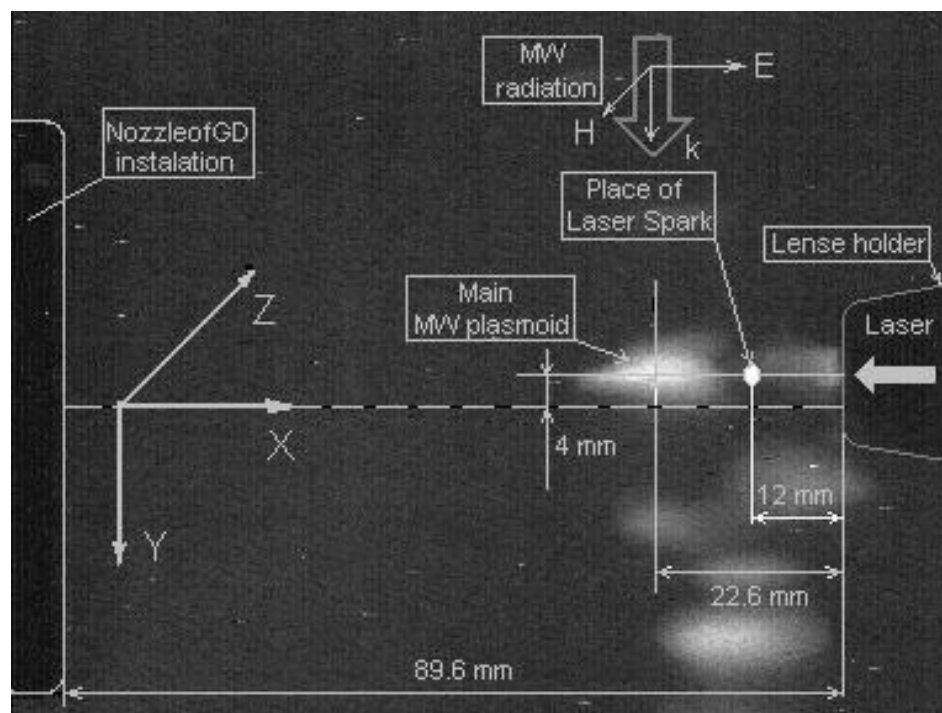


Fig.S.2. Structure and dimensions of the working area

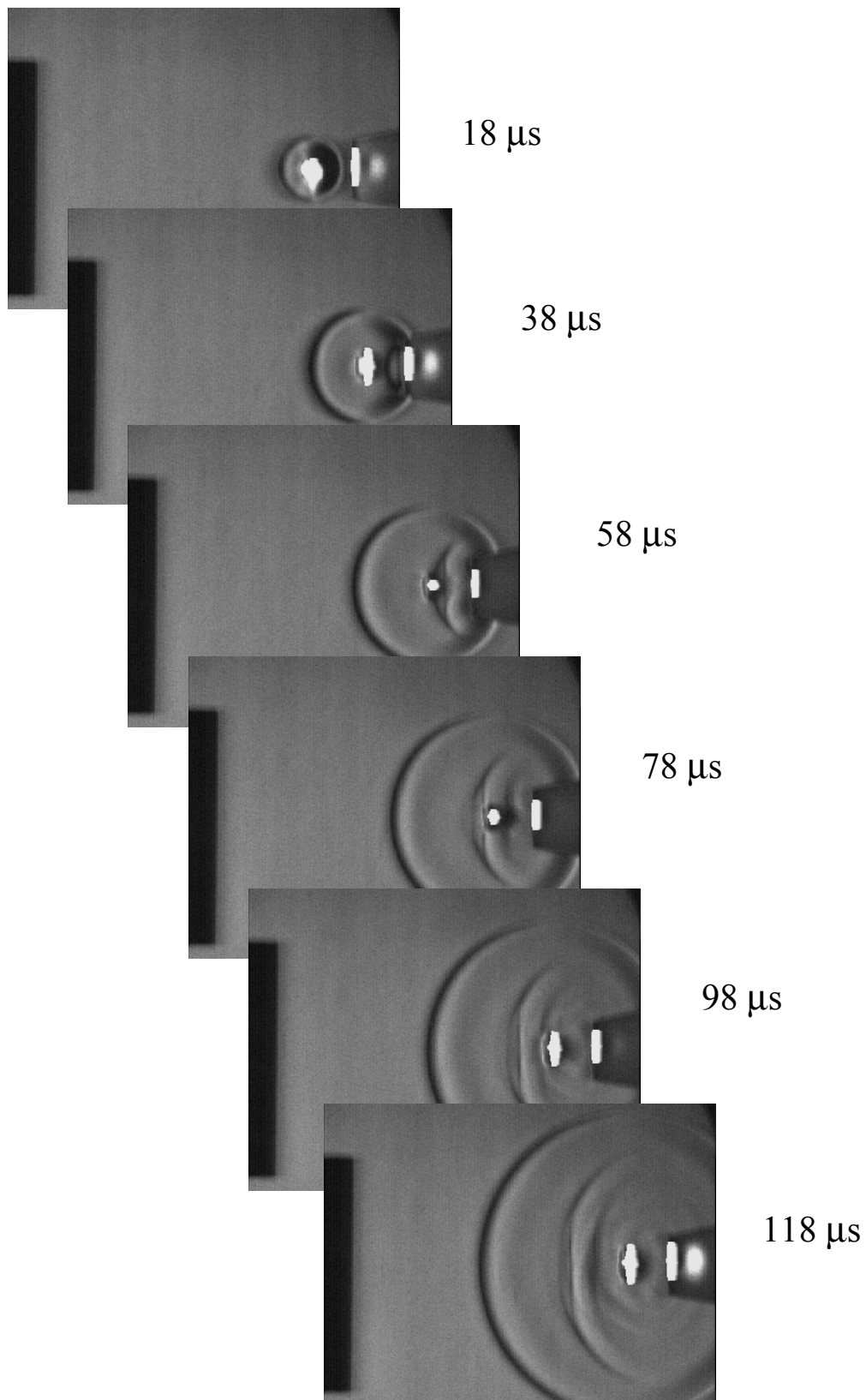


Fig.S.3. Sequence of shock wave structures, arising after laser breakdown in quiescent air

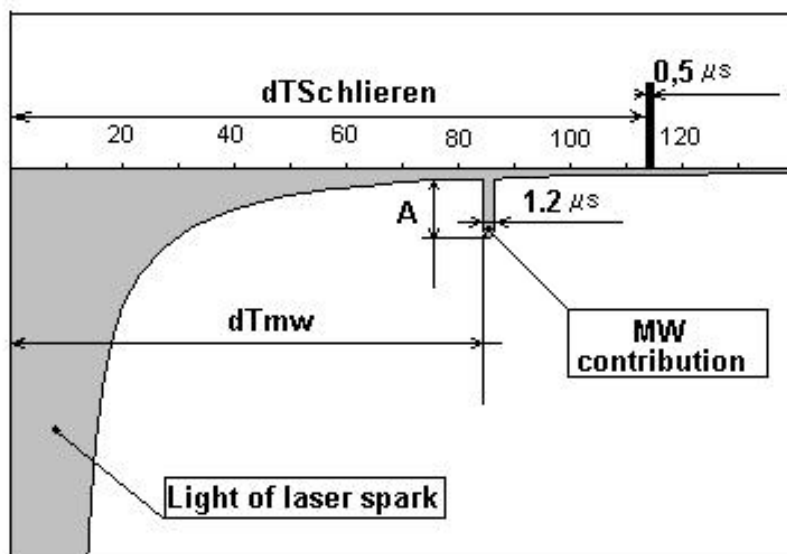


Fig.S.4. Time diagram on the output of PMT registration channel and position of Schlieren diagnostic impulse

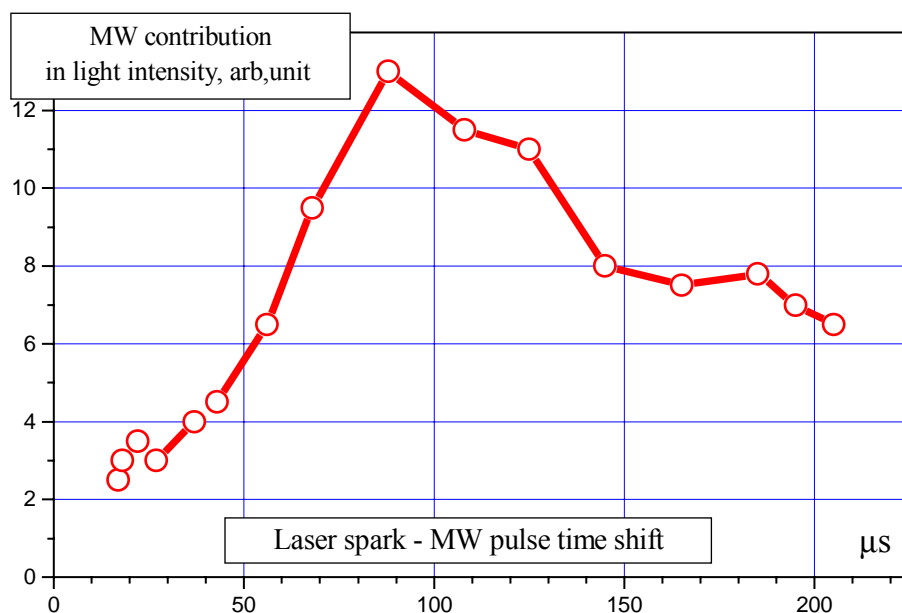


Fig.S.5. MW contribution in light intensity vs Laser-MW time shift

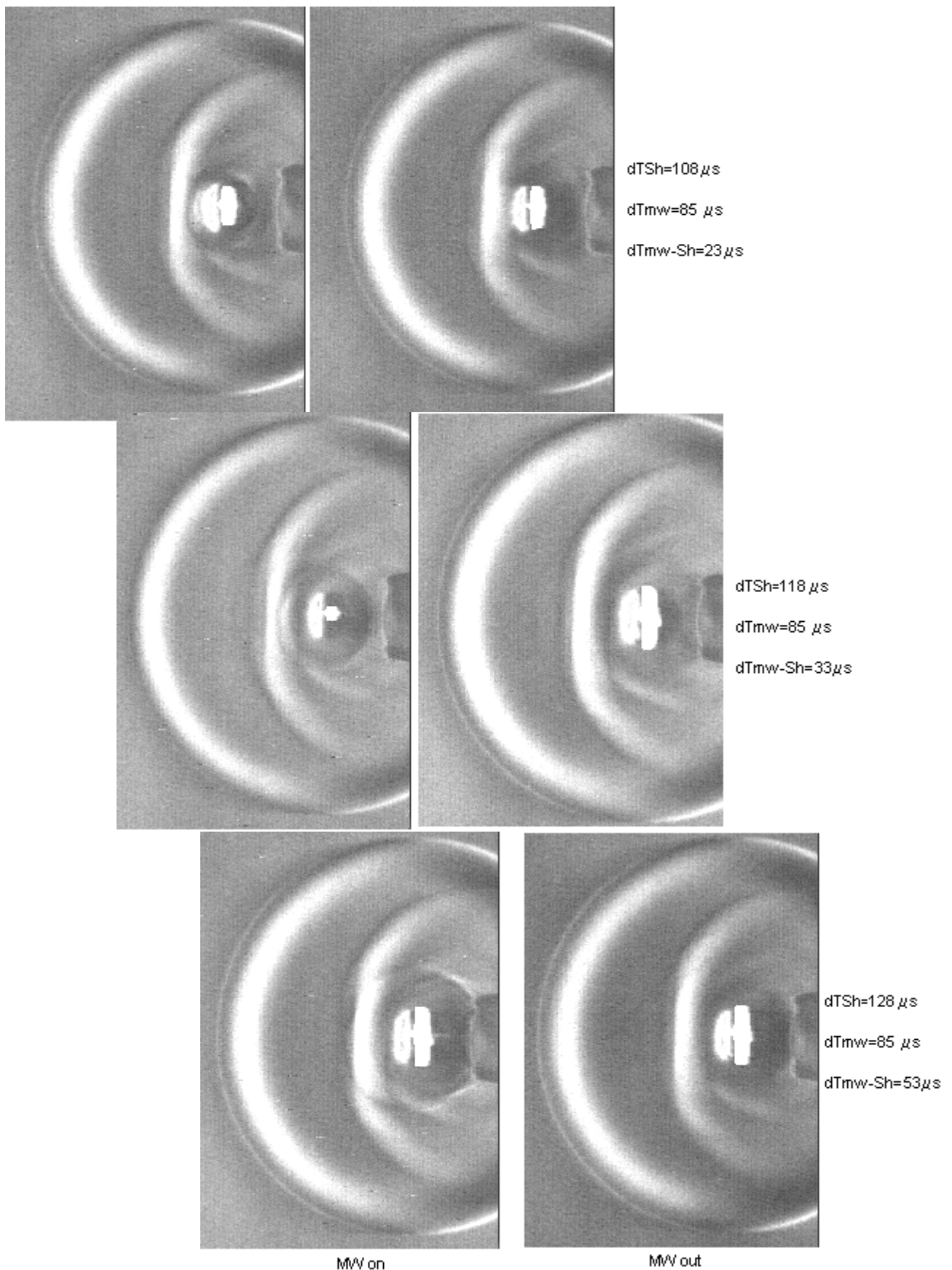


Fig.S.6. Shock wave structures, showing the MW energy deposition